

# THE SHAPE OF THE IONISED GAS ABUNDANCE DISTRIBUTION IN SPIRAL GALAXIES

Laura Sánchez Menguiano



Universidad de Granada  
Programa de Doctorado en Física y Matemáticas  
December 2017

# The shape of the ionised gas abundance distribution in spiral galaxies

Laura Sánchez Menguiano<sup>1\*</sup>

In Partial Fulfillment of the Requirements  
for the Degree of Doctor of Philosophy

Under the supervision of:  
Sebastián Sánchez Sánchez<sup>2</sup>  
Isabel Pérez Martín<sup>3</sup>

<sup>1</sup> Instituto de Astrofísica de Andalucía (CSIC), Spain

<sup>2</sup> Instituto de Astronomía, Universidad Nacional Autónoma de México

<sup>3</sup> Dpto. de Física Teórica y del Cosmos, Universidad de Granada, Spain

\* Esta tesis doctoral se ha realizado con el apoyo del MINECO a través de la ayuda BES-2013-062927 (proyectos AYA2012-31935 y AYA2016-79724-C4-4-P).



CSIC

Consejo Superior de Investigaciones Científicas

Editor: Universidad de Granada. Tesis Doctorales  
Autora: Laura Sánchez Menguiano  
ISBN: 978-84-9163-736-3  
URI: <http://hdl.handle.net/10481/49074>

Laura Sánchez Menguiano, for the Doctor of Philosophy degree in Physics,  
presented on 20<sup>th</sup> December 2017, at Universidad de Granada.

TITLE: ***“The shape of the ionised gas abundance distribution  
in spiral galaxies”***

SUPERVISORS: Dr. Sebastián Francisco Sánchez Sánchez  
Dr. Isabel Pérez Martín

EXAMINING COMMITTEE:

PRESIDENT: Dr. Brad Gibson  
SECRETARY: Dr. Almudena Zurita  
BOARD MEMBERS: Dr. Casiana Muñoz-Tuñón  
Dr. Armando Gil de Paz  
Dr. Mónica Relaño  
ACTING MEMBERS: Dr. Simon Verley  
Dr. Jorge Iglesias-Páramo  
EXTERNAL REFEREES: Dr. Fabio Bresolin  
Dr. R. Pierre Martin

The following publications were a result of work conducted during doctoral  
study:

**Shape of the oxygen abundance profiles in CALIFA face-on spiral  
galaxies** by L. Sánchez-Menguiano, S. F. Sánchez, I. Pérez, R. García-Benito,  
B. Husemann et al. Published in *Astronomy & Astrophysics*, Volume 587, id.A70.  
Year: 2016. DOI: 10.1051/0004-6361/201527450.

**Evidence of ongoing radial migration in NGC 6754: azimuthal  
variations of the gas properties** by L. Sánchez-Menguiano, S. F. Sánchez,  
D. Kawata, L. Chemin, I. Pérez et al. Published in *The Astrophysical Journal  
Letters*, Volume 830, id.L40. Year: 2016. DOI: 10.3847/2041-8205/830/2/L40.

**Arm and interarm abundance gradients in CALIFA spiral galaxies**  
by L. Sánchez-Menguiano, S. F. Sánchez, I. Pérez, V. P. Debattista, T. Ruiz-Lara  
et al. Published in *Astronomy & Astrophysics*, Volume 603, id.A113. Year: 2017.  
DOI: 10.1051/0004-6361/201630062.

**The shape of oxygen abundance profiles explored with MUSE: evi-  
dence for widespread deviations from single gradients** by L. Sánchez-  
Menguiano, S. F. Sánchez, I. Pérez, T. Ruiz-Lara, L. Galbany et al. Accepted for  
publication in *Astronomy & Astrophysics*. Year: 2017. arXiv:1710.01188.

La doctoranda Laura Sánchez Menguiano y los directores de la tesis Dr. Sebastián Francisco Sánchez Sánchez y Dra. Isabel Pérez Martín, garantizamos, al firmar esta tesis doctoral, que el trabajo ha sido realizado por la doctoranda bajo la dirección de los directores de la tesis y hasta donde nuestro conocimiento alcanza, en la realización del trabajo, se han respetado los derechos de otros autores a ser citados, cuando se han utilizado sus resultados o publicaciones.

The doctoral candidate Laura Sánchez Menguiano and the thesis supervisors Drs. Sebastián Francisco Sánchez Sánchez and Isabel Pérez Martín, guarantee, by signing this doctoral thesis, that the work has been done by the doctoral candidate under the direction of the thesis supervisors and, as far as our knowledge reaches, in the performance of the work, the rights of other authors to be cited (when their results or publications have been used) have been respected.

Granada, 31 de octubre de 2017

*Doctoranda/Doctoral candidate:*



Laura Sánchez Menguiano

*Directores de la Tesis/Thesis supervisors:*



Dr. Sebastián F. Sánchez Sánchez



Dra. Isabel Pérez Martín



# Acknowledgements

Casi me atrevería a decir que siento más responsabilidad escribiendo esta sección de agradecimientos que la tesis en sí. Aunque mi nombre sea la *cara visible* de este manuscrito, hay mucha gente detrás que, directa o indirectamente, ha hecho posible que tú, la persona que tiene ahora mismo en sus manos mi humilde trabajo, puedas estar leyendo mis palabras. Por ello, me siento en la obligación de dar lo mejor de mí (la escritura nunca ha sido mi punto fuerte) para ser capaz de reflejar cuán importante ha sido tener el apoyo de las personas que me rodean para haber llegado hasta aquí.

En primer lugar, agradecer a mis directores de tesis, Sebas e Isa, por haber creído en mí y haberme concedido la oportunidad de aportar mi granito de arena a la ciencia. Un granito pequeño, pero mío. Por haberme guiado en este camino que a veces se hacía cuesta arriba. Por hacerme sentir parte de vuestra familia. Por ser mis directores de tesis, y mis amigos.

También quiero agradecer a todos los miembros del grupo de Astrofísica Galáctica del Departamento de Física Teórica y del Cosmos de la Universidad de Granada. Por tratarme como a una más del grupo y hacerme sentir que pertenezco a este lugar (aunque venga de la competencia). Cuando tienes compañeros dispuestos a echarte una mano, los obstáculos se hacen un poco más pequeños. Gracias especialmente a Almu, que junto con Isa, me introdujeron en este mundo tan desafiante y sorprendente como es la investigación. ¡Y por no dejarme sola ante semejante desafío!

Gracias a todos los investigadores que han aportado sus ideas a mi trabajo. A los que han compartido conmigo los más y los menos en alguno de mis artículos. A los que han estado conmigo en algún congreso o *workshop*, y por supuesto, durante alguna de mis estancias. Si alguna vez me he sentido fuera de lugar en este mundillo, vosotros me habéis hecho sentir un poco más en casa.

Gracias a todas esas personas que me he cruzado a lo largo del camino y me han acompañado al menos durante un trocito del trayecto. Hacéis que la vida sea un poquito más sencilla y más divertida. Mis amigos de la Facultad de Sevilla, de la Facultad de Madrid, mis amigos del doctorado, mis amigos de todos los rincones del mundo. Y por supuesto, mis AMIGAS (sí, las que van con mayúsculas). Gracias por hacerme sentir parte de un grupo (y más que un grupo, una segunda familia) desde que era pequeñita. Con vosotras

nunca olvido lo valioso que es haber encontrado esas personas con las que compartir la vida. Os quiero.

Y llegamos a uno de los pilares fuertes. No puedo imaginarme siquiera haber conseguido llegar a donde estoy y siendo la persona que soy sin ellos. Mi familia. Desde los más lejanos a los más cercanos, todos y cada uno de ellos que me han dado forma. Y en la cúspide, ellos. Mis padres (venga, y por qué no, también mi hermano). Si me siento orgullosa de ser la persona que soy, infinitamente más orgullosa me siento de contar con ellos. Me tocó la lotería. Desde siempre he contado con su apoyo, con su cariño y con su comprensión. Han alabado mis éxitos y no han criticado ni uno sólo de mis fracasos. Los mejores padres del mundo. Y mi hermano, que a pesar del coñazo que es aguantarle, no cambio ninguna de sus bromas (qué desconcertante e incomprensible es a veces el amor). Hasta las estrellas.

Y con esto acabo. Que noooo. Que es bromaaa. ¡Cómo me iba a olvidar de ti (sin tilde, ¿te acuerdas?)! Mi otro gran pilar. El miembro más reciente de mi familia. El gran amor de mi vida. Con tu tesis tan reciente, y esos agradecimientos que me hicieron llorar a moco tendido, siento una enorme presión. Pero como de los dos el poeta siempre has sido tú, y con el acuerdo de por vida que tenemos no me puedes dejar después de leer esto, me libero de esa presión y me propongo simplemente recordarte todo eso que ya sabes. Porque lo sabes, ¿verdad? Que no sólo tengo que agradecerte tu inconmensurable ayuda para escribir esta tesis, tu disponibilidad en el día a día, tus sabios consejos, tu plantilla (qué de tiempo me has ahorrado por Dios), sino en definitiva, tu decisión (para mi desacertada, pero a la que estoy eternamente agradecida y de la que no me pienso quejarme nunca) de elegirme a mí entre todas las opciones, y como consecuencia, el estar ahí SIEMPRE para todo lo que necesito. Si ya fui afortunada con esa primera lotería, contigo me volvió a tocar por segunda vez. He conocido la felicidad más absoluta en esta vida gracias a ti. El mejor compañero de viaje que cualquiera pudiera siquiera soñar. Mis amigas siempre me dijeron que cuando llegara esa persona (¡mira que has tardado!) sería LA persona. ¡Y qué razón tenían! Ya no me imagino ningún momento de mi vida que no esté compartiendo contigo. Siempre INFINITO.

Así que ahora que sabéis que este trabajo es fruto del esfuerzo de muchas personas, espero que lo miréis con buenos ojos y seáis comprensivos con una investigadora que se está iniciando en un mundo tan difícil como este.

Atentamente,

*Laura*

*“Pedes in terra ad sidera visus”*







# Contents

	<b>Acknowledgements</b>	<b>v</b>
	<b>Summary</b>	<b>1</b>
	<b>Resumen</b>	<b>3</b>
<b>1</b>	<b>Introduction</b>	<b>7</b>
	1.1 Spiral galaxies . . . . .	9
	1.1.1 Spiral structure in disc galaxies . . . . .	13
	1.2 Interstellar Medium . . . . .	16
	1.2.1 H II regions . . . . .	17
	1.3 Measurement of gas-phase metallicity . . . . .	19
	1.4 Gas abundance distribution in spiral galaxies . . . . .	22
	1.4.1 Radial distribution . . . . .	22
	1.4.2 Azimuthal distribution . . . . .	25
	1.5 This thesis . . . . .	26
<b>2</b>	<b>Data and sample selection</b>	<b>29</b>
	2.1 CALIFA data . . . . .	31
	2.1.1 Sample selection and characterisation . . . . .	33
	2.2 AMUSING data . . . . .	36
	2.2.1 Sample selection and characterisation . . . . .	37
<b>3</b>	<b>Methodology</b>	<b>43</b>
	3.1 Measurement of the emission lines: FIT3D/Pipe3D . . . . .	45
	3.1.1 Dust extinction and reddening correction . . . . .	49
	3.2 Selection of star forming regions . . . . .	50
	3.2.1 Extraction of individual H II regions . . . . .	50
	3.2.2 Spaxel-by-spaxel extraction . . . . .	54
	3.3 Derivation of the oxygen abundances . . . . .	56
	3.4 Deprojection of galaxies . . . . .	60
<b>4</b>	<b>Oxygen abundance radial profiles with CALIFA</b>	<b>63</b>
	4.1 Derivation of the gradient . . . . .	66

4.2	Abundance gradient distribution . . . . .	68
4.3	Abundance gradients by galaxy types . . . . .	70
4.4	Common abundance gradient . . . . .	75
4.5	Deviations from negative gradient . . . . .	78
4.5.1	Flattening in the outer regions . . . . .	78
4.5.2	Oxygen abundance inner drop . . . . .	81
4.6	Dependence on the used calibrators . . . . .	82
4.7	Brief summary . . . . .	86
<b>5</b>	<b>Oxygen abundance radial profiles with AMUSING</b>	<b>87</b>
5.1	The shape of the abundance profiles . . . . .	89
5.2	Main abundance gradient distribution . . . . .	94
5.2.1	Influence of the density of the environment . . . . .	95
5.2.2	Effects of bars . . . . .	97
5.2.3	Dependence on the shape of the abundance profile . . . . .	98
5.3	Location of the inner drop and outer flattening . . . . .	99
5.4	A common oxygen abundance gradient . . . . .	101
5.5	The characteristic slope as a normalisation scale . . . . .	102
5.6	Dispersion of the gradient and mixing scalelength . . . . .	107
5.7	Dependence on the used calibrator . . . . .	110
5.8	Brief summary . . . . .	115
<b>6</b>	<b>Arm and interarm abundance gradients</b>	<b>117</b>
6.1	Analysed galaxies . . . . .	120
6.2	Classification and tracking of spiral arms . . . . .	121
6.3	Arm and interarm oxygen abundance gradients . . . . .	124
6.3.1	Comparison between flocculent and grand design galaxies . . . . .	124
6.3.2	Comparison between barred and unbarred galaxies . . . . .	129
6.4	Possible caveats of the analysis . . . . .	131
6.5	Brief summary . . . . .	134
<b>7</b>	<b>Non-radial variations of the abundance distribution</b>	<b>137</b>
7.1	Analysed galaxies . . . . .	140
7.2	Local abundance variations . . . . .	141
7.2.1	2D residual abundance maps . . . . .	143
7.2.2	Correlation with light residuals . . . . .	143
7.2.3	Dependence on galaxy properties . . . . .	144
7.3	Azimuthal variations: The case of NGC 6754 . . . . .	150
7.3.1	Residual abundance and velocity maps . . . . .	150
7.3.2	Azimuthal residual abundance and velocity profiles . . . . .	153
7.3.3	Comparison with simulations . . . . .	155
7.3.4	Radial migration in NGC 6754 . . . . .	156
7.4	Brief summary . . . . .	159

---

Conclusions and future work	161
Conclusiones y trabajo futuro	167
Appendices	175
<b>A</b> CALIFA sample characterisation tables	177
<b>B</b> AMUSING sample characterisation tables	191
<b>C</b> CALIFA sample characterisation plots	203
<b>D</b> AMUSING sample characterisation plots	211
List of Acronyms	239
List of Figures	241
List of Tables	245
References	247



# Summary

The study of the gas-phase chemical composition of spiral galaxies has proven to be a powerful tool to improve our knowledge on the evolution of these complex systems. In particular, the analysis of H II regions (regions of ionised gas associated with star formation) is of great importance, as it is through the birth and death of stars that the galaxies chemically evolve.

In this thesis we use two sets of high-quality integral field spectroscopic (IFS) data from two different surveys, CALIFA and AMUSING, to characterise the oxygen abundance distribution of the ionised gas in star-forming (SF) regions of spiral galaxies. The first survey provides a sample of 122 disc galaxies extracted from a well-defined, statistically significant mother sample, representative of galaxies in the Local Universe. The latter provides a sample of 102 galaxies that allows us to complement the study based on CALIFA data using a higher spatial resolution dataset.

The abundance distribution of the analysed galaxies is determined based on the O3N2 strong-line indicator (although others are also tested). To measure the emission lines involved we apply FIT3D, an extensively tested code designed to deal with spatially resolved IFS data.

The study of the 2-dimensional (2D) ionised gas abundance distribution is addressed by analysing separately the radial and azimuthal trends. The large number of SF regions provided by both analysed samples, together with the good coverage of the galaxy discs with high spatial resolution, allow us to undertake this study as never done before.

The radial abundance distribution is mainly characterised by a negative gradient, that seems to present a statistically characteristic slope similar for all spiral galaxies in the sample (independent of galaxy properties such as the presence of bars). Besides this gradient, a significant number of galaxies also display a drop in the abundances towards the inner parts of the discs and a flattening in the outermost regions. The existence of these features in the radial profiles is very common, revealing that the widely accepted scenario in which the oxygen abundance distribution of spiral galaxies is well described by a single radial negative gradient might be incomplete. Deviations from this single behaviour are needed to be considered for a proper characterisation of the distribution.

As a first approach to the analysis of the azimuthal abundance distribu-

tion we have performed a study based on CALIFA data for a subsample of 63 galaxies, comparing the radial gradients displayed by the spiral arms and the area outside them (interarm region). Connecting this study with theories on the nature of the spiral structure, we distinguish between flocculent and grand design galaxies according to the symmetry, continuity, and strength of the spiral arms. We also differentiate between barred and unbarred galaxies to assess the effect of the presence of bars (considered as drivers of radial redistribution of material in these galaxies) in the abundance distribution. We find that flocculent and barred galaxies (separately) present subtle differences in the arm and interarm abundance distributions, not observed in grand design and unbarred systems. We interpret these results as flocculent arms being associated with transient local density instabilities, whereas grand design arms are linked to quasi-stationary density waves. Moreover, this suggests that bars may have a direct effect on the abundance distribution (although not reflected in the overall radial profiles).

Finally, we carry out a direct analysis of the non-radial abundance distribution based on AMUSING data. First, we perform a statistical analysis for a subsample of 24 galaxies to study the presence of local abundance variations. We find differences in the residual abundances (derived by removing the radial abundance distribution to the observed one) spatially coincident with the brightest regions of the disc (that seem to correspond to the spiral arms in most cases). These differences present a significant dependence with the morphology of the spiral arms (flocculent vs. grand design arms) and the galaxy mass, suggesting that these properties might be the main drivers of local abundance variations in spiral galaxies. In addition, we develop a methodology to analyse the azimuthal distribution of the abundance residuals and we apply it to one galaxy of the sample, NGC 6754, which present some of the highest local abundance variations. In this case, we also study the gas kinematics to assess the effect of radial migration predicted by simulations in the formation of azimuthal abundance variations. We present, for the first time, clear signatures of ongoing gas radial migration affecting the abundance distribution consistent with simulations showing transient spiral arms whose pattern speeds decrease with radius.

To sum up, this thesis comprises the most complete 2D characterisation of the oxygen abundance distribution of the ionised gas in a large and statistically significant sample of spiral galaxies up to date. We show that this distribution display a wide range of features such as inner drops, outer flattenings, and azimuthal variations, as opposed to the simplistic view of a single radial decline. These features display clear trends with galaxy properties such as spiral structure, mass, or bar presence. These results provide strong constraints to chemical evolution models aimed at explaining the formation and evolution of spiral galaxies, trying to do our bit in the comprehension of the Universe around us.



# Resumen

El estudio de la composición química del gas en galaxias espirales ha demostrado ser una herramienta poderosa para mejorar nuestro conocimiento acerca de la evolución de estos complejos sistemas. En particular, el análisis de las regiones H II (regiones de gas ionizado asociadas con formación estelar) resulta de gran importancia, ya que es a través del nacimiento y la muerte de estrellas como las galaxias evolucionan químicamente.

En esta tesis usamos datos de espectroscopía de campo integral (IFS, por sus siglas en inglés) de alta calidad provenientes de dos proyectos diferentes, CALIFA y AMUSING, para caracterizar la distribución de abundancias de oxígeno del gas ionizado en regiones de formación estelar de galaxias espirales. El primero de estos cartografiados espectroscópicos nos proporciona una muestra de 122 galaxias de disco extraídas de una muestra *madre* bien definida, estadísticamente significativa y representativa de galaxias del Universo Local. El segundo nos provee con una muestra de 102 galaxias que nos permite complementar el estudio basado en los datos de CALIFA usando un conjunto de datos de mayor resolución espacial.

La distribución de abundancias de las galaxias analizadas se obtiene a partir del indicador O3N2 basado en el uso de líneas de emisión fuertes (aunque otros indicadores son también revisados). Para medir las líneas de emisión involucradas en su uso aplicamos FIT3D, un código examinado extensamente en la bibliografía y diseñado para tratar con datos de IFS espacialmente resueltos como los aquí utilizados.

El estudio de la distribución en dos dimensiones (2D) de abundancias del gas ionizado es abordado analizando separadamente las tendencias radial y acimutal. El gran número de regiones de formación estelar proporcionado por ambas muestras analizadas, junto al buen cubrimiento de los discos de las galaxias con una alta resolución espacial, nos permite llevar a cabo este estudio como nunca antes se había hecho.

La distribución radial de abundancias se caracteriza principalmente por un gradiente negativo, que parece presentar una pendiente característica estadísticamente similar para todas las galaxias espirales de la muestra (e independiente de propiedades de las galaxias como la presencia de barras). Además de este gradiente, un número significativo de galaxias muestra también una caída en la abundancia hacia las partes internas de los discos y

un aplanamiento en las regiones más externas. La existencia de estas características en los perfiles radiales es muy común, revelando que el escenario ampliamente aceptado en el cuál la distribución de abundancias de oxígeno de las galaxias espirales se puede describir adecuadamente con un único gradiente radial negativo puede ser incompleto. Desviaciones respecto a este comportamiento único son necesarias para una correcta caracterización de la distribución.

Como un primer acercamiento al análisis de la distribución acimutal de abundancias hemos llevado a cabo un estudio basado en los datos de CALIFA para una submuestra de 63 galaxias comparando los gradientes radiales exhibidos por las regiones de formación estelar de los brazos espirales y del área fuera de ellos (región interbrazo). Con el fin de conectar este estudio con teorías sobre la naturaleza de la estructura espiral hemos distinguido entre galaxias *floculentas* y *gran diseño* de acuerdo a la simetría, continuidad y definición de los brazos espirales. También diferenciamos entre galaxias barradas y no barradas para evaluar el efecto de la presencia de barras (consideradas causantes de redistribución radial de material en estas galaxias) en la distribución de abundancias. Encontramos que las galaxias *floculentas* y *barradas* (por separado) presentan diferencias sutiles entre la distribución de abundancias del brazo y del interbrazo, no observadas en sistemas *gran diseño* y no barrados. Interpretamos estos resultados asociando brazos *floculentos* con inestabilidades locales transitorias en la densidad, mientras que brazos de tipo *gran diseño* están conectados con ondas de densidad cuasi-estacionarias. Además, los resultados sugieren que las barras pueden tener un efecto directo en la distribución de abundancias (aunque no se refleje en los perfiles radiales globales).

Finalmente, llevamos a cabo un análisis de la distribución no radial de abundancias basado en los datos de AMUSING. En primer lugar, realizamos un análisis estadístico de una submuestra de 24 galaxias para estudiar la presencia de variaciones locales en la abundancia. Encontramos diferencias en los residuos de abundancias (obtenidos al sustraer la distribución radial a la observada) espacialmente coincidentes con las regiones más brillantes del disco (que parecen corresponder a los brazos espirales en la mayoría de los casos). Estas diferencias presentan una dependencia significativa con la morfología de los brazos (*floculentos* o *gran diseño*) y la masa de las galaxias, sugiriendo que estas propiedades pueden ser los principales responsables de las variaciones locales de abundancia en galaxias espirales. En segundo lugar, desarrollamos una metodología para analizar la distribución acimutal de los residuos de abundancia y la aplicamos a una galaxia de la muestra, NGC 6754, que presenta algunas de las variaciones locales de abundancia más grandes. En este caso también estudiamos la cinemática del gas para evaluar el efecto que tiene el fenómeno de migración radial ya predicho por simulaciones en la formación de variaciones acimutales de abundancia. Presentamos, por primera vez, huellas claras de migración radial de gas

en curso afectando a la distribución de abundancias. Estos resultados son consistentes con simulaciones mostrando brazos espirales transitorios cuyos patrones de velocidad decrecen con el radio.

En resumen, esta tesis constituye la caracterización más completa hasta la fecha de la distribución en 2D de abundancias de oxígeno del gas ionizado en una muestra grande y estadísticamente significativa de galaxias espirales. Mostramos que esta distribución presenta un gran abanico de características como caídas internas de la abundancia, aplanamientos externos y variaciones acimutales, en contraposición a la visión simplista de un declive radial. Estos distintivos muestran claras tendencias con propiedades de las galaxias como el tipo de estructura espiral, la masa, o la presencia de barras. Los resultados mostrados en esta tesis proporcionan fuertes restricciones a los modelos de evolución química cuyo objetivo es explicar la formación y evolución de galaxias espirales, intentando aportar nuestro grano de arena en la comprensión del Universo que nos rodea.



*The longest journey begins with a single step.*

— Lao Tse



# Introduction

## Contents

1.1	Spiral galaxies . . . . .	9
1.1.1	Spiral structure in disc galaxies . . . . .	13
1.2	Interstellar Medium . . . . .	16
1.2.1	H II regions . . . . .	17
1.3	Measurement of gas-phase metallicity . . . . .	19
1.4	Gas abundance distribution in spiral galaxies . . . . .	22
1.4.1	Radial distribution . . . . .	22
1.4.2	Azimuthal distribution . . . . .	25
1.5	This thesis . . . . .	26



THE CURIOUS NATURE OF HUMAN BEINGS has always made us wonder about the origin of our existence and the role we play in the Universe. Common questions such as where we are in the Universe, how large it is or whether we are alone in this vast amount of space make of astronomy one of the most popular branches of Physics, the field of research that can give us the answer to such big questions.

Although astronomy is the oldest natural science, going back to ancient civilizations in history such as the Babylonians, Greeks or Chinese, extragalactic astronomy, known as the study of celestial objects outside our own Galaxy, is a relatively new science. By the end of the eighteenth century, astronomers had already discovered a significant number of astronomical objects with a fuzzy structure in contrast with the point-like nature of stars, which they called ‘nebulae’. An intriguing spiral structure was even observed in some of them. However, the vision of the Universe was limited to our Galaxy, the Milky Way, and therefore all these objects were thought to belong to it. It was not until the 1920s when Edwin Hubble measured the distance to some of these nebulae and demonstrated they were located beyond the Milky Way limits. Hubble’s discovery marked the beginning of extragalactic astronomy. Still, despite the youth of this branch of astronomy, there has been a tremendous progress in the study of these extraordinary beautiful objects nowadays known as galaxies.

## 1.1 SPIRAL GALAXIES

Galaxies are the building blocks of the large scale structure of the Universe. Billions and billions of these gravitationally bound systems formed by stars, gas, dust, and dark matter shape the distribution of matter in the Universe. Galaxies come in a diversity of shapes and sizes. The vast variety of properties displayed by these objects (morphology, dynamics, environment, etc.) hampers a definitive galactic classification. Several attempts have been made to group them according to the similarities found in these systems. The most famous and widely adopted scheme was proposed by Edwin Hubble in 1926 and is known as the Hubble sequence or Hubble tuning-fork diagram (see Fig. 1.1). Based on this diagram, galaxies are classified according to their morphology, that is, their apparent shape and structure, into four major groups:

**Elliptical galaxies (E)** These systems present an apparent elliptical shape with variable elongation. They are supported via internal agitation due to the random motions of their stars. Elliptical galaxies are mainly formed by old stellar populations, whereas the presence of gas, dust and young stars is scarce. An example of elliptical galaxy (NGC 1132) can be seen in Fig. 1.2(a).

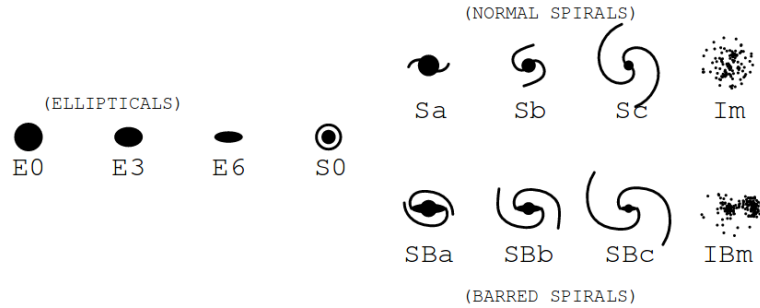


**Figure 1.1:** Schematic representation of the Hubble sequence based on galaxy morphologies. Extracted from Mo et al. (2010).

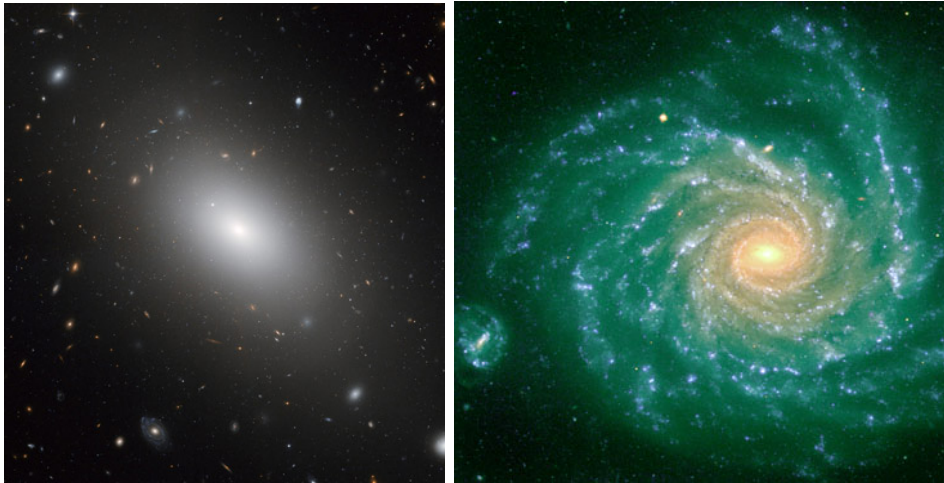
**Spiral galaxies (S)** Also known as disc galaxies, these objects are formed by an spherical nucleus (bulge) surrounded by a flat disc supported by rotation and showing a spiral structure (the spiral arms). They present stars with a wide range of ages, as well as a large amount of gas and dust, following a non-uniform distribution. Although old stars can be found in any part of these galaxies, most of the gas, dust and young stars are concentrated in the spiral arms. Some galaxies can also exhibit a central bar-like structure (SB). In Fig. 1.2(b) we show an image of NGC 1232, a typical spiral galaxy.

**Lenticular galaxies (S0)** These systems presents characteristics of both elliptical and spiral galaxies. They have a central bulge and a flat disc, as in the case of spiral galaxies, but without any spiral pattern. In the same way as elliptical galaxies, lenticular systems lack large amounts of gas and dust. The bulge component is more dominant than that in a spiral galaxy. Lenticular galaxies may also have a central bar. Figure 1.2(c) displays an example of lenticular galaxy, NGC 5866.

**Irregular galaxies (I)** These objects do not present a well defined shape but little sign of symmetry and regularity, and are very rich in gas and dust. Some have bar-like structures and other show vague signs of spiral arms. Others are totally irregular. The Large Magellanic Cloud (LMC, see Fig. 1.2(d)) is a clear example of irregular galaxy.

For historical reasons, ellipticals and lenticulars are also known as early-type galaxies, while the spirals and irregulars are referred to as late-type systems. This nomenclature was originally based on the belief that the Hubble classification represented an evolutionary sequence in which new galaxies were born as ellipticals that latter flattened and developed into spirals with the passage of time. However, this view of the Hubble sequence





(a) Elliptical galaxy NGC 1132.

Credits: NASA/ESA Hubble Space Telescope.

(b) Spiral galaxy NGC 1232.

Credits: FORS1, 8.2-meter VLT Antu, ESO.



(c) Lenticular galaxy NGC 5866.

Credits: NASA/ESA Hubble Space Telescope.

(d) Irregular galaxy LMC.

Credits: Robert Gendler.

**Figure 1.2:** *Types of galaxy morphologies*

is nowadays totally rejected, being the current belief that the morphology is determined by the combination of galaxy properties such as the mass of these systems and the environment in which they are formed (Melnick & Sargent 1977; Dressler 1980; Postman & Geller 1984; Bamford et al. 2009; Wilman & Erwin 2012).

More recently, a new classification with a more physical meaning has been proposed based on the position of individual galaxies within a colour-magnitude diagram (CMD). In the Local Universe, the distribution of galaxy colours is bimodal (Strateva et al. 2001; Blanton et al. 2003; Baldry et al. 2004; Bell et al. 2004; Blanton & Moustakas 2009). This bimodality leads us to group galaxies into a star-forming “blue cloud” and a more quiescent “red sequence”, with an in-between region known as “green valley” (see Fig. 1.3). However, this classification is not disconnected with morphology (although there is no one-to-one relation between them). Spiral and irregular galaxies tend to populate the blue cloud, whereas elliptical galaxies are mainly found in the red sequence (Strateva et al. 2001; Bell et al. 2004). Therefore, the colour bimodality is accompanied by a bimodality with respect to other physical properties including morphology, star formation rate, and surface brightness (e.g. Strateva et al. 2001; Kauffmann et al. 2003b,c).

The colour-magnitude diagram was thought to be intimately associated with a time evolution in which the green valley represented the transition state. In this evolution, star-forming galaxies would transform into the red sequence of quiescent passively evolving ones as they run out of gas (Faber et al. 2007; Bell et al. 2007; Schiminovich et al. 2007; Gonçalves et al. 2012). This gas quenching might be induced by stellar or active galactic nuclei (AGN) feedback, ram pressure stripping, or simply gas consumption. Nowadays, we know that the star formation in the last  $\sim 8$  Gyr is concentrated in spiral systems, whereas elliptical galaxies have increased significantly their mass in this period without involving star formation processes (e.g. Wolf et al. 2003; Bell et al. 2004). This makes us think that there has to be a transformation in early-type systems for them to acquire mass linked to mergers or accretion. In this way, new research suggests that there may not be a single transition scheme but two distinct paths with different physical

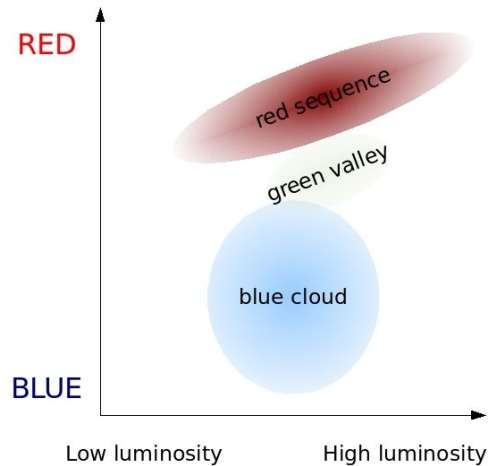


**Figure 1.3:** Schematic representation of the galaxy Colour-Magnitude diagram. Taken from Wikipedia (by Joshua Schroeder).

timescales. The first one is followed by galaxies leaving the blue cloud as disc-dominated systems (that will become passive red spirals). The other path is taken by late-type galaxies rapidly transformed into bulge-dominated systems via mergers and interactions with other systems (e.g. Schawinski et al. 2014).

This interpretation suggests that most of elliptical galaxies are the result of merger events between two or more galaxies and therefore, live preferentially in regions of very high local density like the centre of clusters or groups. Spirals, on the opposite, are mainly located in the field as isolated systems or at the outskirts of clusters and groups (Melnick & Sargent 1977; Dressler 1980; Postman & Geller 1984; Bamford et al. 2009; Wilman & Erwin 2012). As a consequence, the evolution of elliptical galaxies is dominated by violent and intense episodes occurred early in their lives (timescales of 2-3 Gyr), while the late evolution of spiral galaxies is ruled by slow, mild and continuous processes (timescales of  $\sim 8$  Gyr). Thus, the analysis of spiral galaxies is a crucial element at understanding the role of secular evolution<sup>1</sup> in building the observed Universe and gives us a better comprehension of, not only these systems, but also the initial conditions and progenitors that gave rise to elliptical galaxies. As these galaxies are the largest contributor to the star formation rate, and it is through the new generations of stars that the galaxies are enriched, they are fundamental to understand how metals are generated and increase in the Universe.

### 1.1.1 SPIRAL STRUCTURE IN DISC GALAXIES

One of the most characteristic features in disc galaxies is the spiral structure. This structure is easily distinguishable due to the association of the spiral arms with ongoing star formation. It is the presence of young, hot and bright stars that inhabit them which makes the structure so predominant in light (optical and UV regimes). According to the Galaxy Zoo project, spiral galaxies represent about two thirds of all massive galaxies in the Local Universe (Lintott et al. 2011; Willett et al. 2013), which suggests that there has to be a mechanism involved that makes stable this spiral structure.

A direct conclusion that can be inferred from observations is that not all spiral galaxies show the same appearance regarding their spiral structure. The basis of a classification system for these galaxies according to the appearance of the spiral arms was first introduced by Hubble (1926) based on the degree of winding (pitch angle) of the arms. Spiral galaxies were therefore scaled from Sa to Sd, with Sd systems presenting the most open arms

---

<sup>1</sup>Secular evolution refers to a relatively slow dynamical evolution due to internal processes induced by a galaxy's spiral arms, bars, galactic winds, black holes and dark matter haloes (Kormendy & Kennicutt 2004; Falc3n-Barroso & Knapen 2013).



(a) Grand design galaxy.

Credits: NASA Spitzer Space Telescope.

(b) Multi-armed galaxy.

Credits: NASA/ESA Hubble Space Telescope.



(c) Flocculent galaxy.

Credits: NASA/ESA Hubble Space Telescope.

**Figure 1.4:** *Classification of disc galaxies according to the spiral structure*

and the Sa ones the most tightly wound<sup>2</sup>. A more rigorous classification scheme based in the shape of the spiral arms was proposed by Elmegreen & Elmegreen (1982) and afterwards revised in Elmegreen & Elmegreen (1987). This way, spirals can be roughly divided into flocculent and grand design galaxies according to the symmetry and continuity of the spiral pattern. Flocculent galaxies present small and patchy spiral arms while grand designs are characterised by the presence of long, symmetric and continuous arms. This classification is based on 12 arm classes whose opposite ends are represented by pure flocculent and grand design galaxies. The intermediate classes show characteristics of both types, i.e. one prominent arm with some fragmented ones, tightly wrapped ringlike structure or inner/outer symmetric arms together with feathery or irregular spiral pattern. The distinctions

<sup>2</sup>This sequence also represents a decrease in the size and luminosity of the bulge and an increase in the gas content from Sa to Sd galaxies.

between some of these divisions is not straightforward as some galaxies can present characteristics of more than one class, being these cases very difficult to classify. For this reason, it was proposed later a simpler division into three types (see Elmegreen 1990): grand design galaxies (with two main spiral arms, Fig. 1.4(a)), multi-armed spirals (Fig. 1.4(b)) and flocculent galaxies (with many short arms, Fig. 1.4(c)).

However, this spiral classification based on flocculent and grand design systems is not always unambiguous. Multi-band studies have shown that galaxies can exhibit characteristics of both flocculent and grand design structures depending on the observed spectral range. In particular, some galaxies present grand design arms in the infrared band, sensitive to the presence of dust and old stars, and a more flocculent structure in the optical light, dominated by the emission of gas and young stars (e.g. Block & Wainscoat 1991; Thornley 1996; Thornley & Mundy 1997; Elmegreen et al. 1999; Kendall et al. 2011). This finding makes it even more complicated to develop theories that can explain the nature of spiral structure.

Despite its difficulty, we need to understand what makes disc galaxies display such variety of spiral structures, which nature must be directly connected to the mechanisms responsible of generating these structures. However, there is no widely accepted theory that can explain the origin of this diversity of spiral arms. Even the mere presence of this structure is a hot matter of debate. Although there is a general agreement that spirals are caused by density variations in the discs driven by gravitational instabilities, theories diverge in aspects such as the lifetime of these features or the mechanisms generating them. Some theories propose long-lived quasi-stationary patterns (density wave theories, e.g. Lin & Shu 1964; Bertin & Lin 1996), while others support the idea that spiral arms are short-lived, recurrent transient patterns that form through local instabilities which are swing amplified into spiral arms (e.g. Julian & Toomre 1966; Toomre 1990). In the current interpretation, flocculent arms are typically associated with local instabilities, whereas grand design galaxies are linked to the steady state density wave theory (e.g. Dobbs & Bonnell 2008; Dobbs & Baba 2014). However, this is far from being a solved question and observational evidences are necessary in order to distinguish between the different proposed mechanisms that can shape the spiral arms in galaxies. Thanks to the development of new instrumental techniques, these evidences are nowadays within reach.

These observational evidences have to come from the analysis of the baryonic matter in these systems, dominated mainly by stars and gas. The density variations giving rise to the spiral structure affect likewise both components, increasing the density of stars in the arms in one case and triggering star formation as gas collapses in the other. Thus, the observational characterisation of both stars and gas in disc galaxies is crucial to understand the formation of the spiral structure. This thesis will focus on the analysis of the

gas component, in particular, the ionised gas associated with star formation (that will be described in the following sections).

## 1.2 INTERSTELLAR MEDIUM

The term interstellar medium (ISM) is used to describe the gas and dust that occupy the space between the stars. The gaseous interstellar medium is intimately associated with stellar evolution. Stars form from cool dense clouds in the ISM, and at the end of their lives they return matter to it, increasing gradually the amount of metals (metallicity) of the galaxies. The study of the ISM is therefore crucial to understand the chemical evolution of galaxies, as they are tightly associated with star formation processes.

The presence of diffuse matter between the stars was discovered by Johannes Hartmann in 1904 analysing the spectra of stars belonging to binary systems. The orbital movement of the components produce the displacement of the absorption lines caused by the atmospheres of the stars due to the Doppler effect. However, he realised that the spectrum of some stars presented also stationary lines (associated with calcium) that should be generated in the space between the stars and the observer. This was later confirmed through the detection of interstellar sodium by Heger in 1919 in a similar way than Hartmann identified the calcium absorption. Since then, we have acquired significant knowledge about the components and properties of the ISM.

Although the ISM is fundamentally gaseous (by mass, 99% of the ISM is gas and just 1% is dust, Boulanger et al. 2000), the presence of dust is noticeable. The interstellar dust consists of tiny solid grains formed by elements heavier than helium and their compounds. The typical size of a dust particle ( $0.5 \mu\text{m}$ ) is comparable to the wavelength of light, and thus makes them particularly effective at scattering light, as well as absorbing it. Depending on the amount of dust, this phenomenon can significantly reduce the brightness of an observed object, producing an extinction effect.

Regarding the gas component, by mass we can estimate that roughly 70% is hydrogen, 28% is helium and 2% correspond to other elements heavier than helium (Ferrière 2001)<sup>3</sup>. Hydrogen is therefore the most abundant element in the ISM. This element can exist in atomic form (neutral or ionised) or molecular form, depending on the physical conditions of the medium, such as density, temperature and amount of high-energetic radiation. In high-density, low-temperature environments with a low UV flux the hydrogen is mostly in the form of molecular hydrogen ( $\text{H}_2$ ). In environments where the temperature and/or the UV flux is high enough to free the hydrogen atom's

---

<sup>3</sup>Although this estimation comes from the study of our Galaxy, similar percentages can be inferred for any external galaxy.

electron we can find ionised hydrogen (HII), especially where the density is low enough to hamper the recombinations between the free electrons and the positive ions. Finally, atomic hydrogen (HI) is present in environments with intermediate conditions between the mentioned extremes.

Studies on the composition and distribution of the gas in the Milky Way have shown that there are different phases of the ISM characterised by particular values of temperature and density (Knapp 1995; Ferrière 2001), such as the cold atomic clouds, the coronal gas or the H II regions. Among all, H II regions contain just a few per cent of the ISM's mass and occupy a minimum part of its volume ( $\sim 1\%$ ). However, they are of great importance to understand the processes of star formation, and with them, the chemical evolution of galaxies, as it is through the birth and death of stars that the galaxies are chemically enriched (Peimbert & Costero 1969; Peimbert & Spinrad 1970).

### 1.2.1 H II REGIONS

H II regions are the result of the photoionisation of clouds of gas and are associated with star formation. The ionising photons come from young and hot stars of the first spectral types (O-B, effective temperatures of  $2 \cdot 10^4 - 6 \cdot 10^4$  K). These hot stars emit UV radiation with enough energy as to ionise hydrogen and other elements. The ionisations are followed by the corresponding recombinations, finally reaching a local equilibrium between these two processes. This balance determines the ionisation level of the different elements present in the nebula (Osterbrock 1989).

At a first order, the physical processes that take place in these gaseous nebulae are well known. We have been able to determine their physical properties from observations and develop models capable of reproducing them. The first and simplest model of an H II region was derived by Bengt Strömgren in 1937. This model assumes an homogeneous region (of constant density) of gas consisting entirely of hydrogen in which interior a single star is being formed. When the star starts to emit photons, they ionise the surrounding hydrogen forming a spheric region completely ionised. This region is known as the Strömgren sphere and its radius determines the size of the H II region. The radius depends on the intensity of the source of ionising photons and the density of the region (Strömgren 1939).

Actually, the scenario is far more complex. Depending on the size of the H II region there may be several thousand stars within it. Each star ionises a roughly spherical region of the surrounding gas (Strömgren sphere), but the combination of the ionisation spheres and the expansion of the heated nebula into surrounding areas (with a possible change of conditions due to dust effects) create sharp density gradients that result in complex and inhomogeneous shapes. For instance, studies on the Orion Nebula, the closest



**Figure 1.5:** *The Orion Nebula (M42) H II region. Credits: Jim de Lillo & the ESA/ESO/NASA Photoshop FITS Liberator.*

and one of the best known and most studied H II regions (Bohlin & Savage 1981; Osterbrock et al. 1992; Pogge et al. 1992; Esteban et al. 1998; Ferland 2001; O’dell 2001; Esteban et al. 2004; Sánchez et al. 2007; Takahashi et al. 2013; Bally et al. 2015, e.g.), have revealed this region presents a form of thin blister of ionised material (see Fig. 1.5). Observations of Galactic H II regions such as the Orion Nebula have been important tools to better understand the structure of these regions and improve models able to explain them (Osterbrock & Flather 1959; Zuckerman 1973; Baldwin et al. 1991; Rubin et al. 1991).

The high brightness of the H II regions allows us to observe them up to considerable distances in the Universe. Thanks to this fact, we can study H II regions in external galaxies and, thus, characterise the structure and properties of the gaseous ISM in the diverse range of conditions present in galaxies. In particular spiral galaxies, due to the large amount of gas present in them, can contain hundreds of H II regions, providing excellent statistics to study the variation of star-formation properties within and between galaxies.

Some of the first observational works analysing the statistical properties of H II regions in external spiral galaxies were performed by Kennicutt (1988) and Kennicutt et al. (1989a). In these works, they found a significant dependence of some H II regions properties (luminosity, size, number of detected regions) on the morphological type of their host galaxy. Since then, a large amount of works have been focused in the study of the properties of H II regions such as the luminosity, the equivalent width, the size



or the luminosity function (e.g. Kennicutt et al. 1989b; Rozas et al. 1996; Ho et al. 1997; Knapen 1998; Rozas et al. 1999; Alonso-Herrero & Knapen 2001; Cedrés & Cepa 2002; Helmboldt et al. 2005; Sánchez et al. 2012b). However, among all properties, the one that has received more attention is the metallicity of the H II regions, which depends on previous stages of the chemical evolution of the galaxies and determines the chemistry of the stars to come. As a consequence, its study is important in understanding the processes involved in the formation and evolution of galaxies.

### 1.3 MEASUREMENT OF GAS-PHASE METALLICITY

In astronomy, all chemical elements heavier than helium are collectively termed ‘metals’. The mass fraction of a baryonic component (gas, stars) in metals is referred to as its metallicity. Oxygen alone constitutes (by number) nearly 50% of the metals, making it the best proxy for studying the gas metallicity.

H II regions are, together with planetary nebulae, the only form of the interstellar material which emits strongly in the optical spectral region through a set of well defined emission lines. The main mechanisms producing these emission lines are collisional transitions of metals such as oxygen or nitrogen and recombinations of hydrogen and helium. Metals such as carbon, nitrogen, and oxygen also produce recombination lines, but they are much weaker due to their lower abundances with respect to hydrogen and helium. Therefore, nebular emission lines from individual H II regions have been, historically, the main tool at our disposal to measure the gas-phase metallicity. A typical spectrum of an H II region and the most important emission lines present are shown in Fig. 1.6.

The most direct method developed to measure abundances from observed spectra requires using temperature-sensitive line ratios such as  $[\text{O III}] \lambda\lambda 4959, 5007 / [\text{O III}] \lambda 4363$ . This is known as the  $T_e$ -method (Peimbert & Costero 1969; Stasińska 1978; Pagel et al. 1992; Vilchez & Esteban 1996; Castellanos et al. 2002; Kennicutt et al. 2003; Bresolin et al. 2004; Izotov et al. 2006, among many others). However, the weakness of some of these lines (that become even fainter as the metallicity increases<sup>4</sup>) hampers their detection and makes this method only applicable to H II regions in very nearby galaxies for which very high Signal to Noise ratio (S/N) spectra are observable.

For this reason, alternative procedures based on relations (calibrations) between metallicity and the intensity of strong and more easily observable lines (indicators) were proposed. This way, two families of calibrators have

---

<sup>4</sup>When the amount of metals increases, a more efficient cooling mechanism begins to act through the metal lines, which produces a decrease in the temperature.

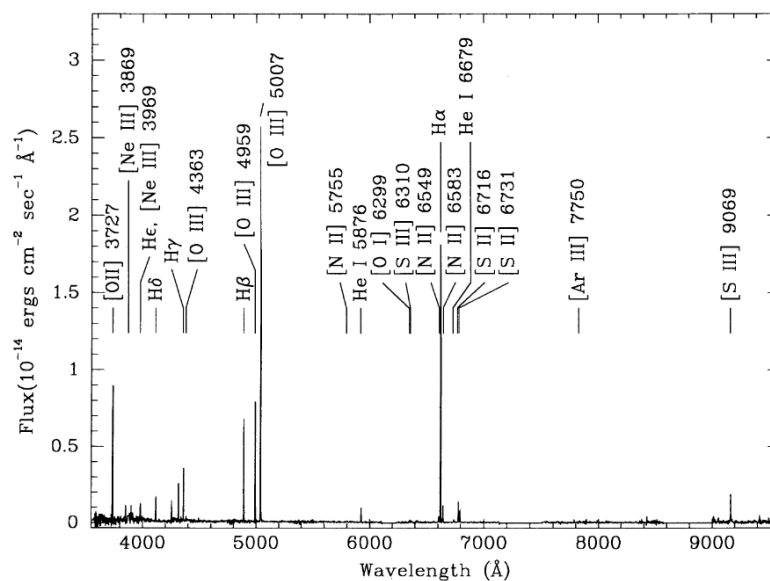


**Figure 1.6:** Example of a spectrum of an HII region in NGC 2541 taken from Zaritsky et al. (1994). The main emission lines are labeled.

been developed and are widely used today: empirical calibrators based on direct estimations of oxygen abundances and theoretical calibrators based on photoionisation models. Some of the most commonly used indicators based on these ratios and the subsequent calibrations are the following:

**R23** Firstly introduced in Pagel et al. (1979) and defined as

$$R23 = \log_{10} \left( \frac{[\text{O II}] \lambda 3727 + [\text{O III}] \lambda \lambda 4959, 5007}{H\beta} \right). \quad (1.1)$$

Since then, a substantial effort has been put in calibrating  $R23$ , both via empirical (Zaritsky et al. 1994; Pilyugin 2000; Pérez-Montero & Díaz 2005) and theoretical (McGaugh 1991; Kewley & Dopita 2002; Kobulnicky & Kewley 2004) calibrators. One of the biggest issues with this abundance indicator is its double-valued behaviour with oxygen abundance, requiring therefore additional criteria to distinguish between the two existing branches (the two possible metallicity values for a given  $R23$  value).

**N2** Defined as

$$N2 = \log_{10} \left( \frac{[\text{N II}] \lambda 6583}{H\alpha} \right), \quad (1.2)$$

this indicator proposed by Denicoló et al. (2002) is single-valued and the involved lines are so close in wavelength that the effects of reddening are minimised. However, it suffers from uncertainties due to its

dependence on the ionisation parameter and the N/O ratio, being most suitable for the low-metallicity regime. Some empirical calibrations for this index are presented in Pettini & Pagel (2004), Pérez-Montero & Díaz (2005), and Marino et al. (2013).

**O3N2** Introduced by Alloin et al. (1979), this index is given by

$$O3N2 = \log_{10} \left( \frac{[\text{O III}] \lambda 5007 / H\beta}{[\text{N II}] \lambda 6583 / H\alpha} \right). \quad (1.3)$$

This indicator is also almost unaffected by reddening due to the close distance in wavelength between the involved lines. In addition, it presents certain advantages over *R23* and *N2* especially when applied to galaxies at high redshift. The most popular calibrations making use of this index are provided in Pettini & Pagel (2004) and Marino et al. (2013).

**S23** Proposed by Vilchez & Esteban (1996), this indicator is also relatively independent of reddening. However, it is double-valued and makes use of sulphur lines that are quite weak and are located in the infrared band for galaxies at high redshift. It is given by

$$S23 = \log_{10} \left( \frac{[\text{S II}] \lambda \lambda 6717, 6731 + [\text{S III}] \lambda \lambda 9076, 9532}{H\beta} \right) \quad (1.4)$$

Both empirical (e.g. Christensen et al. 1997; Díaz & Pérez-Montero 2000; Pérez-Montero & Díaz 2005) and theoretical (e.g. Kewley & Dopita 2002) calibrations have been proposed based on this index.

Besides the mentioned abundance indicators, many others have been also developed making use of alternative ratios such as  $[\text{N II}]/[\text{O II}]$ ,  $[\text{S II}]/[\text{O II}]$ ,  $[\text{N II}/\text{S II}]$  or  $[\text{O III}/\text{S II}]$ , giving rise to new calibrations (e.g. Pilyugin 2000; Kewley & Dopita 2002; Dopita et al. 2006, 2013; Pérez-Montero 2014; Dopita et al. 2016).

However, not all the calibrators provide consistent abundances. The discrepancies usually manifest as a systematic offset, with  $T_e$ -based empirical calibrations deriving abundance values that are at least 0.2 – 0.4 dex lower than strong-line methods based on photoionisation models. For a deeper revision of the different methods, their strengths and their caveats, see López-Sánchez et al. (2012).

All the mentioned methods of estimating abundances, based on the use of collisional lines, depend highly on the electron temperature, which could lead to systematically underestimated gas-phase metallicities (Esteban et al. 2004; Peimbert et al. 2005; Toribio San Cipriano et al. 2016). This can be overcome by measuring abundances making use of recombination lines,

which ratios are independent of the electron temperature. However, due to the faintness of these lines (much weaker than the auroral lines used in the  $T_e$ -method), the use of large telescopes is needed in order to obtain deep and high-resolution spectra. Even in these latter cases, this method of deriving abundances is only feasible in very nearby and bright gaseous nebula (e.g. Peimbert et al. 1993; Peimbert 2003; García-Rojas et al. 2004, 2006; Bresolin 2007; López-Sánchez et al. 2007; Esteban et al. 2009).

Therefore, the use of the strong-line method is so far the most suitable tool to characterise the gas abundance distribution in external galaxies. This way, the improvement in photoionisation models and the development of larger telescopes and better instruments to gather spectroscopic data, have exponentially boosted our knowledge regarding the gas abundance distribution in spiral galaxies.

## 1.4 GAS ABUNDANCE DISTRIBUTION IN SPIRAL GALAXIES

A complete characterisation of the gas abundance distribution involves, not only the study of radial variations, but also azimuthal changes related with the presence of a bar or the spiral structure. Although the radial distribution of the chemical abundances in disc galaxies has been studied for decades it has not been until the last few years that a proper characterisation of the two-dimensional (2D) extension of these systems has been feasible.

### 1.4.1 RADIAL DISTRIBUTION

Indistinctly of the method used to derive the abundances (see Sect. 1.3), at present it is unquestionable that spiral galaxies exhibit in general a negative trend in metallicity (see Fig. 1.7). The first study suggesting the presence of radial abundance gradients in galaxies was Searle (1971). The author interpreted the observed increase in the  $[\text{O III}]/\text{H}\beta$  and  $\text{H}\alpha/[\text{N II}]$  ratios with the galactocentric radius as a large-scale radial abundance gradient, with O and N abundances having low values at the outskirts and increasing towards the centre. This interpretation was later confirmed by other studies during the 1970s (e.g. Shields 1974; Comte 1975; Smith 1975; Peimbert 1979).

Since then, an extensive body of literature has been amassed on the subject of abundance gradients in nearby galaxies supporting these negative trends (Martin & Roy 1992; Vila-Costas & Edmunds 1992; Zaritsky et al. 1994; van Zee et al. 1998; Kennicutt et al. 2003; Bresolin et al. 2009b; Moustakas et al. 2010; Rosales-Ortega et al. 2011; Bresolin et al. 2012; Marino et al. 2012; Patterson et al. 2012; Rich et al. 2012, among many others). In the Milky Way, the presence of a gas abundance gradient has also been

extensively reported (e.g. Shaver et al. 1983; Deharveng et al. 2000; Pilyugin et al. 2003; Esteban et al. 2005; Quireza et al. 2006; Rudolph et al. 2006; Balser et al. 2011; Esteban et al. 2017).

The existence of these abundance gradients is directly related to the process of formation and evolution of spiral galaxies. Chemical models agree that spiral discs build up through accretion of material, which leads to an inside-out growth (Matteucci & Francois 1989; Boissier & Prantzos 1999). The accretion brings gas into the inner parts of the discs, where it reaches high densities that trigger violent and quite efficient star formation. Thus, there is a fast re-processing of gas in the inner regions, which leads to a population of old, metal-rich stars surrounded by a high-metallicity gaseous environment, while the outer regions are populated by younger, metal-poor stars formed from poorly enriched material. In this context, the study of metallicity gradients provides strong constraints for the main parameters describing these chemical evolution models (Koeppen 1994; Edmunds & Greenhow 1995; Tsujimoto et al. 1995; Carigi 2000; Prantzos & Boissier 2000; Chiappini et al. 2001; Mollá & Díaz 2005; Fu et al. 2009; Pilkington et al. 2012; Gibson et al. 2013).

However, gas metallicity studies have also presented some hints of the existence of some behaviours in the oxygen abundance profiles that deviate from the pure inside-out scenario: A decrease or a nearly flat distribution of the abundance in the innermost region of discs, first observed by Belley & Roy (1992); and a flattening in the gradient in the outer regions measured in several works (Martin & Roy 1995; Vilchez & Esteban 1996; Roy & Walsh 1997, among others). Despite the wide variety of mechanisms proposed to explain the presence of these features (such as radial migration, Minchev et al. 2011, 2012; or satellite accretion, Qu et al. 2011; Bird et al. 2012), its origin is still unclear.

All the previously mentioned studies were limited by statistics, either in the number of observed H II regions or in the coverage of these regions across

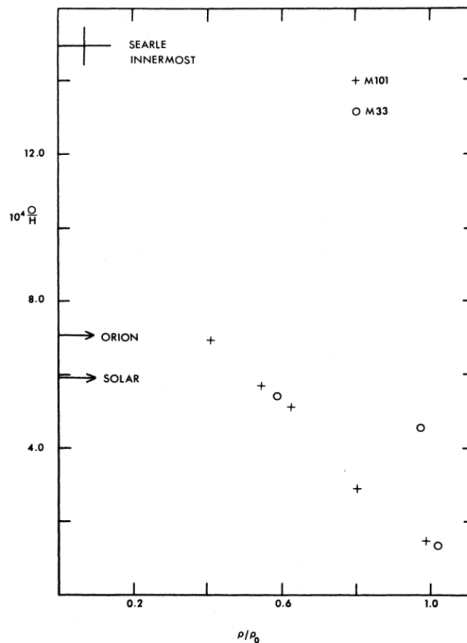


**Figure 1.7:** Oxygen abundance gradients in M101 and M33 taken from Smith (1975).

the galaxy surface. Gas-phase chemical studies have significantly benefited from the development of Integral Field Spectroscopy (IFS) techniques that have allowed the 2D characterisation of the abundance distribution in galaxies.

Moreover, IFS surveys offer the opportunity of extending the study to a large number of objects, allowing for meaningful statistical analysis. Still, until recently, this technique was rarely used in a survey mode, with just a few exceptions such as the SAURON survey (Bacon et al. 2001), the Disk Mass Survey (Bershady et al. 2010) and the ATLAS3D Survey (Cappellari et al. 2011). However, these pioneering projects were not optimal for a statistical study of the properties of H II regions because of the incomplete coverage of the full extent of the galaxies, the very limited wavelength range for gas-phase studies or the lack of late-type galaxies in the sample. A proper statistical study able to analyse the gas abundance distribution across the whole galaxy discs started with the development of the PINGS project (Rosales-Ortega et al. 2010), which acquired IFS mosaic data for a dozen very nearby galaxies. This project was followed by the observation of a larger sample of face-on spiral galaxies (Mármol-Queraltó et al. 2011) as part of the feasibility studies for the CALIFA survey (Calar Alto Legacy Integral Field Area). The advent of recent surveys such as CALIFA (Sánchez et al. 2012a), SAMI (Croom et al. 2012) or MaNGA (Bundy et al. 2015) allowed extending the study to much more representative samples of nearby galaxies by covering all morphologies.

Based on large-statistics samples of H II regions extracted from galaxies observed by CALIFA and PINGS, Sánchez et al. (2012b, 2014) studied the distribution of metals within star-forming galaxies and provided the strongest evidence so far for a characteristic gas abundance gradient out to two effective radii ( $r_e$ ). These studies also confirmed the existence of deviations from this gradient with unprecedented statistics, deviations that were already observed by other IFS works on individual galaxies (e.g. Bresolin et al. 2009b; Sánchez et al. 2011; Rosales-Ortega et al. 2011; Bresolin et al. 2012; Marino et al. 2012).

Plenty of studies on the radial abundance gradients have analysed possible relations between the slope and some properties of the galaxies. For instance, it has been observed that interacting galaxies present shallower gradients than isolated systems (Kewley et al. 2010; Rupke et al. 2010b; Rich et al. 2012; Miralles-Caballero et al. 2014; Rosa et al. 2014; Sánchez et al. 2014). In the case of the luminosity or mass of the galaxies, no trends of the abundance slope with these properties have been found (Zaritsky et al. 1994; Garnett et al. 1997; Sánchez et al. 2014; Ho et al. 2015). However, there is also a disagreement in some results. McCall et al. (1985), Vila-Costas & Edmunds (1992), and Oey & Kennicutt (1993) stated a dependence of the abundance slope on the morphological type of galaxies, with

later types showing steeper gradients. On the contrary, other studies have suggested gradients independent of galaxy morphological type (Diaz 1989; Zaritsky et al. 1994; Sánchez et al. 2014) when normalising to a physical scale of the disc. A correlation between the abundance slope and the presence of a bar has also been claimed, with barred galaxies presenting flatter gradients (Vila-Costas & Edmunds 1992; Martin & Roy 1994; Zaritsky et al. 1994; Roy 1996; Dutil & Roy 1999). Although, again, the opposite result has been shown by recent works on either stellar or gas-phase metallicity (Sánchez et al. 2012b, 2014; Sánchez-Blázquez et al. 2014; Cheung et al. 2015). These contradictory results, maybe due to the use in some studies of small and heterogeneous samples and/or out-of-date abundance calibrators, confirm the necessity of analysing the radial abundance distribution with new improved calibrators and larger sample of galaxies.

#### 1.4.2 AZIMUTHAL DISTRIBUTION

Unlike the analysis of the radial distribution of the gas-phase abundances, that has been extensively studied, the azimuthal distribution has been barely assessed observationally. At first glance, the chemical distribution of the ISM in spiral galaxies was considered to be highly homogeneous (Scalo & Elmegreen 2004). However, radial movements undergone by gas and stars have been invoked lately to produce small inhomogeneities in the galaxy chemical distribution. Although the causes of this so-called radial migration still remain unclear, several simulations have attempted to understand this important phenomenon in galaxy evolution, finding that both gas and stars might migrate (e.g. Minchev et al. 2014; Grand et al. 2015). In particular, recent simulations have shown that radial migration can induce azimuthal variations of the stellar metallicity distribution (Di Matteo et al. 2013; Grand et al. 2016). Regarding the gas content, streaming motions along the spiral arms have been proposed (Grand et al. 2015; Baba et al. 2016), which could also produce azimuthal variations of the gas abundance.

The first approach followed in the search for evidences of azimuthal variations in the metallicity has been made by analysing the scatter relative to the radial abundance gradients. However, there have been just a few studies in this regard, all of them focused on individual galaxies. Analysis on NGC 300 (Bresolin et al. 2009a), M 33 (Bresolin 2011), or NGC 628 (Berg et al. 2015) reveal small scatter values consistent with the uncertainties in the abundance measurements. On the other hand, other observational studies on M 31 (Sanders et al. 2012), NGC 6754 (Sánchez et al. 2015), and M 101 (Kennicutt & Garnett 1996; Li et al. 2013; Croxall et al. 2016) have found a substantial dispersion that can be taken as an evidence of the presence of azimuthal variations. In the case of M 101 it has been suggested that these variations may be the result of a recent tidal interaction already

reported in this galaxy (Mihos et al. 2012).

Another approach to study azimuthal differences is the analysis of the arm-interarm abundance variations. However, even fewer works have focused on this study, all of them not finding evidences of chemical differences between arm and interarm regions. Martin & Belley (1996), analysing a sample of 7 galaxies, did not observe significant variations in the gas metallicity between these two distinct regions. Cedrés & Cepa (2002) carried out a study for two galaxies analysing different properties of the H II regions (distribution, H $\alpha$  equivalent width, metallicity) of the arm and interarm regions, observing similar trends in their properties.

On a larger scale, a few other studies have analysed global azimuthal asymmetries by dividing the disc of the galaxies in sectors and comparing the trends observed in the oxygen abundances for the different areas (Rosales-Ortega et al. 2011; Zinchenko et al. 2016). The former study was focused on NGC 628, while the latter analysed 88 late-type spiral galaxies. In both cases, the observed variations were small and attributed to the uncertainties involved in the analysis of the abundances.

Finally, Cedrés et al. (2012) studied the 2D distribution of the gas metallicity of another two galaxies and found that the presence of azimuthal inhomogeneities depends on the calibrator used to derive the metallicity. Recently, Vogt et al. (2017) studied the oxygen abundance distribution of the spiral galaxy HCG 91c and found some signatures of azimuthal variations associated with the spiral structure of the galaxy. Similar conclusions have been claimed for NGC 1365 by Ho et al. (2017).

In summary, most of the studies that have analysed hitherto the gas-phase abundance distribution either were focused on a low number of spiral galaxies or did not present a good spatial coverage of the discs. Therefore, there are still a lot of open questions whose answer can help us to further understand how galaxies form and evolve. A proper analysis of the oxygen abundance distribution on a significantly large sample of galaxies and with a good coverage of the galaxy extent is needed in order to reach meaningful statistical results.

## 1.5 THIS THESIS

In this thesis we try to shed some light into the study of the gas-phase oxygen abundance distribution in spiral galaxies in order to better understand the formation and evolution of these objects. With such purpose we make use of two sets of observational data extracted from two different projects: CALIFA (Sánchez et al. 2012a) and AMUSING (Galbany et al. 2016). We



derive the radial distribution of the oxygen abundance of a sample of spiral galaxies by analysing CALIFA data. We characterise all features presented in these radial profiles (inner drop, negative gradient, and outer flattening, see Sect. 1.4.1) and study any possible dependence with some properties of the galaxies. Moreover, we carry out a first approach to the study of the azimuthal abundance distribution by analysing the oxygen abundance gradients in the arm and inter-arm regions in a subset of these galaxies. In this analysis we separate the sample in flocculent and grand design galaxies (see Sect. 1.1.1) in order to link possible arm/interarm differences in the abundance distribution with differences in the mechanisms shaping the spiral structure of the galaxies. However, despite of the great advantages that CALIFA data offer, they still do not provide the spatial resolution needed to detect more subtle azimuthal variations in the gas abundance distribution.

In this regard, the development of MUSE (Multi Unit Spectroscopic Explorer, Bacon et al. 2010) has meant a new revolution in the progress of IFS by combining a large FoV with high spatial resolution, helping us to go further in the study of the gas-phase spatially resolved chemical distribution. These two characteristics combined allow us to increase the number of H II regions detected in individual galaxies with respect to previous studies and better trace their distribution across the galaxy discs. Moreover, thanks to the high spatial resolution, unprecedented in spectroscopic studies, we can avoid any dilution effect in the detection of the H II regions and segregate them with the same quality as with photometric data.


This way, in a complementary fashion, we also analyse AMUSING data in a different sample of galaxies to derive the radial oxygen abundance distribution. This analysis allows us to improve some aspects of the study performed with CALIFA data, such as the development of a new methodology to fit the shape of the radial profiles and detect automatically the existence of an inner drop or/and outer flattening when present. As a second approach to the study of the azimuthal abundance distribution, AMUSING data also offers us the opportunity to derive the intrinsic scatter of the radial gradients. Finally, a proper analysis of these azimuthal distribution is feasible thanks to the high spatial resolution of these data.

The outline of this thesis is as follows. In Chapter 2 we describe the data used along this thesis (CALIFA and AMUSING) and the sample of galaxies defined on the basis of these two surveys. Chapter 3 is devoted to explain the methodology applied to obtain the oxygen abundance distribution of the gas-phase. In Chapters 4 and 5 we show the results in regards of the radial abundance distribution analysed using the CALIFA sample and the AMUSING sample, respectively. The arm/interarm analysis of the abundance distribution is provided in Chapter 6. In Chapter 7 we present the analysis of the azimuthal distribution. Finally, the main conclusions and ideas for future work are outlined.



*We are an impossibility in an impossible universe.*

— Ray Bradbury



# Data and sample selection

## Contents

2.1	CALIFA data . . . . .	31
2.1.1	Sample selection and characterisation . . . . .	33
2.2	AMUSING data . . . . .	36
2.2.1	Sample selection and characterisation . . . . .	37



SPECTROSCOPIC ANALYSIS are regarded as the best approach to study the properties of both stars and gas in galaxies. Until recently, spectrographs were able to obtain spectra of just a limited number of objects/areas in each shot. The advent of IFS techniques allows to gather multiple spectra simultaneously, offering the opportunity to acquire spatially resolved spectra of extended objects. Its two-dimensional (2D) spatial coverage makes feasible the extraction of several hundreds or even thousands of spectra across the entire extent of nearby galaxies. This capability results crucial in the study of the variations of gas properties throughout the whole galaxy disc.

Moreover, using this technique in a “survey mode” to investigate large samples of objects is very advantageous to perform meaningful statistical analyses on unprecedented scales. Current IFS surveys (e.g. ATLAS<sup>3D</sup>, Cappellari et al. 2011; CALIFA, Sánchez et al. 2012a; SAMI, Croom et al. 2012; MaNGA, Bundy et al. 2015) have shown the potential of this kind of data to deliver important insights on key questions about the formation and evolution of galaxies at low redshifts.

The study carried out along this thesis is based on two different data sets associated with two different IFS surveys: CALIFA and AMUSING. In this chapter we describe the main characteristics of these two surveys (Sect. 2.1 and Sect. 2.2 for CALIFA and AMUSING, respectively), defining the sample selection of galaxies and their properties for both datasets (Sect. 2.1.1 and Sect. 2.2.1, respectively).

## 2.1 CALIFA DATA

The Calar Alto Legacy Integral Field Area (CALIFA) survey (Sánchez et al. 2012a) was designed to provide the largest and more comprehensive view of individual galaxy properties in the Local Universe up to date. High quality data for 667 nearby galaxies ( $0.005 < z < 0.03$ ) were collected using the PMAS instrument (Potsdam Multi-Aperture Spectrograph, Roth et al. 2005) mounted to the 3.5m telescope of the Calar Alto observatory in a mode called PPak (PMAS fiber Package, Kelz et al. 2006).

The observed 542 galaxies of the main sample were selected randomly (based on visibility limitations) from a diameter-selected sample of 937 galaxies drawn from Sloan Digital Sky Survey (SDSS) seventh data release (DR7, Abazajian et al. 2009). This way, galaxies with  $45'' < D_{25} < 80''$  in the  $r$ -band image were chosen to fit well within the IFU field-of-view (FoV). CALIFA main sample is fully described and characterised in Walcher et al. (2014). The other 125 galaxies were part of extension programs with different selection criteria according to the aims of each of them (see Sánchez et al. 2016a, for information about the extension sample). As a *legacy* project, CALIFA collaboration has distributed all the data to the public through

three data releases (DR1, Husemann et al. 2013; DR2, García-Benito et al. 2015; and DR3, Sánchez et al. 2016a), the third and final one taking place the 11<sup>th</sup> of April 2016.

Regarding the observing strategy, the adopted PPak configuration consists of 382 fibres of 2.7'' diameter each, 331 of them (the science fibres) covering an hexagonal FoV of 74''x64''. 36 fibres are devoted to the sky subtraction and the remaining ones are assigned to calibration purposes. In order to have a filling factor of 100% along the full FoV and increase the spatial resolution, a dithering scheme of three pointings was adopted. Two different complementary setups were chosen for the observations:

(1) The low-resolution setup (V500) with a nominal resolution of  $\lambda/\Delta\lambda \sim 850$  at 5000 Å (FWHM  $\sim 6$  Å) and covering the wavelength range from 3745 to 7500 Å; and (2) The mid-resolution setup (V1200) with a better spectral resolution of  $\lambda/\Delta\lambda \sim 1650$  at 4500 Å (FWHM  $\sim 2.7$  Å) and ranging from 3650 to 4840 Å. The first setup is intended to study the stellar populations and the properties of the ionised gas, while the second one is more appropriate to study the stellar and ionised gas kinematics given its higher resolution.

The reduction of the CALIFA data is performed using a fully automatic pipeline that was upgraded and improved during the course of the project. All the standard steps for fibre-based IFS data reduction are included, like bias and flat-field corrections, spectral extraction, wavelength calibration and fibre transmission correction, sky subtraction and flux calibration (all routines from the R3D package, Sánchez 2006). Information about the different versions of the pipeline and the corresponding improvements can be found in the mentioned articles describing the successive data releases. As output, the pipeline provides a regular-grid datacube, with  $x$  and  $y$  coordinates indicating the right ascension and declination of the target and  $z$  being the step in wavelength for all galaxies in the sample. An inverse-distance weighted image reconstruction scheme was performed as the interpolation method to reconstruct the datacube. As a result, we have

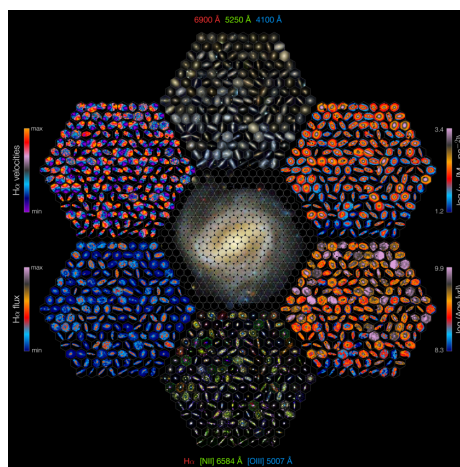


**Figure 2.1:** Promotional image of the CALIFA DR2. It shows 1) 3-color broadband images (top center), 2) stellar mass surface densities (top right), 3) ages (bottom right), 4) narrowband images (bottom center), 5) H $\alpha$  emission (bottom left), 6) H $\alpha$  kinematics (top left) and 7) CALIFA logo (central). From García-Benito et al. (2015).

individual spectra for each sampled spaxel<sup>1</sup> of  $1'' \times 1''$  and a final spatial resolution for the datacubes of  $\text{FWHM} \sim 2.5''$ .

In this thesis, we use the CALIFA V500 datacubes reduced with version 1.5 of the pipeline (described in García-Benito et al. 2015) for all the galaxies comprising our sample, described below.

### 2.1.1 SAMPLE SELECTION AND CHARACTERISATION

The uniqueness of the CALIFA survey in terms of observed sample and data quality makes this survey an excellent dataset to characterise the ionised gas in spiral systems. However, not all the galaxies are suitable for such purposes and the following criteria have been adopted to select the subset of CALIFA galaxies used in this thesis:

- (a) Spiral galaxies with morphological types between Sa and Sm, including barred galaxies.
- (b) Face-on galaxies, with an inclination angle  $i < 60^\circ$ , to avoid uncertainties induced by inclination effects.
- (c) Galaxies with no evident signatures of interaction or merging (i.e. tails, bridges, rings, etc.).
- (d) Galaxies with  $\text{H}\alpha$  detected along different galactocentric distances up to 4 disc effective radii with a S/N for the spaxels above 4 on average.

The classification according to morphological type and into interacting or non-interacting galaxy was based on the visual inspection carried out by Walcher et al. (2014, see details in the article). The inclination angles were also extracted from Walcher et al. (2014). After imposing these restrictions, the original sample of 458 galaxies observed up to that moment (June 2014) was reduced to 129. Table A.1 of Appendix A lists the galaxies composing our sample with some of their main characteristics.

Figure 2.2 shows the comparison of the distribution of morphological types, absolute  $B$ -band magnitudes, and disc effective radii ( $r_e$ ) between the spiral galaxies in the CALIFA mother sample and the subsample used in this thesis. There is a clear deficiency of earlier (Sa-Sab) and later (Sc-Sdm) spirals; the sample is dominated by intermediate ones. The lack of early types may be due to the imposition of having ionised gas throughout the discs, which we have prioritised to perform a detailed 2D study of the gas metallicity. The distribution of galaxies according to their absolute magnitude clearly shows an absence of faint galaxies, with values above -18 mag. This fact is a consequence of a selection effect in the definition of the

---

<sup>1</sup>Unit in which the IFU divides the observed field.

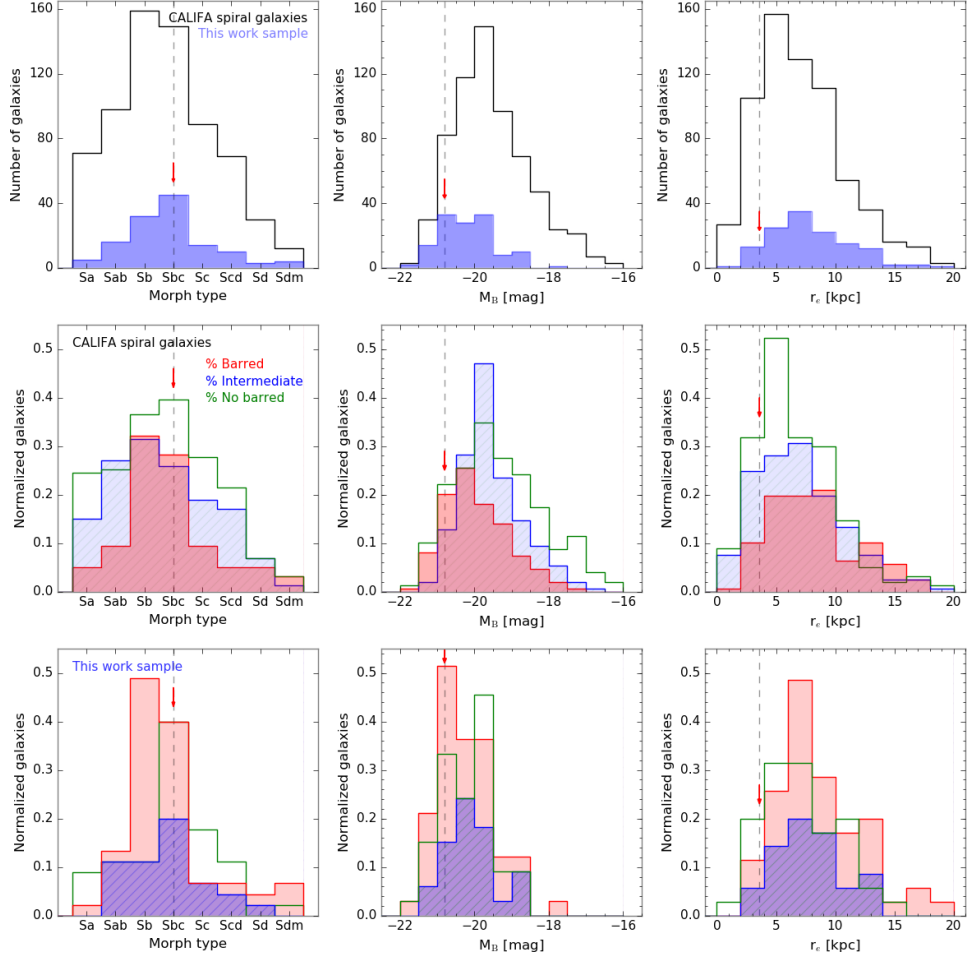


**Figure 2.2:** Distribution of morphological types (top left), absolute  $B$ -band magnitudes (top middle), and disc effective radii (top right) of the spiral galaxies in the CALIFA mother sample (unfilled black histograms) and the galaxies selected in this thesis (filled blue histograms). The middle and bottom panels show the normalised distributions separated according to the presence or absence of bars: barred galaxies (red histograms), unbarred galaxies (green histograms) and not clearly identified galaxies (blue histograms). The dashed grey line and the red arrow mark the location of the MW in each panel. The values for the absolute  $B$ -band magnitude ( $M_B = -20.8$  mag) and the disc effective radius ( $r_e = 3.6$  kpc) are taken from Karachentsev et al. (2004) and Bovy & Rix (2013, considering  $r_e \sim 1.67r_d$ ), respectively.



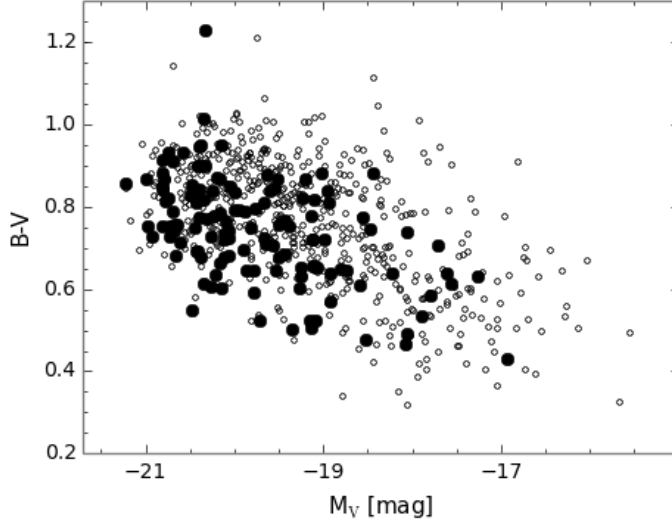


**Figure 2.3:** *Distribution of the spiral galaxies in the CALIFA mother sample (empty small dots) and the galaxies selected in this thesis (filled large dots) in the  $(B - V)$  vs  $M_V$  colour-magnitude diagram.*

CALIFA mother sample (Walcher et al. 2014). The CALIFA mother sample was created by applying a size selection criterion defined by a minimum apparent isophotal size. A size-limited sample like this favours inclined over face-on systems because the inclination increases the apparent isophotal size (because the surface brightness increases). This effect causes these inclined galaxies to dominate the low-luminosity population of galaxies. Because we selected only face-on galaxies with  $i < 60^\circ$ , we automatically discarded all these faint galaxies. Moreover, this fact contributes to the deficiency of Sc-Sdm galaxies due to the found correlation between the morphological type of the galaxies and the mass (thus, with the luminosity), where later types present lower masses and luminosities (Roberts & Haynes 1994; González Delgado et al. 2015). For the distribution of galaxies according to their disc effective radius, we obtained similar distributions for the CALIFA spiral galaxies and our sample: the sample is dominated by galaxies with  $r_e$  between 4 and 10 kpc. Furthermore, there are no significant differences in the distribution when the galaxies are separated into barred and non-barred galaxies, galaxies of all sizes are present in both cases. For the sake of comparison, Fig. 2.2 also displays the values of the shown parameters (morphological type, absolute  $B$ -band magnitude, and disc effective radius ( $r_e$ )) for the Milky Way (MW) as dashed grey lines and red arrows, all of them within the ranges covered by our sample of galaxies.

Figure 2.3 shows the distribution of our sample (filled dots) and the total sample of CALIFA spiral galaxies (empty dots) along the  $(B - V)$  vs  $M_V$  colour-magnitude diagram. Our sample covers the same range as the CALIFA spirals above  $M_V \sim -17$  mag, excluding the faint galaxies below this limit for the reasons explained above.

We note that despite the mentioned constraints imposed by the criteria adopted to define the sample (hereafter CALIFA sample), the selected set of galaxies is well suitable to carry out the study presented in this thesis, that is, a detailed 2D study of the gas metallicity distribution in spiral galaxies.

## 2.2 AMUSING DATA

Additionally to the use of CALIFA data in this thesis, the analysis of other datasets like AMUSING allow us to complement the studies based on CALIFA in aspects where this survey presents some limitations, such as the spatial resolution, improving the knowledge we can obtain from the study of the oxygen abundance distribution of the ionised gas in spiral galaxies.

AMUSING (All-weather MUSE Supernova Integral-field Nearby Galaxies, PI Anderson/Galbany; Galbany et al. 2016) is an ongoing project aimed at studying the environments of supernovae (SNe) by means of the analysis of a large number of nearby SN host galaxies (redshifts typically between 0.005 and 0.06, with exceptional cases up to 0.1; see Fig. 2.4 for the range covered by the subsample analysed in this thesis). The AMUSING mother sample comprises up to date more than 300 galaxies. 227 of these galaxies are part of the long term observing campaign (expanding four semesters so far) carried out by the project. The remaining ones have been included after a careful search in the ESO archive fulfilling the criteria imposed by AMUSING (galaxies observed with MUSE where SNe have been discovered). As a consequence, the mother sample is composed by a wide variety of galaxy types with the only characteristic in common of hosting or having hosted a SN.

The data were collected as part of a filler programme with the MUSE instrument (Bacon et al. 2010, 2014), located at the VLT UT4 telescope of the Cerro Paranal Observatory. In its Wide Field Mode, this integral-field spectrograph presents a FoV of approximately  $1' \times 1'$  and a pixel size of  $0.2''$ , which limits the spatial resolution of the data to the atmospheric seeing during the observations. Regarding the covered wavelength range, MUSE spans from  $4750 \text{ \AA}$  to  $9300 \text{ \AA}$ , with a spectral sampling of  $1.25 \text{ \AA}$  and a spectral resolution  $\lambda/\Delta\lambda \sim 1800 - 3600$  (from the blue edge of the spectrum to the red end).

The AMUSING data analysed in this thesis have been reduced using version 1.2.1 of the MUSE pipeline (Weilbacher et al. 2014) and the Reflex

environment (Freudling et al. 2013). This pipeline layout includes the standard processes like bias subtraction and flat-fielding, flux and wavelength calibration. The sky subtraction was performed using either an offset pointing to a blank sky position, or blank sky regions within the science frames, and making use of algorithms from the Zurich Atmosphere Purge package (ZAP; Soto et al. 2016). The effects of Galactic extinction were also corrected according to the reddening estimates from Schlegel, Finkbeiner, & Davis (1998). Finally, a geometric calibration is performed to distribute the individual slices of the image within the FoV and reconstruct the datacube. More information about the data reduction can be found in Galbany et al. (2016) and Krühler et al. (2017).

For some galaxies, the observations were split into different pointings covering different areas of the galaxies to construct a mosaic. A set of  $\sim 100\,000$  spectra is delivered per pointing, reaching up to an impressive number of  $\sim 600\,000$  spectra for the most extended galaxies (mosaics composed by six pointings), and a total of more than 35 million spectra for the full sample.

The median seeing during the observations of the analysed dataset (described in Sect. 2.2.1) is  $1.1''$  (80% of the values ranging between  $0.8''$  and  $1.8''$ ), corresponding to a median physical resolution of  $\sim 460$  pc. The typical exposure time of each pointing is  $\sim 50$  minutes and the limiting surface brightness in  $g$ -band covers the range between  $22.6$ – $24.9$  mag/arcsec<sup>2</sup> (10-th and 90-th percentiles), with a median value of  $24.0$  mag/arcsec<sup>2</sup>.

### 2.2.1 SAMPLE SELECTION AND CHARACTERISATION

The large percentage of spiral galaxies in the AMUSING mother sample allows as to study in this thesis, and for the first time, the oxygen abundance distribution of the ionised gas in a meaningful statistical sample with an unprecedented spatial resolution. However, not all the galaxies are suitable for the analysis carried out along this thesis. We first remove galaxies with low image quality (visually presenting low signal in the source or/and with seeing values above  $2''$ ) and those that are too small (projected semi-major axis in the sky smaller than  $\sim 15''$ ) to properly derive the abundance distribution without mixing information (very large physical size of the detected H II regions). Galaxies for which the centre of the galactic discs is not mapped are also discarded from the sample. From the remaining galaxies we then select the subset that fulfils the following criteria:

- (a) Spiral galaxies with morphological types between Sa and Sm, including barred galaxies.
- (b) Intermediate to low inclined galaxies ( $i < 70^\circ$ ) to minimise uncertainties induced by inclination effects.

- (c) Galaxies with at least 10 H II regions to properly derive the abundance radial profiles.
- (d) Galaxies with enough radial coverage of the abundance profiles (at least a range of 0.5 disc effective radii).

Regarding the morphological type criterion, the classification is based on the information provided in the extragalactic database *HyperLeda*<sup>2</sup> (Makarov et al. 2014). However, due to the higher quality of the analysed data over the previously available ones, a visual inspection of the images reconstructed from the MUSE datacubes is done to check the galaxies. Indeed, two galaxies that were classified by *HyperLeda* as elliptical or lenticular are kept in the sample because of the presence of a clear spiral structure observed with our data (PGC 55442 and NGC 0232), and two galaxies classified as spirals are discarded for actually being lenticular (NGC 4772 and NGC 6962). Moreover, for the galaxies with no morphological information in the mentioned database (18), a visual selection is performed, all of them being finally included. After imposing these restrictions, the sample is reduced to 102 galaxies. General information about these galaxies including the morphological type, redshift, stellar mass and disc effective radius is given in Table B.2 (Appendix B).

The AMUSING mother sample has not been defined based on their galaxy properties, as opposed to the CALIFA mother sample, but on the presence of SNe. However, here we argue that the subsample used in this thesis (hereafter AMUSING sample) is representative of the galaxy population in the Local Universe. A criterion based on the occurrence on the galaxy being host to a SN is proposed as a valid selection to find galaxies properly populating the galaxy mass distribution (galaxies hosting SNe Ia) and the typical observed ranges of star formation rates (galaxies hosting core-collapse SNe). In Fig. 2.4 we check the veracity of this statement by comparing this sample with the CALIFA subsample (see Sect. 2.1.1), which is also analysed along this thesis and, as previously mentioned, was extracted from a well defined, statistically significant sample and representative of galaxies in the Local Universe (Walcher et al. 2014). The top panel of Fig. 2.4 shows the normalised distribution of morphological types of the 84 galaxies of the sample for which *HyperLeda* information on this regards is available (red dashed histogram) and the CALIFA galaxies (which morphological classification is presented in Walcher et al. 2014, blue solid histogram). The sample is dominated by galaxies of intermediate morphological types ranging from Sb to Sc, although spirals of all morphological types are found. Despite the lack of Sab galaxies in favour of Sa systems with respect to the CALIFA sample, the coverage of morphological types is very similar in both samples.

---

<sup>2</sup><http://leda.univ-lyon1.fr>

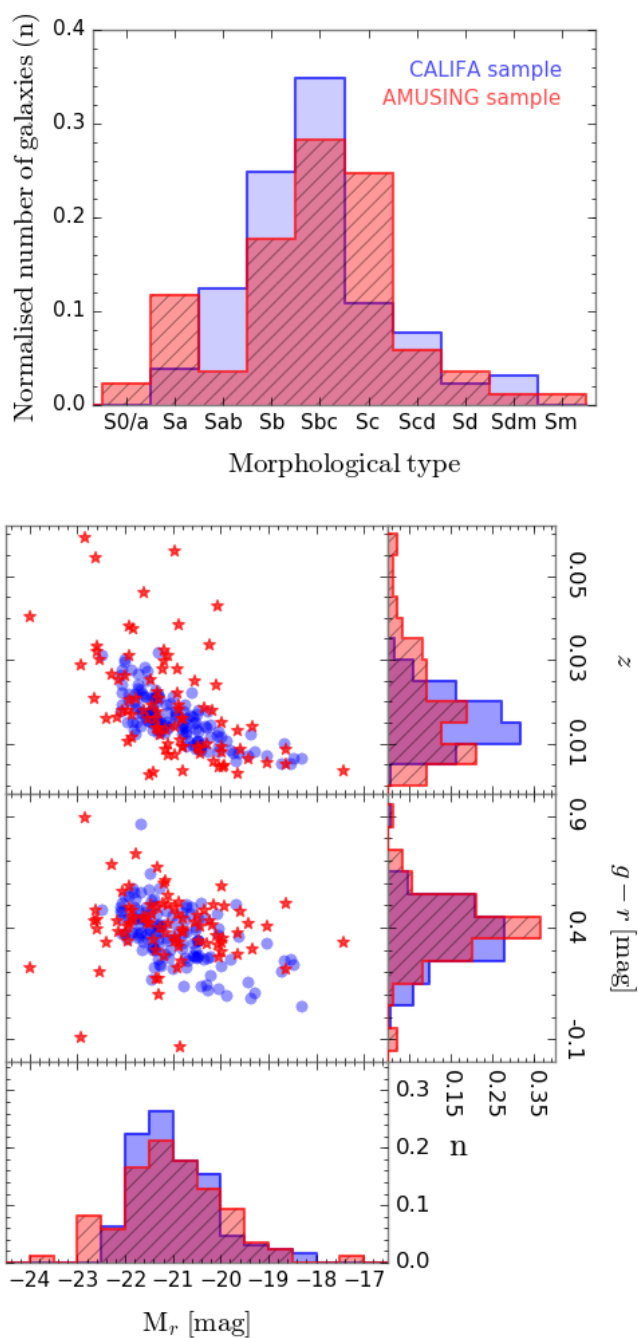


**Figure 2.4:** Characterisation of the AMUSING analysed sample (red dashed histograms and stars) as compared with the CALIFA analysed sample (blue solid histograms and circles). The plot shows the distribution of morphological types (top), and the redshift and  $g - r$  colour distributions as a function of the absolute  $r$ -band magnitudes (bottom). The normalised frequency histograms for the three parameters are also shown.

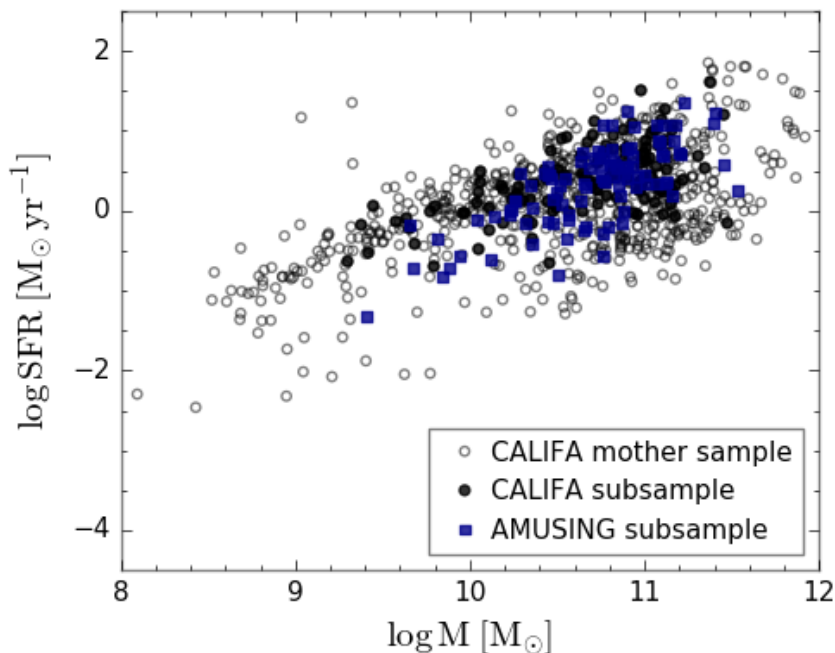


**Figure 2.5:** *SFR vs. integrated stellar mass relation for both CALIFA and AMUSING samples. The complete CALIFA mother sample is represented by unfilled black circles. The CALIFA and AMUSING subsamples of galaxies used in this thesis are indicated by filled black circles and blue squares, respectively.*

The bottom panel of Fig. 2.4 shows the redshift and  $g - r$  colour distributions as a function of the absolute  $r$ -band magnitudes, together with their corresponding frequency histograms for both AMUSING (red stars and red dashed histograms) and CALIFA (blue circles and blue solid histograms) samples. The absolute  $r$ -band magnitudes and  $g - r$  colours for AMUSING galaxies are computed from the flux density in  $r$ -band and  $g$ -band images recovered from the data. In the case of the CALIFA galaxies, these values were directly extracted from the SDSS DR7 catalogue. The coverage of both samples is again very similar for all the explored parameters, with the exception of the tail towards higher redshifts of the AMUSING galaxies, as no redshift criterion was applied to define the sample. If we do not consider the galaxies with  $z > 0.03$ , restricting ourself to the range covered by the CALIFA sample, a two-sample Kolmogorov-Smirnov test<sup>3</sup> (KS test) yields  $p$ -values above the significance level (5%) for the three parameters, concluding that the two samples present statistically similar distributions.

<sup>3</sup>The two-sample KS test is a statistical test used to determine if two datasets differ significantly based on a parameter called  $p$ -value. If this parameter is below a significant level (usually 5%) then we can conclude that the two sample are drawn from different distributions, and the opposite for  $p$ -values above the significance level.

Figure 2.5 shows the star formation rate (SFR)-stellar mass plane of the galaxies in the sample, both from CALIFA (black circles) and AMUSING (blue squares) surveys. The complete CALIFA mother sample, that is representative of all types of galaxies observed in the Local Universe, is also represented (unfilled black circles). This graphic is useful to distinguish star forming galaxies, that occupy a “star forming main sequence”, in a similar way as a colour-magnitude diagram (see Sect. 1.1). In this figure we can see that both CALIFA and AMUSING galaxies cover the same range of values, corresponding mainly to the star forming main sequence (blue cloud in a CMD) and part of the green valley. Therefore, we can confirm that our sample of galaxies is not biased but we cover all ranges of SFR we can find in spiral galaxies.

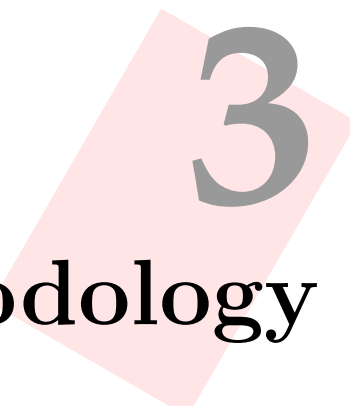
Therefore, in sight of this comparison, we can conclude that the AMUSING sample is also suitable for carrying out a detailed study of the oxygen abundance distribution of the ionised gas in spiral galaxies, and for drawing statistical conclusions applicable to spiral galaxies in the Local Universe. Together with the CALIFA sample, both datasets will be the basis of the subsequent analysis presented along this thesis in the following chapters.





*It is a mistake to think you can solve any major problems just with potatoes.*

— Douglas Adams



# Methodology

## Contents

3.1	Measurement of the emission lines: FIT3D/Pipe3D . . .	45
3.1.1	Dust extinction and reddening correction . . . . .	49
3.2	Selection of star forming regions . . . . .	50
3.2.1	Extraction of individual H II regions . . . . .	50
3.2.2	Spaxel-by-spaxel extraction . . . . .	54
3.3	Derivation of the oxygen abundances . . . . .	56
3.4	Deprojection of galaxies . . . . .	60



FROM THE MOMENT WE HAVE AT OUR DISPOSAL the datacubes provided by the corresponding reduction pipeline of the instrument for the selected targets, there is still a long way off until we obtain the information (in the proper format) needed to carry out the study of interest. This long way passes through the choice of the suitable tools that can help us to derive the desired information and the overall procedure designed to make the most of our data. This part of the process is crucial when someone has to decide whether they should rely on your results or not.

In this chapter we explain the methodology followed during this study to perform the study of the gas abundances. In Section 3.1 we describe the code used to measure the flux of the emission lines, process that also involves the subtraction of the stellar component contribution. We also explain the analysis required to select the star forming regions, either by detecting the individual H II regions (Sect. 3.2.1) or by extracting the spaxel-wise information (Sect. 3.2.2). Finally, the derivation of the corresponding oxygen abundance values is described in Section 3.3.

### 3.1 STELLAR CONTRIBUTION SUBTRACTION AND MEASUREMENT OF EMISSION LINES: FIT3D/PIPE3D

The spectrum of a galaxy gives us information about the different emitting sources that compose it, mostly stars and ionised gas. The emission of each of these components is characterised by different and particular features. A typical spectrum of a galaxy (or a portion of it) presents a set of well-defined emission lines associated with the ionised gas, superimposed to the underlying stellar spectrum that is characterised by the absorption lines and the continuum emission. In order to study the properties of the individual components, in our case the ionised gas, it is necessary to decouple them. In other words, to accurately measure the emission line fluxes, the stellar contribution must be estimated and subtracted from the galaxy spectrum to derive a pure gas spectrum for each individual spaxel or H II region. This is not a trivial task since some of the emission lines (e.g. the Balmer series) can be, in some cases, strongly affected by the absorption features of the stellar population.

Several tools have been developed to model the underlying stellar population and decouple it from the emission lines (e.g. pPXF, Cappellari & Emsellem 2004; STARLIGHT, Cid Fernandes et al. 2005; STECKMAP, Ocvirk et al. 2006b,a; GANDALF, Sarzi et al. 2006; ULySS, Koleva et al. 2009; FIT3D, Sánchez et al. 2011). Most of them are based on the assumption that the star formation history (SFH) of a galaxy can be approximated as a sum of discrete star formation (SF) bursts and, therefore, that the stellar spectrum can be considered as the result of the combination of spectra

of different simple stellar populations (SSP) with different ages and metallicities.

In this work, we make use of a fitting package named FIT3D<sup>1</sup> to model both the continuum emission and the emission lines. Originally, this tool was developed to analyse the properties of the ionised gas. However, during the last few years FIT3D has been improved, presenting new capabilities that allow for a more reliable characterisation of the underlying stellar population and a good estimation of the errors of the derived parameters. Nowadays, FIT3D is part of a more complete spectroscopic analysis pipeline named PIPE3D (Sánchez et al. 2016c), developed to characterise the properties of both the stellar populations and the ionised gas. This tool was designed to deal with spatially resolved data from optical IFS surveys, in particular CALIFA, MaNGA and SAMI, and the new generation of IFS instruments like MUSE.

To properly subtract the underlying stellar population, it is needed to adopt a spatial binning in order to increase the S/N of the spectra and obtain an accurate estimation of the stellar contribution. With such purpose, PIPE3D uses an algorithm named CS-binning and based on a continuity criterion for the surface brightness and a goal for the S/N ratio (in our case, 40 for CALIFA data and 150 for AMUSING). This algorithm allows the user to reach a compromise between increasing the S/N and preserving the shape of the original object (i.e., without mixing areas of the galaxy with very different physical properties).

In the modelling of the stellar contribution adopted in this thesis, FIT3D uses an SSP template grid that comprises 156 individual populations covering 39 stellar ages between 0.001 and 14.1 Gyr and four metallicities between 0.004 and 0.03. This grid combines the GRANADA models from González Delgado et al. (2005) for  $t < 63$  Myr with those provided by the MILES project (Vazdekis et al. 2010; Falcón-Barroso et al. 2011) for older ages (following Cid Fernandes et al. 2013). This way, FIT3D fits each spectrum with a linear combination of the SSP templates that are collected in the library after correcting for the appropriate systemic velocity and velocity dispersion (including the instrumental dispersion) and taking into account the effects of dust attenuation. We adopted the Cardelli et al. (1989) law for the stellar dust extinction with  $R_V = 3.1$ .

Once we have an estimation of the stellar continuum, PIPE3D performs a procedure designed to decouple the analysis of the emission lines from the spatial binning required for the stellar populations. This procedure, called *dezonification* (see Cid Fernandes et al. 2013), takes into account the relative contribution of each spaxel to the spatial bin in which it is aggregated, using the ratio between the  $V$ -band intensity map before and

---

<sup>1</sup><http://www.astroscu.unam.mx/~sfsanchez/FIT3D>

after performing the binning scheme (the so-called *dezonification* map). This map is multiplied to the stellar model of the datacube (where all the spaxels within the same spatial bin present the same spectrum) and the resulting cube is spatially smoothed with a Gaussian kernel to obtain a continuous model of the underlying stellar population. Finally, this model is subtracted from the original datacube providing a pure emission line cube.

To measure the emission line fluxes on the pure gas cube, FIT3D performs a multi-component fitting using a single Gaussian function per emission line plus a low-order polynomial function. When more than one emission line was fitted simultaneously (e.g. for doublets and triplets like the [N II] lines), the systemic velocity and velocity dispersion were forced to be equal to decrease the number of free parameters and increase the accuracy of the deblending process. The measured line fluxes include all lines required in determining the gas metallicity using strong-line methods, that is, H $\alpha$ , H $\beta$ , [O II]  $\lambda$ 3727<sup>2</sup>, [O III]  $\lambda$ 4959, [O III]  $\lambda$ 5007, [N II]  $\lambda$ 6548, [N II]  $\lambda$ 6584, [S II]  $\lambda$ 6717, and [S II]  $\lambda$ 6731. FIT3D provides the intensity, equivalent width (EW), systemic velocity, and velocity dispersion for each emission line.

The estimation of the errors of the parameters is done by performing a Monte Carlo (MC) simulation, where the original emission line spectrum is perturbed by a noise spectrum that includes both the original estimated errors and the uncertainties in the best fit SSP model (standard deviation around the best SSP model). This way, the uncertainties of the subtraction of the underlying stellar population are propagated to the parameters derived for the emission lines.

This method of measuring the emission lines based on Gaussian fitting is applied for the H II regions analysis. However, this procedure is very time consuming, and infeasible especially when the number of spectra to analyse is very high, as for a spaxel-wise analysis of the AMUSING datacubes. Therefore, in this case PIPE3D adopts a different scheme to extract the main properties of the emission lines (flux intensity, velocity and velocity dispersion, and equivalent width). This scheme is described in detail in Sánchez et al. (2016b). In summary, it is based on an optimal extraction algorithm that uses as initial guess for the velocity and the velocity dispersion of each emission line the ones derived using the Gaussian fitting procedure for the strongest emission line, H $\alpha$ . Adopting a Gaussian shape for each considered emission line the algorithm performs a weighted momentum analysis, where the weight of each line property is the normalised intensity of the Gaussian distribution. From the initial guess of the kinematics properties described before it is derived a first estimation of the intensity, velocity and velocity dispersion of each line. This procedure is repeated through a set of 50 MC realisations of the spectra, modified according to the errors derived based on

---

<sup>2</sup>This particular emission line, although covered by CALIFA, is out of the wavelength range of MUSE, that spans from 4750 Å to 9300 Å.

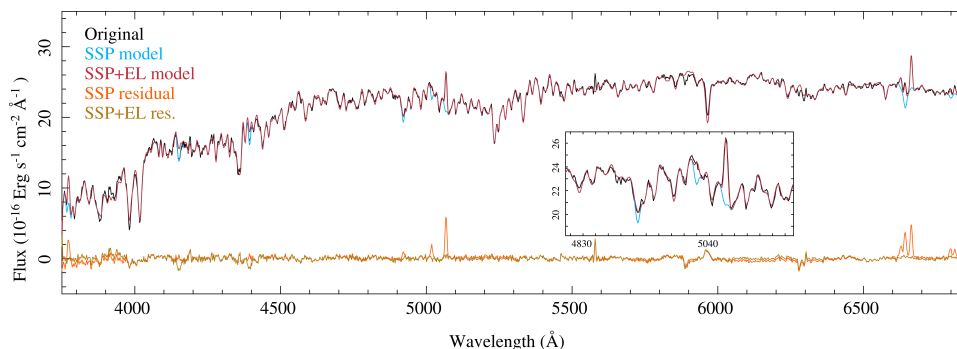


**Figure 3.1:** Example of a FIT3D fit to the central spectrum (5'' diameter) of NGC 6754 extracted from the CALIFA V500 datacube. The black line represents the original spectrum, along with the best fitted stellar population (SSP model, light blue), and the best fitted combination of stellar population and emission lines (SSP+EL model, red). The pure emission line spectrum after subtracting the best stellar population model is shown as a solid orange line (SSP residual). Finally, the total residual of the subtraction of both the stellar population and the emission line models is represented as a light green line (SSP+EL res.). The inset is focused on the H $\beta$ -[O III] spectral region to highlight the quality of the fit. Extracted from Sánchez et al. (2016a).

the residuals on the stellar population analysis. Following this strategy, we obtain an estimation of both the considered parameters (mean values of the intensity, velocity and velocity dispersion), and their corresponding errors (standard deviation around those mean values).

As indicated above, FIT3D fits both the underlying stellar population and the emission lines. In addition to the parameters derived for the emission lines, the fitting algorithm therefore provides information related to the stellar population: the luminosity-weighted ages and metallicities, the average dust attenuation, the mass-weighted ages and metallicities, the average mass-to-light ratio, and the individual weights of the multi-SSP decomposition that in essence trace the SFH.

The entire procedure of fitting and subtracting the underlying stellar population and measuring the emission lines using FIT3D, together with its implementation to CALIFA data and other algorithms of PIPE3D are extensively described in Sánchez et al. (2011), Sánchez et al. (2016c) and Sánchez et al. (2016b). In these articles the authors also carry out a comparison of the results of the analysis using this tool with other widely used packages (namely STARLIGHT, Cid Fernandes et al. 2005, and STECKMAP, Ocvirk et al. 2006b,a), finding that the parameters derived with FIT3D are fully compatible with those provided by the other codes. To illustrate the quality of the performance of FIT3D in different datasets and regions of the galaxies dominated by different physical processes we show as an example the fit of the central spectrum (5'' diameter) of NGC 6754 from the CALIFA data in Fig. 3.1 and of two H II regions from AMUSING data in Fig. 3.2. In these

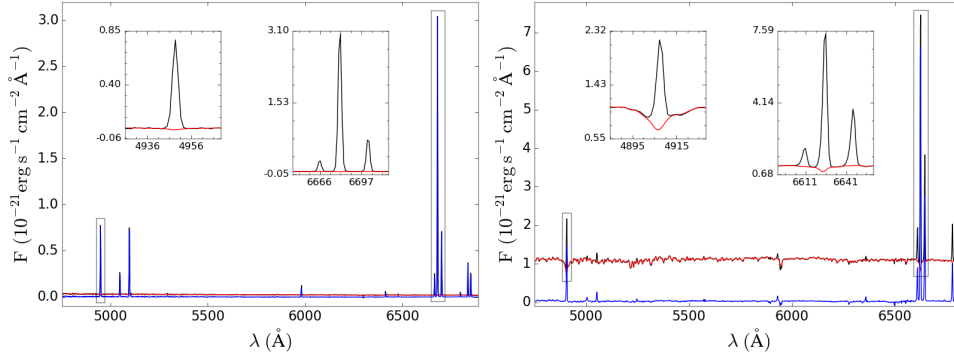


**Figure 3.2:** Two typical spectra of  $H\text{II}$  regions observed in the AMUSING sample with different levels of stellar contribution. The black line represents the observed spectrum, along with the best fitted stellar population performed by FIT3D (SSP model, red line). The pure emission line spectrum after subtracting the SSP model is shown as a blue line. The insets are focused on the  $H\beta$  and  $H\alpha - [NII]$  spectral regions to highlight the quality of both the spectra and the subtraction of the underlying stellar continuum.

figures it is possible to appreciate the good quality of the fitting of both the stellar populations and the emission lines. In particular, it is clear the good recovery of the emission line fluxes even in the case of strong absorptions (e.g., in the case of the  $H\beta$ , see inset of Fig. 3.1). The examples of Fig. 3.2 show different levels of contribution of the stellar continuum in the spectrum of the  $H\text{II}$  regions. In cases where the stellar contribution is low, its effect on the emission lines recovery is negligible (compare blue and black lines of the left panel). On the other hand, if the contribution is significant (see right panel), the performance of FIT3D is quite remarkable, being able to properly model the underlying stellar absorption in features such as  $H\alpha$  and  $H\beta$  (see insets of Fig. 3.2).

### 3.1.1 DUST EXTINCTION AND REDDENING CORRECTION

The presence of dust in the interstellar medium (ISM) has an impact on the observed emission coming from the ionised gas. This influence depends on different characteristics, such as the size of the dust grains or the wavelength of the emitted photons, being the dust able to absorb and even scatter light (see Chapter 1). This phenomenon (called extinction) is also known as *interstellar reddening* because it is stronger at short wavelengths (blue) than at long wavelengths (red). As a consequence of this effect, the ratios between the emission lines (used to determine abundances, see Sect. 3.3) change.

Prior to the derivation of the oxygen abundances it is therefore needed to correct the emission line ratios from this effect. In spectroscopic studies of

H II regions the flux of the emission lines is usually represented with respect to the H $\beta$  flux. This way, the corrected ratio of fluxes for a given emission line located at a wavelength  $\lambda$  can be derived with the following equation:

$$\left(\frac{F_\lambda}{F_{H\beta}}\right)_{obs} = \left(\frac{F_\lambda}{F_{H\beta}}\right)_{corr} \times 10^{-0.4(A_\lambda - A_{H\beta})}, \quad (3.1)$$

where  $(F_\lambda/F_{H\beta})_{obs}$  and  $(F_\lambda/F_{H\beta})_{corr}$  are the observed and corrected emission line ratio, respectively, and  $A_\lambda$  is the absolute extinction at the corresponding wavelength.

To determine  $A_\lambda$  we make use of the extinction law  $A(\lambda)/A(V)$  from Cardelli et al. (1989), with  $R_V = 3.1$ . The value of  $A(V)$  is obtained from the H $\alpha$ /H $\beta$  Balmer decrement, considering the theoretical value for the unobscured H $\alpha$ /H $\beta$  ratio of 2.86, which assumes a case B recombination ( $T_e = 10\,000$  K,  $n_e = 100$  cm $^{-3}$ , Osterbrock 1989).

This method allows us to obtain reddening corrected emission line ratios that now can be used with the empirical calibrators to derive the oxygen abundances (see Sect. 3.3) and study their 2D distribution.

## 3.2 SELECTION OF STAR FORMING REGIONS

The use of emission lines is essential in the determination of the chemical abundance of the ionised gas in galaxies. This gas can be found forming clouds of ionised hydrogen due to the photoionisation of the interstellar gas by O-B stars (Aller 1984; Osterbrock 1989). These clouds are known as H II regions and are associated with areas where star formation is taking place, as only hot, massive, young stars are able to ionise the surrounding material. Generally, the determination of the ionised gas abundances in external galaxies is based on strong-line indicators (see Sect. 3.3) that have been calibrated using H II regions in nearby systems and even the Milky Way.

In this section we describe how we have selected those regions in terms of two different methods that in the next chapter will be proved to be equivalent under certain conditions (see Chapter 4). The spectra coming from these regions are analysed as described above (Sect. 3.1).

### 3.2.1 EXTRACTION OF INDIVIDUAL H II REGIONS

There are several packages developed for the automatic selection of H II regions that are publicly available (e.g. HII PHOT, Thilker et al. 2000; REGION, Fathi et al. 2007; HII EXPLORER, Sánchez et al. 2012b). In this thesis we make use of HII EXPLORER<sup>3</sup>, which has been designed especially to

<sup>3</sup>[http://www.astroscu.unam.mx/~sfsanchez/HII\\_explorer](http://www.astroscu.unam.mx/~sfsanchez/HII_explorer)



deal with CALIFA data but modified accordingly to handle other datasets such as AMUSING data. The validity of this tool to select H II regions is highly proved against the other mentioned packages in a comparison done in Sánchez et al. (2012b).

The procedure performed by HIIEXPLORER to detect the H II regions and extract the corresponding spectra is based on two assumptions: (a) H II regions are peaky and isolated structures with a strongly ionised gas emission, particularly in H $\alpha$ , that is significantly higher than the stellar continuum emission and the average ionised gas emission across the rest of the galaxy; (b) H II regions have a typical physical size of about a few hundred parsecs (González Delgado & Pérez 1997; Oey et al. 2003; Lopez et al. 2011).

A more detailed description of this algorithm can be found in Sánchez et al. (2012b), with a few modifications presented in Sánchez et al. (2015). Basically, the main steps of the process are as follows: (i) First we create a narrow-band image of each galaxy (120 Å-width) centred at the redshifted wavelength of H $\alpha$  for the considered target. (ii) This image is used as an input for HIIEXPLORER. The algorithm detects the brightest pixel in the map and then adds all the adjacent pixels up to a distance of 3.5'' if their fluxes exceed 10% of the peak intensity. After the first region is detected and separated, the corresponding area is masked from the input image and the procedure is repeated until no peak with a flux exceeding the median H $\alpha$  emission flux of the galaxy is found. If two peaks are close to each other ( $d < 7''$ ), the algorithm will assign to the region with the brightest peak pixels that might belong to the faintest one. In order to reassociate pixels within this “overlapping” region, HIIEXPLORER computes the flux ratio between those pixels and both peaks. These pixels will belong to the region presenting the largest ratio providing such value is above 10%. This criterion avoids the extension of regions into others, producing a “straight” division between them. The final result is a segmentation FITS file describing the pixels associated with each detected H II region. Afterwards, (iii) the integrated spectrum corresponding to each segmented region is extracted from the original datacube, and the corresponding position table of the detected area is provided. Finally, each extracted spectrum is decontaminated by the underlying stellar population using FIT3D, and the emission line fluxes are measured by fitting each line with a Gaussian function (as described in Sect. 3.1).

We must note here that, in practice, the segregated H II regions obtained for the CALIFA galaxies may aggregate several classical ones due to the resolution of the data, in particular for the most distant galaxies. Detailed simulations on the effect of resolution loss (Mast et al. 2014) have demonstrated that on average each selected region at  $z \sim 0.02$  may comprise 1 – 3 H II regions of those detected in low redshift galaxies ( $z \sim 0.002$ ). For

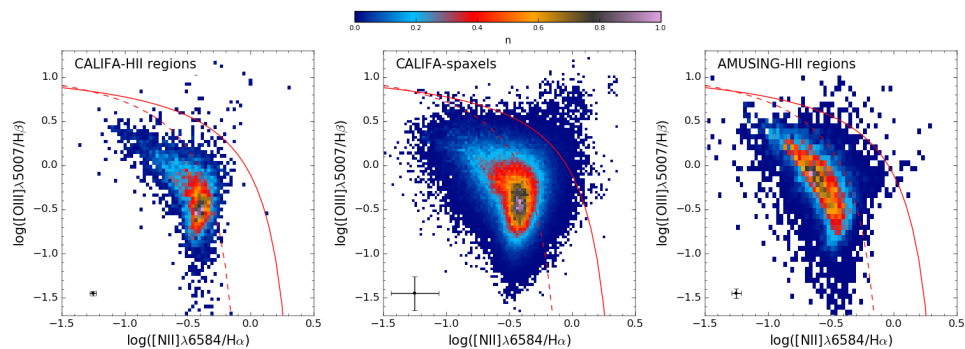


**Figure 3.3:** Normalised density distribution along the BPT diagram of the detected H II regions (left) and the spaxels with  $EW(H\alpha)$  above  $6 \text{ \AA}$  (middle) for the CALIFA galaxies, and of the detected H II regions for the AMUSING galaxies (right). The solid and dashed lines in both panels represent the Kewley et al. (2001) and Kauffmann et al. (2003a) demarcation curves. SF regions are considered to be below the Kewley et al. (2001) curve.

this reason, analyses focused on additive properties on individual H II regions like the  $H\alpha$  luminosity function are not feasible. However, this segmentation method is perfectly suitable for the study of line ratios, chemical abundances and ionisation conditions, and therefore, for the purpose of this study.

In the case of the AMUSING galaxies, some adjustments in the code have been done to adapt the algorithm to the higher spatial resolution of these data with respect to CALIFA. The distance value used to aggregate pixels to each region is reduced to  $0.9''$  and the minimum flux fraction between the pixels and the peak is set to 1%. Except for these two modifications, the performance of HIIEXPLORER is exactly the same. For this study, only the regions with  $S/N > 3$  in  $H\alpha$  emission are considered as candidates to be SF regions (to guarantee the reliability of their detection).

HIIEXPLORER allows us to detect clumpy ionised regions. However, not all these regions may be associated with star formation (and are not therefore actual H II regions) as some of them may be ionised by other sources as AGNs or compact shocks. The intensity of strong lines has been broadly used to discern between different types of emission according to their main excitation source throughout the so-called diagnostic diagrams (e.g. Baldwin et al. 1981; Veilleux & Osterbrock 1987). The most common, and that used here, was proposed by Baldwin et al. (1981, hereafter BPT diagram). This diagram makes use of the  $[N II] \lambda 6584/H\alpha$  and  $[O III] \lambda 5007/H\beta$  line ratios, which are less affected by dust attenuation because of the proximity in wavelength space of the emission lines involved in each ratio. For this diagram, different demarcation lines have been proposed to distinguish between SF regions and other sources of ionisation. The most popular ones are the Kauffmann et al. (2003a) and Kewley et al. (2001) curves. These two

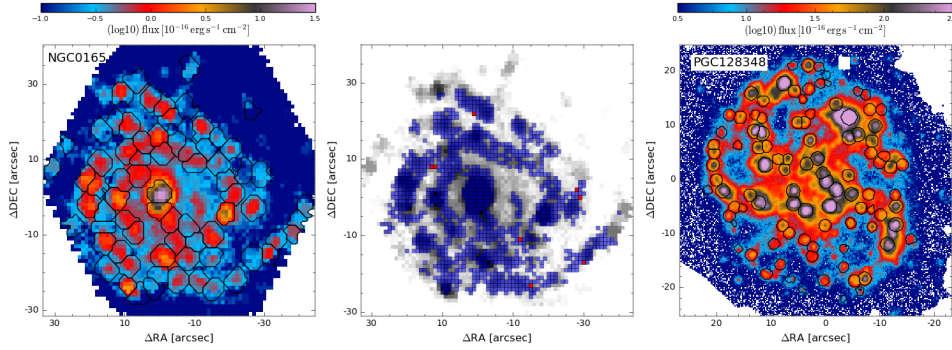


**Figure 3.4:**  $H\alpha$  maps in units of  $(\log_{10}) 10^{-16} \text{ erg s}^{-1} \text{ cm}^{-2} \text{ arcsec}^{-1}$  derived for one galaxy of the CALIFA sample, NGC 0165 (left), and one galaxy of the AMUSING sample, PGC 128348 (right). The detected  $H\text{II}$  regions are shown as black segmented contours. For NGC 0165, the location of the spaxels classified as SF regions (blue dots) and AGNs (red dots) according to the BPT diagram superimposed on the IFS-based  $H\alpha$  map is also represented (middle).

demarcation lines have a different origin. The Kewley et al. (2001) curve was derived theoretically using photoionisation models and corresponds to the maximum envelope for ionisation produced by O-B stars. The Kauffmann et al. (2003a) curve has an empirical origin, based on the analysis of the emission lines for the integrated spectra of SDSS galaxies. It describes well the envelope for classical  $H\text{II}$ /SF regions that are found in the discs of late-type spiral galaxies (e.g. Osterbrock 1989). However, it excludes certain kinds of SF regions already observed in galaxies (Kennicutt et al. 1989b; Ho et al. 1997 and, more recently, Pérez-Montero & Contini 2009 and Sánchez et al. 2014). For this reason, and in order to avoid biasing our sample towards classical disc regions, we adopt the Kewley et al. (2001) curve to select our  $H\text{II}$  regions (located below this curve).

In most cases these diagrams are very useful in distinguishing between strong ionisation sources, such as classical  $H\text{II}$ /SF regions and powerful AGNs. However, they are less accurate in distinguishing between low-ionisation sources, such as weak AGNs, shocks, and/or post-AGBs stars (Stasińska et al. 2008; Cid Fernandes et al. 2011; Morisset et al. 2016). As a consequence, alternative methods have been proposed. In this thesis, in addition to the use of the BPT diagram we also adopt the WHAN diagram ( $W_{H\alpha}$  versus  $[\text{N II}]/H\alpha$ , Cid Fernandes et al. 2011). This diagram uses the  $EW(H\alpha)$  to take into account weak AGNs and ‘retired’ galaxies, that is, galaxies that have stopped forming stars and are ionised by hot low-mass evolved stars. We have been more restrictive in the  $EW$  range than Cid Fernandes et al. (2011) and established the limit in  $6 \text{ \AA}$  rather than  $3$  to assure a significant percentage (20%) of young stars contributing to the emission of the  $H\text{II}$  regions (given the strong correlation between both parameters, see Sánchez et al. 2014).

Figure 3.3 shows the  $[\text{O III}] \lambda 5007/\text{H}\beta$  vs.  $[\text{N II}] \lambda 6584/\text{H}\alpha$  diagnostic diagram for the H II/SF regions in all 129 CALIFA galaxies (left panel) and 102 AMUSING galaxies (right panel) of our sample. The solid and dashed lines represent the Kewley et al. (2001) and Kauffmann et al. (2003a) demarcation curves, respectively. Finally, Fig. 3.4 shows an example of an  $\text{H}\alpha$  map for one spiral galaxy of the CALIFA sample, NGC 0165 (left panel), and another one of the AMUSING sample, PGC 128348 (right panel), where the location of the H II regions is superimposed as black segmented contours. For these particular galaxies we detected 72 and 103 H II regions, respectively.

### 3.2.2 SPAXEL-BY-SPAXEL EXTRACTION

The study of ionised gas abundances using H II regions presents some disadvantages, namely the low number of detections in a single galaxy and the restriction of this study to isolated areas of the galaxies. IFS studies offer the opportunity to overcome these limitations providing full two-dimensional (2D) information spaxel by spaxel to properly map the spatially resolved properties of galaxies. The fact that the spaxel size of the CALIFA datacubes is of the order of the size of a typical H II region (or even larger depending on the redshift of the galaxy) allows us to perform this kind of analysis for the study of the ionised gas abundance without resolving the ionised structure of those regions. However, in the case of the AMUSING galaxies, the spaxel size of the datacubes is smaller than the typical size of an H II region (at the average redshift of the sample). Thus, a spaxel-by-spaxel analysis is not recommended for those observations for which the physical spatial resolution (eventually determined by the atmospheric seeing, typically  $\sim 1''$  for our data) allows us to resolve the ionising structure of the H II regions, leading to erroneous estimations of the oxygen abundance.

Therefore, in order to increase the number of analysed objects part of the AMUSING project and rely on a significantly large sample, we restrict the abundance analysis for these galaxies to the study of segregated H II regions. The spaxel-by-spaxel analysis is limited to the CALIFA data, for which the study of the H II regions is also performed for comparison purposes.

As a result of the FIT3D fitting process, we obtained the set of 2D intensity maps (spaxel by spaxel) for the emission lines that are required to determine the gas metallicity. To guarantee realistic measurements of the emission line fluxes employed in the determination of the oxygen abundance for each spaxel, we discarded the spaxels with flux values lower than  $1\sigma$  over the continuum level (except for  $\text{H}\alpha$ , for which a fixed limit of  $0.2 \cdot 10^{-16} \text{ erg s}^{-1} \text{ cm}^{-2}$  is imposed in order to ensure that all the selected spaxels are associated with ionised gas). Although the selected lower limit is  $1\sigma$  per spaxel, this additional requirement on the  $\text{H}\alpha$  flux implies that most of the spaxels present a signal-to-noise ratio (S/N) higher than 3 for all the lines

involved in the analysis (62% for [O III]  $\lambda 5007$ , 91% for [N II]  $\lambda 6584$ , 88% for H $\beta$ , and 100% for H $\alpha$ ). From all the spaxels with flux values above this limit, we now selected those that are associated with SF, making use of the emission line ratios through the BPT diagram. In a similar way as for the H II regions, SF spaxels are considered to be under the Kewley et al. (2001) curve and present an  $\text{EW}(\text{H}\alpha) > 6\text{\AA}$ .

In addition to the light from the ionised SF regions, there is a background of diffuse nebular emission that extends over the whole disc of the galaxies and can blur the contribution of the SF regions, which is the subject of our study. However, most of the diffuse ionised emission has been excluded by the  $1\sigma$  limit imposed to the flux of the selected spaxels and the EW criterion, since this emission is dominated by the stellar continuum. For a comparison of the location in the BPT diagram for low-ionisation emission sources see, for instance, Kehrig et al. (2012), Papaderos et al. (2013) and Gomes et al. (2015).

The middle panel of Fig. 3.3 shows the [O III]  $\lambda 5007/\text{H}\beta$  vs. [N II]  $\lambda 6584/\text{H}\alpha$  diagnostic diagram for the spaxels in all 129 galaxies of our CALIFA sample above the considered flux limit and with  $\text{EW}(\text{H}\alpha) > 6\text{\AA}$ . Again, the solid and dashed lines represent the Kewley et al. (2001) and Kauffmann et al. (2003a) demarcation curves, respectively. Some points dominated by SF ionisation might be present above the Kewley et al. (2001) curve as a result of the errors of the considered emission lines. They are, therefore, excluded from further analysis by our criteria for selecting spaxels associated with SF activity. However, the spaxels that present larger errors are those with a low S/N, and they do not affect our conclusions significantly.

The middle panel of Fig. 3.4 shows the location of the selected spaxels in a particular spiral galaxy of the CALIFA sample, NGC 0165, over-plotted to the H $\alpha$  map. Blue dots correspond to the spaxels classified as SF regions and red dots are those that lie higher than the Kewley et al. (2001) curve and can therefore be associated with AGNs. The figure shows that the selected spaxels follow the H $\alpha$  emission. The classification of red points as ionised by AGNs in this galaxy as well as in other cases is clearly wrong because of their distance to the galactic centres. This misclassification is most probably due to the errors in the considered emission lines. As in the previous case, they could cause some spaxels that are dominated by SF ionisation to lie higher than the Kewley et al. (2001) curve in a similar way that errors could produce the opposite effect with spaxels associated to AGNs. As these spaxels represent only the 2% for the whole sample, including them would not alter our results significantly, and thus they have been discarded from the further analysis. For this particular galaxy, 1 201 spaxels are associated with SF regions.

In total, the 129 galaxies composing the CALIFA sample provide 7 206 H II regions and 186 079 spaxels classified as SF regions. In the case of the

AMUSING sample, we detect a total number of 14 345 H II regions for the 102 selected galaxies, almost twice as with CALIFA despite being around 20% less galaxies.

### 3.3 DERIVATION OF THE OXYGEN ABUNDANCES

Once the SF regions have been selected and their corresponding reddening-corrected emission line fluxes determined, we can proceed to measure the ionised gas abundances. As mention in Chapter 1, the two straight-forward methods to compute the oxygen abundance require either temperature sensitive line ratios such as  $[\text{O III}] \lambda\lambda 4959, 5007 / [\text{O III}] \lambda 4363$  (Peimbert & Costero 1969; Stasińska 1978; Pagel et al. 1992; Vilchez & Esteban 1996; Izotov et al. 2006; Pérez-Montero 2017) or line ratios involving recombination lines (Peimbert et al. 1993; Peimbert 2003; García-Rojas et al. 2004, 2006; Bresolin 2007; López-Sánchez et al. 2007; Esteban et al. 2009). However, some of these auroral or nebular lines are very faint, and the recombination ones even fainter. As a result of the weakness of the involved lines, the both methods can only be applied to nearby and low-metal objects for which very high S/N spectra are observable.

It becomes therefore necessary to look for indirect methods that allow us to estimate the chemical abundances in the cases where the direct methods are not feasible. To do this, abundance indicators based on the relations between metallicity and the intensity of strong and more readily observable lines have been developed. These methods have first been proposed by Alloin et al. (1979) and Pagel et al. (1979). Since then, several calibrators have been proposed and are widely used nowadays, based on both direct estimations of oxygen abundances (Zaritsky et al. 1994; Pilyugin 2000; Denicoló et al. 2002; Pettini & Pagel 2004; Pérez-Montero & Díaz 2005; Pilyugin & Thuan 2005; Pilyugin et al. 2010; Marino et al. 2013) and photoionisation models (Dopita & Evans 1986; McGaugh 1991; Kewley & Dopita 2002; Kobulnicky & Kewley 2004; Dopita et al. 2006, 2013; Pérez-Montero 2014; Dopita et al. 2016).

In this work we aim to derive the spatial distribution of the oxygen abundance across spiral galaxies. For this purpose, we adopt the empirical calibrator based on the O3N2 index that was first introduced by Alloin et al. (1979):

$$\text{O3N2} = \log \left( \frac{[\text{O III}] \lambda 5007}{\text{H}\beta} \times \frac{\text{H}\alpha}{[\text{N II}] \lambda 6584} \right). \quad (3.2)$$

This index (i) is only weakly affected by dust attenuation because of the close distance in wavelength between the lines in both ratios, (ii) presents a monotonic dependence on the abundance and (iii) uses emission lines covered

by both CALIFA and AMUSING wavelength ranges. One of the most popular calibrations for this index has been proposed by Pettini & Pagel (2004, hereafter PP04). However, this indicator lacks observational points at the high-metallicity regime ( $12 + \log(\text{O}/\text{H}) > 8.2$ ) and instead uses predictions from photoionisation models. Therefore, we here adopt the improved calibration proposed by Marino et al. (2013, hereafter M13), where

$$12 + \log(\text{O}/\text{H}) = 8.533 - 0.214 \times \text{O3N2}. \quad (3.3)$$

This calibration uses  $T_e$ -based abundances of  $\sim 600$  H II regions from the literature together with new measurements from the CALIFA survey, providing the most accurate calibration to date for this index. The increase in the number of regions used in this calibration is especially significant in the high-metallicity regime, where previous calibrators based on this index lack of high-quality observations of H II regions with auroral lines at this high-abundance end (e.g. Pettini & Pagel 2004; Pérez-Montero & Contini 2009).

We note that the linear regression derived in M13 between the O3N2 parameter and the oxygen abundance is valid for the interval  $8.17 < 12 + \log(\text{O}/\text{H}) < 8.77$ . H II regions presenting values outside this range are therefore not considered in the analysis. The derived abundances have a calibration error of 0.08 dex, much larger than the typical one associated with the errors in the measured emission lines that are taken into account via MC simulations ( $\sim 0.02 - 0.05$  dex).

Due to the wide variety of abundance indicators, the derived O/H abundances often show systematic disagreements between them (e.g. Kewley & Ellison 2008; López-Sánchez et al. 2012). Despite the choice of the M13 empirical calibrator as the adopted abundance indicator in this thesis (used for the reasons listed before), we have also determined abundances using several other calibrators to test the reliability of our results and their dependence on the adopted method.

With such purpose, in the case of CALIFA data we have selected some of the most widely used indicators: (i) the calibration proposed by PP04 for the O3N2 index, (ii) the Pilyugin et al. (2010, hereafter P10) calibration for the ONS index, (iii) and the Dopita et al. (2013, hereafter D13) calibration based on the MAPPINGS IV code developed by the authors. The PP04 calibration for the O3N2 index, as already mentioned, is one of the most popular calibrations used for this index and is defined as  $12 + \log(\text{O}/\text{H}) = 8.73 - 0.32 \times \text{O3N2}$ . This calibration is not valid in the low-metallicity regime ( $12 + \log(\text{O}/\text{H}) < 8$ ), but as we do not reach this limit, this effect will not affect our results. The P10 ONS calibration makes uses of the  $N_2/R_2$  and  $S_2/R_2$  ratios (defined as  $R_2 = [\text{O II}] (\lambda 3727 + \lambda 3729)$ ,  $N_2 = [\text{N II}] (\lambda 6548 + \lambda 6584)$ ,  $S_2 = [\text{S II}] (\lambda 6717 + \lambda 6731)$ ) as temperature and metallicity indexes and is valid over the whole range of explored metal-

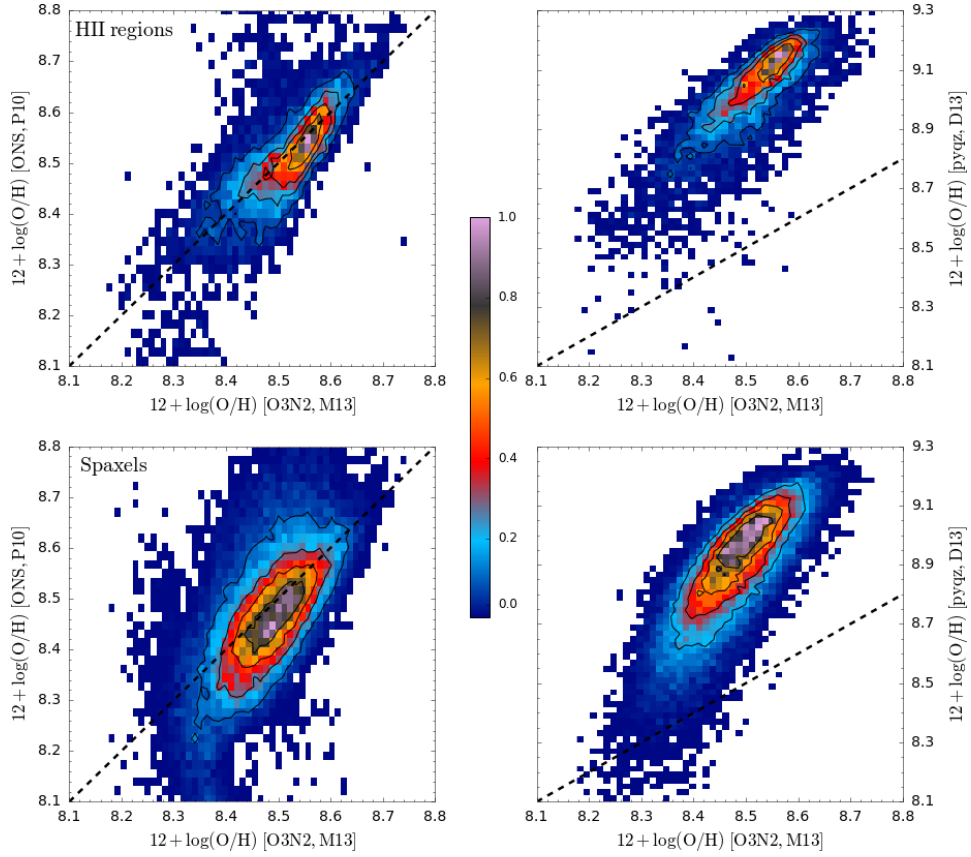


**Figure 3.5:** Comparison of the oxygen abundance distribution of the  $H_{II}$  regions (top panels) and the SF spaxels (bottom panels) among different calibrators for the CALIFA sample: M13 for the O3N2 index vs the P10 calibration for the ONS index (left panels) and M13 vs the calibration based on pyqz code (D13, right panels). The black contours show the density distribution of the SF spaxels/ $H_{II}$  regions, the outermost one including 80% of the total number of elements and decreasing 20% in each consecutive contour. The black dashed lines indicate the 1:1 relation between the represented calibrators.



licities. The derived relations to determine the oxygen abundances using this calibration are given by P10. Finally, the D13 calibration is based on a grid of photoionisation models covering a wide range of abundances and ionisation parameters typical of H II regions in galaxies. This calibration can be used through a Python module implemented by the authors, known as `pyqz`, which is publicly available<sup>4</sup>.

Figure 3.5 illustrates this comparison for the oxygen abundances of the 129 CALIFA galaxies in our sample, using both the individual H II regions (top panels) and the SF spaxels (bottom panels). The left panels represent the distribution of oxygen abundance values derived using the M13 calibration for the O3N2 index against the P10 calibration for the ONS index. In the right panels we show the same distribution of the M13 calibration, but this time versus the D13 calibration based on the `pyqz` code. All panels show a tight correlation between the compared calibrators.

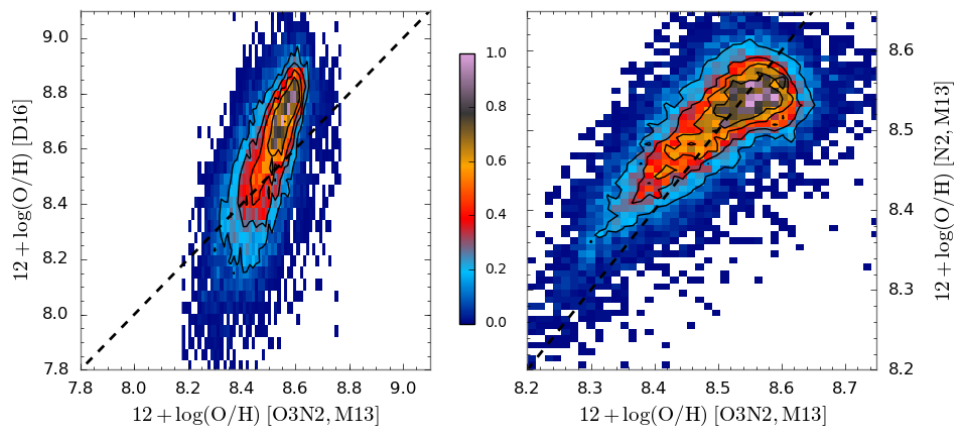
In the case of AMUSING data, the limited wavelength range in the blue regime covered by MUSE does not allow us to compare our derivation of the oxygen abundances indicator with the mentioned calibrators, which use emission lines that are out of this range (in particular [O II]  $\lambda 3727$ ). Therefore, for the analyses carried out along this thesis using this sample of galaxies we have to choose other less common abundance indicators to be compared with the M13 calibration for the O3N2 index, like the ones based on the sulphur lines. In particular, we make use of (i) the calibrator described in Dopita et al. (2016, hereafter D16), (ii) and the calibration proposed in Marino et al. (2013) for the N2 index (hereafter N2-M13). The D16 calibrator is based on photoionisation models and makes use of H $\alpha$ , [N II]  $\lambda 6584$  and [S II]  $\lambda\lambda 6717, 6731$  emission lines. This calibrator is almost linear up to an abundance of  $12 + \log(\text{O}/\text{H}) = 9.05$  and it is independent of reddening (it invokes lines located close together in wavelength). Finally, the N2-M13 indicator is based in the N2 index, defined as  $N2 = \log([\text{N II}]\lambda 6584/H\alpha)$ . This calibrator is also independent of reddening and has a monotonic behaviour, but presents the disadvantage of saturating in the high-metallicity regime.

Figure 3.6 shows the comparison of the oxygen abundances of the H II regions for the 102 AMUSING galaxies in our sample using the mentioned calibrators. The left panel represent the distribution of oxygen abundance values derived using the M13 calibration for the O3N2 index against the D16 indicator. In the right panel we show the same distribution of the M13 calibration, but this time versus the M13 calibration based on the N2 index. Similarly to the indicators used for the CALIFA data, in this case all panels show also a tight correlation between the compared calibrators.

The correlations found in the comparison among calibrators, for both

---

<sup>4</sup><http://dx.doi.org/10.4225/13/516366F6F24ED>



**Figure 3.6:** Comparison of the oxygen abundance distribution of the  $H_{II}$  regions among different calibrators for the AMUSING sample: M13 indicator for the O3N2 index vs the D16 calibration based on sulphur lines (left panel) and O3N2-M13 vs the M13 calibration for the N2 index (right panel). The black contours show the density distribution of the  $H_{II}$  regions, the outermost one including 80% of the total number of elements and decreasing 20% in each consecutive contour. The black dashed lines indicate the 1:1 relation between the represented calibrators.

CALIFA and AMUSING data, suggest that our qualitative results presented along this thesis should not be contingent upon the choice of the used calibrator, although the actual values for abundances and derived measurements may change. We will go deep into this issue in the next chapters when we describe the obtained results in each of the different abundance analyses performed.

### 3.4 DEPROJECTION OF GALAXIES

The disc of spiral galaxies is known to be an axisymmetric component which sometimes appears elliptical due to the effect of inclination. The greater the ellipticity, the more inclined the disc is with respect to our line of sight. Although we have selected galaxies with  $i < 60 - 70^\circ$ , the difference with respect to a face-on system ( $i < 0^\circ$ ) is still appreciable. Thus, we need to deproject the galaxy discs to carry out the best possible characterisation of the oxygen abundance distribution.

To deproject the galaxy images it is necessary to determine the two deprojection angles of the disc: the position angle (PA) and the inclination angle ( $i$ ). The PA is the angle between the North and the semimajor axis of the galaxy, measured towards the East, while  $i$  is the angle between the perpendicular to the plane of the galaxy and the line of sight. To first order, one can estimate the inclination of a spiral galaxy by assuming that the galaxy is an infinitely thin disc.

For the study of the abundance gradient with CALIFA galaxies (Chapter 4), these morphological parameters were extracted from Walcher et al. (2014), computed by performing a light moments analysis (see details in the article for more information in this regard). However, during the course of this thesis and after carrying out that study we performed a two-dimensional photometric decomposition of the CALIFA sample and the position angle and ellipticity of all galaxies were also derived as a by-product of such decomposition. Due to the improvements of this analysis, that we think is more realistic due to its two-dimensional approach, over the previous one, we decided to use these new values of the photometric parameters for the study of the arm-interarm abundance distributions (Chapter 6). As mentioned, these parameters were obtained as a by-product of the two-dimensional photometric decomposition of the galaxies performed using the GALaxy Surface Photometry 2 Dimensional Decomposition (GASP2D) algorithm developed in Méndez-Abreu et al. (2008). From the  $g$ ,  $r$  and  $i$  band images of the SDSS DR7, GASP2D iteratively fits a model with different morphological components (i.e. bulge, disc, bar component, etc.) to the 2-D observed light distribution of the analysed galaxies. This fit is performed by means of a non-linear least-squares minimisation based on a robust Levenberg-Marquardt method (Moré et al. 1980) using the MPFIT algorithm (Markwardt 2009). The actual implementation and a detailed description of the code is provided in Méndez-Abreu et al. (2008, 2014). By performing the two-dimensional decomposition, GASP2D provides us with the best combination of these components that better fit the observed light distribution. Among the set of structural parameters resulting from this fit, we can name the ellipticity ( $e$ ) and PA of the bulge/disc, the bar length, etc., depending on its specific morphology. The results of the photometric decomposition of the entire CALIFA observed sample and the corresponding structural parameters are presented in Méndez-Abreu et al. (2017).

Figure 3.7 shows the differences in the values of the deprojection angles PA and  $i$  derived using both approaches. We can see that for most of the galaxies these differences are lower than  $10^\circ$  (difference that means an error of  $\pm 5^\circ$  in the parameters, error that is well accounted in the abundance gradient derivation, see Sect 4.1). However, there are about 15% of the galaxies that present differences above  $10^\circ$  in the inclination angle. For these galaxies the differences in the deprojection angles may affect the results, producing noticeable differences in the radial abundance distribution. For consistency, we have decided to present in this thesis the results that have been already published, maintaining the analysis of the abundance gradients with the PA and  $i$  angles derived using the first method (light moments analysis). As future work (see Chapter 7.4) we plan to repeat the analysis using a larger sample of galaxies (considering all the galaxies finally observed with CALIFA) and with the deprojection angles derived with GASP2D, in

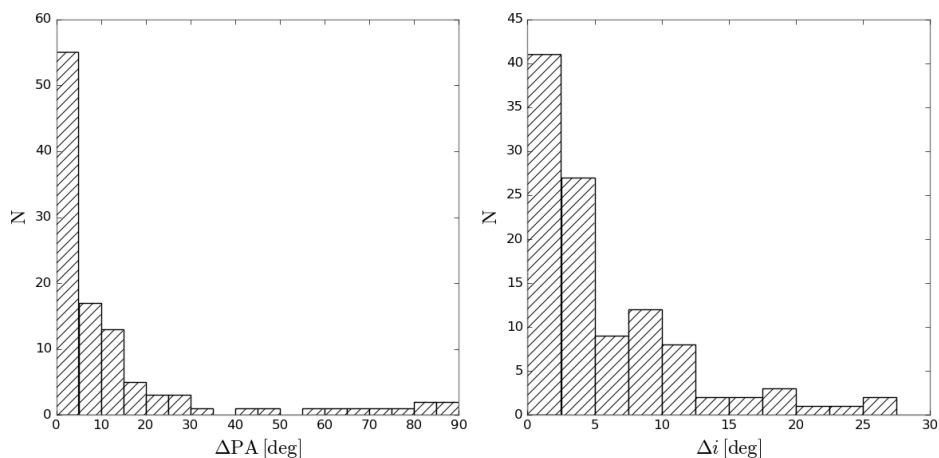


**Figure 3.7:** Comparison of the PA and  $i$  angles derived for CALIFA galaxies using two different approaches: light moments analysis and the two-dimensional decomposition of the galaxies with GASP2D. See text for more details.

order to assess the effects that these differences may produce on the radial abundance distribution.

For AMUSING galaxies, the PA and  $i$  values were derived by fitting ellipses of variable ellipticity and position angle to the outermost isophotes of the galaxies in a  $g$ -band image recovered from the data, by means of the ELLIPSE IRAF task. For the galaxies that are larger than the FoV of MUSE or very close to its limit (32) a proper characterisation of the outermost isophotes is highly hampered using these data and therefore, the Second Digitized Sky Survey (DSS2) red-band (POSS-II F, Reid et al. 1991) images were used instead.

Table A.1 of Appendix A and Table B.1 of Appendix B list the values of the position and inclination angles of our CALIFA and AMUSING samples, respectively. For the CALIFA galaxies that are part of the arm-interarm analysis carried out in Chapter 6, the two values derived for these parameters, as explained above, are provided.

We must note that we have preferred not to correct for the inclination effects in galaxies with inclinations below  $35^\circ$ , as the uncertainties in the derived correction exceed the very small effect on the spatial distribution of the spaxels (Sánchez et al. 2014).

*A hypothesis or theory is clear, decisive, and positive, but it is believed by no one but the man who created it. Experimental findings, on the other hand, are messy, inexact things which are believed by everyone except the man who did that work.*

— Harlom Shapley

# 4

## Oxygen abundance radial profiles with CALIFA

### Contents

4.1	Derivation of the gradient . . . . .	66
4.2	Abundance gradient distribution . . . . .	68
4.3	Abundance gradients by galaxy types . . . . .	70
4.4	Common abundance gradient . . . . .	75
4.5	Deviations from negative gradient . . . . .	78
4.5.1	Flattening in the outer regions . . . . .	78
4.5.2	Oxygen abundance inner drop . . . . .	81
4.6	Dependence on the used calibrators . . . . .	82
4.7	Brief summary . . . . .	86



.....

THE FIRST WORKS AIMED AT studying the oxygen abundance distribution of spiral galaxies were focused on the analysis of the radial distribution. All these studies predicted an almost universal negative metallicity gradient once it is normalised to the galaxy optical size (Boissier & Prantzos 1999, 2000), evidence in favour of the inside-out growth models for disc formation (see Chapt. 1). Several observational studies have found this radial decrease in the oxygen abundance across the discs of nearby galaxies (e.g. Peimbert 1979; Garnett 1986; Vila-Costas & Edmunds 1992; Zaritsky et al. 1994; van Zee et al. 1998; Bresolin et al. 2009b; Moustakas et al. 2010; Rich et al. 2012; Sánchez et al. 2012b, 2014), as well as in our own Galaxy (Shaver et al. 1983; Deharveng et al. 2000; Pilyugin et al. 2003; Esteban et al. 2005; Balser et al. 2011; Esteban et al. 2017).

However, gas metallicity studies have also presented evidence of the existence of some behaviours in the radial oxygen abundance profiles that deviate from the pure inside-out scenario: A decrease or a nearly flat distribution of the abundance in the innermost region of discs, first observed by Belley & Roy (1992) and afterwards confirmed by other works (e.g. Rosales-Ortega et al. 2011; Sánchez et al. 2012b, 2014); and a flattening of the gradient in the outer regions measured in several works (Martin & Roy 1995; Vilchez & Esteban 1996; Roy & Walsh 1997; Bresolin et al. 2009b; Sánchez et al. 2011; Bresolin et al. 2012; Marino et al. 2012, among others). These features have been theoretically suggested to be motivated, for instance, by the presence of radial migration (Minchev et al. 2011, 2012). Nevertheless, their origin is still unknown.

In this chapter, we make use of full 2D information in analysing CALIFA data spaxel by spaxel with the goal of characterising the radial gas abundance profile in a sample of face-on spiral galaxies. We do not only focus on the broadly analysed gradient, but also on the deviations from this simple negative trend, such as inner drops and outer flattenings. We also aim to compare the results with those obtained following the classical procedure of H II region analysis. These results have been published in Sánchez-Menguiano et al. (2016b).

Along the chapter, we describe the procedure to derive the gradients (Sect. 4.1) and analyse their distribution (Sect. 4.2). The comparison of the gradient distributions derived using the two methodologies (spaxel by spaxel and H II region analysis) is also performed in Sect. 4.2. We also study the dependence of the slope on different properties of the galaxies (Sect. 4.3), and the existence of a common abundance gradient (Sect. 4.4). Finally, deviations from this general gradient are also analysed (Sect. 4.5).

## 4.1 DERIVATION OF THE GRADIENT

To derive the radial distribution of the oxygen abundance for each galaxy, we deproject the galactocentric distances of the selected SF regions (spaxels/H II regions) using the position angle and ellipticity of the galaxy discs (see Sect. 3.4 for details in the derivation of these parameters). The deprojected galactocentric distance for each spaxel is then normalised to the disc effective radius, as suggested in Sánchez et al. (2012b) and Sánchez et al. (2013). This parameter was taken from Sánchez et al. (2014), which was derived from the disc scale-length based on an analysis of the azimuthal surface brightness profile (SBP), explained in Appendix A of the cited article. The values of  $r_e$  are given in Table A.1 of this thesis. Other normalisation length-scales are also used for better comparison with other studies, such as the  $r_{25}$  radius, which is defined as the radius corresponding to a surface brightness level of 25 mag/arcsec<sup>2</sup> in the SDSS DR7  $r$ -band, and the physical scale of the galaxy, that is, the galactocentric distances in kpc.

Finally, we obtain the radial distribution of the oxygen abundance for each galaxy. To characterise this profile, we perform an error-weighted linear fit to the derived oxygen abundance mean values for radial bins of  $0.25 r_e$  within the range between  $0.5$  and  $2.0 r_e$ . The radial binning is made to minimise possible azimuthal differences in the oxygen abundance distribution, and the size of the bins is chosen to match the seeing value. We exclude the innermost region ( $r/r_e < 0.5$ ), which sometimes presents a nearly flat distribution or even a drop towards the centre (e.g. Belley & Roy 1992; Rosales-Ortega et al. 2011; Sánchez et al. 2012b, 2014). We also omit the outer region ( $r/r_e > 2.0$ ), which is found to have a flattening in the abundance gradient for galaxies covering regions beyond  $r_{25}$  (e.g. Martin & Roy 1995; Vilchez & Esteban 1996; Roy & Walsh 1997; van Zee et al. 1998; Bresolin et al. 2009b; Rosales-Ortega et al. 2011; Bresolin et al. 2012; Marino et al. 2012; López-Sánchez et al. 2015). This range is defined by visual inspection of each individual galaxy, discarding the regions where we observed the mentioned features. The linear fit is weighted using the standard deviations of (mean) values within each bin and considering only the bins that contain at least nine values of the oxygen abundance. This minimum number of values required for each bin has been determined to ensure a precision in the derived mean that is ten times better than the dynamic range of abundance values covered in the fit, taking into account the dispersion in the measurements.

It is important to note that uncertainties in the determination of the deprojected galactocentric distances can significantly affect the derivation of the abundance gradients. Moreover, as the radial galactocentric distances are normalised to the disc effective radius, the uncertainties in the determination of the  $r_e$  can also contribute to the scatter obtained on the final



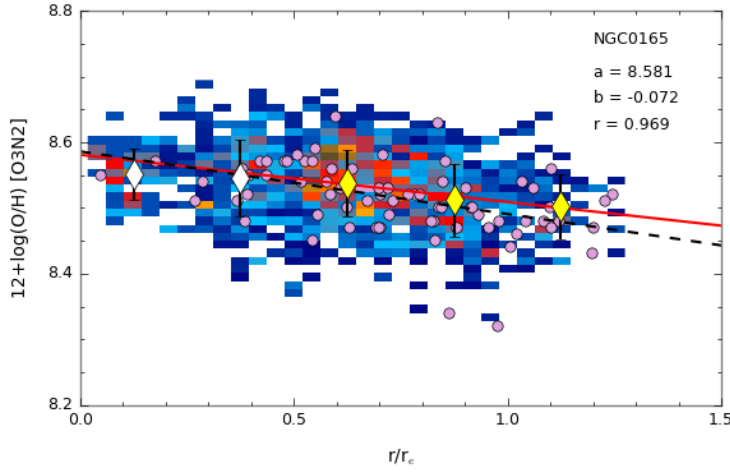


**Figure 4.1:** Radial density distribution of the spaxels in the oxygen abundance-galactocentric distance space for one galaxy of the sample (see Fig. 3.4 for a position map of the SF regions). The radial distances are deprojected and normalised to the disc effective radius. The diamonds represent the mean oxygen abundance values, with the error bars representing the corresponding standard deviations, for bins of  $0.25 r_e$  and the red solid line the error-weighted linear fit derived for values within the range between  $0.5$  and  $2.0 r_e$  (yellow diamonds). The parameters of the fit are shown in the upper right corner, including the zero point ( $a$ ), the slope ( $b$ ) and the correlation coefficient ( $r$ ). The violet dots correspond to the oxygen abundances derived for the individual  $H II$  regions, and the dashed black line is the linear regression for these points.

oxygen gradients. On one hand, performing MC simulations, we obtained that an error of  $5^\circ$  in the inclination and PA of the galaxies can produce a dispersion in the gradient distribution of at most  $0.05 \text{ dex}/r_e$  ( $0.02 \text{ dex}/r_e$  on average). On the other hand, comparing different methods to derive the  $r_e$  (as described in Sánchez et al. 2014) and taking into account both the nominal errors and the differences among them, the overall contribution to the dispersion in the gradient distribution coming from the derivation of the  $r_e$  is at most  $0.04 \text{ dex}/r_e$  ( $0.01 \text{ dex}/r_e$  on average). All these uncertainties are well accounted for by our error estimation of the gradient ( $0.05 \text{ dex}/r_e$ , see Sect. 4.2).

In Fig. 4.1 we present an example of the abundance gradient for the same galaxy shown in Fig. 3.4, NGC 0165, using both the spaxel-wise information (colour map) and the individual  $H II$  regions (violet dots). The diamonds represent the mean oxygen abundance values of the radial bins, with the error bars indicating the corresponding standard deviations. The red solid line is the error-weighted linear fit derived for values within the range between  $0.5$  and  $2.0 r_e$  (yellow diamonds), and the dashed black line is the linear regression for the individual  $H II$  regions. This figure illustrates

the procedure explained before to derive the oxygen abundance gradient. From the original 129 galaxies, we were able to fit 122 lines, and the remaining galaxies were discarded from further analysis because of the low number of spaxels associated with SF regions that are needed to carry out the linear fit. This final sample provides more than 185 000 oxygen abundance values, approximately 8 230 of them beyond two disc effective radii, and with more than 7 100 H II regions to compare with, around 605 beyond  $2 r_e$ . Figure ?? of Appendix C shows the observed radial abundance distribution for all the galaxies, and the slope and oxygen abundance values at one disc effective radius for all of them are listed in Table A.2 of Appendix A.

## 4.2 ABUNDANCE GRADIENT DISTRIBUTION

Figure 4.2 shows the distribution of the correlation coefficient, zero-point, and slope of the abundance gradients for the final sample using both the spaxel-wise information (red dashed histogram) and the individual H II regions (blue filled histogram).

We focus first on the spaxel-wise analysis. For almost all galaxies the correlation coefficient is larger than 0.75. If we perform a Student's t-test to check the significance of the correlation, we obtain that for  $\sim 80\%$  of the galaxies the oxygen abundance and the radial distance (normalised to the disc effective radius) are significantly correlated to the 95% level (0.05).

The distribution of zero points ranges between 8.4 and 8.7, reflecting the mass-range covered by the sample as a consequence of the well-known  $\mathcal{M}-Z$  relation (e.g. Tremonti et al. 2004; Sánchez et al. 2013). The presence of a peak in the distribution and a small standard deviation is result of the sample selection, which entails a lack of low-luminosity galaxies (see Sect. 2.1.1).

Finally, the distribution of slopes presents a characteristic value of  $\alpha_{\text{O/H}} = -0.07 \text{ dex}/r_e$  with a standard deviation of  $\sigma \sim 0.05 \text{ dex}/r_e$ . We perform a Lilliefors test (Lilliefors 1967) to assess the compatibility of the distribution with a Gaussian, obtaining a test statistics of 0.07 and a P-value of 0.62, showing that the distribution of slopes has a clear peak and is remarkably symmetric. We run a MC simulation to estimate the contribution of the errors in the derived slopes to the  $\sigma$  of the distribution, obtaining that these errors can only explain 49% of the width distribution. We may have underestimated the errors involved in the determination of the slopes, particularly the effect of the inclination. Otherwise, the remaining  $\sigma$  must have another origin that we investigate in more detail in Sect. 4.3.

The analysis for the individual H II regions leads us to very similar results. In this case, we have a wider distribution for the correlation coefficients, but we have to note that the number of points involved in the linear fit is larger using all the individual H II regions, since we do not apply any kind of radial

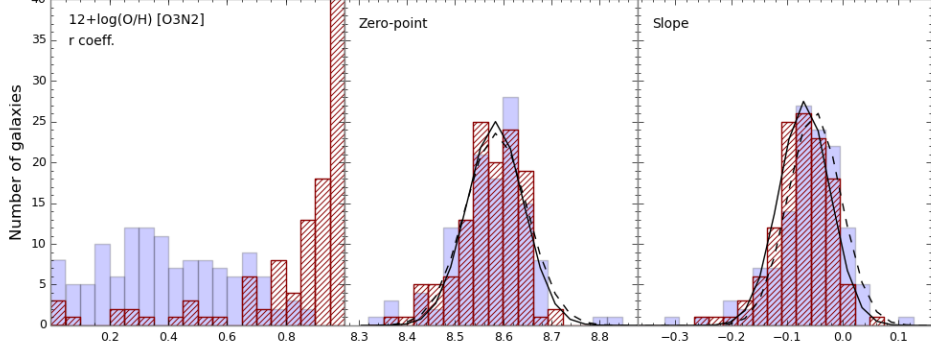


**Figure 4.2:** Distribution of correlation coefficients (left panel), zero points (middle panel), and slopes (right panel) of the linear fits derived for the oxygen abundance gradients of the final sample of 122 galaxies using spaxel-wise information (dashed red bars) and the individual H II regions (filled blue bars). For both the zero point and slope distributions the lines represent the Gaussian distribution of the data (solid line for spaxels, dashed line for individual H II regions), assuming the mean and standard-deviation of the distribution of each analysed parameter and sampled with the same bins.

**Table 4.1:** Oxygen abundance gradient slopes derived using different calibrators and distance normalisations.

Calibrator	$\alpha_{\text{O/H}} - \text{spaxels}$		
	[dex/ $r_e$ ]	[dex/ $r_{25}$ ]	[dex/kpc]
O3N2 [M13]	$-0.07 \pm 0.05$	$-0.08 \pm 0.06$	$-0.009 \pm 0.008$
O3N2 [PP04]	$-0.11 \pm 0.07$	$-0.12 \pm 0.09$	$-0.014 \pm 0.012$
ONS [P10]	$-0.06 \pm 0.06$	$-0.08 \pm 0.07$	$-0.008 \pm 0.009$
pyqz [D13]	$-0.14 \pm 0.09$	$-0.15 \pm 0.10$	$-0.019 \pm 0.014$
Calibrator	$\alpha_{\text{O/H}} - \text{H II regions}$		
	[dex/ $r_e$ ]	[dex/ $r_{25}$ ]	[dex/kpc]
O3N2 [M13]	$-0.05 \pm 0.06$	$-0.06 \pm 0.06$	$-0.008 \pm 0.010$
O3N2 [PP04]	$-0.08 \pm 0.09$	$-0.09 \pm 0.09$	$-0.011 \pm 0.014$
ONS [P10]	$-0.06 \pm 0.09$	$-0.08 \pm 0.11$	$-0.008 \pm 0.012$
pyqz [D13]	$-0.11 \pm 0.09$	$-0.13 \pm 0.11$	$-0.015 \pm 0.015$

binning to the data. The correlation coefficient is larger than 0.32 for  $\sim 60\%$  of the galaxies, which corresponds to a significance level of 98% (0.02). The distribution of zero points covers almost the same range as for the spaxels (between 8.3 and 8.8), allowing us to draw the same conclusions. Finally, the distribution of slopes presents a characteristic value of  $\alpha_{O/H} = -0.05 \text{ dex}/r_e$  with a standard deviation of  $\sigma \sim 0.06 \text{ dex}/r_e$ . The Lilliefors test gives a test statistic of 0.08 and a P-value of 0.28, very similar to the one described for the spaxel-wise analysis. The MC simulation yields a contribution of 44% of the errors in the derived slopes to the distribution width, again insufficient to explain the  $\sigma$  of the distribution.

If we use different scales to normalise the radial distances like  $r_{25}$  and the physical scale of the galaxy (radius in kpc) for both the spaxel-wise and the individual H II region analysis, we obtain in all cases a similar and narrow distribution, although for the physical scale the distribution is clearly asymmetric, with a tail towards large slopes. We note that our range of masses is narrow, and consequently, so is the range of  $r_e$  and  $r_{25}$ , which in turn causes the distribution when normalising to the physical scale narrow as well, in contrast to what we should obtain for a wider range of masses. Table 4.1 shows a comparison among the oxygen abundance slopes derived using the different calibrators described in Sect. 3.3 and the different normalisations for the radial distance described before. In this table we present the values using both the spaxels and the individual H II regions.

For the sake of clarity, below in the next sections we only show the results of this study based on the use of the M13 calibrator. However, we have reproduced the analysis using all the proposed calibrators, with no significant differences between the obtained results (as suggested by the comparison showed in Sect. 3.3). The most relevant ones are provided in Sect. 4.6.

### 4.3 ABUNDANCE GRADIENTS BY GALAXY TYPES

After deriving the oxygen abundance gradient for all galaxies, we analyse whether there is a dependence of the slope on different properties of the galaxies. We focus this analysis on three properties: the differences in the morphological type, the effect of the bars, and the luminosity of the galaxies. We show in Sect. 4.2 that the oxygen abundance distribution obtained for both the spaxels and H II regions are equivalent and accordingly lead to the same results, therefore we carry this analysis out for the spaxel-wise information alone.

Figure 4.3 shows the slope distribution as a function of the morphological type of the galaxy (top panel), the presence or absence of bars (middle panel), and the  $g$ -band absolute magnitude of the galaxies (bottom panel).

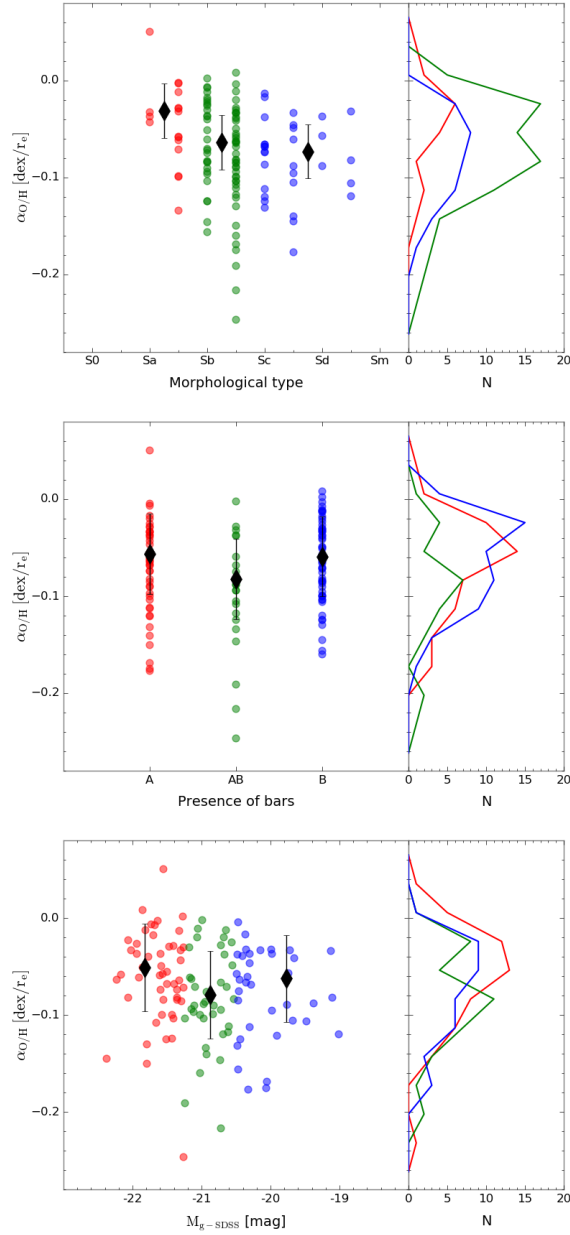


**Figure 4.3:** Distribution of the abundance slopes as a function of the morphological type of the galaxies (left panel), the presence or absence of bars (middle panel) and the  $g$ -band absolute magnitude of the galaxies (right panel). We also show the histograms for each distribution, where  $N$  is the number of galaxies and colours indicate the different classification types: (i) early spirals, Sa-Sab (red); intermediate spirals, Sb-Sbc (green); late spirals, Sc-Sm (blue) for the left panel. (ii) Clearly unbarred galaxies (red); clearly barred (blue); an intermediate stage (green) for the middle panel. (iii) Luminous galaxies,  $M_{g-SDSS} < -21.25$  mag (red); intermediate galaxies,  $-21.25 < M_{g-SDSS} < -20.5$  mag (green); faint galaxies,  $M_{g-SDSS} > -20.5$  mag (blue) for the right panel. Black diamonds represent the median values for the distributions, together with the standard deviation shown as error bars.

We also show the histograms for each distribution, where  $N$  is the number of galaxies. The limits used in the classification based on the luminosity of the galaxies were chosen to ensure a similar number of elements in each bin (i.e. comparable from a statistical point of view). We have tried to follow a similar criterion in the separation by morphological types, but the deficiency of Sa-Sab galaxies and the criterion of not considering Sb as early type prevents us from obtaining a comparable number of objects in each bin.

The slope distribution by morphological types seems to vary in a way that the earlier spirals present flatter gradients than the later type ones. The median values for the distributions together with the standard deviations are

$$\text{Sa} - \text{Sab} : \alpha_{O/H} = -0.04 \text{ dex}/r_e \text{ and } \sigma = 0.04 \text{ dex}/r_e \quad (n_{\text{gal}} = 17)$$

$$\text{Sb} - \text{Sbc} : \alpha_{O/H} = -0.07 \text{ dex}/r_e \text{ and } \sigma = 0.05 \text{ dex}/r_e \quad (n_{\text{gal}} = 74)$$

$$\text{Sc} - \text{Sm} : \alpha_{O/H} = -0.07 \text{ dex}/r_e \text{ and } \sigma = 0.04 \text{ dex}/r_e \quad (n_{\text{gal}} = 31).$$

We perform a two-sample Kolmogorov-Smirnov test (KS test) to check if the differences found between the distributions are significant. The significance level of the KS test is 5%, meaning that values below this limit come from different distributions. We derive a P-value of 7% for the distributions with the largest differences (between early and late spirals), a P-value of 10% for the test comparing the early and intermediate types, and a P-value of 92% between intermediate and late ones. We also perform an Anderson-Darling test (AD test), which is more suitable when the samples comprise only few objects, with a resulting P-value of 8% for the early-late comparison, a P-value of 16% for the test comparing the early and intermediate type, and a P-value of 73% in the intermediate-late case. This clearly shows that the observed differences are negligible.

For the distribution of slopes depending on the presence or absence of bars we define three different groups: galaxies with no bar (A), galaxies that may have a bar, but where the bar is not clearly visible (AB), and clearly barred galaxies (B). The results are as follows:

$$\text{A} : \alpha_{O/H} = -0.06 \text{ dex}/r_e \text{ and } \sigma = 0.05 \text{ dex}/r_e \quad (n_{\text{gal}} = 46)$$

$$\text{AB} : \alpha_{O/H} = -0.09 \text{ dex}/r_e \text{ and } \sigma = 0.06 \text{ dex}/r_e \quad (n_{\text{gal}} = 23)$$

$$\text{B} : \alpha_{O/H} = -0.06 \text{ dex}/r_e \text{ and } \sigma = 0.04 \text{ dex}/r_e \quad (n_{\text{gal}} = 53).$$

We find negligible differences for these distributions. This is confirmed by the KS test, which gives a P-value of 52% for the comparison of the A-AB distributions, a P-value of 50% for the A-B distributions, and a P-value of 10% for the AB-B distributions (from the AD tests we obtain P-values of 39%, 27% and 5% for each bin, respectively).

Finally, to analyse the distribution of slopes depending on the luminosity of the galaxies, we divide the sample again into three groups: luminous (L,

$M_{g\text{-SDSS}} < -21.25$  mag), intermediate (I,  $-21.25 < M_{g\text{-SDSS}} < -20.5$  mag), and faint (F,  $M_{g\text{-SDSS}} > -20.5$  mag) galaxies. We obtain these results:

$$\begin{aligned} \text{L} : \quad & \alpha_{O/H} = -0.06 \text{ dex}/r_e \text{ and } \sigma = 0.05 \text{ dex}/r_e \quad (n_{\text{gal}} = 49) \\ \text{I} : \quad & \alpha_{O/H} = -0.09 \text{ dex}/r_e \text{ and } \sigma = 0.05 \text{ dex}/r_e \quad (n_{\text{gal}} = 37) \\ \text{F} : \quad & \alpha_{O/H} = -0.07 \text{ dex}/r_e \text{ and } \sigma = 0.05 \text{ dex}/r_e \quad (n_{\text{gal}} = 36). \end{aligned}$$

The statistical tests yield a P-value of 13% for the KS test in the case with the largest differences, that is, when comparing luminous and intermediate galaxies. The remaining KS tests return a P-value of 67% for the comparison between luminous and faint galaxies and a P-value of 72% when analysing the intermediate and faint distributions (a P-value of 19%, 50%, and 52%, respectively, for the AD tests).

Similar results for all these separations are found when using any scale-length normalisation for the radial distance instead of the disc effective radius, either the  $r_{25}$  radius or the physical scale of the galaxy (i.e. the radial distance in kpc). This is also the case when using other alternative calibrators (see Sect. 4.6).

The results of this analysis contradict some previous studies, which did find a relation between the slope in the gas abundance gradient and some properties of the galaxies, such as the morphology, the mass, or the presence of bars. The dependence of the slope on the morphology of the galaxies is still an open question. Early studies found a correlation between the abundance slope and the morphological type of galaxies, with later types showing steeper gradients (Vila-Costas & Edmunds 1992; Oey & Kennicutt 1993). Other studies, however, suggested gradients independent of galaxy type (Diaz 1989; Zaritsky et al. 1994), when normalising to a physical scale of the disc (e.g. the  $r_{25}$  radius or the disc scale-length  $r_d$ ). The contradictory results might be due to the small and heterogeneous samples and inconsistent methods of measuring metallicity gradients.

For the effect of bars the conclusions likewise disagree. It is well known that roughly 30–40% of the spiral galaxies have a strong bar in optical wavelengths, 60% if we take into account weaker bars (e.g. Sellwood & Wilkinson 1993; Marinova & Jogee 2007; Sheth et al. 2008; Aguerri et al. 2009; Masters et al. 2011). Gas kinematic data show the presence of strong non-circular motions in bars (Huntley 1978; Zurita et al. 2004; Holmes et al. 2015), indicating that the bar constitutes a major non-axisymmetric component of the galaxy mass distribution (Sellwood & Wilkinson 1993). Bars have been proposed as a key mechanism in the dynamical evolution of disc galaxies. For instance, they are able to contribute to the redistribution of matter in the galaxy by exchanging angular momentum with the disc, inducing gas flows (Athanasoula 1992; Friedli 1998). This radial movement can produce

a mixing and homogenisation of the gas, changing the abundance profiles in the disc and causing a flattening in the gas abundance gradients (Friedli et al. 1994; Friedli & Benz 1995; Portinari & Chiosi 2000; Cavichia et al. 2014).

Different studies have observed this flattening in the gas abundance gradient of barred galaxies and found a correlation between the abundance slope and the presence of a bar (Vila-Costas & Edmunds 1992; Martin & Roy 1994; Zaritsky et al. 1994), independently of the adopted normalisation radius. However, recent works on either stellar or gas-phase metallicity have not found evidence of such a correlation between them (Sánchez et al. 2012b, 2014; Sánchez-Blázquez et al. 2014; Cheung et al. 2015). Our results support this absence of a correlation between oxygen gradient and the presence of bars. However, stellar radial migration due to bars may enlarge the effective radius of the disc (Debattista et al. 2006), which could compensate for the effect on the oxygen abundance values and produce the same gradient as in absence of bars. We have checked this possibility and confirm that there is no such effect on the disc effective radius, as can be inferred from the bottom right panel of Fig. 2.2. This fact, together with the absence of correlation between oxygen gradient and the presence of bar, suggests that bars alone may not have such a strong influence on the chemical evolution of disc galaxies as predicted by simulations.

Finally, no trends with the luminosity or mass of the galaxies have been found in previous studies when normalising to a physical scale of the disc (Zaritsky et al. 1994; Garnett et al. 1997; Ho et al. 2015); this agrees with our results. However, a recent study by Belfiore et al. (2017) reports a dependence of the abundance gradient with the stellar mass of the galaxies. The authors found that more massive galaxies present steeper gradients up to a mass of  $\log (M/M_{\odot}) = 10.5$ ; for higher mass values the trend is inverted.

We note that several studies that found correlations with some properties of the galaxies measured the abundance gradients in absolute scale (i.e. kpc). When normalising the galactocentric distances to scale lengths such  $r_{25}$ ,  $r_d$  or  $r_e$ , the correlations sometimes disappear. This can partially be understood as a size effect. If galaxies with steeper metallicity gradients measured in  $\text{dex kpc}^{-1}$  are smaller in their physical sizes (small  $r_{25}$ ), then the steep  $\text{dex kpc}^{-1}$  metallicity gradients would be compensated for when the galaxy sizes are taken into account. Sánchez et al. (2012b, 2013) stated the importance of defining the gradient normalised to the disc effective radius, since this parameter presents a clear correlation with other properties of the galaxies, such as the absolute magnitude, the mass, or the morphological type.



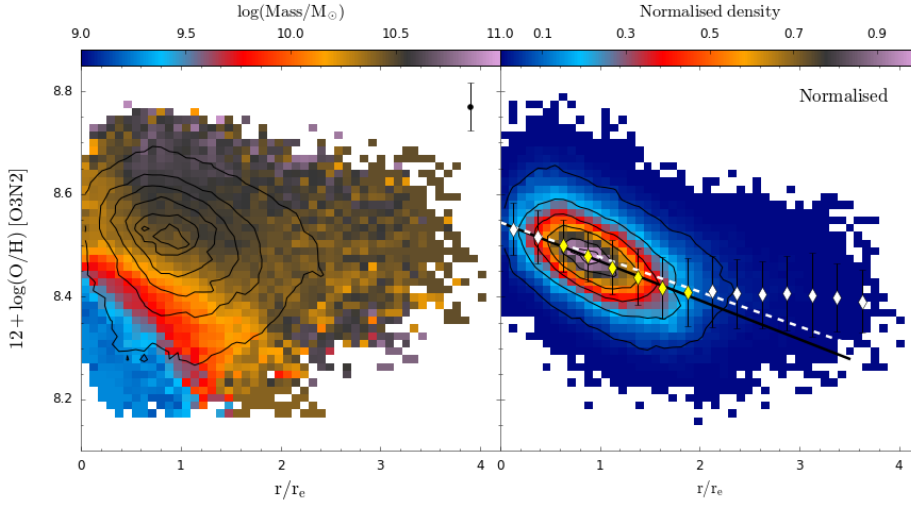


**Figure 4.4:** *Left: Radial distribution of the oxygen abundance derived using the M13 calibration of the O3N2 index for the entire galaxy sample. The colour bar displays the integrated stellar mass of each galaxy (in log scale). For clarity, only the oxygen abundance values with a contribution of at least 1% of the total number of spaxels are plotted. The average error of the derived oxygen abundances is indicated as an error bar located at the top right side of the panel. Right: Normalised radial density distribution of the oxygen abundance. The diamonds represent the mean oxygen abundance values for bins of  $0.25 r_e$  (with the standard deviations indicated by the error bars). The solid-black line represents the error-weighted linear fit derived for those mean values within the range between  $0.5$  and  $2.0 r_e$  (yellow diamonds), and the dashed white line represents the linear relation corresponding to the characteristic values of the zero-points and slopes derived in Sect. 4.2 for the individual galaxies assuming a Gaussian distribution for both parameters. For both panels, the black contours show the density distribution of the star-forming spaxels, the outermost one including 95% of the total and decreasing 20% in each consecutive contour.*

## 4.4 COMMON ABUNDANCE GRADIENT

Both the fact that the distribution of the derived oxygen abundance gradients for all the galaxies in the sample is compatible with a Gaussian distribution and the lack of correlations found between the slope values and the analysed properties of galaxies as the morphological type or the luminosity suggests the existence of a characteristic value for the slope that is common to all type of spiral galaxies (interacting galaxies were not considered in the study and are not included in this statement).

It is easier to illustrate this result if we represent the radial distribution of the oxygen abundance for all the galaxies in the same figure. This is shown in the left panel of Fig. 4.4. The black contours represent the density distribution of the star-forming spaxels. Although the radial gradient can be discerned through the contour plot, the wide range of abundances blurs the

result. To clarify the origin of this widening, we colour-code each represented abundance according to the integrated stellar mass of the host galaxy in log scale. For clarity, only the oxygen abundance values with a contribution of at least 1% of the total number of spaxels are plotted. Adopting this scheme, it is evident that the abundances present a common radial gradient, but with an offset depending on the mass, as expected from the  $\mathcal{M} - \mathcal{Z}$  relation (and as discussed in Sect. 4.2). To remove this dependence on the mass from the map, we rescaled the oxygen abundances of each galaxy following the analytical form of the  $\mathcal{M} - \mathcal{Z}$  relation (Tremonti et al. 2004) derived by Sánchez et al. (2013), applying an offset according to the integrated stellar mass of the galaxy and normalising to the average value for the whole sample of  $\sim 8.5$ . The outcome is shown in the right panel of Fig. 4.4, where the common abundance gradient presented by all galaxies in the sample can be clearly seen. The abundance distribution is represented again as a density map, both with a colour-code image (normalised to one) and a contour map. The diamonds represent the mean oxygen abundance values, with the error bars indicating the corresponding standard deviations, for bins of  $0.25 r_e$ . An error-weighted linear regression (solid black line) to the mean values restricted to the spatial range between  $0.5$  and  $2.0 r_e$  (yellow diamonds) derives a slope of  $\alpha_{O/H} = -0.075 \pm 0.016 \text{ dex}/r_e$ , totally compatible with the characteristic slope of  $\alpha_{O/H} = -0.07 \pm 0.05 \text{ dex}/r_e$  derived in Sect. 4.2 for the individual galaxies assuming a Gaussian distribution (dashed-white line). The presence of this characteristic gradient is also confirmed when using other alternative calibrators (see Sect. 4.6).

This characteristic slope is independent of the integrated stellar mass of the galaxies. Figure 4.5 shows the averaged radial profiles of the oxygen abundance for our sample of galaxies split in four mass bins with a similar number of elements ( $\log (M/M_\odot) \leq 10.2$ , blue diamonds;  $10.2 < \log (M/M_\odot) \leq 10.5$ , red squares;  $10.5 < \log (M/M_\odot) \leq 10.75$ , yellow dots;  $\log (M/M_\odot) > 10.75$ , purple triangles). The derived gradients (computed between  $0.5$  and  $2.0 r_e$ ) of those four profiles are consistent within the errors with the characteristic slope displayed by the entire sample (see inset of Fig. 4.5). We note that this result is only valid for masses larger than approximately  $10^{9.5} M_\odot$ , which corresponds to the range covered in this study. Below this limit, other works have found that the gradients seem to flatten (Sánchez & Sánchez-Menguiano 2017; Belfiore et al. 2017).

Several works have detected the mentioned gradient in the MW (e.g. Shaver et al. 1983; Deharveng et al. 2000; Pilyugin et al. 2003; Esteban et al. 2005; Quireza et al. 2006; Rudolph et al. 2006; Balser et al. 2011; Esteban et al. 2017), deriving values for the slope between  $-0.04$  and  $-0.06 \text{ dex}/\text{kpc}$ . If we express the gradient in  $\text{dex}/r_e$  to easily compare with our results, and considering a value of the disc effective radius for our Galaxy of  $r_e = 3.6 \text{ kpc}$  (Bovy & Rix 2013), we obtain a slope between  $-0.14$  and

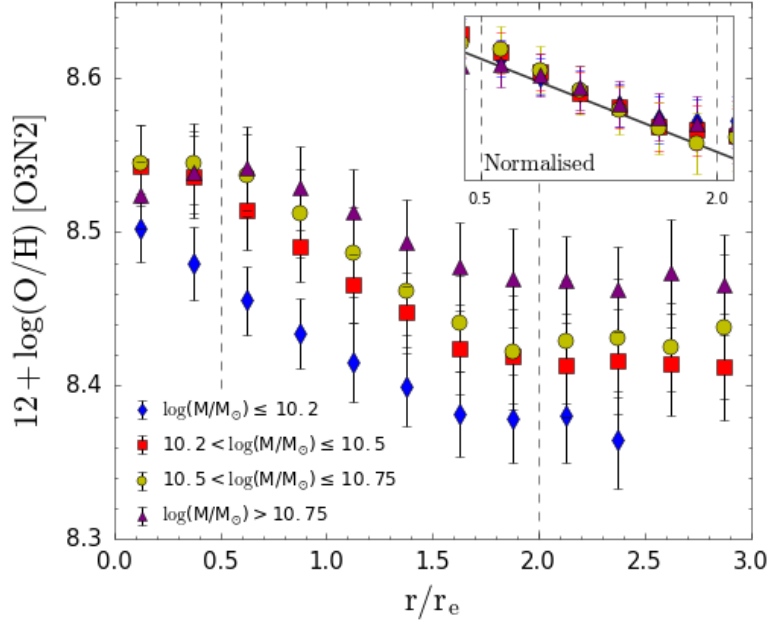


**Figure 4.5:** Average oxygen abundance radial profiles derived considering galaxies in four different bins according to their integrated stellar mass. The limits of the bins were chosen to ensure a similar number of elements in each bin:  $\log(M/M_{\odot}) \leq 10.2$ , blue diamonds;  $10.2 < \log(M/M_{\odot}) \leq 10.5$ , red squares;  $10.5 < \log(M/M_{\odot}) \leq 10.75$ , yellow dots;  $\log(M/M_{\odot}) > 10.75$ , purple triangles. The symbols represent the mean oxygen abundance values for bins of  $0.25 r_e$  (standard deviations are indicated by the error bars). Dashed vertical lines delimit the three different behaviours in the oxygen abundance profiles (i.e. drop in the inner parts, common gradient between  $0.5$  and  $2.0 r_e$ , and the flattening in the outer parts). The inset represents the linear regime and normalising the abundances at the middle of the radial range to the value corresponding to the characteristic slope displayed by the entire sample (solid line).

$-0.22 \text{ dex}/r_e$ , which is slightly larger than the mean value of our slope distribution ( $-0.08 \text{ dex}/r_e$ , see Table 4.1). However, deriving the abundance gradient for the MW is not straightforward and presents several obstacles: (i) the measurements are affected by dust and it is difficult to determine distances, which is necessary to derive radial abundance gradients; (ii) the use of different abundance diagnostics such as optical and IR collisionally excited lines (CELs), optical and radio recombination lines (RRL) or thermal continuum emission can yield differences in the results (Rudolph et al. 2006); (iii) azimuthal abundance variations have been reported in the MW (Pedicelli et al. 2009; Balser et al. 2011) that would complicate any analysis of the radial gradients; and finally (iv) the value of the disc scale-length, and therefore the disc effective radius, is still controversial, with large discrepancies among different results (typical values are in the range  $2 - 4 \text{ kpc}$ , e.g. Sackett 1997; Hammer et al. 2007; van der Kruit & Freeman 2011; Bovy &

Rix 2013). All these factors may contribute to an incorrect estimate of the oxygen abundance gradient in our Galaxy, which would explain the differences found in this value between the MW and external galaxies. Another aspect to take into account is the different radial range considered in the derivation of the gradient. While in our work the gradients were computed between 0.5 and  $2.0 r_e$  (see Sect. 4.1), it is obtained within a typical range between 5 and 15 kpc for the MW, which roughly corresponds to 1.4 and  $4.2 r_e$  (using again a value of 3.6 kpc for the  $r_e$ , Bovy & Rix 2013). This fact may also contribute to the differences in the gradient values.

The origin of this negative abundance gradient goes back to the inside-out scenario for the formation of disc galaxies (described in Chapter 1), where the inner parts form first, followed by the formation of the outer regions. Further evidence in the CALIFA survey comes from the analysis of the SP, either from the study of the SFH (Pérez et al. 2013) or from the study of the radial age gradient (González Delgado et al. 2014, 2015; Ruiz-Lara et al. 2016). This scenario is understood as a result of the increased timescales of the gas infall with radius and the consequent radial dependence of the SFR. This radial decrease in the chemical abundance has been well established since a long time (Searle 1971). However, the statement that this gradient presents a characteristic slope independent of many properties of the galaxies was only recently expressed (Sánchez et al. 2012b), which imposes stronger restrictions on our current understanding of disc galaxy growth. The existence of a common gradient in the abundances indicates that the chemical evolution of these disc-dominated galaxies is tightly correlated with the mass growth.

## 4.5 DEVIATIONS FROM NEGATIVE GRADIENT

This negative gradient is derived limiting the fitted interval between 0.5 and  $2.0 r_e$ . As previously stated (see Sect. 4.1), out of this range deviations with respect to this lineal behaviour appear.

### 4.5.1 FLATTENING IN THE OUTER REGIONS

All these gradients are derived up to two disc effective radii. Beyond this point, the linear behaviour ends and we find a flattening in the oxygen abundance distribution. The right panel of Fig. 4.4 shows the appearance of this abundance flattening, with around 8 230 spaxels at these outer regions. By inspecting the galaxies individually, we detect this flattening in 57 of them, corresponding to 82% of the galaxies with reliable oxygen abundance values at these large galactocentric distances. The onset of the flattening seems to be always located around  $2 r_e$  even if we separate the sample in different bins according to the integrated stellar mass (see Fig. 4.5), although

the lower mass bins lack of points at these outer regions. In the same figure we show that the abundance value of the flattening depends on the mass of the galaxies because of the mentioned  $\mathcal{M} - \mathcal{Z}$  relation.

In the MW some authors have claimed, based on the analysis of both H II regions and planetary nebulae, that the observed radial abundance gradient may flatten at the outer parts of the Galaxy (Fich & Silkey 1991; Vilchez & Esteban 1996; Maciel et al. 2006). However, there are recent studies that do not find evidences of such flattening (Caplan et al. 2000; Henry et al. 2010; Esteban et al. 2017).

In external galaxies, several studies analysing the gas content on galaxies have recently found that beyond the isophotal radii  $r_{25}$ , the metallicity radial distribution flattens to a constant value independent of the galactocentric distance, in contrast to the negative abundance gradient present at smaller distances (e.g. Martin & Roy 1995; Vilchez & Esteban 1996; Roy & Walsh 1997; van Zee et al. 1998; Bresolin et al. 2009b; Werk et al. 2010; Rosales-Ortega et al. 2011; Werk et al. 2011; Bresolin et al. 2012; Marino et al. 2012; Sánchez et al. 2012b; López-Sánchez et al. 2015; Marino et al. 2015). This change in the abundance distribution has not only been detected in the gas, but also in the stellar metallicity (e.g. Yong et al. 2006; Carraro et al. 2007; Vlajić et al. 2009, 2011). However, all these works were based on individual galaxies or a very limited sample of objects. Sánchez et al. (2014) represents the first unambiguous detection of such a flattening in a statistically significant large sample of galaxies. This is the first work confirming the flattening by using spaxel-by-spaxel information, increasing the number statistics (which gains importance especially in these outer regions) and improving the spatial coverage across the discs.

Average oxygen abundance radial distributions similar to the one shown in Fig. 4.4 have been created for the same subsamples analysed in Sect. 4.3 (i.e. according to the morphological type, presence or absence of bars and luminosity). No significant differences are found between them, which means that the flattening at the outer regions seems to be a universal property of spiral galaxies. It is also important to note that although Fig. 4.4 was created using the M13 indicator based on the O3N2 index, the flattening is independent of the adopted calibrator; it is present when performing the analysis with all the explored calibrators (see Sect. 4.6).

The nature of this possible flattening is still under debate. Because of the extreme conditions of the outermost parts of galaxies (very low gas densities and long dynamical timescales), these regions play a key role in studying the mechanisms involved in their evolution and, therefore, the existence of this flattening can be of great importance in constraining chemical evolution models.

The flattening, although observed in the more metal poor regions of the galaxies, displays a relatively high abundance value, which ranges between

8.4 and 8.6 (left panel of Fig. 4.4). An estimate of the time necessary to enrich the ISM of the outer parts of discs to these abundance levels, assuming a constant SFR equal to the present observed value, is higher than 10 Gyr (see Bresolin et al. 2012, for details of the calculation). According to cosmological hydrodynamical simulations, in the inside-out growth scenario the outer regions of galaxy discs are formed during the last 4 – 6 Gyr (Scannapieco et al. 2008, 2009). Therefore, if star formation has proceeded at the same rate as observed today, the enrichment of the ISM caused by stellar evolution in these outer parts cannot produce these observed high gas abundance values during the lifetime of these regions.

Different mechanisms have been proposed to explain this enrichment in the outer parts of discs in non-interacting galaxies. One of them is a metal-mixing scenario induced by large-scale processes of angular momentum transport, such as radial gas flows (Lacey & Fall 1985; Goetz & Koepfen 1992; Portinari & Chiosi 2000; Ferguson & Clarke 2001; Schönrich & Binney 2009; Bilitewski & Schönrich 2012; Spitoni et al. 2013, among others), resonance with transient spiral structure (Sellwood & Binney 2002; Minchev et al. 2012; Roškar et al. 2012; Daniel & Wyse 2015), or the overlap of spiral and bar resonances (Minchev & Famaey 2010; Minchev et al. 2011). In the chemical evolution model developed for the MW by Cavichia et al. (2014), the presence of the bar induces radial gas flows in the disc whose net effect is to produce this flattening of the oxygen gradient at the outer disc. However, as pointed out by the authors, the differences are small compared with the model without the bar and probably cannot be distinguished by the observations. Minor mergers and perturbations caused by orbiting satellite galaxies are also suggested to increase the metal content in the external regions (Quillen et al. 2009; Qu et al. 2011; Bird et al. 2012; López-Sánchez et al. 2015). A slow radial dependence of the star formation efficiency (SFE) at large galactocentric distances is another possible explanation to the flattening (Bresolin et al. 2012; Esteban et al. 2013). An alternative interpretation arises from recent cosmological simulations that propose a balance between outflows and inflows (through ‘wind recycling’ accretion) with the intergalactic medium (IGM) as a mechanism governing the gaseous and metal content of galaxies (Oppenheimer & Davé 2008; Oppenheimer et al. 2010; Davé et al. 2011, 2012). Finally, it may well be that a fraction of the metals are recycled in the halo of the galaxy and do not escape, being mixed with the incoming gas, as mentioned by Veilleux et al. (2005), and producing the observed flattening.

All these mechanisms are not mutually exclusive, and a possible balance between them could be responsible for the actual chemical evolution of extended discs and the flat abundance of the outermost parts. Moreover, the dominant mechanism could be different for structurally different galaxies.

### 4.5.2 OXYGEN ABUNDANCE INNER DROP

In addition to this flattening in the outer parts, we find that 27 (22%) galaxies of the sample display some anomalies in their oxygen abundance profiles in the inner parts, namely a nearly flat distribution (8 galaxies, 6.5%) or even a drop towards the centre (15 galaxies, 15.5%). The presence of this feature is not visible when representing the radial distribution of the oxygen abundance for all the galaxies in our sample (Fig. 4.4), but it does appear when separating the sample into different stellar mass bins (Fig. 4.5), only in the case of the more massive galaxies. While the lowest stellar mass galaxies do not display any sign of this feature, this drop is progressively more evident with increasing galaxy mass. The presence of the inner drop and the trend with the galaxy mass are also independent of the adopted calibrator (see Sect. 4.6).

This feature has also been found in several observational studies (Belley & Roy 1992; Rosales-Ortega et al. 2011; Sánchez et al. 2012b, 2014) and simulations (Mollá & Díaz 2005; Cavichia et al. 2014).

For our Galaxy, the studies on gas abundance have not been able to properly trace the oxygen abundance at these innermost parts of the disc and therefore were not able to find evidence of this behaviour. However, a chemical evolution model developed by Cavichia et al. (2014) has detected this ‘drop’ (or flattening) in the gas abundances of the inner regions as caused by the presence of a bar. According to this model, the presence of the bar induces radial flows that increase the  $\alpha$  at the corotation radius, which also produces an increase in the oxygen abundance. This results in an apparent decrease or flattening of the abundance in the central regions. A recent study focused on stellar populations (Hayden et al. 2014) has detected a flattening in the metallicity of the inner regions of the Galaxy, more significant in the low- $[\alpha/M]$  ( $\alpha$  element abundances) stars. They also explained this feature by the existence of a central bar that produces a mixing of stars in these inner regions.

The analysis presented here can help us to confirm this scenario where the inner drop is caused by the influence of a bar. If the bar were the dominant effect that produces this decrease at inner regions, then it would be expected to detect it more frequently in barred galaxies. However, our analysis yields that only 30% of galaxies in the sample showing the drop are barred (52% if we also consider the galaxies that are supposed to have a bar but where it is not clearly visible).

Another explanation proposed by observational studies on gas abundance for external galaxies, like NGC 628 (Sánchez et al. 2011) and later using CALIFA data in a large sample of galaxies (Sánchez et al. 2014), is that this inner decrease was associated with the presence of a circumnuclear star-forming ring of ionised gas related to the inner Limbland resonance.

To explore the possibility that the abundance drop is due to the presence of a star-forming ring, a visual inspection of the H $\alpha$  intensity maps for the galaxies with signs of this drop has been carried out. This analysis shows that 48% of the galaxies present evidence of a star-forming ring that is spatially located at these inner galactocentric distances ( $r/r_e \sim 0.3 - 0.5$ ). However, this scenario must be confirmed by a more robust and detailed analysis of the stellar and gas kinematics.

Despite these two possible explanations (influence of a bar or a circumnuclear star-forming ring), the physical origin of this drop is not still well established. On the other hand, if the origin of this drop were due to radial motions of the gas, it would also have an impact on the overall distribution of abundances at larger radii. To explore this possible effect, we derive the mean value for the slope of the abundance gradients only for the galaxies presenting this feature, obtaining a mean  $\alpha_{O/H} = -0.10 \text{ dex}/r_e$  and  $\sigma = 0.04 \text{ dex}/r_e$ . This value is slightly higher than the one derived for the galaxies without evidence of this inner drop in the abundances, which is  $\alpha_{O/H} = -0.06 \text{ dex}/r_e$  and  $\sigma = 0.05 \text{ dex}/r_e$ . A two-sample KS test suggests that the two distributions are different (P-value of 3%), consistent with a radial movement of the gas as the cause of this feature.

Finally, 37% of the galaxies displaying this inner abundance drop neither shows evidence of a star-forming ring nor of a bar. This suggests that another mechanism related to radial movements is responsible for causing this feature.

To shed some further light on this question, we investigated the presence of this feature depending on the integrated stellar mass of the galaxies. We conclude that the galaxies displaying the strongest oxygen abundance inner drop are the most massive ones (Fig. 4.5), suggesting that stellar mass plays a key role in shaping the inner abundance profiles.

## 4.6 DEPENDENCE OF THE RESULTS ON THE USED CALIBRATORS

In this section we confirm the conclusions arisen from this analysis based on the Marino et al. (2012) calibration for the O3N2 index by replicating the figures that support our main results using three of the most commonly used empirical calibrators: (i) the one described in Pettini & Pagel (2004, PP04) for the O3N2 indicator, (ii) the Pilyugin et al. (2010, P10) calibration for the ONS index, and (iii) the Dopita et al. (2013, D13) calibrator based on the `pyqz` code (see Sect. 3.3 for a brief description of these additional calibrators).

Figure 4.6 shows the distribution of the slope values of the oxygen abundance gradients for the galaxies using the spaxel-wise information (red



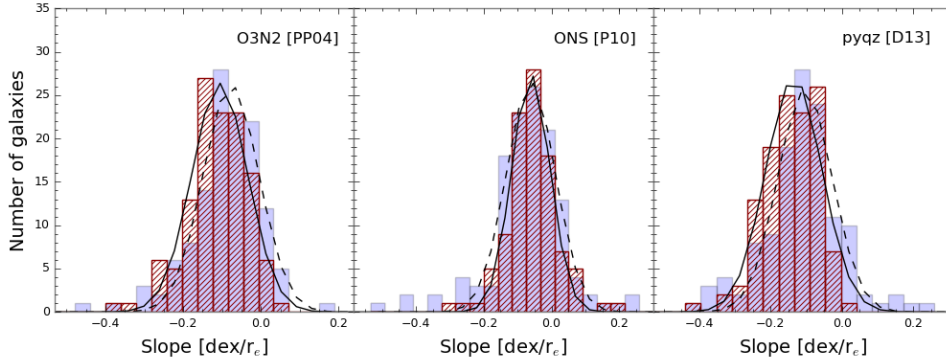


**Figure 4.6:** Distribution of slope values of the oxygen abundance gradients derived for the galaxy sample based on the O3N2 (PP04, left panel), ONS (P10, middle panel), and pyqz (D13, right panel) calibrators using spaxel-wise information (dashed red bars) and the individual H II regions (filled blue bars). We also represent the Gaussian distribution of the data (solid line for spaxels, dashed line for individual H II regions), assuming the mean and standard-deviation of the distribution of slopes and sampled with the same bins.

dashed histogram) and the individual H II regions (blue filled histogram). We can see that in the three cases both distributions are very similar, confirming the equivalence of the two methodologies in the derivation of the oxygen abundance gradients independently of the chosen calibration.

We have also studied the influence of some galaxy properties, namely the morphological type, the presence of bars and the luminosity of the galaxies, on the oxygen abundance slope when we use these three alternative calibrators. The outcome of this analysis is shown in Fig. 4.7. Similarly to O3N2-M13 (see Sect 4.3), we find no significant dependence on any of the analysed properties. The largest differences appear in the morphological type, where the trend of steepening the slope from early to late types is inverted for the ONS-P10 calibrator. However, the p-values derived from the KS (55% for the early-intermediate comparison, 14% for the early-late one, and 8% for the intermediate-late comparison) and AD (37%, 20%, and 3%, respectively) tests are above the significant level of 5%. Therefore, the observed trend does not seem statistically significant. In the remaining cases, all the derived p-values are also above 5%, indicating the absence of correlation with any of the remaining properties for any of the analysed calibrators.

Finally, the existence of a common abundance gradient is also confirmed with the proposed alternative calibrators. This result is illustrated in the left panels of Fig. 4.8 (see Sect. 4.4 for details). As in the case of O3N2-M13, these characteristic slopes are compatible with the ones derived in Sect. 4.2 assuming a Gaussian distribution for the distribution of values of the individual galaxies:  $\alpha_{O/H} = -0.115 \pm 0.011 \text{ dex}/r_e$  for the

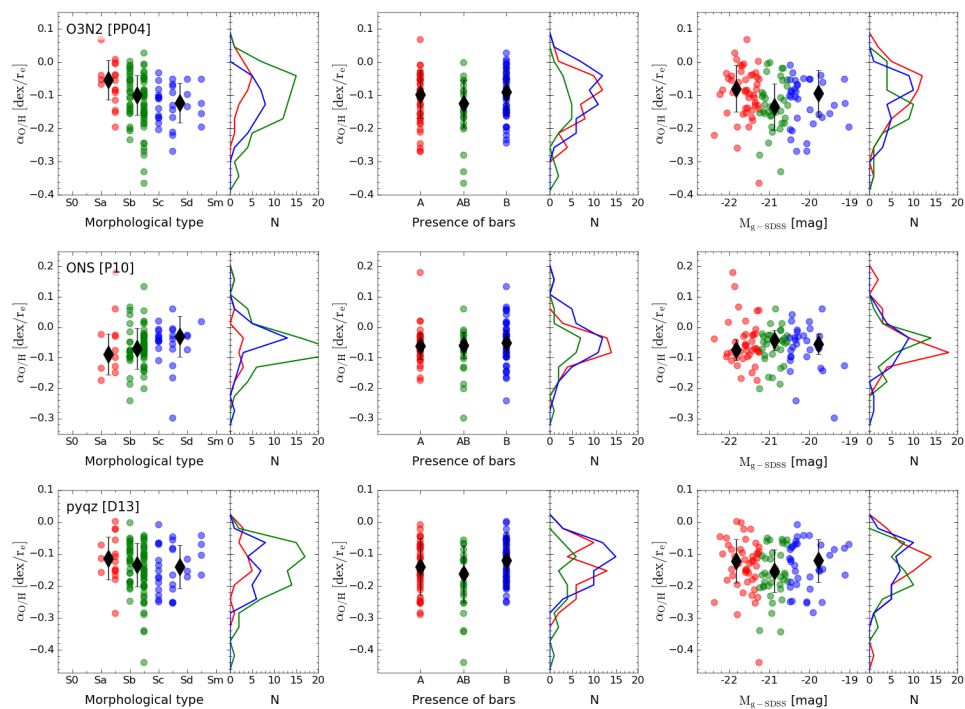


**Figure 4.7:** Distribution of the abundance slopes as a function of different galaxy properties using the *O3N2* (PP04, top row), the *ONS* (P10, middle row), and the *pyqz* (D13, bottom row) calibrations. The analysed properties are: the morphological type of the galaxies (left panels), the presence or absence of bars (middle panels) and the *g*-band absolute magnitude of the galaxies (right panels). See Fig. 4.3 for more details.

*O3N2* (PP04) calibrator (against  $\alpha_{O/H} = -0.11 \pm 0.07 \text{ dex}/r_e$  derived in Sect. 4.2),  $\alpha_{O/H} = -0.094 \pm 0.014 \text{ dex}/r_e$  for the *ONS* (P10) calibrator (against  $\alpha_{O/H} = -0.06 \pm 0.06 \text{ dex}/r_e$ ), and  $\alpha_{O/H} = -0.128 \pm 0.013 \text{ dex}/r_e$  for the *pyqz* (D13) one (against  $\alpha_{O/H} = -0.14 \pm 0.09 \text{ dex}/r_e$ ). The right panels of Fig. 4.8 represent the average profiles for the different mass bins introduced in Sect. 4.2. The insets of these panels show that the slope of the gradients for these calibrators is also independent of the galaxy mass (similarly to the *O3N2*-M13 case). Finally, the presence of the outer flattening (always located around  $2 r_e$ ) and the inner drop (at  $\sim 0.5 r_e$ ) is also observed with the three calibrators. Again, we can see in the right panels that this inner drop is progressively more evident with increasing the galaxy mass.

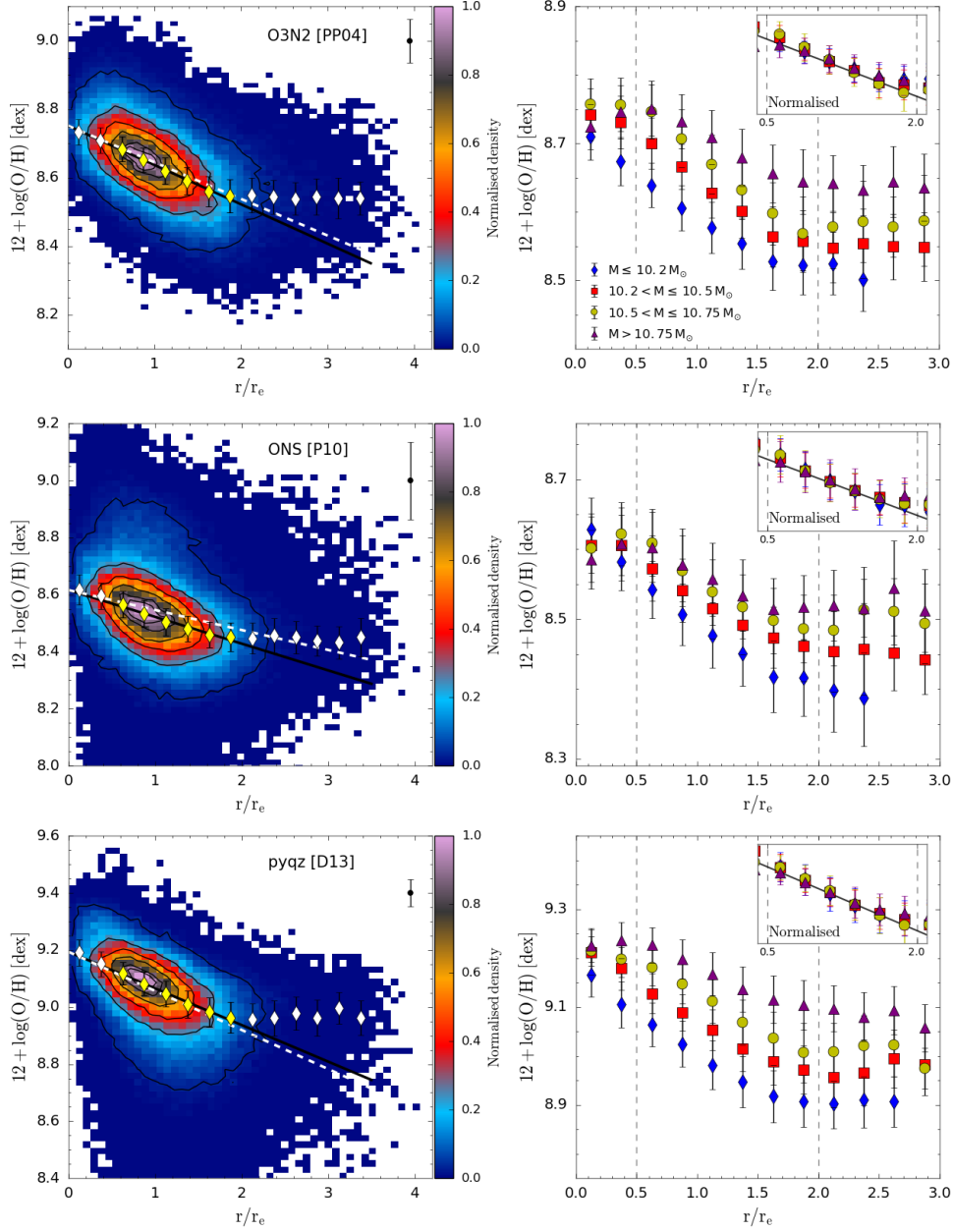


**Figure 4.8:** Radial distribution of the oxygen abundance for the entire CALIFA sample using the O3N2 (PP04, top row), the ONS (P10, middle row), and the pyqz (D13, bottom row) calibrations. The average profiles for different stellar-mass bins are also shown. See Figs. 4.4 and 4.5 for more details.

## 4.7 BRIEF SUMMARY

The existence of a radial decrease in the chemical abundances of nearby spiral galaxies has been well established by observations for decades (Searle 1971; Comte 1975; Smith 1975; Peimbert 1979; Shaver et al. 1983). Since then, this gradient has been confirmed by other works, restricted to individual galaxies or to limited samples of galaxies (Martin & Roy 1992; Kennicutt et al. 2003; Rosales-Ortega et al. 2011; Bresolin et al. 2012; Marino et al. 2012; Patterson et al. 2012). With the advent of IFS surveys like CALIFA, abundance studies using larger samples of H II regions have become feasible (Sánchez et al. 2012b, 2014), with the same results as in previous studies.

In this work we go a step further and analyse for the first time the oxygen abundance distribution for a large sample of galaxies spaxel by spaxel, taking advantage of the full 2D information provided by the CALIFA survey, which improves the statistics. This final sample provides more than 185 000 oxygen abundance values and more than 7 100 H II regions with which to compare our results. The analysis using the H II regions was previously performed by Sánchez et al. (2014) with a different sample of galaxies that were also extracted from the CALIFA mother sample. With spaxel-by-spaxel analysis, we here take approximately four times more line emitting spaxels into account that are associated with star formation regions than in the classical procedure of detecting H II regions. Our results are therefore mainly based on an independent set of measurements, reinforcing and expanding on the Sánchez et al. (2014) results.

We have analysed the oxygen abundance distribution for a sample of 122 face-on spiral galaxies spaxel by spaxel. The obtained results have been compared to those obtained following the classical procedure of detecting H II regions, leading to equivalent results that point to the same conclusions: (i) the existence of a common abundance gradient, independent of other properties of galaxies, in particular the presence of bars, which seems not to have the flattening effect predicted by numerical simulations; (ii) the existence of a flattening of the abundance gradient in the outer regions of discs, which seems to be a common property of disc galaxies; and (iii) the existence of a drop of the abundance in the inner regions of disc galaxies, only visible in the most massive ones and most probably associated to radial movements of the gas (sometimes a bar or a circumnuclear star-forming ring).

These results support the scenario in which disc galaxies present an overall inside-out growth. However, possible deviations are shown with respect to this simple scenario that affect the abundance profiles in both the innermost and outermost regions of galaxies.

*If we knew what it was we were doing, it  
would not be called research, would it?*

— Albert Einstein



5

# Oxygen abundance radial profiles with AMUSING

## Contents

5.1	The shape of the abundance profiles . . . . .	89
5.2	Main abundance gradient distribution . . . . .	94
5.2.1	Influence of the density of the environment . . . . .	95
5.2.2	Effects of bars . . . . .	97
5.2.3	Dependence on the shape of the abundance profile . . . . .	98
5.3	Location of the inner drop and outer flattening . . . . .	99
5.4	A common oxygen abundance gradient . . . . .	101
5.5	The characteristic slope as a normalisation scale . . . . .	102
5.6	Dispersion of the gradient and mixing scalelength . . . . .	107
5.7	Dependence on the used calibrator . . . . .	110
5.8	Brief summary . . . . .	115



THE ANALYSIS ON THE RADIAL abundance distribution performed in the previous chapter has meant an improvement in our knowledge in this regard with respect to earlier works. The good coverage of the galaxy discs thanks to the spaxel-by-spaxel approach achievable with CALIFA data, together with the large size of the analysed sample, allow us to go deeper in aspects not well-explored before such as the existence of the abundance inner drop.

However, the spatial resolution of the CALIFA data leaves still room to improve the characterisation of the gas abundance radial distribution. Performing this analysis with AMUSING data can help us in this regard due to the combination of its large FoV with high spatial resolution. Both characteristics together allow us to increase the number of H II regions detected in each galaxy and therefore better trace its abundance distribution, avoiding the dilution effects present in the spaxel-by-spaxel analysis with CALIFA.

In this chapter, we take advantage of the high spatial resolution of the AMUSING data to characterise the oxygen abundance radial profile in a large sample of spiral galaxies as never done before. For this purpose we develop a new methodology to automatically fit these profiles taking into account the different shapes observed. This procedure allows us to detect the presence of any possible deviation in the radial distribution with respect to the universal negative gradient (i.e. the inner drop and the outer flattening). Thanks to the sample size we are able to state meaningful statistical conclusions. Moreover, the study of possible trends with different properties of the galaxies allows us to shed light into the origin of these deviations, and the role of such properties in the chemical evolution of the galaxies.

Along the chapter, we explain the procedure developed to fit the observed radial abundance profiles and analyse their shape (Sect. 5.1). We also study the dependence of the slope of the main gradient on different properties of the galaxies (Sect. 5.2). The analysis of the location of the inner abundance drop and the outer flattening when existing is performed in Sect. 5.3. We also explore the existence of a common oxygen abundance gradient (Sect. 5.4). In Sect. 5.5 we define a new normalisation scale for the radial profiles based on this characteristic abundance gradient. We also study the dependence of the dispersion relative to the main abundance gradient with different galaxy properties (Sect. 5.6). Finally, the effect of using different calibrators in the derivation of the abundance profiles is addressed in more detail in Sect. 5.7.

## 5.1 THE SHAPE OF THE ABUNDANCE PROFILES

In order to obtain the radial distribution of the abundances for the 102 galaxies comprising the AMUSING sample, we have followed the methodology extensively explained in Chapter 3. We have (i) detected the candi-

dates to be H II regions using HIIEXPLORER, (ii) subtracting then the stellar contribution and measuring the emission line fluxes with PIPE3D for each region, (iii) we have discarded the regions not associated with star formation, and finally for the remaining ones (iv) we have derived the oxygen abundances using the Marino et al. (2013) calibration for the O3N2 index. Besides, we have also employed the calibration described in Dopita et al. (2016, D16), and the one proposed in Marino et al. (2013) for the N2 index (M13-N2) to test the robustness of the results derived from this study (see Sect. 3.3 for details). After all these steps, we deproject the galactocentric distances of the H II regions using the position angle and ellipticity of the galaxy discs (see Sect. 3.4 for details in the derivation of these parameters). The deprojected radial abundance distribution is afterwards normalised to the disc effective radius ( $r_e$ ), as suggested in Sánchez et al. (2012b) and Sánchez et al. (2013). This parameter was determined from the disc scale-length ( $r_d$ ) through the relation  $r_e = 1.67835 r_d$  (Sánchez et al. 2014). To obtain the disc scalelength we derived the surface brightness profile of the galaxies by fitting ellipses to the  $g$ -band light distribution recovered from the data. To do that we used the `ellipse IRAF` task and fixed the ellipticity and PA values of the successive ellipses matching those of the outer disc (already derived to deproject the galaxies). We then fitted these profiles with the classical exponential decline (Freeman 1970), obtaining the value of the corresponding disc scalelength. The values of  $r_e$  are given in Table B.1 (Appendix B).

Once the deprojected oxygen abundance radial distribution of the H II regions, normalised to  $r_e$ , was derived for the 102 galaxies in our sample, we applied a purely automatic procedure (without human supervision) to fit this distribution, detecting the existence of an inner drop and/or an outer flattening when present. This procedure was designed as follows. The abundance radial distribution of each galaxy is fitted four times, to cover the four possible shapes that have been described in the literature: i) single linear profile, ii) broken linear profile due to the presence of an outer flattening, iii) broken linear profile caused by an inner drop, and iv) doubly-broken linear profile with both an inner drop and an outer flattening. The four mentioned profiles are characterised by these three mathematical functions:

- (a) The single profile used to fit the abundance distribution is a linear regression:

$$O/H(r) = a \cdot r + b, \quad (5.1)$$

where  $a$  is the slope and  $b$  is the zero-point of the linear fit.

- (b) For the broken profile, the function is constructed by a sum of two linear regressions to be able to fit the principal negative gradient and the possible inner drop or outer flattening, with the radial position of



the new feature ( $h_i$ , with  $i = 1$  for the inner drop and  $i = 2$  for the outer flattening) as a free parameter in the fit:

$$O/H(r) = (a_1 \cdot r + b_1) \cdot (1 - W_i) + (a_2 \cdot r + b_2) \cdot W_i, \quad (5.2)$$

where

$$W_i = \frac{\pi/2 + \arctan\left(\frac{r - h_i}{\beta}\right)}{\pi}, \quad (5.3)$$

and imposing this condition

$$a_1 \cdot h_1 + b_1 = a_2 \cdot h_1 + b_2 \quad (5.4)$$

to guarantee the continuity of the function, so the oxygen value derived with each linear component is the same at the radial distance at which the consecutive components intersect ( $h_i$ ). For each galaxy this fit is performed twice, to cover the two cases where the broken profile is applicable: negative gradient with an inner drop and gradient with an outer flattening. To distinguish both fits, we imposed lower and upper boundaries on  $h_i$  restricting the position of the start of the inner drop to the first half of the covered radial range and the onset of the outer flattening to the second half. In addition, the imposed boundaries avoid that these fits are dominated by just one H II region.

- (c) For the doubly-broken profile, we introduced another linear component in the sum to fit the cases where both an inner drop and an outer flattening may be present in the galaxy, being the principal negative gradient the component in the middle of both features:

$$O/H(r) = (a_1 \cdot r + b_1) \cdot (1 - W_1) + (a_2 \cdot r + b_2) \cdot W_1 \cdot (1 - W_2) + (a_3 \cdot r + b_3) \cdot W_2, \quad (5.5)$$

with the following restrictions for continuity:

$$a_1 \cdot h_1 + b_1 = a_2 \cdot h_1 + b_2 \quad (5.6)$$

$$a_2 \cdot h_2 + b_2 = a_3 \cdot h_2 + b_3. \quad (5.7)$$

The  $W_i$  terms are used in the equations to introduce the change of domain among the linear components, acting like a switch: for  $r < h_i$ ,  $W_i \simeq 0$  and for  $r > h_i$ ,  $W_i \simeq 1$ . For instance, in equation 5.2, for  $r < h_i$  we only have contribution of the first term to the fitting function and for  $r > h_i$  the whole contribution comes from the second term. For equation 5.5 it is a bit more complicated but the mechanism is the same: the first term of the equation only comes into play for  $r < h_1$  and the third one for  $r > h_2$ . The intermediate term plays a part then between both radial positions ( $h_1 < r < h_2$ )

due to the intersected region where the factors are both contributing (as  $W_1 = 1$  for  $r > h_1$  and  $1 - W_2 = 1$  for  $r < h_2$ ). This way of constructing the fitting function allows us to find automatically not only the slope and zero-point of all the individual linear components but also the radial position at which the inner drop and outer flattening start using a single and continuous functional form. The  $\beta$  parameter was set to a small number to make a very steep transition between consecutive linear components. In this case, we considered  $\beta = 1 \cdot 10^{-8}$ , although its actual value does not affect the results as long as it is much smaller than  $1''$ .

Based on the residuals of the four fittings, we selected automatically which was the most suitable one in each case, in the way explained below. We should keep in mind that as soon as we add new components to the fit, the residuals (or scatter) are going to decrease. Therefore, we checked if this reduction in the residuals was statistically significant, making use of a MC simulation. To do that, we generated for each galaxy a ‘random’ radial distribution of the oxygen abundances within the error bars of the measured abundance values, repeating this process for  $N = 100$  iterations. We fitted each of these distributions with the four functional forms described before, deriving in all cases the distribution of the residuals of the abundances around the best fitted function. Then, we fitted each of these ‘residual’ distributions with a Gaussian function and we determined if the difference between the mean value derived for the single linear fit (using equation 5.1) and the mean value for the new fit was higher than the standard deviation value. If this is the case, we can consider that the reduction of the scatter is significant in a statistical way. Finally, to consider this ‘improved’ fitting valid, we imposed another condition: there has to be a significant change in the slope between the consecutive linear components of the corresponding function (equation 5.2 and 5.5). In order to check this, we fitted again a Gaussian function to the distribution of slopes of the different components, verifying that, similarly to the scatter distribution, the mean values for the inner drop and/or outer flattening were outside the interval ranged between the mean value derived for the principal negative gradient plus or minus the standard deviation.

Figure 5.1 represents examples of the four different cases that can be found when performing the radial fit (black solid line) of the oxygen abundance distribution of the H II regions (transparent black symbols): single abundance negative gradient (first panel), presence of an inner abundance drop (second panel), presence of an outer abundance flattening (third panel), and presence of both an inner drop and outer flattening (fourth panel). In Appendix D we show the deprojected oxygen abundance radial distribution of the H II regions for the whole sample of galaxies. The slope and zero-point values of the principal negative gradient derived from this fitting, together with the radial distance of the inner drop and/or outer flattening, when

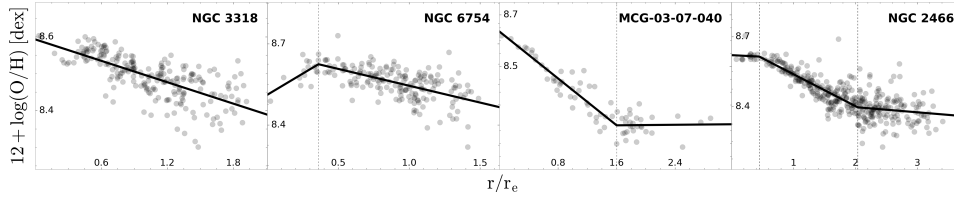


**Figure 5.1:** Examples of the different shapes found in the oxygen abundance radial distribution of the H II regions (black markers with transparency). The radial distances are deprojected and normalised to the disc effective radius. The solid black line represents the fit to the distribution. The dashed vertical lines correspond to the radial position of the inner drop and/or outer flattening.

present, are shown in Table B.2 (Appendix B) for all galaxies in the sample.

Applying this procedure with the chosen criteria we can guarantee that the detection of the inner/outer features is reliable. The methodology relies on a sufficient sampling of the H II regions along the covered galactocentric distances for a proper statistical determination of the presence of these features. Otherwise, our procedure seems to stick to the more simple scenario (single slope) and finds better results if those features are neglected.

In the analysed sample, we find that 55 galaxies exhibit a single abundance gradient. A broken profile due to an inner drop is observed in 21 objects. There are 10 galaxies presenting a broken profile with an outer flattening. Finally, 16 spiral galaxies display a doubly-broken profile in the abundance radial distribution. As we can see, the cases with a clear presence of deviations from the simple negative gradient are as common as the finding of a single behaviour in the radial profiles. This fact suggests that the common view in which the oxygen abundance distribution in spiral galaxies decreases following a single radial gradient might be incomplete and deviations from this single behaviour are needed to be considered for a proper characterisation of the distribution.

In the case of the abundance profiles derived using the M13-N2 calibrator, we find that: 68 galaxies display a single abundance gradient, 21 of them present a broken profile due to an inner drop, 11 spiral galaxies exhibit a broken profile with an outer flattening, and finally only 2 objects display a doubly-broken profile. For the D16 calibrator, the number of galaxies exhibiting a single abundance gradient increases to 72. The broken profile due to the inner drop is observed in 11, while the broken profile with an outer flattening is observed in 10 objects. Finally, 9 spiral galaxies display a doubly-broken profile. Despite the number of galaxies where an inner drop and/or outer flattening decreases when using the other two calibrators, it can be seen that the presence of deviations from the single behaviour is still remarkable.

Some of these analysed galaxies (7) present peculiarities that can affect

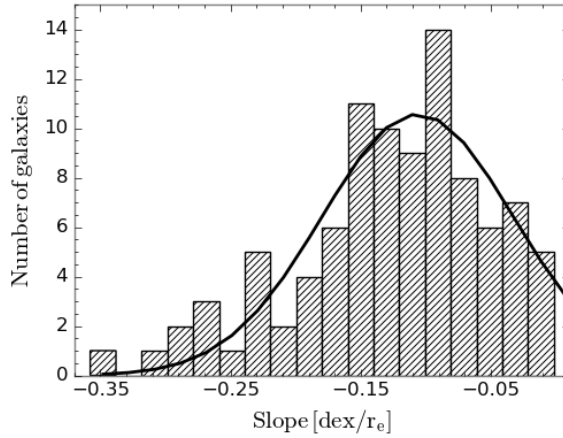


**Figure 5.2:** *Distribution of slope values of the oxygen main abundance gradients (normalised to the disc effective radius) derived for the galaxy sample. Solid black line represents the Gaussian distribution of the data assuming the mean and standard-deviation of the distribution of slope values and sampled with the same bins.*

the abundance distribution and, although they remain as part of the sample, they were discarded from further analysis: (i) Two galaxies, NGC 232 and NGC 7469, were discarded for having a very powerful AGN in the centre that can contaminate the emission coming from the H II regions (presenting also jets); (ii) another galaxy, NGC 1516A, was removed for being in a very advanced stage of merging; (iii) two more galaxies, UGC 3634 and UGC 6332, were discarded for having a ring-like structure, which affects the accuracy of the derivation of the gradient; (iv) and finally the last two discarded galaxies, NGC 3447 and NGC 7580, are very distorted due to a recent interaction. Therefore, from now on we show results based on a sample of 95 galaxies.

## 5.2 MAIN ABUNDANCE GRADIENT DISTRIBUTION

Figure 5.2 shows the distribution of slopes of the main oxygen abundance gradients (see Sect. 5.1) derived for the galaxy sample of 95 galaxies. This distribution expands along a wide range of values between approximately  $-0.35$  and  $0.03$  dex/ $r_e$ , presenting a clear peak located at  $-0.11$  dex/ $r_e$ . The shape of the distribution suggests the existence of a characteristic gradient more or less similar for all spiral galaxies in the sample. Although using different abundance calibrators and/or different scale lengths to normalise the gradients, several previous works have found this similarity in the slope distribution with a Gaussian function, supporting the existence of the mentioned characteristic gradient (Sánchez et al. 2012b, 2014; Ho et al. 2015). In the analysis performed in Chapter 4 we showed that the slopes of

the oxygen abundance gradients in CALIFA spiral galaxies display a distribution peaking at  $-0.07 \text{ dex}/r_e$  ( $\sigma = 0.05$ ), in agreement (within the errors) with the value reported in this chapter. The distribution of slopes for the M13-N2 and D16 calibrators can be found in Fig. 5.11 of Sect. 5.7. In both cases the distributions present a similar peak, but located at  $-0.23 \text{ dex}/r_e$  for D16 and at  $-0.06 \text{ dex}/r_e$  for M13-N2, reinforcing the idea of a characteristic gradient (although the actual value of the slope changes depending on the used calibrator).

As found with the CALIFA sample, despite the presence of a clear peak in the distribution of the slopes, the large standard deviation found ( $\sigma = 0.07 \text{ dex}/r_e$ ) indicates a possible dependence of such gradients with some particular properties of the galaxies. In this section we will analyse the influence of some characteristics such as the density of the environment, the presence of bars or the type of abundance profile displayed (according to Sect. 5.1) on the main abundance gradient.

### 5.2.1 INFLUENCE OF THE DENSITY OF THE ENVIRONMENT

Numerical simulations have predicted the presence of shallower gradients in interacting galaxies (or galaxies that have undergone an interaction in the past) due to gas flows induced by the interaction (e.g. Barnes & Hernquist 1996; Mihos & Hernquist 1996; Dalcanton 2007; Rupke et al. 2010a; Torrey et al. 2012). This prediction has been confirmed by observational works (e.g. Kewley et al. 2010; Rupke et al. 2010b; Miralles-Caballero et al. 2014; Rosa et al. 2014; Sánchez et al. 2014).

We classified our galaxies based on the density of their environment to study the possible effect on the abundance gradients. Galaxies were grouped in: isolated (S), part of a group of at least three galaxies (G), in pair (P), and with evidence of real interactions (I). This classification was performed attending to the information found in literature. In Table B.1 (Appendix B) we show for each galaxy in the sample the corresponding classification and the references used to classify it.

The top panel of Fig. 5.3 displays the distribution of slope values according to the environment. The black diamonds represent the mean values within each segregation, with the error bars indicating the standard deviation. The mean and standard deviation values of the distribution are the following ones:

$$S : \alpha_{O/H} = -0.12 \text{ dex}/r_e \text{ and } \sigma = 0.07 \text{ dex}/r_e \quad (n_{\text{gal}} = 59)$$

$$G : \alpha_{O/H} = -0.13 \text{ dex}/r_e \text{ and } \sigma = 0.08 \text{ dex}/r_e \quad (n_{\text{gal}} = 26)$$

$$P : \alpha_{O/H} = -0.14 \text{ dex}/r_e \text{ and } \sigma = 0.07 \text{ dex}/r_e \quad (n_{\text{gal}} = 7)$$

$$I : \alpha_{O/H} = -0.15 \text{ dex}/r_e \text{ and } \sigma = 0.01 \text{ dex}/r_e \quad (n_{\text{gal}} = 3).$$

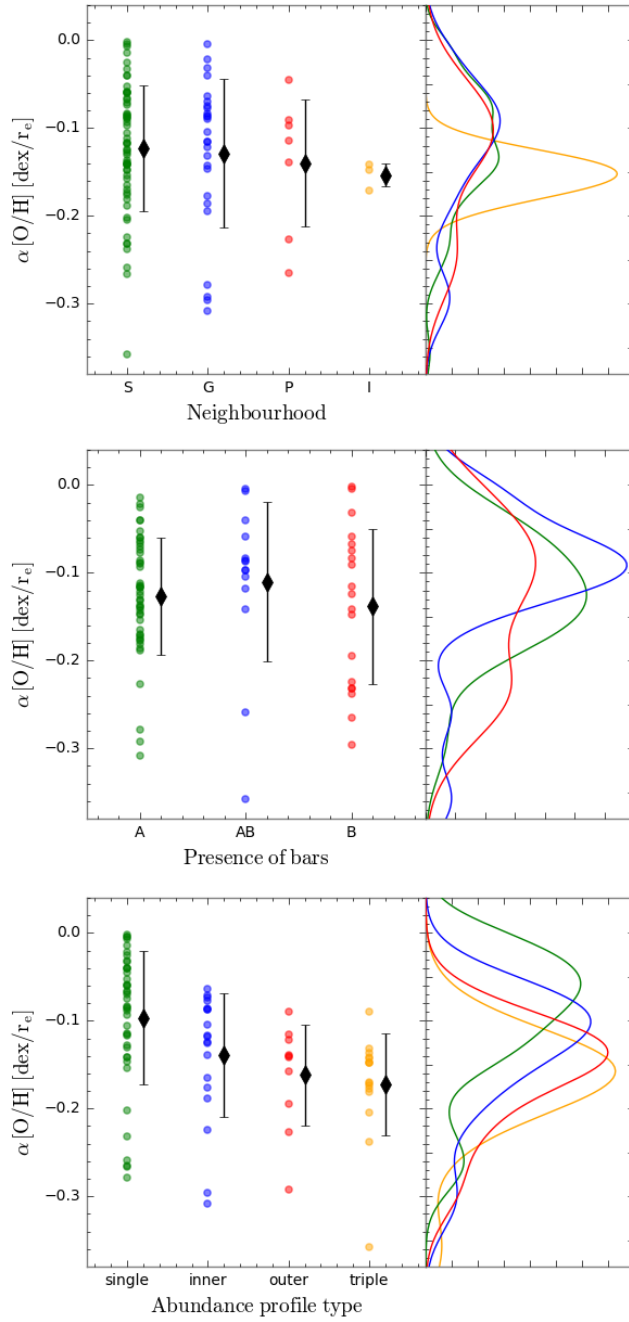


**Figure 5.3:** Distribution of slopes depending on: (i) the environment of the galaxies (isolated, green; in groups, blue; paired, red; interacting, yellow) for the top panel, (ii) the presence or absence of bars (clearly unbarred galaxies, green; clearly barred, red; and an intermediate stage, blue) for the middle panel, and (iii) the shape of the abundance profile (single profile, green; broken profile with inner drop, blue; broken profile with outer flattening, red; and a doubly-broken profile with presence of both inner drop and outer flattening, yellow) for the bottom panel. The black diamonds represent the mean values within each segregation, with the error bars indicating the standard deviation.

Although the mean values seem to suggest a trend, the small differences in these values and the high standard deviations found lead us to claim that galaxies present a similar slope independently of the environment where they are. Similar results are found when using the other two calibrators (see Sect. 5.7 and Fig. 5.12 therein). However, we have to note that very distorted galaxies due to a recent interaction or to a very advanced stage of merging have been discarded from this analysis since for those objects the definition of the centroid and the disc effective radius are dubious. Therefore, this statement does not necessary contradict previous works claiming the existence of shallower gradients in interacting galaxies.

### 5.2.2 EFFECTS OF BARS

Numerical simulations predict that the non-axisymmetrical potential of bars induce radial motions that can homogenise the gas producing shallower gradients (Friedli et al. 1994; Friedli & Benz 1995; Cavichia et al. 2014). On the other hand, observations diverge in their conclusions. Some works have found evidence of flatter gradients in barred galaxies with respect to unbarred systems (Vila-Costas & Edmunds 1992; Martin & Roy 1994; Zaritsky et al. 1994; Dutil & Roy 1999). However, recent studies based on larger statistical samples have not found evidence of such correlation between the slope of the abundance gradient and the presence of a bar (Sánchez et al. 2014).

In order to test these results, we define three different groups according to the presence or absence of bars: galaxies with no bar (A), galaxies that may have a bar but it is not clearly visible (AB), and clearly barred galaxies (B). This information was collected from the extragalactic database *HyperLeda* (Makarov et al. 2014). The galaxies for which such information is not published (16) were not considered in this comparison, but were not excluded from the rest of the analysis.

Figure 5.3 (middle panel) shows the distribution of slopes according to the presence of bars. The black diamonds represent the mean values within each group, with the errorbars indicating the standard deviation. These values are:

$$A : \alpha_{O/H} = -0.13 \text{ dex}/r_e \text{ and } \sigma = 0.07 \text{ dex}/r_e \quad (n_{\text{gal}} = 46)$$

$$AB : \alpha_{O/H} = -0.11 \text{ dex}/r_e \text{ and } \sigma = 0.09 \text{ dex}/r_e \quad (n_{\text{gal}} = 14)$$

$$B : \alpha_{O/H} = -0.14 \text{ dex}/r_e \text{ and } \sigma = 0.09 \text{ dex}/r_e \quad (n_{\text{gal}} = 19).$$

We can see that unbarred (green) and barred galaxies (blue and red) present a similar distribution of slopes with very similar mean values. This suggests a lack of correlation between the abundance slope and the barred/unbarred nature of galaxies, in agreement with Sánchez et al. (2014) and the results

found in Chapter 4 for the CALIFA galaxies. This lack of correlation also appears when using the other two calibrators (see Sect. 5.7 and Fig. 5.12 therein).

### 5.2.3 DEPENDENCE ON THE SHAPE OF THE ABUNDANCE PROFILE

The existence of different types of abundance profiles in the galaxy sample is associated with the presence of deviations from the most commonly reported behaviour in the abundance radial distribution. An interesting point to investigate would be the effect of the presence of these deviations in the main abundance gradient. To this end, we show in the bottom panel of Fig. 5.3 the dependence of the slope in the negative gradient with the shape of the abundance profile: a single gradient (green), a broken linear profile due to the inner drop (blue) and to the outer flattening (red), and a doubly-broken linear profile due to the presence of both features (yellow). For this analysis we have discarded 10 galaxies not presenting signs of the presence of the outer flattening but for which the MUSE FoV does not cover the full disc extent, and therefore may display this feature and we are not able to detect it.

The slope distributions represented in the bottom panel of Fig. 5.3 show a trend in the slope with the shape of the abundance profile, with the single profiles presenting the shallowest gradients and the doubly-broken profiles the steepest ones. The mean and standard deviation values (in units of dex/ $r_e$ ) of the distributions are:

$$\begin{aligned} \text{Single :} & \quad \alpha_{O/H} = -0.10 \text{ and } \sigma = 0.07 \text{ (} n_{gal} = 42 \text{)} \\ \text{Broken (inner) :} & \quad \alpha_{O/H} = -0.14 \text{ and } \sigma = 0.07 \text{ (} n_{gal} = 19 \text{)} \\ \text{Broken (outer) :} & \quad \alpha_{O/H} = -0.16 \text{ and } \sigma = 0.06 \text{ (} n_{gal} = 10 \text{)} \\ \text{Doubly - broken :} & \quad \alpha_{O/H} = -0.17 \text{ and } \sigma = 0.06 \text{ (} n_{gal} = 16 \text{)}. \end{aligned}$$

These results indicate that the presence of the inner drop and the outer flattening does have an effect on the negative abundance gradient displayed by spiral galaxies. This general trend is also observed in the cases where the M13-N2 and D16 calibrators are used (see Fig. 5.12). For the M13-N2 (D16) indicator, we find a total difference of  $-0.04$  ( $-0.09$ ) dex/ $r_e$  between the galaxies presenting a single abundance gradient and the ones displaying a doubly-broken profile (see Sect. 5.7).

In Chapter 4 we already found slightly steeper gradients in galaxies with evidence of an inner drop. The fact that the presence of this feature had an impact on the overall distribution of abundances at larger radii led us to propose the existence of gas radial motions (Lacey & Fall 1985; Portinari & Chiosi 2000; Schönrich & Binney 2009; Spitoni et al. 2013) as the possible cause of this feature. These radial movements would be towards the knee



point in the abundance distribution (drop), outwards in the inner regions and inwards in the outer parts. In this chapter, using a different sample of galaxies and a different dataset, we confirm these results and find a similar situation regarding the presence of the outer flattening. As mentioned in that chapter, different mechanisms have been suggested to explain the origin of the outer flattening in the gas abundances, being radial motions of both gas and stars one of them (e.g. Goetz & Koeppen 1992; Ferguson & Clarke 2001; Sellwood & Binney 2002; Minchev & Famaey 2010; Bilitewski & Schönrich 2012; Roškar et al. 2012; Daniel & Wyse 2015). On the other hand, alternative mechanisms such as minor mergers and satellite accretion (Quillen et al. 2009; Qu et al. 2011; Bird et al. 2012), a radial dependence of the star formation efficiency at large galactocentric distances (Bresolin et al. 2012; Esteban et al. 2013) or a balance between outflows and inflows with the intergalactic medium (Oppenheimer & Davé 2008; Oppenheimer et al. 2010; Davé et al. 2011, 2012) have also been proposed. All these mechanisms are not mutually exclusive and to date we have not been able to distinguish between them. Although we do not discard the other mechanisms to also be involved, the results found in this analysis suggest that radial motions play a fundamental role shaping the abundance profiles of spiral galaxies by producing an abundance drop in the inner regions and/or an abundance flattening in the outermost parts. A deeper study on the connection of these features with radial motions, also from the dynamical and theoretical point of view, might help to further constrain this scenario.

### 5.3 LOCATION OF THE INNER DROP AND THE OUTER FLATTENING

As stated several times along this thesis, the presence on an inner drop and an outer flattening in the radial abundance profiles of some spiral galaxies was already found in several works. However, the few of them that analysed these features in a statistical way using a large sample of galaxies (e.g. Sánchez et al. 2014) always assumed that their location was the same for all the galaxies where they were observed. This was also the case for the analysis carried out in Chapter 4. This assumption was based on a visual inspection of the sample, and afterwards confirmed by the stacking of the abundance profiles of the individual galaxies.

To date, no previous studies have carried out a detailed analysis of these features, determining the actual location of the inner drop and the outer flattening for a large sample of galaxies. Therefore, here we have developed a methodology to fit the radial abundance profiles in an automatic way that allows us to derive the location of these features. Hereafter, we will define  $h_D$  as the galactocentric distance at which the inner drop appears

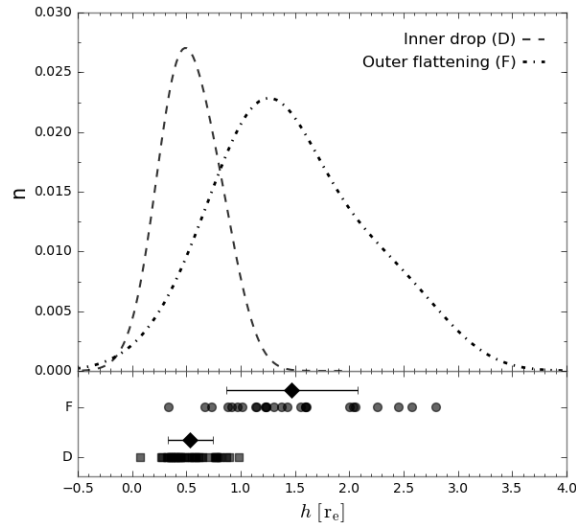


**Figure 5.4:** *Distribution of radial positions (in units of  $r_e$ ) of the inner drop (D, squares) and outer flattening (F, dots) found in some galaxies of the sample. The black diamonds represent the mean values of the position at which these features appear, with the error bars indicating the standard deviations. Dashed and dashed-dotted lines represent the normalised density distributions of the location of the inner drop and outer flattening, respectively.*

( $h_1$  in equations from 5.2 to 5.7) and  $h_F$  as the distance at which the radial gradients flatten ( $h_2$  in equations from 5.2 to 5.7).

In Fig. 5.4 we represent the distribution of values derived for  $h_D$  (dashed line) for the 37 galaxies where the inner abundance drop is detected and the distribution of values of  $h_F$  for the 26 galaxies displaying the outer abundance flattening (dashed-dotted line). These density (normalised to one) distributions were derived considering each radial position as a Gaussian distribution centred at such point with a sigma given by the maximum distance between nearest-neighbours, and summing all these individual Gaussians. In this way we reproduce a smooth distribution that is more peaky in the clustered points. As it can be seen in the figure, the distribution of the radial positions of the inner drop is quite narrow and has a pronounced peak centred at  $\sim 0.5 r_e$  (the mean value of the radial positions is  $0.54 r_e$  and the standard deviation  $0.20$ ), suggesting that the position of the inner drop is very similar in all galaxies where this feature is present. However, the distribution for the outer flattening is much wider, with the flattening occurring between  $0.3$  and  $2.8 r_e$ , and overlapping the distribution of the inner drop. Although the distribution shows a peak at  $\sim 1.5 r_e$  (the mean value of the radial positions is  $1.47 r_e$  and the standard deviation  $0.60$ ), the large range of radii covered by it prevents us to confirm a characteristic location of the outer flattening in the abundances.

The use of the other two calibrators reduces the number of galaxies where the inner abundance drop is detected to 23 for M13-N2 and to 20 for D16. The number of galaxies displaying the outer abundance flattening is also reduced to 13 galaxies in the case of the M13-N2 calibrator and to 19 in the case of D16. However, the distribution of the radial positions of both features is very similar to the one obtained with O3N2 (see Fig. 5.13), with very slight differences in the average positions (inner drop at  $\sim 0.8 r_e$  for M13-N2 and at  $\sim 0.6 r_e$  for D16; outer flattening at  $\sim 1.5 r_e$  and at  $\sim 1.6 r_e$ , respectively).

These results are in agreement with the findings shown in Chapter 4 and previous works (e.g. Sánchez et al. 2014). However, our results seem to contradict the claim that this was also the case for the outer flattening (located approximately at  $\sim 2.0 r_e$ ). These studies were all based on visual inspections of the general shape of the gradient (see Sect. 5.4 below), placing the location of the outer flattening at the position in which the gradient clearly deviates from its linear behaviour (that would happen approximately between  $2 - 2.25 r_e$  according to Fig. 5.5). Indeed, this location has fluctuated between different estimations, being placed at  $2.2 r_e$  by Sánchez et al. (2012b) and around 2 by Sánchez et al. (2014). However, the detailed analysis carried out in this chapter indicates that the knee point is nearer to  $\sim 1.5 r_e$ , with a large dispersion of values among galaxies. Thus, our results do not imply a contradiction, but reflects the need of a more detailed analysis like the one presented here.

## 5.4 A COMMON OXYGEN ABUNDANCE GRADIENT

The existence of a characteristic slope in the oxygen abundance distribution of spiral galaxies was stated in Sánchez et al. (2012b, 2014) and confirmed by our own analysis performed in Chapter 4. In this chapter, following a similar recipe, we derived the radial distribution of the oxygen abundances for the 95 galaxies in the sample and stacked all of them as a single distribution. To do that we rescaled the distributions, as the  $\mathcal{M} - \mathcal{Z}$  relation (Tremonti et al. 2004) produces an offset of the abundance profile according to the integrated stellar mass of the galaxy. To this end, we applied an offset to the distribution of each galaxy by normalising the abundance at the disc effective radius to the average value for the whole sample ( $\sim 8.5$  dex). The final outcome of this analysis is shown in Fig. 5.5. The abundance distribution is represented as a colour-coded density map (normalised to one) and shows clearly a common abundance gradient presented by all galaxies in the sample. The white dots represent the mean oxygen abundance values, with the error bars indicating the corresponding standard deviations, for bins of  $0.3 r_e$ . An error-weighted linear regression (solid red line) to the mean values within the range between  $0.5$  and  $1.5 r_e$  (trying to avoid the regions

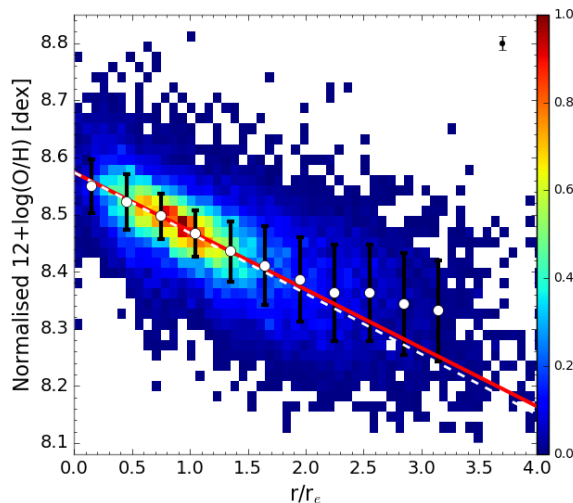


**Figure 5.5:** Radial density distribution of the oxygen abundance after normalising the abundances of each galaxy so that the abundance at  $1r_e$  is equal to the average value for the whole sample at such radius. The white dots represent the mean oxygen abundance values, with the error bars indicating the corresponding standard deviations, for bins of  $0.3 r_e$ . The solid red line represents the error-weighted linear fit derived for those mean values within the range between  $0.5$  and  $1.5 r_e$ , and the dashed white line represents the linear relation corresponding to the characteristic value of the slope derived in Sect. 5.2 for the individual galaxies assuming a Gaussian distribution.

dominated by the presence of the inner abundance drop and outer flattening) derives a slope of  $\alpha_{O/H} = -0.10 \pm 0.03 \text{ dex}/r_e$ . This is compatible with the characteristic slope of  $\alpha_{O/H} = -0.11 (\sigma = 0.07) \text{ dex}/r_e$  derived in Sect. 5.2 for the individual galaxies assuming a Gaussian distribution (dashed-white line).

As with M13-N2 and D16, the common abundance gradient is clearly visible when representing the radial abundance distribution of the whole sample (with a slope of  $\alpha_{O/H} = -0.04$  and  $-0.20 \text{ dex}/r_e$  for M13-N2 and D16, respectively). However, the presence of the inner drop and the outer flattening is not so evident. This is somehow expected due to the wide range of values found for  $h_D$  and  $h_F$  that may blur their signatures when all gradients are stacked together.

## 5.5 THE CHARACTERISTIC SLOPE AS A NORMALISATION SCALE

Recently, Zinchenko et al. (2016) showed the validity of the use of gas abundance maps to determine the geometrical parameters of galaxies (coordinates of the centre, inclination and position angle of the major axis). Generally,

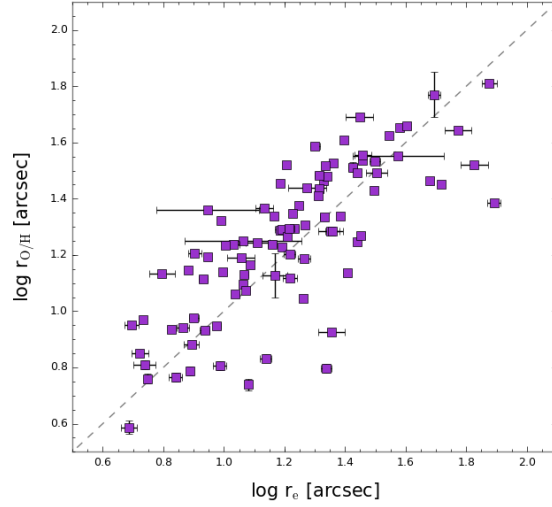


**Figure 5.6:** Radius at which the abundance distribution decays 0.10 dex (given by the decrease in the abundance in one disc effective radius attending to the common abundance gradient, see Fig. 5.5) versus the disc effective radius (in logarithmic scale).

these parameters are derived from the photometric analysis of a galaxy, assuming that the surface brightness of the galaxy is axisymmetric. However, if we consider that the metallicity of the disc is also a function of the galactocentric distances (i.e. the possible azimuthal asymmetries, in case of existing, are small, e.g. Vogt et al. 2017), then we can expect that the abundance map can also be used for the determination of geometrical parameters.

The results presented in Zinchenko et al. (2016) could be a consequence of the oxygen abundance distribution following the surface mass density and therefore the surface brightness of a galaxy, as a result of the local  $\Sigma - Z$  relation (Rosales-Ortega et al. 2012; Sánchez et al. 2013; Barrera-Ballesteros et al. 2016). Due to this connection between both properties, we could define a new scale length based on the abundance maps to normalise the abundance profiles instead of using the disc effective radius. In the previous section we confirmed the presence of a characteristic slope of  $-0.10 \text{ dex}/r_e$  in the abundance distribution. Therefore, we define here a parameter named ‘the abundance scale length’ ( $r_{O/H}$ ) as the radial position at which the abundance distribution of a galaxy decays 0.10 dex. If we represent  $r_{O/H}$  as a function of  $r_e$ , we would expect the distribution of values falling near the 1:1 relation, indicating that the surface brightness and the gas metallicity follow the same distribution. The outcome of this statement is shown in Fig. 5.6, obtaining a tight correlation between both parameters. The values of  $r_{O/H}$  for all galaxies in the sample are shown in Table B.2 (Appendix B).

We normalise now the radial abundance distributions of the galaxy sam-

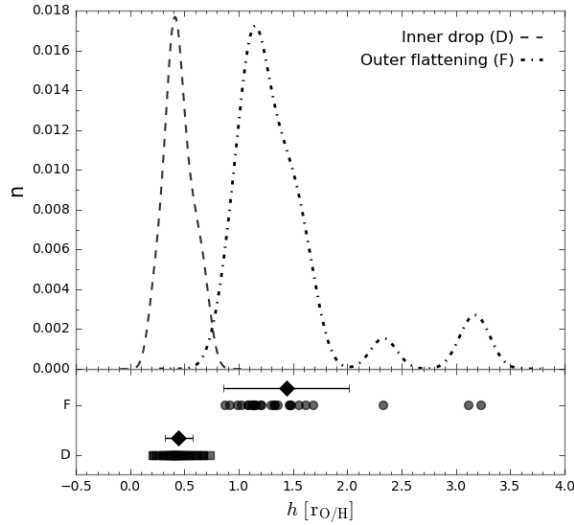


**Figure 5.7:** Same as Fig. 5.4 but normalising the abundance distribution to  $r_{O/H}$ . See caption above for more details.

ple using  $r_{O/H}$  instead of  $r_e$  as previously done, and repeat part of the analysis. The new distributions of radial positions of the inner drop and the outer flattening is shown in Fig. 5.7 (specific values are listed in Table B.2, Appendix B). It can be seen that now the distributions have got significantly narrower, especially in the case of the outer flattening (with the exception of three outliers). The mean values of the radial position of both features are very similar to the derived ones normalising to  $r_e$  ( $h_D = 0.45 r_{O/H}$  and  $h_F = 1.44 r_{O/H}$ ). However, the standard deviations around the mean values have been reduced more than a half of the previous value (from 0.20 to 0.13 for the inner drop and from 0.60 to 0.20 for the outer flattening, not considering the three outliers). This is also the case when using the M13-N2 and the D16 calibrators (see Fig. 5.14), although the reduction of the standard deviation values is smaller than for the M13-O3N2 calibrator (from 0.22 to 0.17 and from 0.22 to 0.16 for the inner drop, from 0.53 to 0.22 and from 0.55 to 0.35 for the outer flattening, using the M13-N2 and the D16 calibrators, respectively).

Finally, we reproduce Fig. 5.5 stacking all the individual abundance distributions of the galaxy sample but using now the new normalisation scale,  $r_{O/H}$ . The result is shown in the left panel of Fig. 5.8 (similar figures for the M13-N2 and the D16 calibrators are shown in Sect. 5.7, Fig. 5.15). By construction, the global abundance distribution presents a characteristic slope of  $-0.10 \text{ dex}/r_{O/H}$  ( $-0.20 \text{ dex}/r_{O/H}$  in the case of the M13-N2 calibrator and  $-0.04 \text{ dex}/r_{O/H}$  for D16). In addition, it is evident now the presence of the inner drop and the outer flattening in the abundances, features that were blurred when normalising the abundance distribution to  $r_e$ . This is because

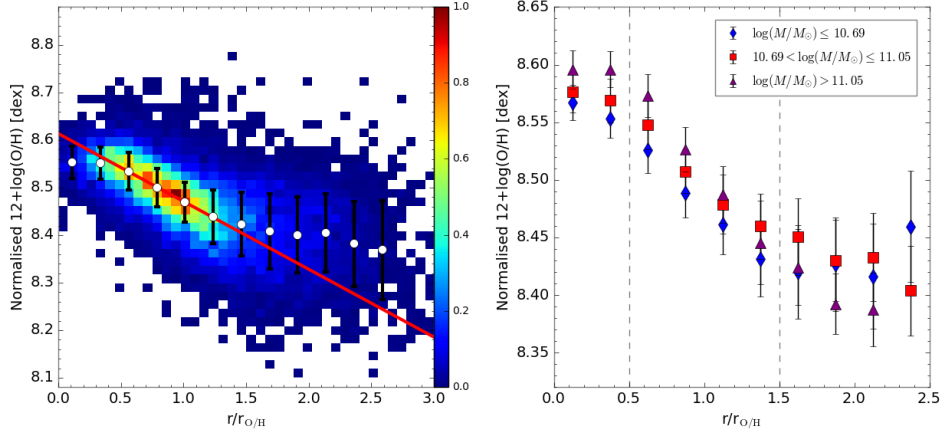


**Figure 5.8:** *Left:* Same as Fig. 5.5 but normalising the abundance distribution to  $r_{O/H}$ . See caption above for more details. *Right:* Mean oxygen abundance radial profiles derived for galaxies belonging to three different stellar mass bins:  $\log(M/M_{\odot}) \leq 10.69$ , blue diamonds;  $10.69 < \log(M/M_{\odot}) \leq 11.05$ , red squares;  $\log(M/M_{\odot}) > 11.05$ , purple triangles. The limits of the bins were chosen to ensure a similar number of elements in each bin. The symbols represent the mean oxygen abundance values, with the error bars indicating the corresponding standard deviations, for bins of  $0.25 r_{O/H}$ . Dashed vertical lines indicate the average position of the inner drop and the flattening in the outer parts.

now these features happen at a similar radial position for the whole sample, so regions presenting different behaviours have not been mixed when stacking the distribution of all the galaxies.

The right panel of Fig. 5.8 shows the average oxygen abundance radial profiles when separating the sample into different bins according to the integrated stellar mass of the galaxies (similar figures for the M13-N2 and D16 calibrators are shown in Sect. 5.7). It can be seen that the presence of the abundance drop in the inner regions of the galaxy discs and the flattening in the outer regions is also easily observable (although for D16 the presence of the inner drop is less evident). We calculated the stellar masses using the mass-luminosity ratio presented in Bell & de Jong (2001). We derived the  $g$  and  $r$  apparent magnitudes from the flux density in the  $g$ - and  $r$ -band images recovered from the data and we used the equations presented in Jester et al. (2005) to transform SDSS magnitudes to the Johnson system. Then we transformed these quantities to luminosities knowing the galaxy distance. Finally, from the  $V$ -band luminosity and the  $B - V$  colour we obtained the stellar masses using the mentioned mass-luminosity ratio. The luminosity and colour values were corrected by dust attenuation. The integrated values were determined from the values derived at one disc effective radius since some galaxies are not fully covered by the FoV of MUSE. We performed a sanity check to test the robustness of the derived stellar masses (with in-

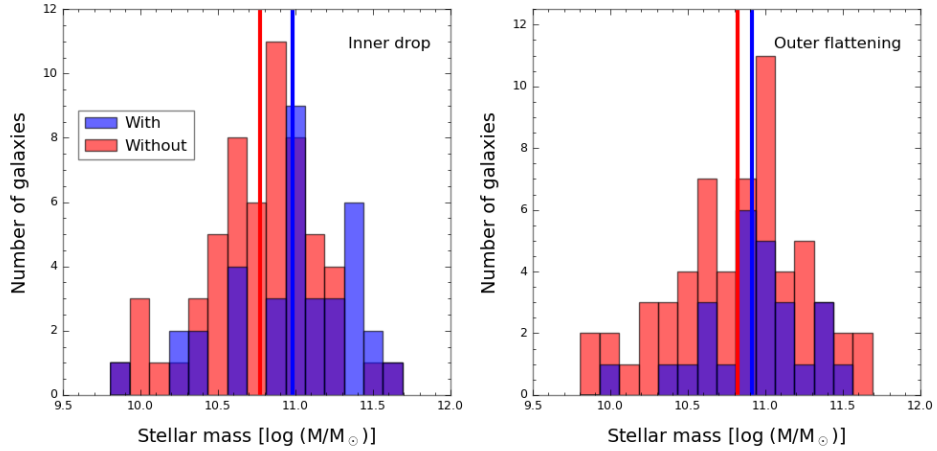


**Figure 5.9:** Distribution of the integrated stellar mass of the galaxy sample for galaxies with (blue) and without (red) presence of an abundance drop in the inner regions of the galaxy discs (left panel) and an abundance flattening in the outer regions (right panel). Vertical lines represent the mean values for each distribution.

tegrated values determined from the values at one disc effective radius) by comparing them with the values derived using directly the integrated masses (derived by summing all the values up to three disc effective radii) in the cases where the extension of the galaxies was completely covered by the FoV of MUSE. The correlation was very good, with a standard deviation of just 0.12 dex, similar to the typical systematic errors on the mass derivation.

The limits of the mass bins were chosen to ensure a similar number of elements in each bin:  $\log(M/M_{\odot}) \leq 10.69$  (blue diamonds),  $10.69 < \log(M/M_{\odot}) \leq 11.05$  (red squares),  $\log(M/M_{\odot}) > 11.05$  (purple triangles). In Chapter 4 we found a dependence of the presence of the inner drop with the integrated stellar mass of the galaxies, with the most massive galaxies presenting the deepest abundance drops. The flattening on the opposite appeared independently of the galaxy mass. Similar trends are obtained in this analysis, confirming the reported result. To explore this result, we represent in Fig. 5.9 the distribution of the integrated stellar mass for the galaxies with (blue histograms) and without (red histograms) presence of the abundance drop in the inner regions (left panel) and the outer flattening (right panel). Again, in the analysis of the outer flattening we have discarded the 10 galaxies for which we do not detect an outer flattening maybe due to an incomplete coverage of the disc extent by the MUSE FoV. It can be seen that galaxies presenting an inner drop are more massive than the galaxies without evidence of this feature. The mean stellar mass for the former ones (blue vertical line) is  $10.98 \pm 0.07$  ( $\log(M/M_{\odot})$ ), whereas in the latter the mean value (red vertical line) is  $10.77 \pm 0.05$  ( $\log(M/M_{\odot})$ ). Regarding the outer flattening, the distributions for the galaxies with and without presence



of this feature cover the same range of masses, with similar mean values ( $10.92 \pm 0.06$  for galaxies with outer flattening and  $10.82 \pm 0.06$  for galaxies with no presence of this flattening). A KS-test yields a p-value value of 1% when comparing the distributions with and without an inner abundance drop, while we obtain a p-value of 40% when analysing the distributions with respect to the presence of the outer flattening. Therefore, this test also confirms the results reported in Chapter 4, that is, there is a dependence of the presence of the inner drop with the galaxy mass, and an absence of such relation in the case of the outer flattening.

## 5.6 DISPERSION OF THE GRADIENT AND MIXING SCALELENGTH

Only a small number of studies focussed on individual galaxies have analysed the scatter relative to the radial abundance gradients, searching for evidences of azimuthal variations in the metallicity. Analysis on NGC 300 (Bresolin et al. 2009a) or M 33 (Bresolin 2011) reveal small scatter values consistent with the uncertainties in the abundance measurements. On the other hand, recent observational studies on NGC 6754 (Sánchez et al. 2015) and M 101 (Croxall et al. 2016), although based on very different approaches to derive the oxygen abundance of the gas component, have both found a substantial dispersion that can be taken as an evidence of the presence of azimuthal variations. The results on NGC 6754 have been confirmed in this thesis by analysing the azimuthal abundance distribution of the galaxy (see Sect. 7.3). However, regarding M 101, a previous study performed by Li et al. (2013) only observed marginal local metallicity inhomogeneities that the authors suggested may be linked to tidal features reported at that time (Mihos et al. 2012).

Due to the large number of H II regions needed to perform a proper analysis of the dispersion of the abundance gradients, an extended study on this topic has not been feasible to date, being limited only to individual galaxies. The number of galaxies in our sample in which a large number of H II regions is detected due to the high resolution of AMUSING data makes this analysis perfectly achievable here. Studying the possible relation between the dispersion and other parameters of the galaxies such as the presence of a bar, the morphological type or the stellar mass can help us to constrain the possible factors that can produce a significant scatter in the abundance gradients.

With this purpose we measured the scatter relative to the radial abundance gradient of each galaxy of the sample as the standard deviation of the differences between the observed abundances and the corresponding values from the linear regression according to their deprojected galactocentric distances. We only derived the scatter in the radial range covered by the

linear behaviour (see Sect. 5.1 for more details about this linear regime). Figure 5.10 represents the distribution of scatter values according to different characteristics of the galaxies: presence of bars (A, clearly unbarred galaxies; B, clearly barred; AB, intermediate stage; top left), environment of the galaxy (S, isolated; G, in group; P, paired, I, in interaction; top right), numerical morphological type according to the de Vaucouleurs system from *HyperLeda* (T, middle left), specific star formation rate (middle right), integrated stellar mass (bottom left), and stellar mass density at one disc effective radius (bottom right). The values of these parameters for all galaxies in the sample are given in Table B.1 (Appendix B), except the scatter values that are provided in Table B.2. The star formation rate (SFR) was derived for each galaxy adopting the classical relation presented in Kennicutt (1998) based on the dust-corrected  $H\alpha$  luminosities. These luminosities were obtained deriving the apparent magnitudes from the flux density in an  $H\alpha$  image recovered from the data and then transforming these quantities to luminosities knowing the galaxy distance. The specific star formation rate (sSFR) for each galaxy was then obtained dividing the SFR by the mass (see Sect. 5.5 for details on the derivation of the galaxy mass). The relations between the scatter and the different properties represented in Figure 5.10 show no significant dependence of the scatter with any of the analysed parameters. Indeed, the measured values are in general lower than the error of the calibrator used to derive the oxygen abundances ( $\sim 0.08$  dex), and therefore, we cannot conclude that the detected scatter has a physical origin.

Due to the reduction of the physical spatial resolution when we move to high redshift, we observe that the scatter increases with the number of the detected H II regions in a galaxy (as the number of these regions decreases with the redshift). In order to avoid this non-physical bias we have discarded those galaxies with  $z > 0.02$  and less than 30 H II regions detected. Reproducing the analysis with the remaining 52 galaxies, we obtain similar results, that is, there is no dependence of the scatter relative to the radial abundance gradient with any of the analysed properties of the galaxies.

The dispersion around the radial abundance gradient of a galaxy can be considered an upper limit to the maximum radial mixing scale, as any radial mixing increases the scatter by moving regions of a certain abundance from one galactocentric distance to another (e.g. Scalo & Elmegreen 2004). If we divide the scatter by the slope of the gradient we obtain a measurement of how far a certain H II region has been able to move from its expected location based on the displayed abundance gradient, that is, the mixing scalelength ( $r_{mix}$ , Sánchez et al. 2015). The derived values of this parameter for our sample typically range between 0.1 and 0.8  $r_e$ , with a median value of 0.4  $r_e$ , very similar to the mixing scalelength of 0.43  $r_e$  derived for NGC 6754 by Sánchez et al. (2015). As in the case of the scatter, we find no significance

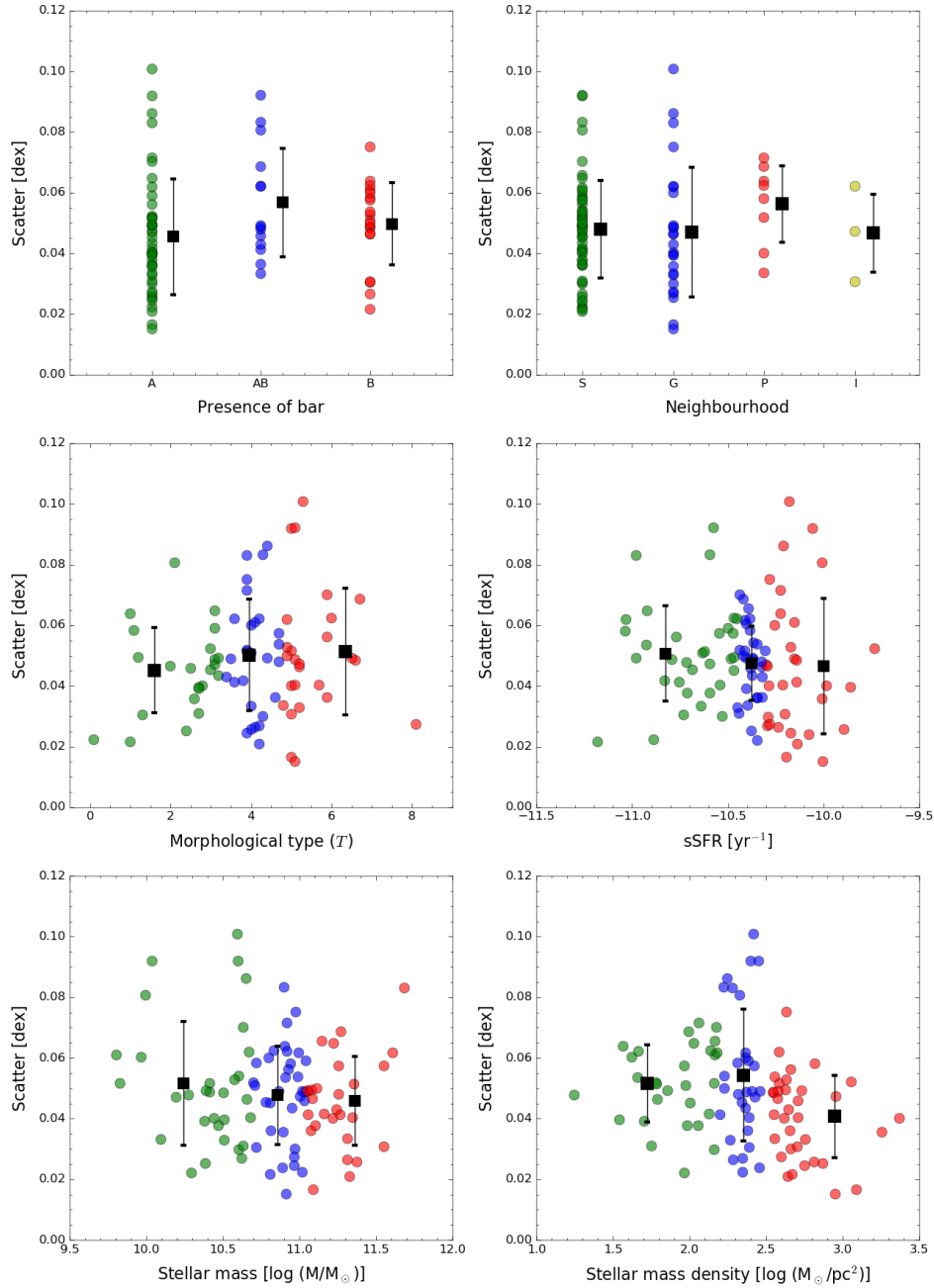


**Figure 5.10:** Distribution of the scatter relative to the radial abundance gradients as a function of: presence of bars ( $A$ , clearly unbarred galaxies;  $B$ , clearly barred;  $AB$ , intermediate stage; top left), environment of the galaxy ( $S$ , isolated;  $G$ , in group;  $P$ , paired,  $I$ , in interaction; top right), numerical morphological type according to the de Vaucouleurs system ( $T$ , middle left), specific star formation rate (middle right), integrated stellar mass (bottom left), and stellar mass density at one disc effective radius (bottom right). The black squares represent the mean values within each segregation, with the errorbars indicating the standard deviation. See text for details on the derivation of these parameters.

dependence of the mixing scalelength with any of the analysed properties of the galaxies.

## 5.7 ON THE USE OF DIFFERENT CALIBRATORS IN THE DERIVATION OF THE ABUNDANCE PROFILES

In this section we assess the effect of using different calibrators on the results presented in this study. With such purpose, we replicate the figures that support our main results using the calibration described in Dopita et al. (2016, D16), and the one proposed in Marino et al. (2013) for the N2 index (M13-N2, see Sect. 3.3 for a brief description of these two additional calibrators). The choice of these empirical indicators is mainly based on the limited wavelength range in the blue regime covered by MUSE, that does not include more widely used emission lines such as  $[\text{O II}]\lambda 3727$ .

Figure 5.11 shows the distribution of slopes of the main oxygen abundance gradients derived for the galaxy sample of 95 spiral galaxies using the M13-N2 (*left*) and D16 (*right*) calibrators. As obtained with O3N2, the abundance distribution in both cases presents a characteristic slope very similar for all galaxies, although the actual value changes ( $-0.23 \text{ dex}/r_e$  for D16 and  $-0.06 \text{ dex}/r_e$  for M13-N2).

We have also analysed the influence of some galaxy properties such as the density of the environment, the presence of bars and the type of abundance profile displayed (according to Sect. 5.1) on the main abundance gradient when we use these two calibrators. The outcome of this analysis is shown in Fig. 5.12. Similarly to O3N2, we only find a dependence of the slope with the shape of the abundance profile, presenting the single profiles the shallowest gradients and the doubly-broken profiles the steepest ones. The mean and standard deviation values of the distributions for the M13-N2 (D16) are the following ones (in units of  $\text{dex}/r_e$ , the nomenclature is explained in Sect 5.2):

$$\text{S} : \alpha_{\text{O}/\text{H}} = -0.06 (-0.22), \sigma = 0.06 (0.13); n_{\text{gal}} = 59 (59)$$

$$\text{G} : \alpha_{\text{O}/\text{H}} = -0.07 (-0.25), \sigma = 0.06 (0.12); n_{\text{gal}} = 26 (26)$$

$$\text{P} : \alpha_{\text{O}/\text{H}} = -0.08 (-0.27), \sigma = 0.05 (0.14); n_{\text{gal}} = 7 (7)$$

$$\text{I} : \alpha_{\text{O}/\text{H}} = -0.05 (-0.33), \sigma = 0.01 (0.12); n_{\text{gal}} = 3 (3).$$

$$\text{A} : \alpha_{\text{O}/\text{H}} = -0.05 (-0.23), \sigma = 0.06 (0.13); n_{\text{gal}} = 46 (46)$$

$$\text{AB} : \alpha_{\text{O}/\text{H}} = -0.06 (-0.22), \sigma = 0.06 (0.15); n_{\text{gal}} = 14 (14)$$

$$\text{B} : \alpha_{\text{O}/\text{H}} = -0.08 (-0.26), \sigma = 0.05 (0.14); n_{\text{gal}} = 19 (19).$$

---

Single :	$\alpha_{O/H} = -0.06 (-0.22), \sigma = 0.06 (0.14); n_{gal} = 55 (59)$
Broken (inner) :	$\alpha_{O/H} = -0.07 (-0.21), \sigma = 0.04 (0.07); n_{gal} = 18 (9)$
Broken (outer) :	$\alpha_{O/H} = -0.08 (-0.28), \sigma = 0.05 (0.09); n_{gal} = 12 (10)$
Doubly – broken :	$\alpha_{O/H} = -0.10 (-0.31), \sigma = 0.04 (0.08); n_{gal} = 2 (9).$

Regarding the presence of inner drops and outer flattenings in the abundance profiles, the use of the new calibrators reduces the number of galaxies where the inner abundance drop is detected to 23 for M13-N2 and to 20 for D16. The number of galaxies displaying the outer abundance flattening is also reduced to 13 galaxies in the case of the M13-N2 calibrator and to 19 in the case of D16. Analysing the distribution of radial positions of both features we obtain a very similar shape to the one obtained with O3N2 (see Fig. 5.13): a narrow distribution for the drop and a quite wider one for the flattening. The average positions of the features are also very similar to the previous case, with only small differences: the inner drop is located at  $\sim 0.8 r_e$  (standard deviation of 0.22) for M13-N2 and at  $\sim 0.6 r_e$  (standard deviation of 0.22) for D16, and the average position of the outer flattening is  $\sim 1.5 r_e$  (standard deviation of 0.53) and  $\sim 1.6 r_e$  (standard deviation of 0.55), respectively.

When normalising the abundance profiles to the abundance scale length  $r_{O/H}$  (see Sect. 5.5 for information about this parameter), the distributions of radial positions for these features get significantly narrower (standard deviations are reduced from 0.22 to 0.17 and from 0.22 to 0.16 for the inner drop, from 0.53 to 0.22 and from 0.55 to 0.35 for the outer flattening, using the M13-N2 and the D16 calibrators, respectively), deriving very similar values for the position of the inner drop and the outer flattening (see Fig. 5.14). In addition, we reproduce the stacking of the abundance distribution with this new normalisation scale in Fig. 5.15. We find a very similar shape for the two calibrators. By construction, the global abundance distribution presents a characteristic slope of  $-0.20 \text{ dex}/r_{O/H}$  in the case of the M13-N2 calibrator and  $-0.04 \text{ dex}/r_{O/H}$  for D16. In addition, the abundance distribution shows clear evidences of the presence of the inner drop and the outer flattening, as in the case of the M13-O3N2 calibrator. The right panel of Fig. 5.15 shows the average abundance radial profiles when separating the sample into different mass bins for both the M13-N2 and D16 calibrators. It can be seen that the presence of the abundance drop in the inner regions of the galaxy discs and the flattening in the outer regions is also easily observable, although for D16 the presence of the inner drop is not so clear. Similarly to M13-O3N2, we find a dependence of the presence of the inner drop with the galaxy mass, with the most massive galaxies presenting the deepest abundance drops. The flattening on the opposite appear independently of the galaxy mass.

In this section we demonstrate that the main results presented in this

chapter do not depend on the choice of the oxygen abundance indicator used. However, we should be aware of the subtle differences that appear when using different calibrators, especially if we focus on the abundance distribution of individual galaxies.

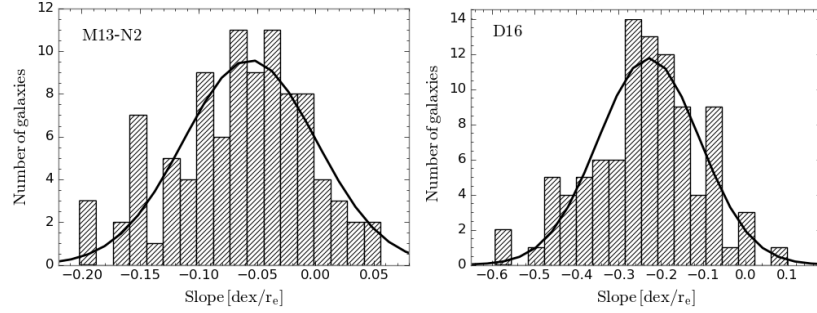


**Figure 5.11:** Distribution of slope values of the oxygen main abundance gradients (normalised to the disc effective radius) derived for the galaxy sample using the M13-N2 (left) and D16 (right) calibrators. Solid black line represents the Gaussian distribution of the data assuming the mean and standard-deviation of the distribution of slope values and sampled with the same bins.

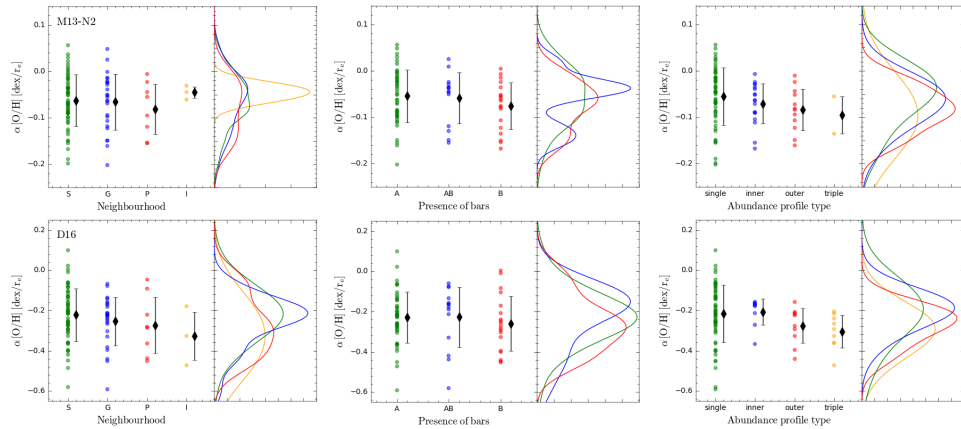


**Figure 5.12:** Distribution of slopes depending on different galaxy properties using the M13-N2 (top panels) and the D16 (bottom panels) calibrators: (i) the environment of the galaxies for the left panel, (ii) the presence or absence of bars for the middle panel, and (iii) the shape of the abundance profile for the right panel. See Fig. 5.3 for more details.

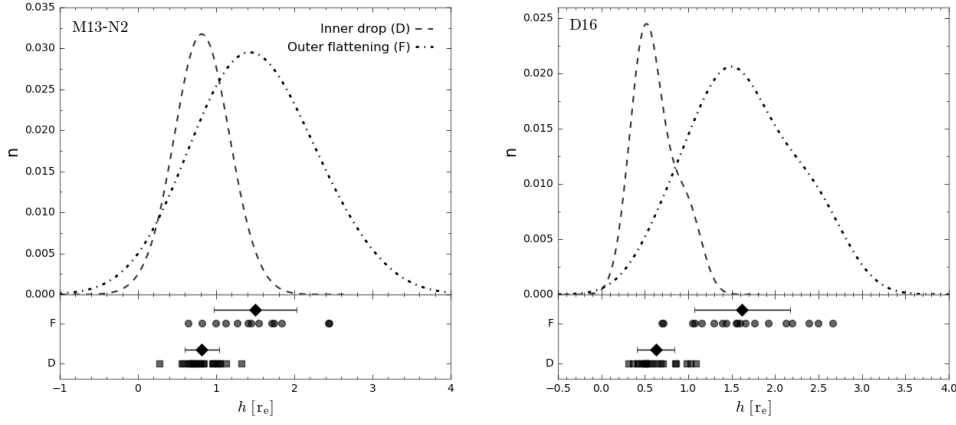


**Figure 5.13:** Distribution of radial positions (in units of  $r_e$ ) of the inner drop (D, squares) and outer flattening (F, dots) found in some galaxies of the sample using the M13-N2 (left panel) and the D16 (right panel) calibrators. The black diamonds represent the mean values of the position at which these features appear, with the error bars indicating the standard deviations. Dashed and dashed-dotted lines represent the normalised density distributions of the location of the inner drop and outer flattening, respectively.

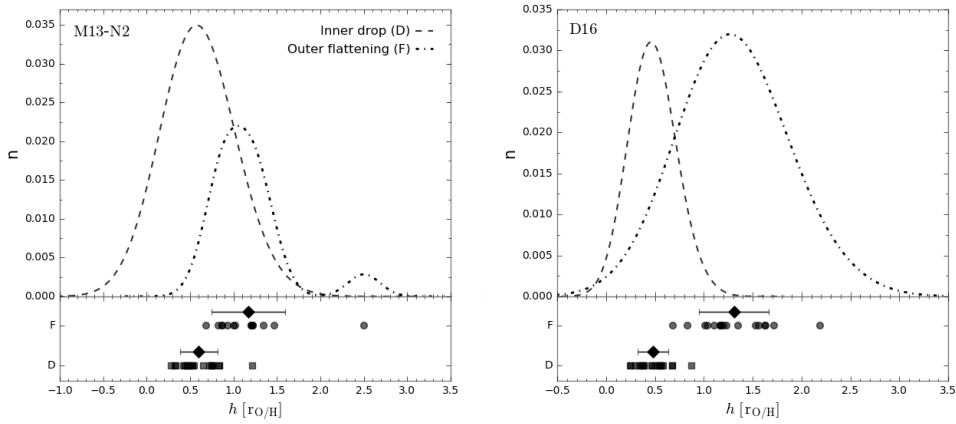


**Figure 5.14:** Same as Fig. 5.13 but normalising the abundance distribution to  $r_{O/H}$ . See caption above for more details.

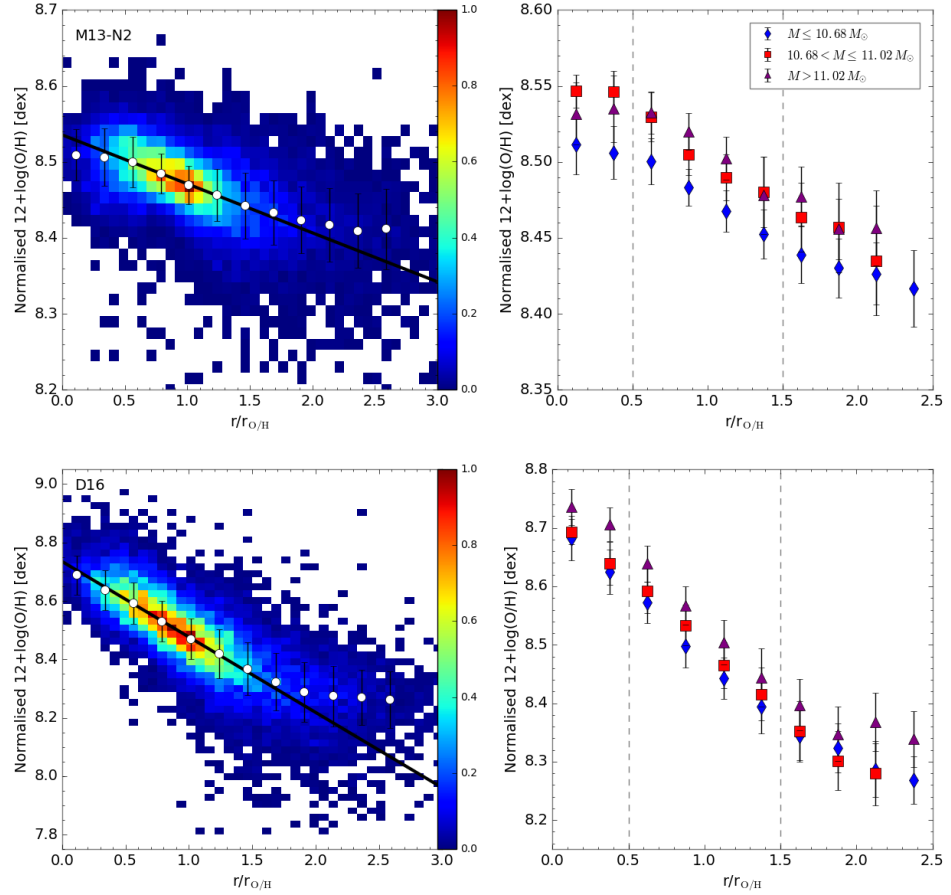


**Figure 5.15:** *Left: Normalised radial density distribution of the oxygen abundance for the M13-N2 (top) and the D16 (top) calibrators. The galactocentric distances are normalised to the abundance scalelength  $r_{O/H}$ . The white dots represent the mean oxygen abundance values, with the error bars indicating the corresponding standard deviations, for bins of  $0.3 r_e$ . The solid black line represents the error-weighted linear fit derived for those mean values within the range between  $0.5$  and  $1.5 r_e$ . Right: Mean oxygen abundance radial profiles derived for galaxies belonging to three different stellar mass bins:  $\log(M/M_\odot) \leq 10.69$ , blue diamonds;  $10.69 < \log(M/M_\odot) \leq 11.05$ , red squares;  $\log(M/M_\odot) > 11.05$ , purple triangles. The limits of the bins were chosen to ensure a similar number of elements in each bin. The symbols represent the mean oxygen abundance values, with the error bars indicating the corresponding standard deviations, for bins of  $0.25 r_{O/H}$ . Dashed vertical lines indicate the average position of the inner drop and the flattening in the outer parts.*



## 5.8 BRIEF SUMMARY

The advent of MUSE, an instrument combining a large FoV with high spatial resolution, allows us to improve the characterisation of the radial abundance distribution of spiral galaxies by increasing the number of H II regions detected in individual galaxies with respect to previous studies. The high spatial resolution also helps to reduce the contamination of the diffuse emission in the detected regions and the dilution effects. All these advantages result in a better mapping of the radial distribution, including the inner and outermost parts where deviations from the linear behaviour appear.

In this chapter we characterised the oxygen abundance radial profile (normalising it to the disc effective radius) of a large sample of 102 spiral galaxies using MUSE data, allowing us to obtain statistically significant results. We developed a new methodology to automatically fit the radial profiles, detecting the presence of possible inner drops and outer flattenings in the abundances. We found 55 galaxies presenting a single abundance gradient, 37 galaxies exhibiting signs of an inner drop, and 26 galaxies showing a flattening in the outermost part of the discs. These numbers reflect that the existence of these features in the radial abundance distribution is very common, leaving behind the scenario where the oxygen abundance distribution of spiral galaxies was well described only by a radial negative gradient.

We derived the distribution of slopes for the abundance gradient, which presents a clear peak suggesting the existence of a characteristic gradient in spiral galaxies (first revealed by Sánchez et al. 2014). If we represent the radial abundance distribution of the whole sample together (applying a different offset to each of the individual gradients to take into account the effects of the  $\mathcal{M} - \mathcal{Z}$  relation), this characteristic gradient is clearly evident, with a slope of  $\alpha_{O/H} = -0.10 \pm 0.03 \text{ dex}/r_e$ . However, we find a small dependence of this slope with the overall shape of the radial profiles, with steepest gradients when the presence of an inner drop or an outer flattening is detected. This suggests that radial motions might be playing an important role shaping the abundance profiles and causing these features. Although future studies are needed to understand these motions and their origin, we are setting important observational constraints for theoretical works on radial migration.

The methodology developed in this analysis allowed us to study the radial position of the inner drop and the outer flattening. To our knowledge, no previous studies have carried out this type of analysis. We find that the inner drop appears at a very similar galactocentric distance for all the galaxies (approximately  $0.5 r_e$ ), while the distribution of the radial positions of the outer flattening covers a wide range of galactocentric distances (with an average position of  $1.5 r_e$ ). In this regard, we find that the radial distance at which the abundance distribution of a galaxy decays the quantity given

by the characteristic abundance gradient correlate very well with the disc effective radius. Using this new normalisation scale (the abundance scale length,  $r_{O/H}$ ), the distributions of radial positions of the inner drop and outer flattening get significantly narrower, especially in the case of the outer flattening, showing a similar radial position of these features for all the galaxies. Finally, we find a dependence of the presence and depth of the inner drop with the integrated stellar mass of the galaxies (with the most massive systems presenting the deepest abundance drop) and an absence of such dependence in the case of the outer flattening (in agreement with what found Chapter 4).

We have also performed, for the first time, an extended study analysing possible dependences of the dispersion of the abundance gradient with some galaxy properties. We find no significant dependence of the dispersion with any of the analysed parameters, deriving values that are compatible with the uncertainties associated with the derivation of the abundances. This result indicates that statistically, galaxies present a high degree of homogeneity in the abundance distribution, and the possible existing azimuthal variations do not affect significantly the general abundance gradient.

In order to test the robustness of our results, we have reproduced the analysis using two other calibrators: the one described in Dopita et al. (2016, D16); and the calibration proposed in Marino et al. (2013) for the N2 index (M13-N2). In general, we obtained a very good agreement between the results based on the three calibrators. The abundance distribution in all cases presents a characteristic slope very similar for all spiral galaxies, although the actual value changes ( $-0.20 \text{ dex}/r_e$  for D16 and  $-0.04 \text{ dex}/r_e$  for M13-N2). In addition, the stacking of the abundance distribution when normalising to the abundance scalelength  $r_{O/H}$  presents the same shape for all calibrators, deriving very similar values for the position of the inner drop and the outer flattening. The most significant difference lies on the number of inner drops and outer flattenings detected in the abundance distribution, that is reduced when using D16 and M13-N2. At this point we should bear in mind that D16 and M13-N2 are indirect calibrators not using any oxygen emission line. The main calibrator used in this thesis (O3N2) is the only one using such information available for the MUSE wavelength range. For this reason we find our results based on O3N2 more reliable than those found using the other calibrators. However, the overall distributions are rather similar in the three cases, strengthening our conclusions.

The results presented in this chapter show the potential of high resolution data in statistically significant samples to characterise the abundance distribution of spiral galaxies, proving more accurate constraints to chemical evolution models to explain the observed behaviour in our attempt to understand how discs form.

*See first, think later, then test. But always see first. Otherwise, you will only see what you were expecting. Most scientists forget that.*

— Douglas Adams



# 6

# Arm and interarm abundance gradients

## Contents

6.1	Analysed galaxies . . . . .	120
6.2	Classification and tracking of spiral arms . . . . .	121
6.3	Arm and interarm oxygen abundance gradients . . . . .	124
6.3.1	Comparison between flocculent and grand design galaxies . . . . .	124
6.3.2	Comparison between barred and unbarred galaxies	129
6.4	Possible caveats of the analysis . . . . .	131
6.5	Brief summary . . . . .	134



.....

THE SPIRAL STRUCTURE IS ONE of the most characteristic features of disc galaxies. In some cases, these patterns are well-defined, symmetric and continuous and are referred to as “grand design” spirals. In other cases, the spiral structure presents less symmetry and is formed of patchy arms that fade over the gaseous disc, leading to “flocculent” galaxies (Elmegreen 1981). This flocculent versus grand design nature of spiral galaxies must be directly connected to the mechanisms responsible for generating the spiral structure. Currently, some theories on this topic suggest that flocculent arms are typically short-lived and recurrent transient patterns associated with local density instabilities, whereas grand design galaxies are linked to the steady state density wave theory that produce long-lived quasi-stationary spiral arms (e.g. Dobbs & Bonnell 2008; Dobbs & Baba 2014). However, this question is far from being resolved.

Regardless of their origin, it is clear that spiral arms are structures where the star formation is enhanced, which may affect the chemical composition of these structures and can produce differences between the arm and interarm regions. However, only a few works have studied arm-interarm abundance variations, not observing significant variations in the gas metallicity between these two distinct regions (Martin & Belley 1996; Cedrés & Cepa 2002).

One of the main caveats of these studies to provide statistically significant conclusions is the low number of analysed objects. In this chapter, we present an extended study of a large sample of galaxies from the CALIFA survey that allows us to derive statistically significant results. For these galaxies, we analyse the oxygen abundance gradient of SF regions for both the spiral arm and the interarm areas. The main goal of this analysis is to determine if there are differences in the abundance distribution of the ionised gas associated with both structures. In addition, we also distinguish between flocculent and grand design galaxies in order to shed some light onto the origin of the spiral structure. To increase the number statistics and properly map the spatially resolved chemical abundance of the gas phase, we have carried out this study analysing the full 2D information provided by the CALIFA data avoiding any binning schemes. At the physical resolution of the CALIFA data (Mast et al. 2014), we have proved (see Chapter 4) that a spaxel-by-spaxel analysis leads to equivalent results to those obtained following the classical procedure of detecting H II regions, with the advantages previously mentioned (i.e. an improvement in the statistics and in the spatial coverage of the gas properties). The results of this analysis have been published in Sánchez-Menguiano et al. (2017).

Along the chapter, we provide a description of the subsample of galaxies used for this study (Sect. 6.1) and the procedure required to separate the information of the arm and the interarm regions and derive the oxygen abundance gradients for both structures (Sect. 6.2). Finally, the comparison of the arm and interarm abundance gradients distinguishing between

flocculent/grand design galaxies and barred/unbarred systems is given in Sect. 6.3.

## 6.1 ANALYSED GALAXIES

For a proper comparison between the abundance distribution of the SF regions belonging to the spiral arms and the interarm regions, it is essential that the analysed spaxels cover a substantial extent of the disc associated with both structures. For this purpose, we discarded from the CALIFA sample (Sect. 2.1) those galaxies for which we do not detect ionised emission associated with star formation covering a continuous and wide area of the disc (i.e. those galaxies where the fraction of non-isolated SF spaxels is lower than 15%). Afterwards, we apply another criterion to guarantee that a statistical characterisation of the arm and interarm regions is feasible (i.e. at least 20% of the SF spaxels belonging to each of both structures). Figure 6.1 shows an example of a galaxy included in this analysis (left panel) and a galaxy that has been discarded due to the low number of spaxels covering the interarm region (right panel). By applying these requirements, most of the discarded galaxies are early types (Sa-Sab), probably due to the need of a good coverage of the ionised gas throughout the disc. However, as no dependence of the abundance gradients with the morphological type has been found (see Sect 4.3), this should not affect the results.

In addition, galaxies whose spiral arms could not be properly traced because they were not clearly defined were also rejected (see Sect. 6.2 for details). These cases correspond mainly to the most flocculent galaxies of the sample, whose fragmented and blurred arms are not easy to track. As a compromise between analysing separately both flocculent and grand design galaxies and avoiding the contamination of the arms from emission coming from the interarm regions we have decided to stick to the galaxies with a clear defined spiral structure. By discarding these flocculent galaxies, we may be diminishing the possible differences between flocculent and grand design systems. However, the qualitative results should not change. To our knowledge, this is the most complete comparison between flocculent and grand design galaxies analysing their abundance distribution up to date.

In the end, the sample analysed in this study comprises 68 galaxies that provide a good 2D coverage of the SF regions over the disc and a good characterisation of both the arm and interarm regions. For this sample of galaxies we carry out a detailed 2D study of the gas metallicity distribution to analyse possible differences between the SF regions found in the spiral arms and those located in the interarm regions.

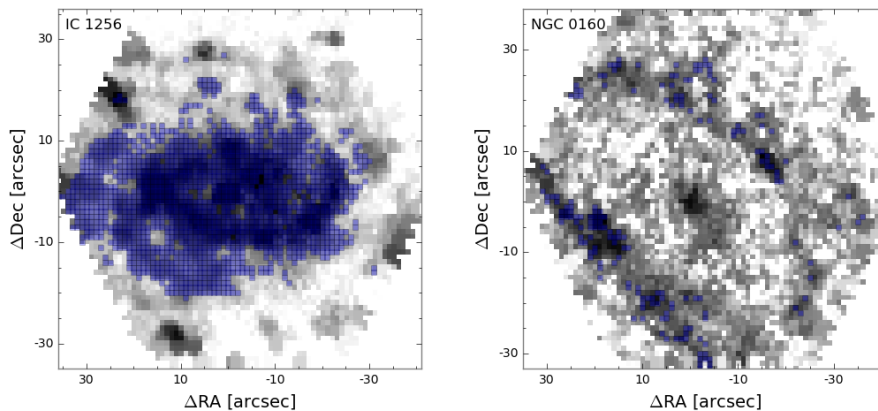


**Figure 6.1:** Location of the spaxels associated with SF regions (blue squares) superimposed on the IFS-based  $H\alpha$  map derived for two CALIFA galaxies, one included in this analysis (IC 1256, left), and another that was discarded because of poor spatial coverage of the SF spaxels across the galactic disc (NGC 0160, right).

## 6.2 CLASSIFICATION AND TRACKING OF SPIRAL ARMS

The classification between flocculent (with small, patchy spiral arms) and grand design (long, symmetric, continuous arms) galaxies (see Sect. 1.1.1 for details) was carried out independently by 14 people based on a visual inspection of the SDSS  $g+u$  deprojected images<sup>1</sup>, where the spiral arms are more easily outlined. We considered a classification to be valid when at least eight people agree on the result, in all other cases the classification was considered ambiguous and the galaxy was discarded from further analysis. This way, the sample was reduced from 68 to 63 (discarding IC 1256, NGC 0477, NGC 1093, NGC 7321 and UGC 09476), of which 45 galaxies are classified as flocculent and 18 as grand design. Table A.1 of Appendix A shows the final classification for all galaxies in the sample used in this analysis and Fig. 6.2 presents a set of example images corresponding to flocculent (F) and grand design galaxies (G).

Once we have classified the galaxies, we depict the spiral arms by visually tracing them on the SDSS  $g$ -band deprojected images to distinguish between the spaxels belonging to the spiral arms and the interarm regions. Then we interpolate the points using a cubic spline (a numeric function that is piecewise-defined by a third-degree polynomial). In the cases where the spiral arms are not continuous, the distinguishable fragmented parts are outlined. The top left panel of Fig. 6.3 shows the spline fit of the detected spiral arms (black lines) superimposed on the SDSS image of NGC 0257. Once the spiral arms are traced, we assign them a width of 4 arcsec (see

<sup>1</sup>Using the seventh data release (DR7, Abazajian et al. 2009).

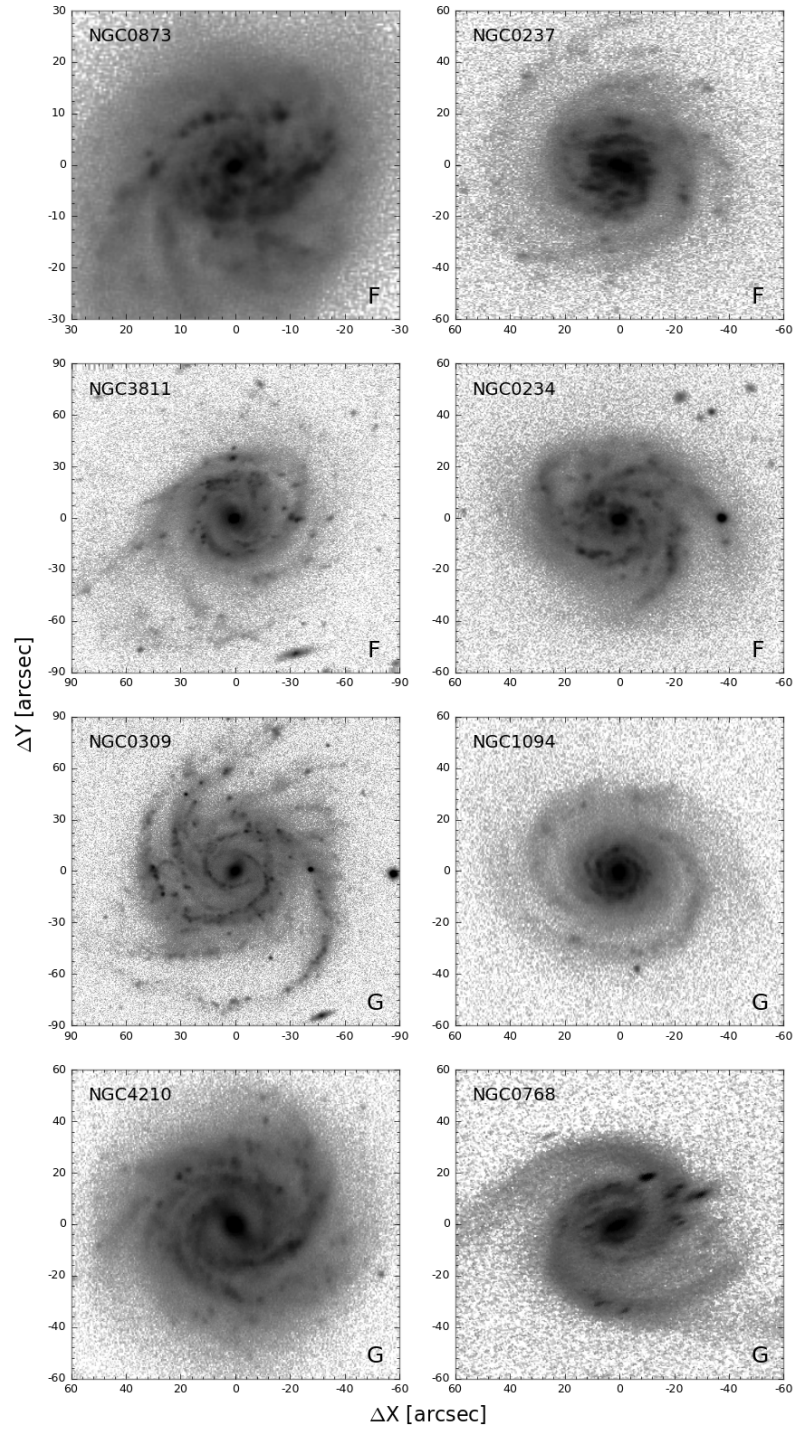


**Figure 6.2:** *Deprojected SDSS  $g + u$  maps for eight galaxies showing the arm classification ( $F$  for flocculent and  $G$  for grand design, see bottom right corner of each image).*



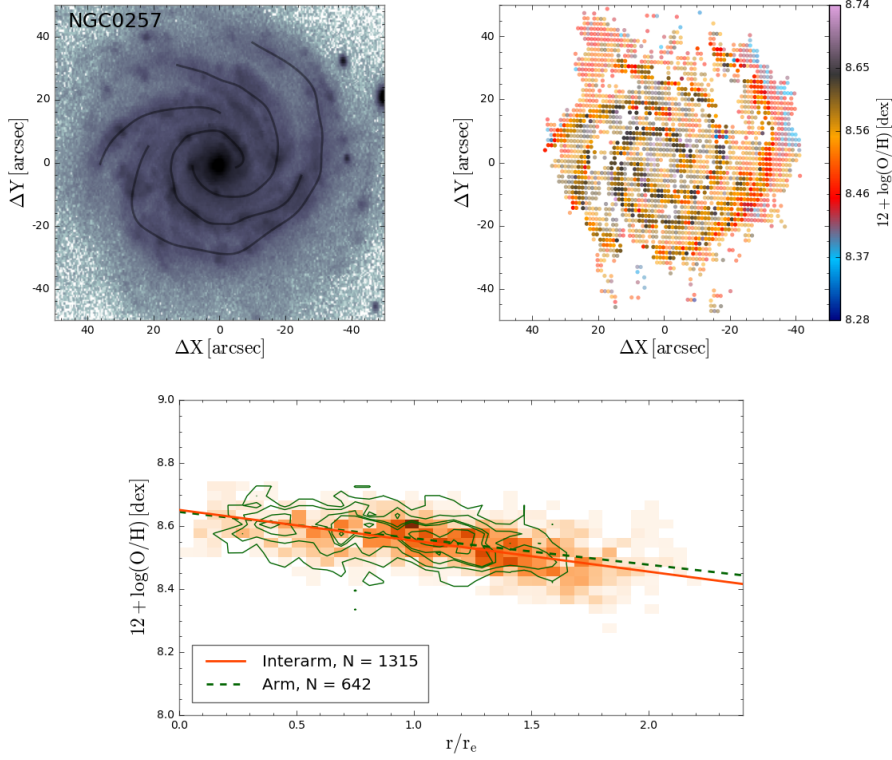


**Figure 6.3:** *NGC0257. Top left panel: Outline of the spiral arms on the deprojected SDSS g-band map. Top right panel: Colour map of the oxygen abundance distribution of the spiral arms (opaque dots) and the interarm region (transparent dots). Bottom panel: Radial density distribution in the oxygen abundance-galactocentric distance space of the spaxels located in the spiral arms (green contours) and those associated with the interarm region (orange colour map). The outermost contour encircles 100% of the total number of spaxels, decreasing by 20% in each consecutive contour. The lines represent the error-weighted linear fit derived for the arm (green dashed line) and interarm (orange solid line) distributions.*

Sect. 6.4 for an explanation of the possible effects on the results obtained using different arm width values), considering as spaxels belonging to the spiral arms those that are at a distance from the closest point of the arm (cubic spline function) of less than 2 arcsec. Thus, we consider that the remaining spaxels are associated with the interarm regions. The top right panel of Fig. 6.3 shows the distinction of the arm and interarm spaxels in an oxygen abundance distribution colour map, respectively represented as opaque and transparent dots.

This procedure has been used in previous works and has been proven successful in tracing other morphological features such as dust lanes in galactic bars (Sánchez-Menguiano et al. 2015).

### 6.3 ARM AND INTERARM OXYGEN ABUNDANCE GRADIENTS

To derive the radial gradients of the oxygen abundance for the arm and the interarm regions of each galaxy we have normalised the deprojected galactocentric distance (see Sect. 3.4 for details on the derivation of the deprojection angles) for the spaxels to the disc effective radius ( $r_e$ , see Appendix A of Sánchez et al. 2014 for details on the computation of this parameter). Then we performed an error-weighted linear fit to the derived oxygen abundance values (see Sect. 3.3) between 0.5 and 2.0  $r_e$ . We excluded the inner- and outermost regions, due to trends that deviate from the pure oxygen decrease (an inner drop and an outer flattening, see Sect. 4.5 for more information). In general, for each galaxy we have approximately 400 arm SF regions and 1200 interarm SF regions that contribute to the derivation of the corresponding gradients, i.e. that are located in the radial range between 0.5 and 2.0  $r_e$ .

In the bottom panel of Fig. 6.3 we present an example of the abundance profiles of the arm (green dashed line) and interarm regions (orange solid line) derived for the galaxy NGC 0257. The radial oxygen distribution for interarm regions is shown as an orange colour map and the distribution for the spiral arms is shown as a green contour map.

#### 6.3.1 COMPARISON BETWEEN FLOCCULENT AND GRAND DESIGN GALAXIES

The main goal of this analysis is to find possible differences in the chemical composition of the ionised gas associated with the arm and interarm regions in order to shed some light on the origin of the spiral structure. We distinguish between flocculent and grand design galaxies as the differences observed in the spiral pattern may be the result of different formation processes of the spiral structure.

Figure 6.4 shows the outcome of the comparison of the derived gradients for the arm and interarm regions for all the individual galaxies. The top panels show the relation between the slope values (left), the zero-points (middle), and scatter (right) of the linear fits. The scatter is measured as the standard deviation of the differences between the observed abundances and the corresponding values from the linear regression according to their deprojected galactocentric distances. These parameters are provided in Table A.2 of Appendix A. Flocculent and grand design galaxies are represented by green and purple markers, respectively. We can see that for both distributions the values are slightly shifted from the one-to-one relation represented by the dashed grey lines, especially in the case of the dispersion. These deviations are observed mostly for the flocculent galaxies. However, we note the

lower number of grand design systems (18) compared to the flocculent ones (45), which prevents us from reaching any strong conclusion about these types of spiral galaxies.

To show these differences more clearly, we represent in the bottom panels of Fig. 6.4 the distributions of the differences in slope values (left), zero-points (middle), and dispersions (right) between the arm and interarm regions divided by the quadratic sum of the errors. The shown distributions are not smoothed. They correspond to a density estimator in which each point is represented by a Gaussian distribution, centred in the actual value of the point, and with a sigma of the maximum distance between nearest neighbours. In this way by summing all the individual Gaussians we reproduce a smooth distribution (normalised to one) which is more peaky in the clustered points. The modal value of the differences between arm and interarm found for flocculent (grand design) galaxies are  $\sim 0.013$  dex/ $r_e$  ( $\sim 0.015$  dex/ $r_e$ ) for the slope,  $\sim 0.011$  dex ( $\sim 0.003$  dex) for the zero-point, and  $\sim 0.003$  dex ( $\sim 0.003$  dex) for the scatter in the linear fit. As can be inferred from these numbers, the observed differences are small. However, all of them are above  $1\text{-}\sigma$  (close to  $2\text{-}\sigma$  for some of them, see bottom panels of Fig. 6.4), indicating that these differences are not due to the uncertainties in the derivation of the parameters.

We performed a Student's  $t$ -test for each of the six distributions to analyse whether these differences between the arm and interarm abundance distributions are statistically significant. In these tests, we compare the observed distributions (position of the peak and width) with a hypothetical Gaussian centred at zero (dashed vertical lines) and with a width of unity which represents the case where no differences are found between the arm and the interarm regions. The resulting p-values of these statistical tests are shown in the top left corner of the bottom panels of the figure. For flocculent galaxies, these p-values are below the significance level of 5% (2% in the slope, 1% in the zero-point and exactly 5% in the scatter), confirming that the observed differences are statistically significant. In the case of the grand design galaxies, the p-values are above the significance level for the slope and zero-point comparison (13% and 77% respectively) and below it for the scatter (4%). This indicates that only the differences in the scatter with respect to the linear fit are statistically significant for these galaxies. However, again, we must be careful with the conclusions we obtain for the analysis of the grand design galaxies because of the low number statistics of these systems in the sample. The inclusion of more grand designs is needed to confirm the results of the Student's  $t$ -test on these galaxies.

The right panels of Fig. 6.4 show that in general the scatter of the oxygen abundances is higher in the interarm regions than within the spiral arms for both flocculent and grand design galaxies. We checked that these results do not rely on the use of a larger number of spaxels belonging to the interarm

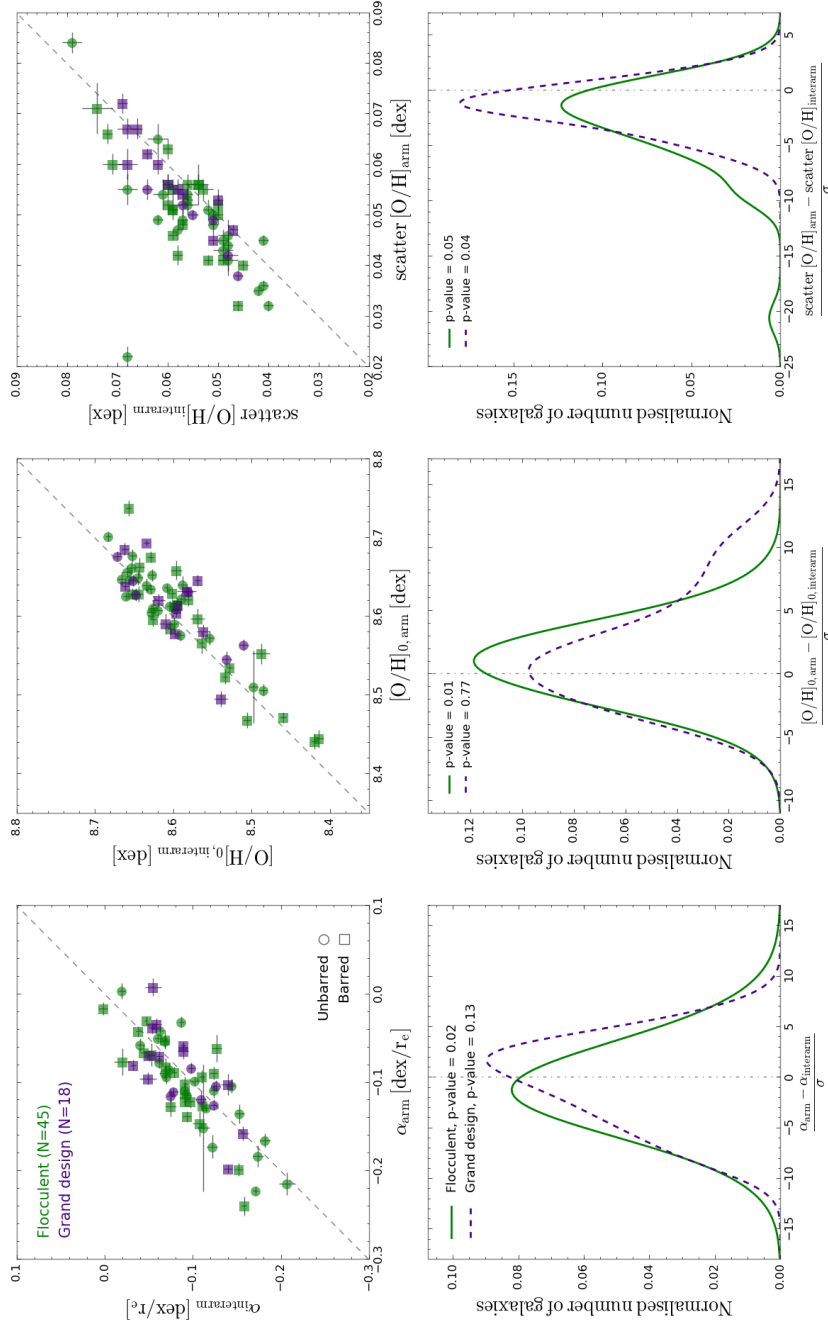


**Figure 6.4:** Top panels: Relation between the slope (left), zero-point (middle) and scatter (right) values of the arm (x-axes) and interarm (y-axes) abundance gradients for flocculent (green) and grand design (purple) galaxies. The dashed grey lines represent the 1:1 relation. Bottom panels: Normalised distributions of the differences in the three mentioned parameters between the arm and interarm regions divided by the quadratic sum of the errors for flocculent (green solid) and grand design (purple dashed) galaxies. The dashed dotted grey lines correspond to the case where no differences are found. The results of the t-tests are shown in the top left corner of the panels (see text for details).

regions. We randomly selected from the spaxels of the interarm area a subsample of equal size to the arm area, and performed the derivation of the dispersion with this subset of spaxels. The conclusion is the same: the interarm regions present higher scatter in the abundance values than the arm regions with respect to the negative gradient. This is an indicator that spirals are important drivers of mixing in galactic discs via the gas shocks that they induce, and maintain a nearly homogeneous chemistry along the streamlines of the gas. However interarm gas is polluted stochastically by young stars forming in situ, leading to an increased scatter.

The 2D coverage of the CALIFA data allows us to assess whether this scatter is the same in the whole interarm region or if there is a dependency on the angular distance from the arms. With this purpose we separate the spaxels of the interarm regions in three groups according to the distance to the closest arm, region 1 being the closest to the spirals and region 3 the farthest away. Region 2 is an intermediate region between 1 and 3. Using only the spaxels belonging to each of these regions we derive the scatter with respect to the linear regression in a similar way as done for the entire interarm region (top right panel of Fig. 6.4). The outcome of this test is shown in Fig. 6.5 for flocculent (left panel) and grand design (right panel) galaxies. Each point represents the scatter of the SF regions within the corresponding interarm region (green for region 1, blue for region 2, and red for region 3) for a particular galaxy. The scatter for the SF regions within the spiral arms is also represented for a better comparison (grey markers). The black diamonds represent the mean values within each region; the error bars indicate the standard deviations. The distribution of values for each region is represented in the right auxiliary panels. For flocculent galaxies, we see that the mean value of the scatter (black diamond) increases when moving away from the spiral arms. However, for grand design galaxies the scatter is larger when moving from region 1 to 2, but if we get a bit farther away (region 3) then it decreases again, indicating that there is no trend of increasing the scatter when moving away from the arms.

These results agree with the current interpretation of some spiral structure theories, according to which the spiral arms of flocculent galaxies are generated by density variations driven by local instabilities, while in grand design galaxies the spiral arms are caused by quasi-stationary density waves (Dobbs & Baba 2014). The fact that grand design galaxies do not exhibit statistically significant differences in the abundance distribution between the arm and interarm regions (see Fig. 6.4) is in agreement with the presence of density waves that affect the gas content of the entire galaxy as these features move across the disc. In addition, the fact that the scatter in the oxygen abundances does not depend on the distance to the spiral arms for grand design systems supports this idea (see Fig. 6.5). The regions closest to the spiral arms change as the density waves move across the galaxy discs

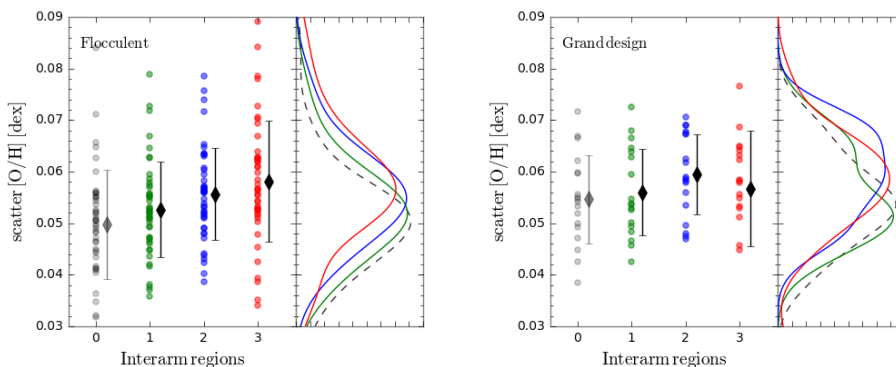


**Figure 6.5:** *Distribution of the scatter of the oxygen abundances in the interarm regions according to the angular distance to the spiral arms for flocculent (left panel) and grand design (right panel) galaxies. Region 0 (grey) represents the arm region. Region 1 (green) is the interarm region closest to the spiral arms and region 3 (red) is the farthest away. Region 2 (blue) represents an intermediate region between 1 and 3. Each point represents the scatter of the SF spaxels within the corresponding interarm region for a particular galaxy. The black diamonds represent the mean values within each region; the error bars indicate the standard deviations. We also show the distribution of values for each region in the right auxiliary panels.*

and this makes the scatter similar in the whole interarm region. On the other hand, in flocculent galaxies, density variations produced by local instabilities only affect specific locations of the discs associated with the spiral arms, making the gas content of these regions (and therefore the chemical composition) different from that found in the interarm regions. The fact that the differences found in this work for these galaxies are small can be explained taking into account that these local instabilities are not static, but are continuously formed and destroyed across the disc, not affecting the same material over a long period of time. In this case, during the lifetime of the spiral arms, the closest areas to them are always the same and, because they are affected by the presence of the arms, due to their proximity, the scatter is lower (as occurs within the spiral arms but to a lesser extent). As we move away from the arms, the gas is less affected by the mixing of the arms and the scatter increases.

Although our results can be explained by this difference in the origin of the spiral structure, other alternative interpretations are also possible. In fact, it is plausible that both flocculent and grand design galaxies are the result of the same mechanism generating the spiral structure. In that case, the differences found in the abundance distribution between the arm and interarm regions in flocculent galaxies (see Fig. 6.4) can be explained simply because the gas outside the spirals is stochastically polluted more than in the grand design galaxies where the star formation is more concentrated in the spiral arms. This could also be the reason why the metallicity scat-

ter increases with increasing distance from the spiral in flocculent galaxies, whereas no statistically significant difference in the scatter of interarm gas by location is found for grand design galaxies (Fig. 6.5). Another explanation for the differences found between flocculent and grand design galaxies is that in grand design spirals the gas mixing could be more efficient. However, we find that the scatter in grand design galaxies is on average higher than in flocculent galaxies (in the arm and in the interarm regions, see Fig. 6.5), allowing us to rule out this interpretation.

### 6.3.2 COMPARISON BETWEEN BARRED AND UNBARRED GALAXIES

Apart from the comparison between flocculent and grand design galaxies, we performed the same tests dividing the sample into barred and unbarred systems. This comparison is shown in Fig. 6.6; as in the previous case, the barred and unbarred galaxies are represented by blue and orange colours, respectively. In this case we have a similar number of barred (34) and unbarred (29) galaxies. The average absolute differences found for unbarred (barred) galaxies are  $\sim 0.005$  dex/ $r_e$  ( $\sim 0.020$  dex/ $r_e$ ) for the slope,  $\sim 0.006$  dex ( $\sim 0.016$  dex) for the zero-point, and  $\sim 0.005$  dex ( $\sim 0.001$  dex) for the scatter in the linear fit. The performed t-tests yield p-values for unbarred galaxies that are clearly above the significance level of 5% in the slope and the zero-point (around 40% and 30%, respectively), but below it in the scatter (1%), indicating that the only significant differences are found between the arm and interarm abundance gradients regarding the scatter for these unbarred systems. On the other hand, small differences are obtained for the barred galaxies (p-values of 0.3% and 1% respectively) in the slope and zero-point of the gradients. No statistically significant differences are found in the scatter of the oxygen gradient between the arm and interarm distributions for the barred galaxies.

This analysis shows that only barred galaxies present (small) differences in the radial oxygen abundance distribution between the arm and interarm regions. We have to be cautious with this conclusion as these differences are even more subtle than those found for flocculent galaxies. Again, an extended study with more galaxies (and better spatial resolution) is necessary to confirm these preliminary results. Despite these caveats, this result may suggest that the presence of a bar induces differences in the abundance distribution of the spiral galaxies. Bars have been proposed as a key mechanism in the dynamical evolution of disc galaxies. For instance, recent numerical simulations from Di Matteo et al. (2013) have shown that radial migration induced by a bar leads to significant azimuthal variations in the metallicity distribution of old stars. In Chapter 7, we will show that radial migration can also affect the gas metallicity distribution producing differences in the abundance distribution of the spiral arms; however, these differences do not

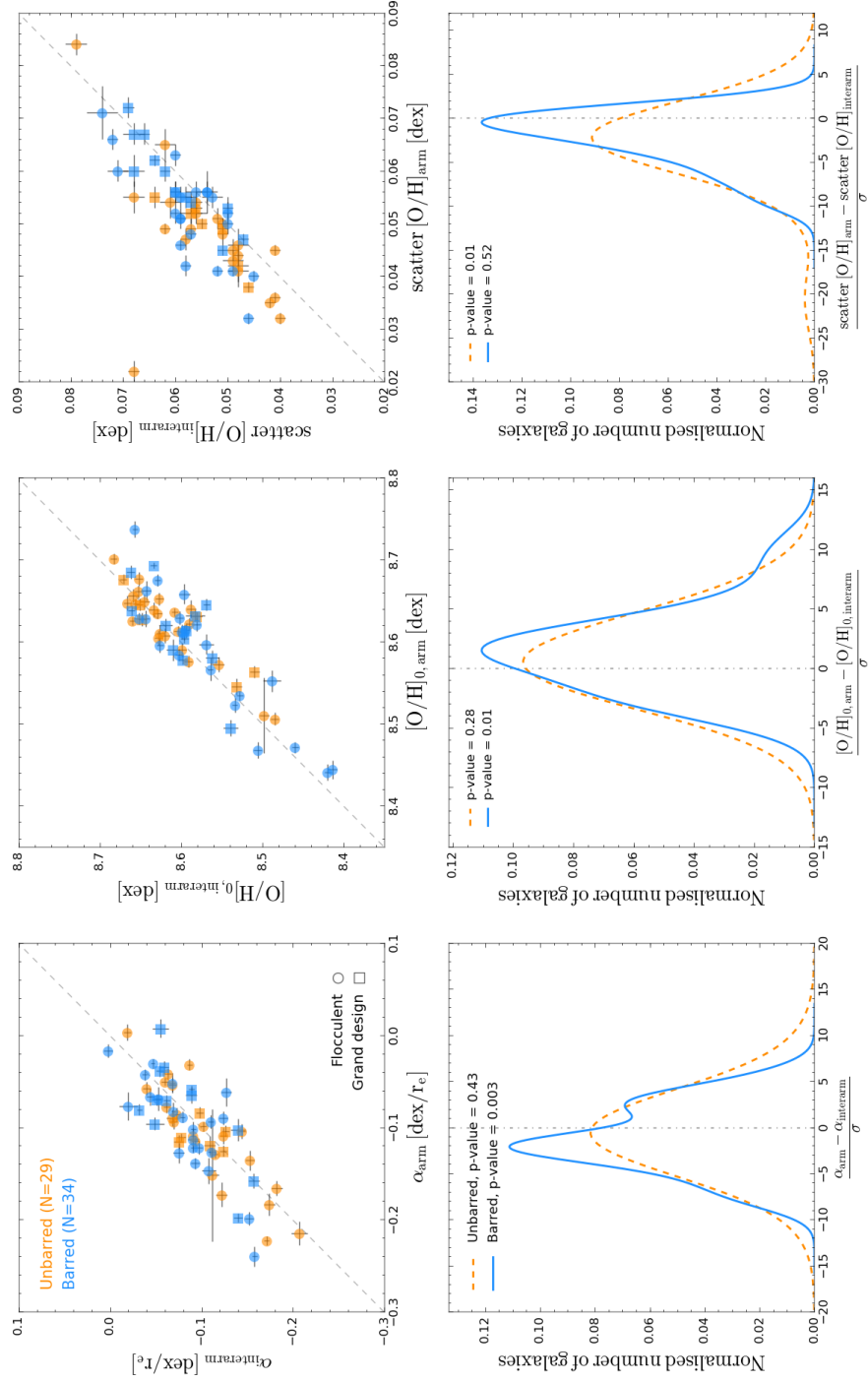


**Figure 6.6:** Same as Fig. 6.4 but distinguishing between barred (blue markers and solid histograms) and unbarred (orange markers and dashed histograms) galaxies. See caption above for more details.



seem to affect the overall abundance gradient for the gas (see Sect. 4.3; Sánchez et al. 2014; Marino et al. 2016) or for the stars (Sánchez-Blázquez et al. 2014).

## 6.4 POSSIBLE CAVEATS OF THE ANALYSIS

The derived results in this study rely strongly on a good arm classification of the galaxies. For this reason, in order to confirm the strength of the results, we have repeated the previously described analysis considering this time only the galaxies for which at least 75% of the classifiers (10 out of 14) agree on the spiral classification. This way, with a reduced sample of 41 galaxies (30 flocculent and 11 grand design) we obtain qualitatively equivalent results.

Another aspect of this analysis that could affect the results is the distinction between the arm and the interarm regions. As stated in Sect. 6.2, we selected a width of 4 arcsec to derive the arm abundance distribution. This value was chosen by visually examining the SDSS  $g$ -band images of the galaxies. As all the galaxies in the sample are located at a similar redshift, we selected an average width of the arm (measured in arcsec) that corresponds approximately to the same physical width for all of them ( $\sim 1.5$  kpc). We checked whether using the same value for the arm width along the arm extension and for all the galaxies is a good approximation. To this end, we show in Fig. 6.7 a perpendicular cut to the arm at three different positions on the deprojected SDSS  $g$ -band images of the galaxies. At the position of the arm centre the flux profile (blue solid line) presents a bump, due to the presence of the arm. Fitting a Gaussian (red solid line) and measuring the FWHM we can estimate the arm width (the value is given in the bottom of the panels). Performing this test for some galaxies with well-defined spiral arms, we find that there is neither a significant dependence of the arm width on radius nor between galaxies. We find that on average, a 4 arcsec-width is representative of this sample. We also performed several tests regarding the effect of using other values of the arm width in the analysis. If we use a width of 2 arcsec we obtain similar results. As we increase this value, the observed differences begin to disappear. When we reach a value of 8 arcsec, these differences become statistically insignificant according to the  $t$ -tests. This result is expected; by increasing the arm width, we include more SF regions belonging to the interarm regions in the analysis and the differences are diluted.

The arm abundance distribution for each galaxy is determined considering the spaxels belonging to all the traced spiral arms together. This increases the number statistics of the arm region, and significantly improves the radial coverage, which in some cases is very limited for individual arms.

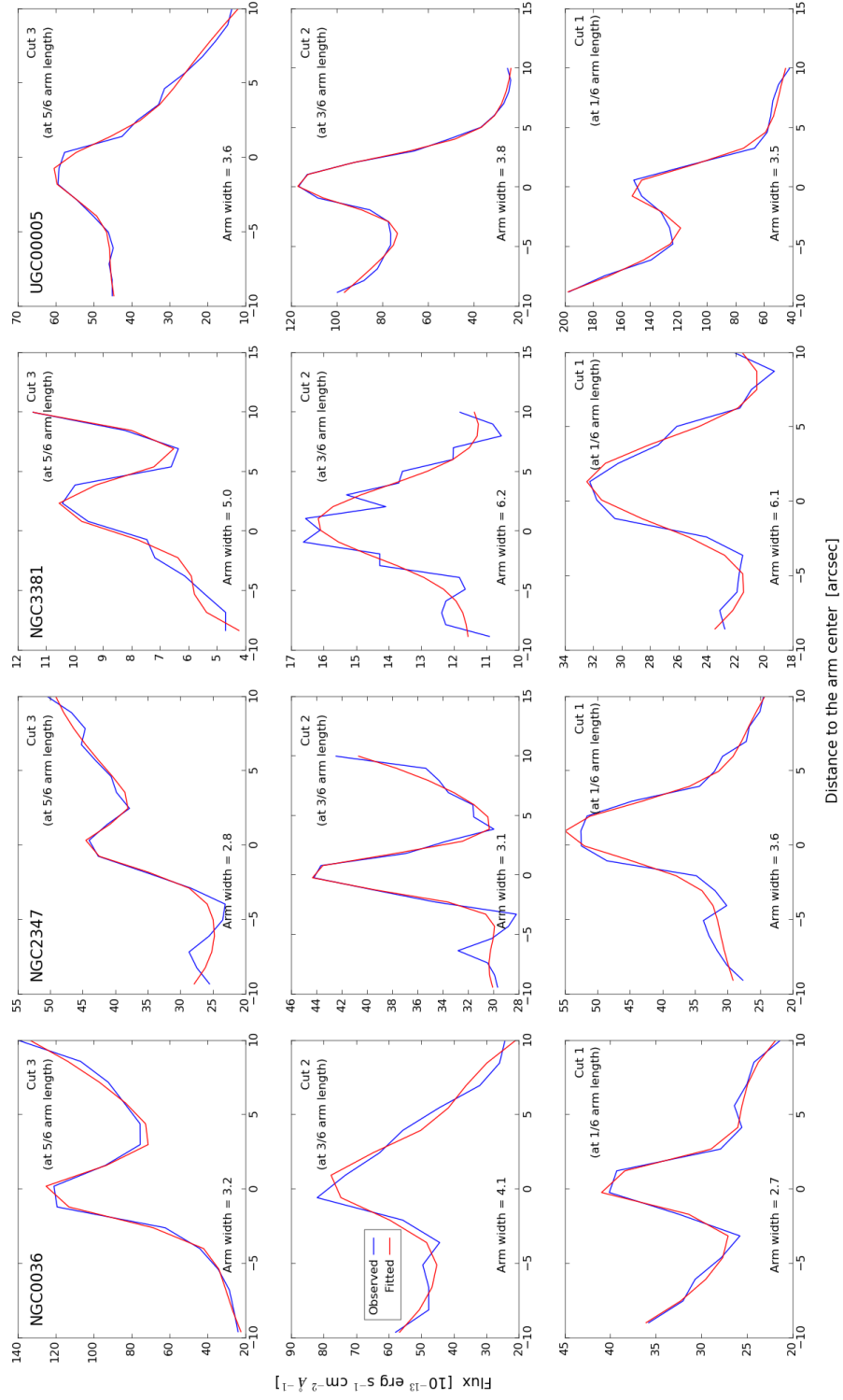


**Figure 6.7:** Perpendicular cut to the spiral arm at three different positions on the deprojected SDSS *g*-band images for four galaxies of the sample. The value of the arm width is given in the bottom of the panels. See text for details.

However, by considering all the spaxels associated with the spiral arms together we are assuming that the physical conditions of the H II regions belonging to the spiral arms do not depend on their association with a particular arm (if no external factors such as a recent merging that can produce differences in the abundance distribution are involved), which is not a strong assumption since the spiral arms are supposed to form a single structure with a common origin. A similar reasoning leads us to group all the spaxels not belonging to the spiral arms together, which we call the interarm region.

The results of this analysis may also be affected by the required S/N of the emission lines involved in the oxygen derivation. In principle, the reliability of the derived oxygen abundance for each spaxel, and thus that of the derived gradients, might improve with a higher S/N cut. However, a general  $3\text{-}\sigma$  cut in all the analysed lines hampers the recovery of the abundance gradient in some galaxies due to a poorer spatial coverage of the oxygen distribution, especially for the outermost interarm regions. For this reason we prefer to use the  $1\text{-}\sigma$  flux cut (see Sect 3.2.2) as this improves the statistical significance of the results. So far this is the best compromise between having a good S/N for all the emission lines and a good coverage of the oxygen abundance distribution together with a large number of analysed galaxies. Moreover, in Chapter 4 we already showed that a  $1\text{-}\sigma$  cut is enough to reproduce the radial trends of the gas-phase oxygen abundance from H II regions. However, considering that in this analysis we are going a step further by comparing the abundance distribution between the arm and interarm regions, we also assess how this cut affects our results. Applying a  $3\text{-}\sigma$  cut reduces the number of galaxies for which we cover a substantial radial range to accurately derive the abundance gradient. Despite the loss of eight flocculent galaxies and the general decrease in the number of the spaxels analysed (especially for the interarm region) in each galaxy, the results point to the same conclusions. The most significant difference is seen when analysing the scatter around the abundance gradient for the grand design galaxies, which now present a similar scatter in the arm and the interarm regions. However, this is somewhat expected since we have reduced the number of spaxels located in the interarm regions. This effect is especially significant in the grand design galaxies where the gas is more concentrated in the spiral arms. The agreement we find supports our methodology and strengthens our conclusions, and therefore we consider that the adopted flux cut is a valid selection criterion.

It is beyond the purpose of this work to make a detailed study of the effects of using different empirical calibrators in the analysis. However, to confirm our results, we have also derived the oxygen radial distributions using some of the most commonly used empirical calibrators: the Pilyugin et al. (2010) calibration for the ONS index and the Dopita et al. (2013) calibration based on the MAPPINGS IV code developed by the authors

(called ‘pyqz’). Qualitatively equivalent results have been found when using the pyqz calibrator. However, in the case of the ONS indicator, only the results regarding the scatter relative to the gradient, which are the largest differences found in the analysis, are compatible. The differences in the slope and zero-point values, which are of the order of  $2\text{-}\sigma$ , are diluted owing to the larger errors associated with the ONS calibrator (approximately three times the errors derived with O3N2). Calibrators based on R23 like ONS are affected by well-known problems (non-linear dependence on O/H; larger errors associated with [O II]  $\lambda 3727$  due to the spectrophotometric calibration of CALIFA data, Sánchez et al. 2012a; need to correct for dust attenuation due to the distance in wavelength between the involved lines, etc.); instead, calibrators based on O3N2 index are not affected by these factors, which makes the Marino et al. (2013) calibrator able to distinguish between the arm and interarm abundance distributions with greater precision.

## 6.5 BRIEF SUMMARY

The existence of a radial decrease in the gas chemical abundances of spiral galaxies was well established by observations decades ago (e.g. Searle 1971; Martin & Roy 1992; Kennicutt et al. 2003; Pilyugin et al. 2004; Rosales-Ortega et al. 2011; Bresolin et al. 2012; Marino et al. 2012; Sánchez et al. 2012b, 2014), supporting the inside-out scenario for disc evolution. However, only a few works have studied possible azimuthal differences in the derived gradient associated with the presence of the spiral structure, which is still an open question.

In this work we have carried out a study of the arm and interarm abundance distributions in a sample of 63 CALIFA spiral galaxies performing a spaxel-by-spaxel analysis. We distinguish between flocculent and grand design galaxies in order to better understand the origin of the spiral structure. For this purpose, we have derived oxygen abundance gradients for both distributions (arm and interarm), to compare the characteristic parameters of the profiles (slope, zero-point, and dispersion) between them. We have also distinguished between barred and unbarred galaxies to assess the effect of the presence of bars in the abundance distribution.

To our knowledge, this is the first observational work finding differences between the gas abundance of spiral arms and interarm regions using a large sample of galaxies. Our analysis yields differences that are subtle and statistically significant only for flocculent galaxies. On average, we find that the ionised gas in the interarm regions of these subgroups of galaxies presents a shallower gradient with a lower zero-point value and a larger dispersion in the oxygen abundances. Furthermore, we find that for flocculent galaxies this dispersion correlates with the angular distance to the spiral arms: the


farthest spaxels present the larger scatter. Grand design galaxies, on the other hand, do not seem to present any trend in the dispersion with the distance to the arms. This result suggests that the mechanisms generating the spiral structure in these galaxies may be different to those producing grand design arms. Another possibility is that these differences may be due to a higher star formation *outside* the spiral arms for the flocculent galaxies and a more concentrated star formation in the spirals for the grand design ones. The small differences between the arm and the interarm abundance distributions found in barred galaxies suggests that bars may have a direct effect on the chemical distribution of these galaxies, even though these differences are not reflected in the overall observed abundance distribution.

The extension of this analysis to a larger sample of galaxies with data of higher quality in terms of spatial resolution and S/N per spatial unit is needed to confirm these results. As a preliminary result, this work finds that bars and flocculent arms are two independent mechanisms that generate differences in the abundance distribution between the spiral arms and the interarm regions. So far, this is the first observational work finding such differences in isolated galaxies.



*Everything has a natural explanation. The moon is not a god, but a great rock, and the sun a hot rock.*

— Anaxagoras



# Non-radial variations of the abundance distribution

## Contents

7.1	Analysed galaxies . . . . .	140
7.2	Local abundance variations . . . . .	141
7.2.1	2D residual abundance maps . . . . .	143
7.2.2	Correlation with light residuals . . . . .	143
7.2.3	Dependence on galaxy properties . . . . .	144
7.3	Azimuthal variations: The case of NGC 6754 . . . . .	150
7.3.1	Residual abundance and velocity maps . . . . .	150
7.3.2	Azimuthal residual abundance and velocity profiles	153
7.3.3	Comparison with simulations . . . . .	155
7.3.4	Radial migration in NGC 6754 . . . . .	156
7.4	Brief summary . . . . .	159





.....

THE MOST CHARACTERISTIC trend observed in the oxygen abundance distribution of spiral galaxies is the radial negative gradient associated with the inside-out growth of the discs. However, in the radial abundance analyses carried out in Chapters 4 and 5, deviations with respect to this simple scenario affecting the abundance profiles in both the innermost and outermost regions of galaxies were reported.

Besides this radial profile, the effect of mechanisms related to the dynamics of the discs like the presence of structures such as spiral arms and bars, the stochasticity of star formation, the gas accretion from satellite or minor mergers, the local enrichment of regions by supernovae and other sources of metals, can produce non-radial variations of the abundance distribution. Although there are some mixing processes that can blur these inhomogeneities (such as interstellar turbulence or super-shell expansions of supernova remnants, Roy & Kunth 1995), their time-scales are still large enough as to allow the persistence of these variations for long periods of time (Roy & Kunth 1995; Scalo & Elmegreen 2004). Therefore, it is expected to observe some degree of chemical inhomogeneity.

Other source of deviations from the radial pattern could be the presence of azimuthal variations induced by radial migration as recently proposed in simulations of spiral galaxies (Di Matteo et al. 2013; Grand et al. 2016). Although these predictions were focused on the stellar component, it is known that both gas and stars are affected by these movements (e.g. Minchev et al. 2014; Grand et al. 2015). Indeed, streaming motions of gas along the spiral arms have been proposed (Grand et al. 2015; Baba et al. 2016), which could produce azimuthal variations of the gas abundance.

In this regard, the arm/interarm analysis carried out in Chapter 6 using CALIFA data revealed the existence of non-radial abundance variations related to the presence of spiral arms (in particular, flocculent ones) and bars. However, the reported differences were very subtle, being possible that the spatial resolution of CALIFA data may be blurring their detection. Therefore, the use of higher quality data in terms of spatial resolution and S/N per spatial unit can help us to be more sensitive to their presence.

This type of data is currently at our disposal with the advent of new instruments such as MUSE. Consequently, it has not been until recently that systematic azimuthal variations of the gas oxygen abundance distribution have been measured (Ho et al. 2017; Vogt et al. 2017), always focused on the study of individual galaxies.

In this chapter, we take advantage of the high spatial resolution of the AMUSING data to address the possible deviations of the abundance distribution with respect to the already analysed radial profile (see Chapters 4 and 5). We study the existence of local abundance variations and, if existing, their possible association with any galaxy structure. This first part of the study has been performed for a large sample of galaxies (Sec.7.1) and

preliminary results are shown here for the first time (Sect. 7.2). In addition, we also analyse the presence of azimuthal patterns in the abundance distribution associated with dynamic effects. For this latter part (Sect. 7.3), we have developed a methodology that has been applied to one galaxy of the sample, NGC 6754, that presents some of the highest local abundance variations measured in the sample, and that has shown hints of radial migration producing azimuthal variations (Sánchez et al. 2015). The study of NGC 6754 has been published in Sánchez-Menguiano et al. (2016a).

## 7.1 ANALYSED GALAXIES

The 102 spiral galaxies comprising our AMUSING sample (defined in Sect. 2.2.1) were perfectly suitable to carry out the radial abundance distribution analysis shown in Chapter 5. However, in order to perform a 2D study on a spaxel-by-spaxel basis seeking for possible local variations, we need to be more restrictive in the sample selection to guarantee a suitable characterisation of the distribution.

For this purpose we discard those galaxies from the AMUSING sample that present a deprojected disc radius smaller than  $\sim 30''$ , as they do not exhibit the high physical spatial resolution needed to detect non-radial variations of the abundance distribution (considering the overall redshift range of these galaxies, see Fig. 2.4). In addition, galaxies for which the analysed spaxels associated with SF regions (see Sect. 3.2.2 for information) provide visually a poor spatial coverage of the disc (patchy and discontinuous) are also discarded.

Finally, we need to consider the technical difficulties of a spaxel-by-spaxel analysis for the AMUSING sample. As described in Sect. 3.2.2, the spaxel size of this dataset ( $0.2''$ ) may allow us to resolve the ionised structure of the H II regions in some galaxies, depending on the atmospheric seeing during the observations and the redshift of the object, for which the empirical calibrators used to derive the oxygen abundances can not be applied (López-Hernández et al. 2013; Terlevich et al. 2014). In those cases, we have to degrade the data to reach a physical spatial resolution of the order of the typical size of an extragalactic H II region (around 400 pc). For this, we perform a spatial binning (squared bins) in order to have a final spatial unit of  $\sim 400$  pc. However, the physical coverage for some galaxies is of the order of a few dozens of kiloparsecs, and thus, its 2D abundance distribution is blurred when degrading the data. For this reason, we establish an upper limit for the size of the bins of  $10 \times 10$  pixels (which is equivalent to a cut in the original physical resolution of  $\sim 140$  pc). All the galaxies that need a larger size of the bins to reach the desired final resolution are therefore discarded from the sample.

All these new selection criteria reduce significantly the galaxies for which this analysis is feasible. In the end, the sample analysed in this study comprises 24 galaxies that provide a good 2D coverage of the ionised gas associated with SF regions over the galaxy disc.

## 7.2 LOCAL ABUNDANCE VARIATIONS

For the final sample of 24 galaxies, the 2D abundance distributions were derived on a spaxel-by-spaxel basis following the procedure described in Chapter 3. In some cases, we make use of the original abundance maps (galaxies presenting a lower spatial resolution). For those galaxies presenting a higher spatial resolution, the flux intensity maps provided by FIT3D (see Sect. 3.2.2) have been degraded to a final physical resolution of  $\sim 400$  pc (see above). Figure 7.1 shows the 2D abundance distribution of one galaxy of the sample, NGC 1762 (middle left). The remaining panels show different plots that will be described along this section. The corresponding figures for the rest of the sample are provided in Appendix D.

We can see clearly in the 2D abundance map of NGC 1762 a radial decline in the abundances, with the highest values (red colours) located in the inner parts of the disc and the lowest ones in the outermost regions (blue colours). In order to highlight the possible non-radial variations of the abundances, the characteristic radial profile (already described in Chapters 4 and 5) has been removed. The so-called abundance residual map is therefore derived by subtracting the azimuthally averaged radial abundance to the observed distribution. These averaged values are measured as the median of the abundances in annuli of  $0.2''$ .

In the case where the oxygen abundance distribution of a spiral galaxy is well described simply by its radial profile, the residual values should follow a Gaussian distribution centred at zero, with a width given by the uncertainties in the derivation of the abundances. The bottom left panel of Fig. 7.1 shows the histogram of residual abundances for NGC 1762. A Gaussian function is fitted to this distribution (black solid line). As opposite to the mentioned case, we can see clear asymmetries in the distribution (highlighted with darker colours) that cannot be well described by a Gaussian distribution, namely a large tail towards positive abundance residuals. In a few cases (as for NGC 3318 and NGC 6708, see figures in Appendix D), the tail appears in the negative regime.

The presence of these asymmetries in the residual abundance distributions hints the existence of non-radial variations in the oxygen abundances, possibly related with morphological features. However, the fact that these asymmetries appear as tails in the distributions suggests that these variations might be restricted to specific and limited areas of the disc, and

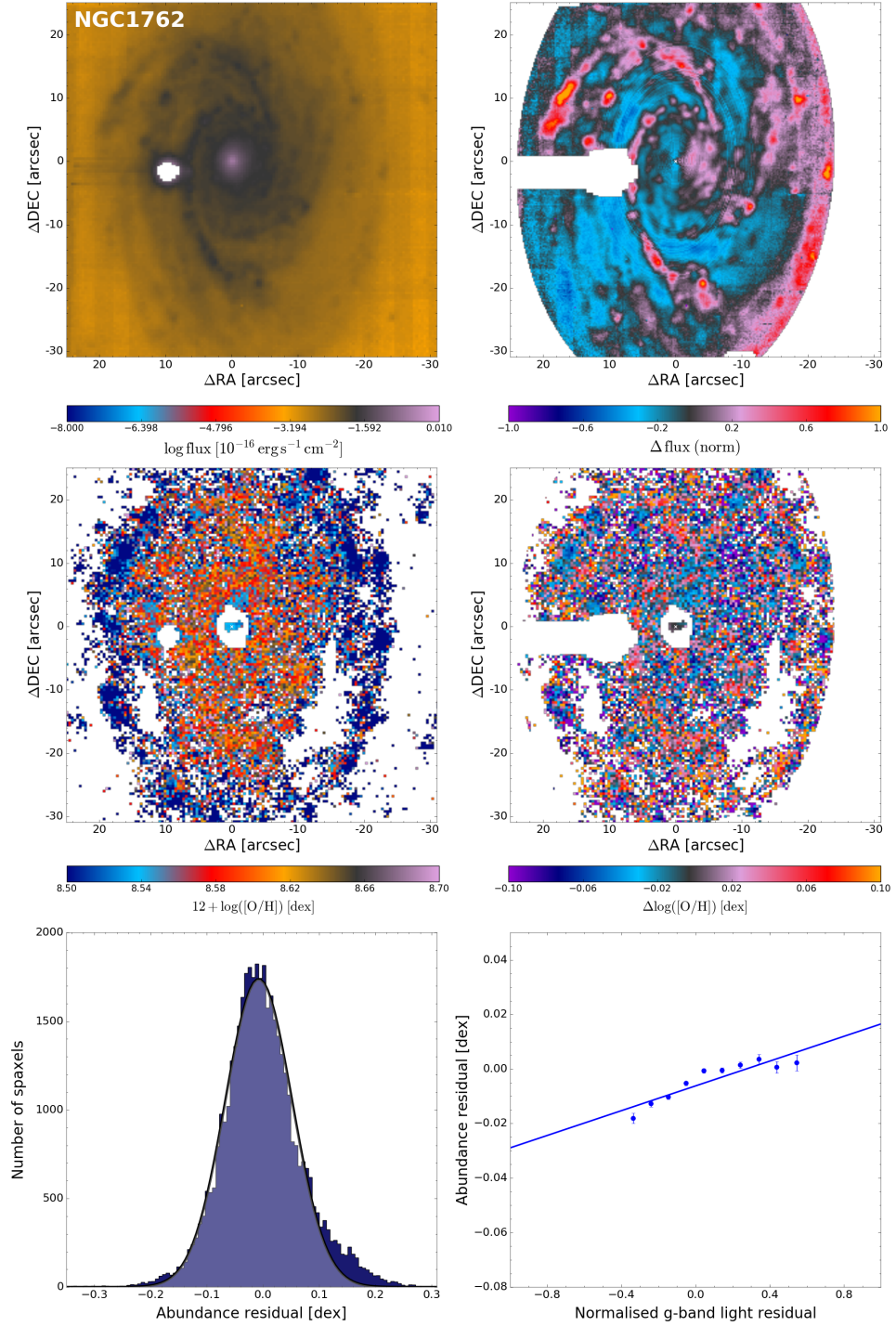


**Figure 7.1:** *Top left: SDSS g-band image. Top right: Normalised g-band light residuals. Middle left: 2D abundance distribution. Middle right: 2D residual abundance distribution. Bottom left: Distribution of the residual abundances together with its Gaussian fit. Deviations from the Gaussian distribution are highlighted with darker colours. Bottom right: Correlation between the abundance and light residuals in bins of 0.1 along the x-axis, together with its error-weighted linear fit. See text for details.*

therefore they do not significantly affect the overall distribution. This hypothesis can be easily tested if we analyse the 2D residual abundance maps searching for coincidences in the location of these asymmetries with any structure within the galaxy.

### 7.2.1 2D RESIDUAL ABUNDANCE MAPS

The middle right panel of Fig. 7.1 shows the 2D map of the residual gas abundances of NGC 1762, together with the SDSS  $g$ -band image extracted from AMUSING data (top left). This type of image allows us to distinguish morphological features displayed by the galaxies such as bars or spiral arms. In particular, for NGC 1762 it is clear the presence of a prominent spiral structure. The residual abundance map clearly show some regions of high residual values (red-orange colours). The amplitude of the abundance variations across the disc can be up to  $0.10 - 0.12$  dex, depending on the galaxy (see figures at the end of the chapter). If we compare this map with the  $g$ -band image, there seems to be a correspondence between these areas of higher abundance residuals and the spiral arms.

In other galaxies, on the opposite, the presence of morphological features seem to be linked with less metal rich regions of the discs. In addition, there are also galaxies that do not seem to present significant increases in the abundance residuals. This result, derived from a visual inspection of the 2D abundance maps, brings to light the need of quantifying the presence of non-radial variations of the oxygen abundances and their possible connection with the spiral arms of the galaxies or other characteristic features.

### 7.2.2 CORRELATION WITH LIGHT RESIDUALS

Inspecting the 2D abundance residual maps of the sample and the SDSS  $g$ -band images, there appears to exist a spatial correlation between the non-radial variations of the gas abundance (when existing) and features easily recognisable in the  $g$ -band images by increases in the light distribution. In most galaxies these features correspond to the spiral arms. Also, in some cases, observed asymmetries (due for instance to interactions with other galaxies) in the galaxies are responsible of these increases in the light. This spatial coincidence can be thus confirmed if we represent the residuals of the abundances with respect to the light residuals derived in the SDSS  $g$ -band. These latter ones are computed by subtracting the characteristic axisymmetric radial profile (obtained by azimuthally averaging the  $g$ -band intensity values) to the observed distribution, and then normalised for a direct comparison between galaxies. In addition, for the determination of the light residuals we have masked some regions associated with imperfections of the image or areas dominated by the sky emission that can lead to a wrong

derivation of the residuals. The central part of the galaxies is also visually masked to avoid the bulge component and analyse only the light residuals linked to the galaxy discs<sup>1</sup>. The top right panel of Fig. 7.1 shows the 2D light residual map of NGC 1762. As mentioned, in this case the highest residuals (pink-red colours) correspond to the most prominent spiral arms.

The outcome of this analysis for NGC 1762 is shown in the bottom right panel of Fig. 7.1. For clarity (due to the large number of spaxels in each galaxy), the residual values have been averaged in bins of 0.1 (along the x-axis, dimensionless). The errors are calculated as the standard deviation divided by the square root of the number of spaxels within each bin. Only the bins containing at least 1% of the total number of spaxels have been represented. The blue solid lines shows the error-weighted linear fit to these mean values. For NGC 1762 we find a clear positive correlation between both parameters. In general, three different behaviors are observed: the metallicity residuals exhibit either a positive, a negative, or a non-existent correlation with the light residuals. The slope of the linear fit (hereafter called  $\gamma$ ) for all the galaxies is provided in Table 7.1 as a measurement of the amplitude of the non-radial variations (largest amplitudes imply largest absolute values of the slope) and as an indicator of the presence of metal-poor or metal-rich regions associated with the brightest areas of the disc (positive  $\gamma$  values imply more metal rich SF regions in the brightest areas than in the rest of the galaxy disc and negative  $\gamma$  values indicate the opposite). This way, we can see that eleven galaxies present a clear positive correlation between the abundance and light residuals ( $\gamma > 0.01$  dex), and seven galaxies present a negative one ( $\gamma < -0.01$  dex). Finally, no evidence of a correlation between both parameters have been found in the remaining six galaxies, indicating the absence of significant non-radial variations in the oxygen abundance distribution in these galaxies.

### 7.2.3 DEPENDENCE ON GALAXY PROPERTIES

Due to the variety of trends observed in the correlation between the abundance residuals and the light residuals, we proceed to investigate if there is a dependence of the  $\gamma$  parameter (which represents the slope of such correlation) with any specific property of the galaxies. This analysis will allow us to asses the possible mechanisms responsible for these non-radial variations in the abundance distribution.

Figures 7.2 and 7.3 show the distribution of  $\gamma$  values as a function of different galaxy properties. The Pearson correlation coefficient  $r$  is indicated in the panels for the continuous variables. The values of these parameters for all galaxies in the sample are given in Table B.1 (Appendix B), except the

<sup>1</sup>We note here that an improved technique for removing the contribution of the bulge component is planned for future work.

**Table 7.1:** Slope values ( $\gamma$ ) of the linear fits in the abundance vs. light residuals correlation.

Galaxy	$\gamma$ [dex]	Galaxy	$\gamma$ [dex]
ESO478-G006	$-0.014 \pm 0.014$	NGC3318	$-0.004 \pm 0.006$
ESO506-G004	$+0.014 \pm 0.017$	NGC3363	$+0.042 \pm 0.035$
ESO570-G020	$-0.009 \pm 0.021$	NGC3464	$+0.064 \pm 0.022$
IC5179	$-0.002 \pm 0.009$	NGC3905	$+0.045 \pm 0.017$
MCG-01-57-021	$-0.034 \pm 0.014$	NGC4806	$-0.083 \pm 0.008$
NGC1080	$+0.029 \pm 0.012$	NGC6708	$-0.037 \pm 0.015$
NGC1762	$+0.023 \pm 0.021$	NGC6754	$+0.038 \pm 0.011$
NGC2370	$+0.021 \pm 0.012$	PGC004701	$-0.006 \pm 0.018$
NGC2466	$+0.001 \pm 0.009$	PGC128348	$-0.032 \pm 0.013$
NGC3120	$+0.019 \pm 0.009$	UGC01395	$+0.028 \pm 0.023$
NGC3244	$-0.026 \pm 0.012$	UGC05691	$+0.011 \pm 0.019$
NGC3278	$-0.004 \pm 0.005$	UGC11214	$-0.053 \pm 0.027$

characteristic oxygen abundance values and the slopes of the main negative gradients that are provided in Table B.2. A more detailed description of the derivation of some of these properties is given in Chapter 5 (Sects. 5.1, 5.5 and 5.6).

Analysing in the first place the role of the bar (Fig. 7.2, top left panel), no clear trends are observed in the distribution. If we exclude the two cases of barred galaxies presenting negative  $\gamma$  values, there seems to be a correlation with barred galaxies presenting the highest values and unbarred galaxies the lowest ones. This means that the presence of the bar would produce a chemical enrichment of the H II regions located in the brightest areas of the disc. However, these two outliers represent the 40% of the cases for barred galaxies, and therefore, we can not make a firm conclusion in this regard. A future study with more galaxies is needed in order to asses if the bar produces non-radial abundance variations or, on the contrary, its presence does not affect significantly the abundance distribution.

The top right panel of Fig. 7.2 represents the dependence of the  $\gamma$  values with the morphological type of the galaxy according to the de Vaucouleurs system from *HyperLeda*. As in the previous case no correlation is found.

If we study the connection of the presence of non-radial variations in the abundance distribution with the morphology of the spiral arms (Fig. 7.2, middle left panel), interestingly, we obtain that grand design galaxies are associated with high values of  $\gamma$ , while flocculent galaxies present lower values of this parameter. The galaxies that have not been properly classified (and called ‘undefined’) are considered to be an intermediate case, as these

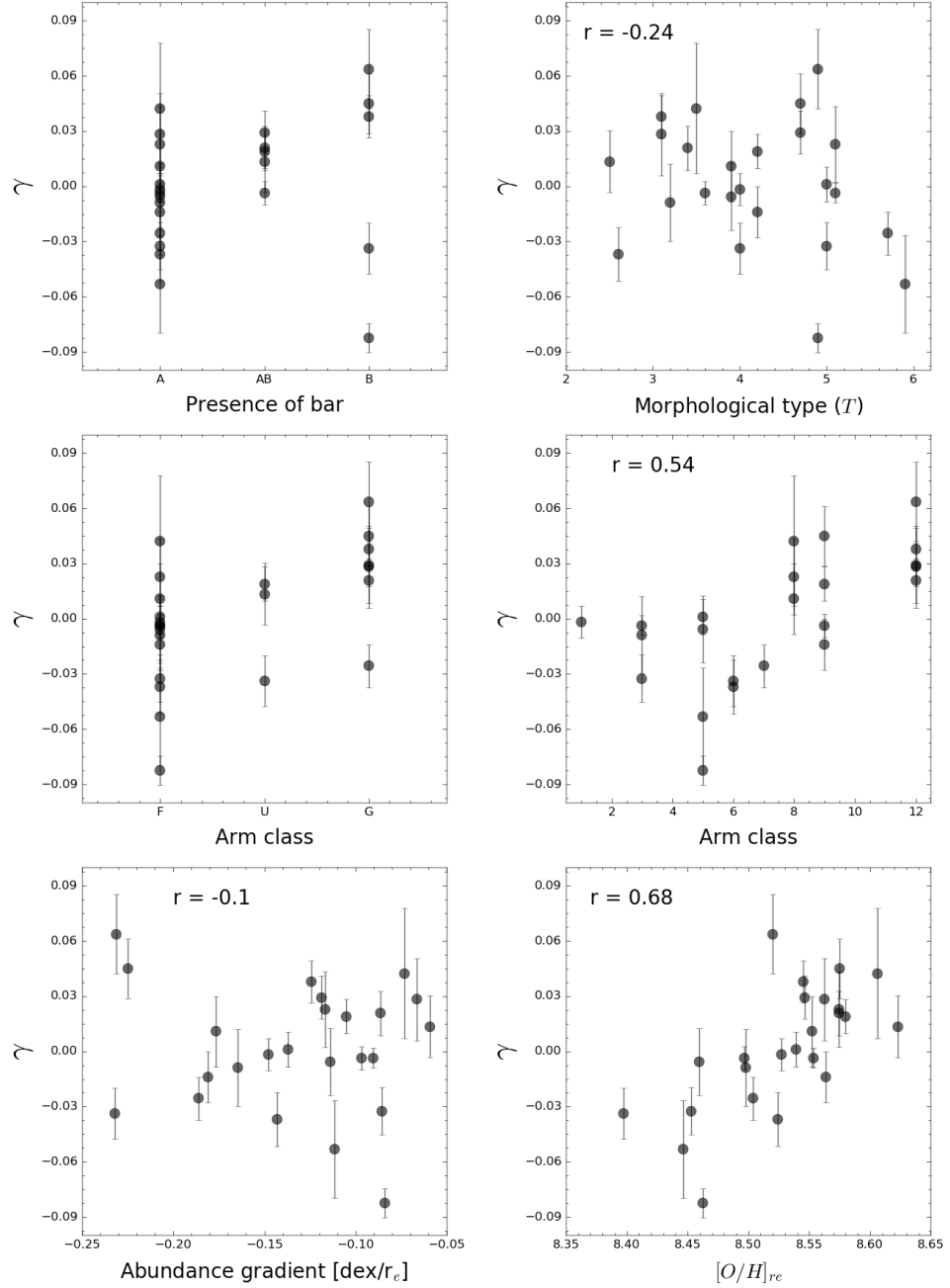


**Figure 7.2:** Distribution of the  $\gamma$  values as a function of: presence of bars (A, clearly unbarred galaxies; B, clearly barred; AB, intermediate stage; top left), numerical morphological type according to the de Vaucouleurs system ( $T$ , top right), arm class (F, flocculent; U, undefined; G, grand design; middle left), extended arm class (from AC 1-12, middle right), oxygen abundance gradient of the galaxy (bottom left), and characteristic abundance of the galaxy (abundance value at one disc effective radius, bottom right). See text for details.



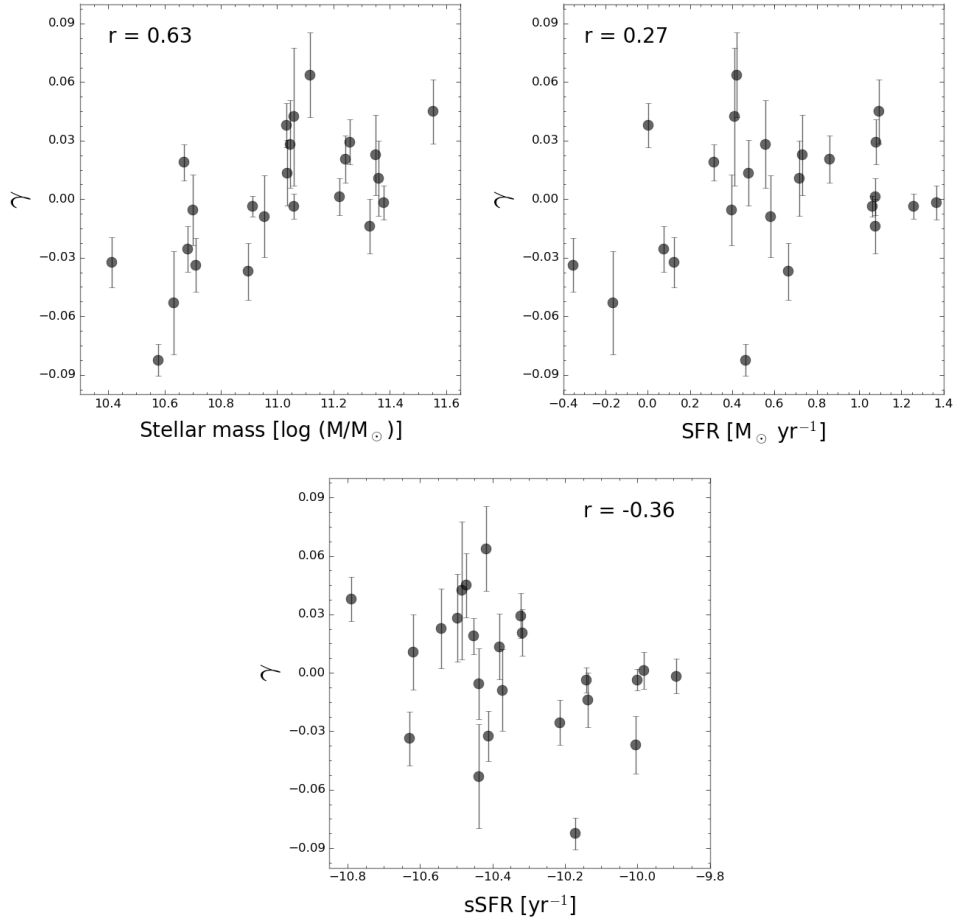


**Figure 7.3:** Distribution of the  $\gamma$  values as a function of: integrated stellar mass (top left), star formation rate (top right), and specific star formation rate (bottom center). See text for details.

galaxies would present characteristics of both flocculents and grand designs. The presence of just three bins does not allow us to properly characterise this trend in the distribution. For this reason, we decide to expand this classification and perform the original one comprising 12 arm classes defined by Elmegreen & Elmegreen (1982), where the first arm classes correspond to the most flocculent arms and the last classes to pure grand design ones, and the intermediate classes presenting characteristics of both types (see Sect. 1.1.1 for details). This is shown in the middle right panel of Fig. 7.2. Now, the mentioned trend is more easily observed ( $r = 0.54$ ), that is, grand design galaxies present higher  $\gamma$  values than the flocculent ones. This means that in grand design systems the brightest areas are more metal-rich with respect to the rest of the disc, whereas the presence of flocculent arms produce that the brightest areas present lower metallicities than the rest of the

disc.

The bottom left panel of Fig. 7.2 represents the dependence of the  $\gamma$  values with the oxygen abundance gradient displayed by the galaxies (and analysed in Chapter 5). We do not find any correlation between both parameters. Although not shown in Fig. 7.2, we have also analysed the dependence with the presence of inner drops and outer flattenings in the radial abundance distribution, again not finding any correlation. Finally, the bottom right panel of Fig. 7.2 shows the dependence with the oxygen abundance value derived at one disc effective radius (characteristic oxygen abundance,  $[\text{O}/\text{H}]_{re}$ ), which is representative of the average value across the galaxy (Zaritsky et al. 1994; Sánchez et al. 2013). In this case we observe a clear correlation of both parameters ( $r = 0.68$ ), with the highest  $[\text{O}/\text{H}]_{re}$  values corresponding to the highest values of  $\gamma$ .

We also analyse the distribution of  $\gamma$  values as a function of the integrated stellar mass of the galaxies. The top left panel of Fig. 7.3 shows a clear correlation between them ( $r = 0.63$ ), with an increase in the metallicity of the brightest regions with respect to the rest of the disc as the stellar mass of the galaxy is higher. We find that less massive ( $M < 10^{11}M_{\odot}$ ) galaxies present more metal-poor SF regions in the brightest areas than in the rest of the disc. Galaxies with intermediate masses ( $M \sim 10^{11}M_{\odot}$ ) present a more homogeneous distribution of the oxygen abundance residuals (not considering the overall gradient) across the discs. Finally, we observe that most massive galaxies ( $M > 10^{11}M_{\odot}$ ) display more metal-rich SF regions in the brightest areas than in the rest of the disc. Due to the well-known mass-metallicity relation, that is consistent with more massive galaxies being more metal-enriched (e.g. Tremonti et al. 2004; Sánchez et al. 2013), the correlations of  $\gamma$  with the characteristic oxygen abundance and the stellar mass of the galaxies are intimately related. However, the dependence of  $\gamma$  with the galaxy mass does not arise as a consequence of a dependence between this parameter and the type of arms displayed by the galaxy (flocculent or grand design), as we do not find any correlation between both of them.

Finally, we analyse the dependence of  $\gamma$  with the SFR of the galaxies (Fig. 7.3, top right panel). The lack of correlation found suggests that the presence of a higher star formation does not produce any increase in the metallicity that can lead to local variations across the disc. If we analyse instead the sSFR, although there is no a clear correlation, we find that galaxies with higher values present in average lower values of  $\gamma$ , while the galaxies with lower sSFR are associated with higher  $\gamma$  values. This trend is not surprising due to the observed behaviours with the SFR and the galaxy mass.

In conclusion, the study of the relation of the  $\gamma$  parameter with the analysed galaxy properties yields that the type of spiral arms (flocculent

vs. grand design) and the stellar mass (or characteristic abundance) are the main drivers for the presence of non-radial variations in the abundance distribution. Regarding the first one, we already showed in Chapter 6 that the type of spiral arms displayed by galaxies had an effect on the abundance distribution producing differences in the arm and the interarm regions. In that case, only significant differences were observed in flocculent galaxies. Now, we observe non-radial variations in both cases, but pointing out to different behaviours (in grand design galaxies the light residuals correlate with the abundance ones, while in the flocculent systems we find an anticorrelation between both parameters). The nature of this analysis is different from the arm/interarm one, as here we study directly the non-radial abundance residuals, whereas in that analysis we compared the radial profiles displayed separately by SF regions of the arm and the interarm areas. Therefore, a direct comparison between the results derived from them is difficult to assess. However, the observed differences reported here could be indicative again of the presence of different mechanisms shaping the spiral structure in both flocculent and grand design galaxies, these mechanisms affecting differently to the generation of non-radial abundance variations. Nevertheless, it is still plausible that both types of spiral arms are caused by the same mechanisms and simply because of the presence of a more stochastically polluted gas outside the spiral arms in flocculent galaxies, we could find more metal-rich H II regions in the interarm areas (not associated with the brightest regions of the disc). In the grand design galaxies, on the opposite, a more concentrated star formation in the spiral arms could increase the metallicity of certain regions associated with high light residuals with respect to the rest of the disc. Nevertheless, this is a hypothesis that has to be more exhaustively studied.

Regarding the effect of the galaxy mass, the found correlation and the lack of such with the SFR suggest that the presence of non-radial abundance variations may be related to the ability of the galaxies to retain metals rather than its current star formation. As is known, oxygen is produced mainly by high-mass stars, and returned to the ISM in their explosion as type II SNe (Osterbrock 1989). These SNe tend to occur in spiral arms, as it is here where short-lived massive stars live preferentially (Osterbrock 1989). In most of the galaxies, we see that the largest light residuals are associated with the spiral arms (see figures at the end of the chapter), although in other cases other factors may be responsible of part of these residuals (such as interactions with other systems). In this regard, a possible explanation of the correlation found between  $\gamma$  and the galaxy mass might be related with the role of the escape velocity in the dispersion of the metals when a SN event happens (of any other local source of metals). The local metal loss is expected to be larger in low mass galaxies with low escape velocities (Barrera-Ballesteros, in prep.), blowing these metals to more distant regions and producing then that

locally the SF regions are more metal-poor with respect to the near regions. More massive galaxies, on the opposite, present higher escape velocities (Barrera-Ballesteros, in prep.), and therefore, the metals remain close to the location of the SN explosion, enriching the surrounding gas with respect to the rest of the disc. This hypothesis also need to be analysed in more detail.

We want to emphasise that all the results shown in this Sect. 7.2 are very preliminary. A most extended study including more tests is needed to confirm our hypotheses in order to asses the physical mechanisms that might cause the observed trends in the non-radial variations of the abundance distribution and properly interpret these results.

### 7.3 AZIMUTHAL VARIATIONS: THE CASE OF NGC 6754

In the previous section we have shown the presence of non-radial abundance variations in a large number of galaxies of the sample, associated with local enrichment effects. In this section we take a step forward analysing the presence of azimuthal patterns in the abundance distribution and their possible connection with radial migratory processes. We have focused this study in one galaxy of the sample, NGC 6754, for which some of the highest local abundance variations have been measured in Sect. 7.2. Besides the abundance distribution, the H $\alpha$  line-of-sight (LOS) velocity is also analysed in order to measure the streaming motions of gas along the spiral arms predicted by simulations and responsible of the possible azimuthal abundance variations. The extension of this study to the rest of the sample is left for future work (see conclusions of this thesis).

The gas content of NGC 6754 was already analysed in Sánchez et al. (2015). Studying the azimuthal distribution of the oxygen abundance residuals for  $\sim 400$  individual H II regions, the authors found a pattern that might be related to radial migration effects. In this thesis we undertake a deeper study using 2D information in a spaxel-by-spaxel basis (see Sect. 7.1) to analyse in detail both the azimuthal distribution of the gas abundance and velocity residuals seeking for definitive observable signatures of radial migration in spiral galaxies.

#### 7.3.1 RESIDUAL ABUNDANCE AND VELOCITY MAPS

As mentioned in Sect. 7.2, to measure azimuthal variations in the abundance distribution of NGC 6754 we first need to remove the characteristic radial profile displayed by this galaxy. To do that we subtract the azimuthally

averaged radial abundance to the observed 2D distribution. The top left-hand panel of Fig. 7.4 displays the 2D distribution of the oxygen abundance, and the top right-hand panel displays the residuals after subtracting the azimuthally averaged radial abundances (top middle). In this panel, we can see clear differences associated with the spiral arms (black markers).

As explained in Sect. 3.1, PIPE3D also provides LOS velocities from which we can derive gas velocity maps of the galaxy for each analysed line. We focus the analysis on the measurements of the H $\alpha$  emission line, as it represents the strongest detected line. The rotation curve,  $v_\theta$ , and the radial velocity component,  $v_R$ , were obtained by least-squares fits of  $v_{\text{sys}} + (v_\theta \cos \theta + v_R \sin \theta) \sin i$  to the observed velocity field,  $v_{\text{obs}}$ , assuming constant coordinates of the mass center, systemic velocity ( $v_{\text{sys}}$ ), disc position angle, and inclination (matching the photometric parameters). The best-fit systemic velocity corresponding to these parameters is  $3247 \pm 9 \text{ km s}^{-1}$ . We sampled the galactocentric radius using  $1''$ -rings (230 pc-rings), roughly similar to the seeing of the observations. With that sampling, rings are uncorrelated, and the least-squares fits were performed with at least 70 degrees of freedom, so that  $v_R$  and  $v_\theta$  are very well constrained (average  $1\sigma$  formal error of  $1.3 \text{ km s}^{-1}$ ). The axisymmetric model velocity field,  $v_{\text{mod}}$ , is then the projection of a smoothed version of  $v_\theta$  only and does not contain the contribution from the fitted  $v_R$ . Therefore, the residual LOS velocities defined as  $\Delta v = v_{\text{obs}} - v_{\text{mod}}$  trace the observed non-circular radial motions, as well as the local departures from axisymmetry of both  $v_R$  and  $v_\theta$  (streaming motions caused by the bar, spiral perturbations, etc.).

The bottom left-hand panel of Fig. 7.4 displays the 2D distribution of the LOS gas velocity and bottom right-hand panel displays the residuals after subtracting the LOS projection of the derived rotation model (bottom middle). This map shows a feature associated with the eastern (left-hand side in this panel) spiral arm, not so evident for the western arm. The reason why this feature is not observed (so clearly) for the western arm may lie in the lower spatial resolution of the data covering this half of the galaxy due to the worse seeing conditions <sup>2</sup>. Therefore, below we will focus on the eastern spiral arm.

---

<sup>2</sup>AMUSING observations of this galaxy were split into two different pointings covering the eastern and western parts of the galaxy under seeing conditions of  $0.8''$  (180 pc) and  $1.8''$  (410 pc), respectively.

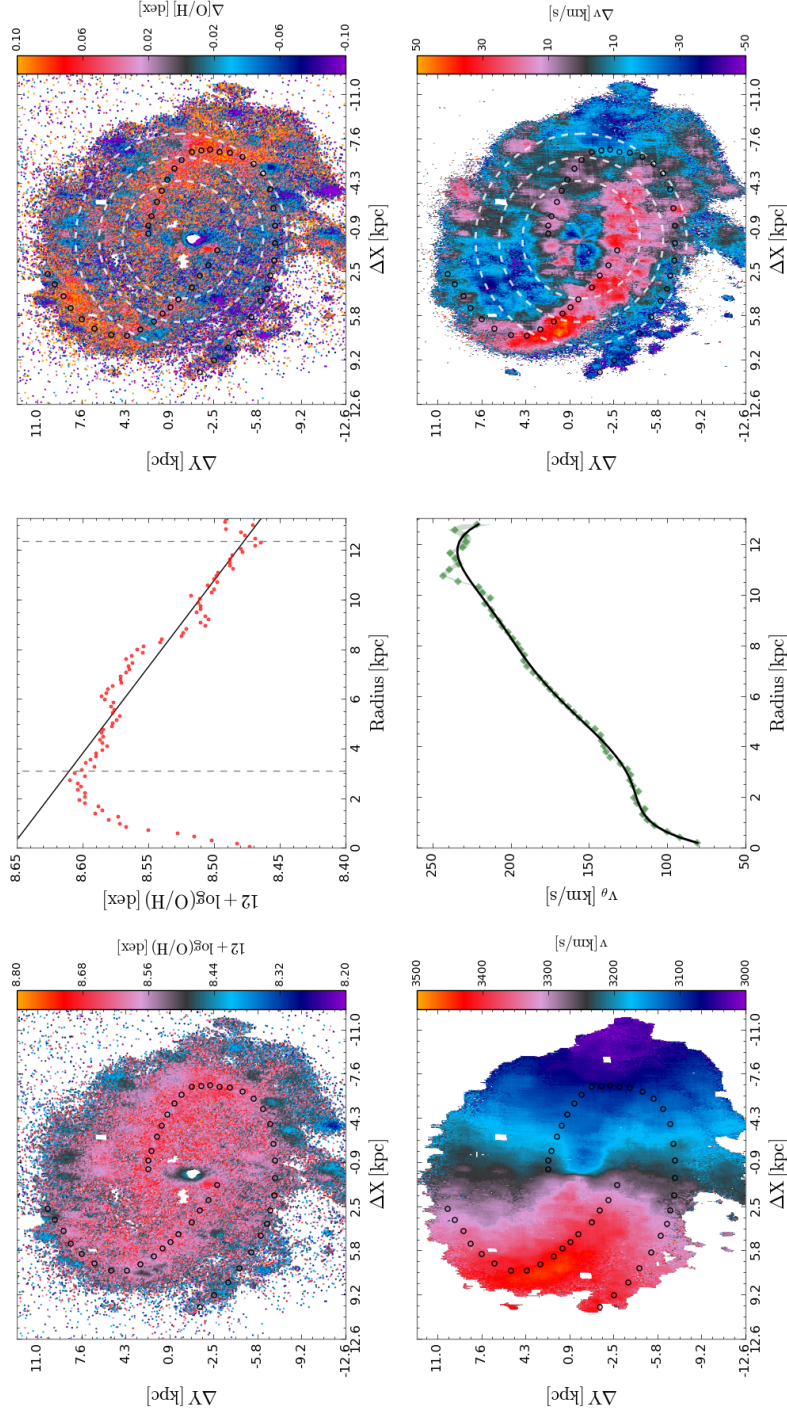


**Figure 7.4:** 2D deprojected distributions of the gas oxygen abundance (top left), residual abundance (top right),  $H\alpha$  LOS velocity (bottom left) and LOS velocity residuals (bottom right). The position  $\Delta X = \Delta Y = 0$  corresponds to the centre of the galaxy. The location of the spiral arms is marked with open circles. Dashed white circles indicate the three radial positions  $R = 4.5, 6.3$  and  $8.1$  kpc of the azimuthal profiles shown in Fig. 7.5. Top middle panel shows the metallicity gradient (black) fitted to the azimuthally averaged radial abundances (red) in the linear regime (delimited by the dashed vertical lines, see Sánchez-Menguiano et al. 2016b for further information). Bottom middle panel shows the ionized gas rotation curve (green) with the  $1\sigma$  formal errors (light green), together with its smoothed version (polynomial fit, solid line).

### 7.3.2 AZIMUTHAL RESIDUAL ABUNDANCE AND VELOCITY PROFILES

The azimuthal profiles of both residuals at three different galactocentric distances (represented as dashed white circles in right-hand panels of Fig. 7.4) are shown in Fig. 7.5. The oxygen abundance residual profiles are indicated by the red solid lines and the H $\alpha$  LOS velocity residual profiles by the blue solid ones. These profiles correspond to three different 2''-wide annuli centred at  $R = 4.5, 6.3$  and  $8.1$  kpc (i.e.  $0.7/1.0/1.3 r_e$ ) with an azimuthal sampling of  $10^\circ$ . In order to connect possible asymmetries in these distributions to the spiral structure, the SDSS  $g$ -band intensity distribution is also represented (black dashed line).

In Fig. 7.5 we can see that around the eastern arm, the azimuthal residual LOS velocity profiles show a peak located just after the peak in the light distribution (leading side of the arm<sup>3</sup>), with an amplitude between  $\sim 28 - 38$  km/s, and a minimum just before the light peak (trailing side<sup>1</sup>). Remarkably, these maxima (minima) in the velocity profile appear together with a decrement (increment) in the azimuthal residual abundance profile at all the radii, with a total amplitude (peak-to-peak) up to 0.09 dex.

In order to interpret these results, in Fig. 7.6, we show a  $g$ -band image of NGC 6754 superimposed to its observed H $\alpha$  velocity map. We consider that the north part of the galaxy (upper side in the figure) is closer to us under the assumption of trailing spiral arms (Hubble 1943) and taking into account that the eastern part is receding from us. In that case, positive (negative) residual velocities indicate radially inward (outward) motions of the gas and tangentially faster (slower) motions of the gas for the eastern spiral arm. Thus, the positive velocity residuals displayed by NGC 6754 in a wide extension of the leading part of the eastern arm can be interpreted either as gas moving radially inward, gas moving tangentially faster, or a combination of both. Following a similar reasoning, the negative velocity residuals in the trailing part can be the result of gas moving radially outward, gas moving tangentially slower, or both. The asymmetries found in the metallicity residuals are in agreement with a transport of metal-rich gas from the inner disc toward the outer regions at the trailing side of the spiral arm and more metal-poor gas from the outer disc toward the inner ones at the leading side, which is strikingly consistent with the velocity asymmetries mentioned above. These trends are observed at all three radii, which indicates strong evidence of the radial migration happening in a large radial range.

---

<sup>3</sup>The leading side of a spiral arm is the edge of the arm that points towards the direction of disc rotation, that is, the front of the arm. The trailing side is, on the other hand, the edge of the arm that points towards the opposite direction of disc rotation, that is, the back of the arm.

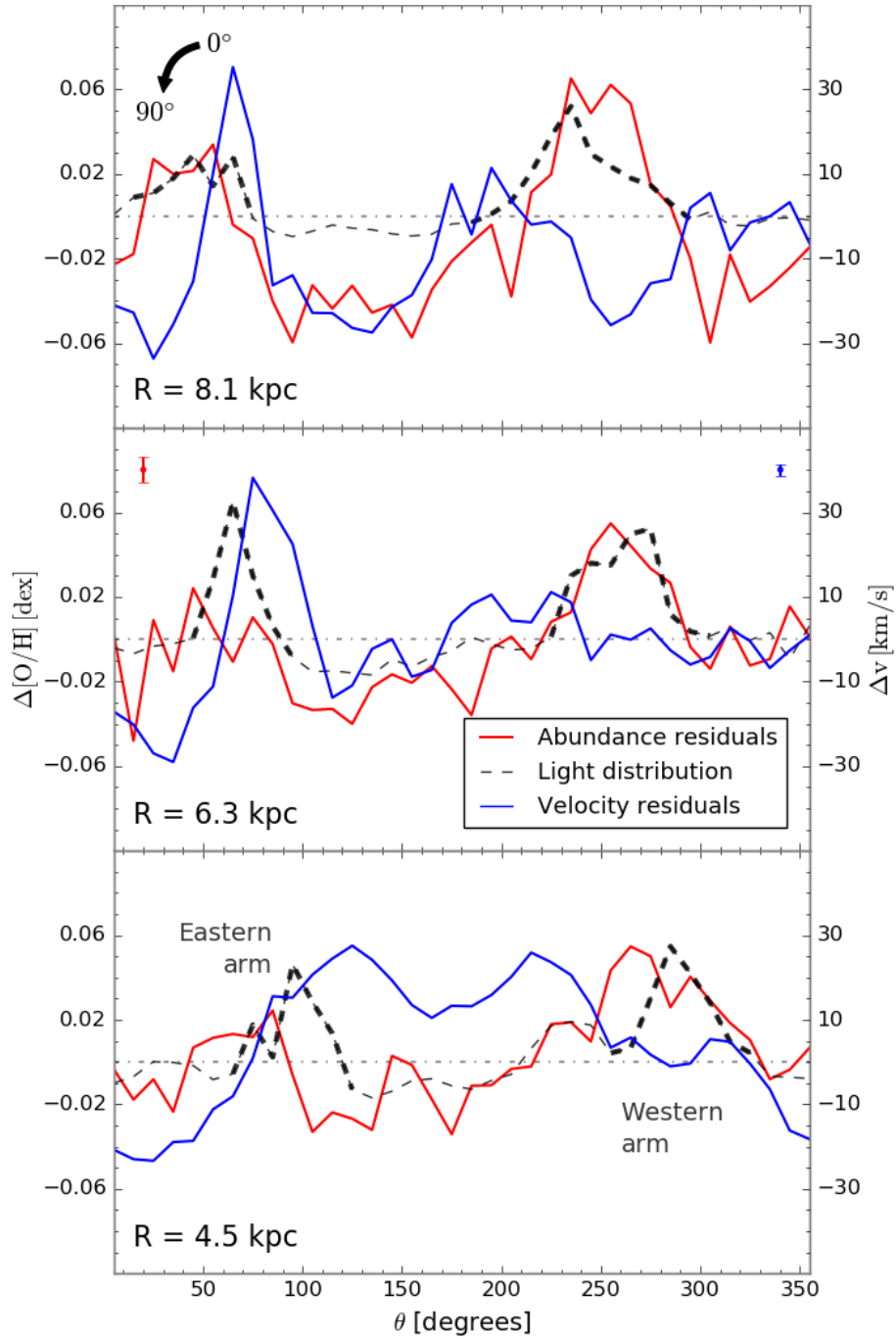


**Figure 7.5:** Azimuthal profiles of the light (black dashed), oxygen abundance residuals (blue, left-hand y-axis) and  $H\alpha$  LOS velocity residuals (red, right-hand y-axis) at three different radii (shown in Fig. 7.4). The position of the spiral arms is marked with the bold dashed line. Mean errors in the azimuthal profiles are denoted by the vertical lines in the middle panel. The angles are measured counter-clockwise from the positive Y-axis in Figure 7.4.



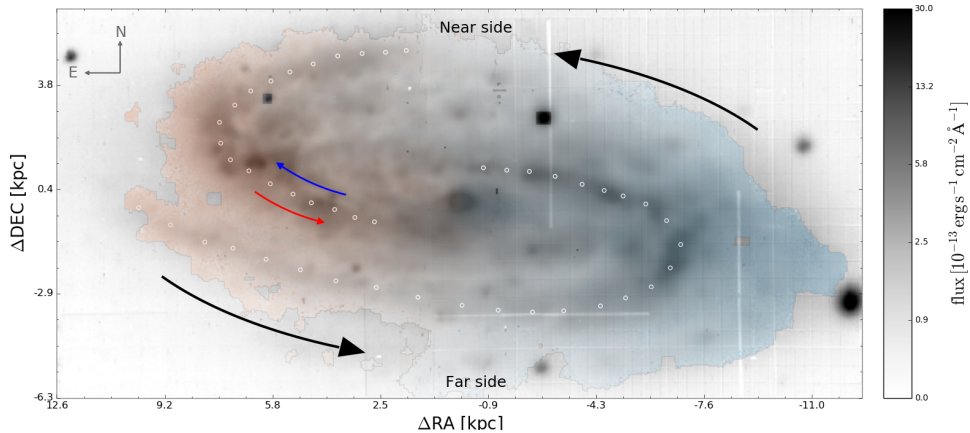


**Figure 7.6:** *g*-band image of NGC 6754 superimposed to the observed  $H\alpha$  velocity map, with red (blue) color denoting the receding (approaching) part of the galaxy. The black arrows indicate the direction of rotation (assuming trailing spiral arms). Radially-inward/tangentially-faster and radially-outward/tangentially-slower motions of the gas along the arms (outlined by open circles) are indicated with red and blue arrows, respectively (see text for a detailed explanation).

### 7.3.3 COMPARISON WITH SIMULATIONS

In order to investigate the behavior of the gas from a theoretical perspective, in this section, we study an isolated Milky Way-sized disc galaxy simulated using the N-body smoothed particle hydrodynamics (SPH) GCD+code. Details of the code are available in Kawata & Gibson (2003) and Kawata et al. (2013). In particular, we analyse the simulation labeled K14 in Grand et al. (2015), which is similar in size to NGC 6754. For this analysis, we focus on a single snapshot of the galaxy that displays a clear bar and two-armed spiral structure and shows clear radial migration of the gas around the spiral arm (Kawata et al. 2014; Grand et al. 2015). The rotation axis and the angle of the spiral arm have been chosen to match the characteristics of NGC 6754.

The azimuthal analysis of the gas content in this simulated galaxy was performed in a similar way as in NGC 6754. Figure 7.7 (right-hand panel) shows the azimuthal profiles of the mass density (black), residual metallicity (red), and residual LOS velocity (blue) for assumed  $i = 63^\circ$ . The mass density distribution shows a clear peak below  $200^\circ$ , which represents the eastern spiral arm. As the western (right-hand side) arm is much weaker, especially in the outer radii in this particular simulation snapshot, we will focus on the stronger eastern (left-hand side) arm to compare with the trends observed in NGC 6754. Consistent with the observations, the residual LOS velocity (metallicity) is lower (higher) on the trailing side of the spiral, while the trend is reversed on the leading side, that is, residual LOS velocity (metallicity) is higher (lower) than the average values at the three analysed

radii matching those chosen for Fig. 7.5.

The simulations allow us to analyse separately the radial and tangential components of the LOS velocity. The left-hand panels of Fig. 7.7 display face-on maps of the residuals of the gas metallicity (top) and tangential velocity field (middle) from the analysed simulation after subtracting the azimuthally averaged values at each radius. In addition, the radial velocity field map is shown in the bottom panel. We can see that the tangential velocity is slower on the trailing side of the eastern spiral arm and faster on the leading edge with respect to the general rotation, whereas the radial velocity points outward on the trailing side and inward on the leading edge. The metallicity map shows the presence of metal-rich (poor) gas particles on the trailing (leading) side of the spiral arm. The combination of both tangential and radial velocity behaviors creates a streaming motion that, along with the well-known negative gas metallicity profile of discs (e.g. Searle 1971; Martin & Roy 1992; Sánchez et al. 2014), causes metal-rich (poor) gas to move toward the outer (inner) regions at the trailing (leading) side of the spiral arm in a large radial range.

### 7.3.4 RADIAL MIGRATION IN NGC 6754

Studying the eastern spiral arm, located in the half of the disc with data of the highest spatial resolution, the residual LOS velocity distribution shows a maximum at the leading side of the spiral arm (larger receding component in the velocity), with an amplitude of  $\sim 30 \text{ km s}^{-1}$ , and a minimum at the trailing edge. The residual abundance distribution is positive at the trailing side and negative at the leading edge, with a total amplitude (peak-to-peak) of  $\sim 0.1 \text{ dex}$ . We note that although NGC 6754 seems to have a companion close by (2MASXJ19112166-5037339), the linear distance between them (26 Mpc) suggests that our results cannot be a consequence of interaction (see also de Mello et al. 1996).

The spatial resolution of the data is crucial in the analysis of azimuthal variations. In this study we find that in order to be sensitive to the signatures left by radial migration, we need a spatial resolution of  $\sim 200 \text{ pc}$ . Otherwise, the signatures in the velocity map are blurred (western arm).

In order to interpret these results we have also analysed the gas content of a simulated galaxy (N-body+SPH) that shows a clear radial gas migration around a spiral morphological feature rotating at a similar speed as the gas at every radius, showing the same trends as our observations. In light of these results, we claim that NGC 6754 shows clear signs of ongoing radial gas migration that produces motions of metal-rich gas toward the outer regions on the trailing side of the spiral arm and metal-poor gas toward inner regions on the leading side. The analysed simulations show amplitudes for the residual LOS velocity of  $\sim 10 - 20 \text{ km s}^{-1}$ , lower than those observed

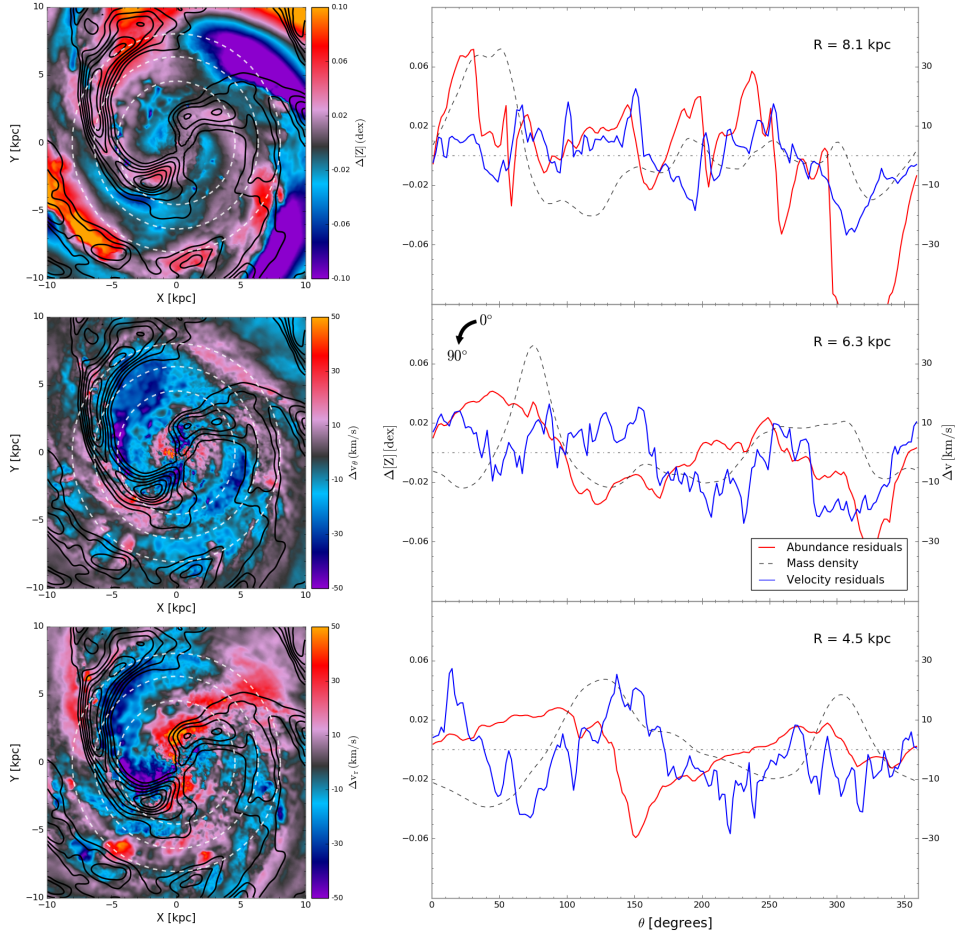


**Figure 7.7:** Chemodynamical results from simulations. Left-hand panels: Face-on maps of the residual gas metallicity (top), tangential residual velocity field (middle) and radial velocity field (bottom) of the simulated galaxy. Contour maps represent the mass density and the dashed white circles indicate the radial position of the azimuthal profiles. Right-hand panel: Same plots as in Fig. 7.5, but here produced from our simulated galaxy.

in NGC 6754. The derived values of the differences in the LOS velocities and metallicities in simulations depend on several factors, such as the amplitude and pitch angle of the spiral arms, the underlying metallicity gradient, amount of metal mixing, feedback, etc. The extension of this analysis to the entire sample described in Sect. 7.1 can provide further constraints on the simulation sub-grid physics.

The fact that these streaming motions are observed in a wide radial range of the spiral arm (at least 4 kpc) puts strong constraints on the nature of the spiral structure. Azimuthal variations in the velocity distribution across a classical density wave-like spiral arm have been suggested by some authors (Minchev & Quillen 2008; Chemin et al. 2016; Pasetto et al. 2016). However, the gas motion should show a clear offset from the spiral arm density peak, and the offset should strongly depend on the radius, as demonstrated in Baba et al. (2016). On the other hand, N-body simulations of disc galaxies commonly show spiral arm features in the morphology whose pattern speeds decrease with radius (e.g. Wada et al. 2011; Grand et al. 2012; Baba et al. 2013). These spiral features can result from the overlap of multiple modes (Comparetta & Quillen 2012), as often claimed in simulations (Masset & Tagger 1997; Quillen et al. 2011; Minchev et al. 2012; Sellwood & Carlberg 2014), which also induce nonlinear growth of their amplitude (Kumamoto & Noguchi 2016). In this work, we have compared our results with simulations showing these spiral arm morphological features that are transient and rotate at a similar speed as the gas at every radius. Although it is not guaranteed that the nature of the spiral arms in the observed galaxy is the same as in the simulations, the consistency found supports this scenario for the spiral structure formation of NGC 6754.

Recently, Ho et al. (2017) analysed the H II region oxygen abundance distribution of NGC 1365 and found azimuthal variations of approximately 0.2 dex over a wide radial range and coinciding with the two spiral arms. The signature we report in NGC 6754 is not observed in NGC 1365 according to the authors. They found that the oxygen abundances of the spiral arms are higher than on both their leading and trailing sides. In addition, the oxygen variations they observed are larger (0.4 dex; peak-to-peak). Ho et al. (2017) constructed for NGC 1365 a simple chemical evolution model inside the frame of density wave theories that is able to reproduce the observations. Therefore, the mechanisms shaping the abundance variations in NGC 1365 and NGC 6754 are likely to be different. In this regard, the extension of this analysis to the rest of the sample analysed in Sect. 7.2 can allow us to assess the scenario for the spiral structure formation in other galaxies.

## 7.4 BRIEF SUMMARY

The first studies of the abundance distribution in spiral galaxies were limited to the finding of an overall negative radial gradient (e.g. Peimbert 1979; Martin & Roy 1992; Zaritsky et al. 1994). Therefore, if existing, non-radial variations in the abundance distribution should have a very small amplitude unfeasible to be detected by the instruments of that time. We have had to wait until nowadays when telescopes and instruments of high spatial resolution have allowed the astronomers to observe for the first time these azimuthal variations.

All the studies up to date are focused on individual galaxies (Sánchez et al. 2015; Ho et al. 2017; Vogt et al. 2017). The AMUSING sample part of this thesis allows us to carry out a statistical study of the abundance azimuthal distribution in a large sample. In this way, we have analysed 24 galaxies fulfilling the needed criteria for such study. For these galaxies, we have studied the existence of local abundance variations and their connection with specific structures of the galaxies. We note that this study is still in progress and preliminary results are shown. With the mentioned purpose, we represented the abundance residuals (once the abundance radial profile has been removed) against the normalised light residuals ( $g$ -band). We call the slope of the linear fit  $\gamma$ . A clear correlation is observed for 18 galaxies of the sample, being in some cases a positive correlation (11,  $\gamma > 0.1$ ) and in others a negative one (7,  $\gamma < -0.1$ ). The first case corresponds to more metal-rich SF regions associated with the brightest areas of the disc (in comparison with the rest of the galaxy disc), while the latter indicates the opposite trend, that is, more metal-poor SF regions in the brightest regions of the disc.

In order to provide a possible explanation to these findings, we analysed the dependence of  $\gamma$  with some properties of the galaxies. We find a correlation of this parameter with the morphology of the spiral arms (flocculent vs. grand design arms), the characteristic abundance of the galaxy, and the integrated stellar mass. This fact suggests that these properties might be the main drivers of local abundance variations in spiral galaxies. For massive galaxies (with high abundances) and grand design systems we find that the light residuals correlate with the abundance residuals. For low-mass galaxies (with low abundances) and flocculent systems, on the opposite, the light residuals anti-correlate with the abundance residuals. Some hypotheses are formulated in order to explain these results, such as the capacity of the galaxies to retain metals. However, a more exhaustive discussion and more tests are needed in order to confirm these hypotheses and interpret the obtained results.

Finally, in a second part of the study, we analyse the azimuthal distribution of the abundance residuals of one galaxy of the sample NGC 6754

for which high local abundance variations have been measured in the first part of the study. The extension of this analysis to the rest of the sample will be carry out in the future. For NGC 6754 we also analyse the  $H\alpha$  LOS velocity distribution to asses the role of radial migration as possible cause of azimuthal abundance variations predicted by simulations. In this study, we present, for the first time, clear signatures of ongoing gas radial migration in which metal-poor gas clouds in the leading side of the arm are moving radially inward and tangentially faster while radially outward and tangentially slower in the trailing edge. The amplitude of the velocity variations is of  $\sim 30 \text{ km s}^{-1}$  and for the abundance variations of  $\sim 0.1 \text{ dex}$  (peak-to-peak). Comparing the observed trends with simulations, we show that this is consistent with spiral morphological features whose pattern speeds decrease with radius. The published result of this study on NGC 6754 (Sánchez-Menguiano et al. 2016a) is the first observational study finding azimuthal differences in the gas abundance distribution.

*It's the questions we can't answer that teach us the most. They teach us how to think. If you give a man an answer, all he gains is a little fact. But give him a question and he'll look for his own answers.*

— Patrick Rothfuss

# Conclusions and future work

DESPITE THE KNOWLEDGE we have achieved in the seeking of the total comprehension of the Universe, how spiral galaxies form and evolve is still a matter of debate. In this thesis we have tried to shed some light into this topic by analysing the abundance distribution of the ionised gas associated with star formation present in these systems.

We have based our study in two different IFS datasets: a sample of 122 galaxies extracted from the CALIFA mother sample, and a sample of 102 galaxies part of the AMUSING project. The large size of both samples allow us to state meaningful statistical conclusions. In order to characterise the 2D abundance distribution we have carried out a series of analyses focused on different aspects of this distribution. Next we will present the main conclusions of each of these analyses and the opened lines of study resulting from our work. Although all these results are based on the use of the calibration proposed by Marino et al. (2013) for the O3N2 index to derive the oxygen abundances, other calibrators have been explored along the thesis in order to assess the effect of the adopted calibrator in the results. We have shown that all the qualitative results are not contingent upon the choice of the used calibrator, although the actual measured values for the analysed parameters may change.

### Study of the radial oxygen abundance distribution

This analysis was first performed in a spaxel-by-spaxel basis using the CALIFA sample (122 galaxies), taking advantage of the full 2D information to properly map the abundance distribution. This type of analysis is feasible because the spaxel size of CALIFA datacubes is of the order of the size of an H II region and prevents us to resolve its ionised structure. With this premise, we also analysed the oxygen abundances derived for individual H II regions for comparison purposes, obtaining equivalent results with both procedures. In addition to the general negative gradient displayed by the galaxies, an inner drop and/or outer flattening were observed in the oxygen abundance radial profile. Concerning the negative trend, we find that there is a common abundance gradient between 0.5 and 2.0  $r_e$  of  $\alpha_{O/H} = -0.075 \pm 0.016 \text{ dex}/r_e$  when normalising the distances to the disc effective radius. By performing a set of KS tests, we determined that this slope is independent on other galaxy properties, such as morphology, absolute magnitude, and the presence or absence of bars. In particular, barred galaxies do not seem to display shallower gradients, as predicted by numerical simulations and reported by early studies (e.g. Zaritsky et al. 1994). Interestingly, we find that a high number of galaxies with reliable oxygen abundance values beyond two effective radii (57) present a flattening of the abundance gradient in these outer regions. This flattening is not associated with any morphological feature, which suggests that it is a common property of disc galaxies. Finally, we detected a drop or truncation of the abundance in the inner regions of 27 galaxies in the sample; this is only visible for the most massive galaxies.

For this study, the morphological parameters ( $i$  and PA angles) of the galaxies needed to derive the deprojected abundance distribution were computed by performing a light moments analysis (Walcher et al. 2014). However, later during the course of this thesis we obtained these parameters as result of a two-dimensional photometric decomposition of CALIFA galaxies (Méndez-Abreu et al. 2017). The comparison of the values for these parameters from both methodologies shows noticeable differences for a small percentage of galaxies (about 15%). As future work, we want to assess the effect of these differences in the derivation of the radial abundance distribution in order to verify the robustness of our results. Moreover, the number of observed galaxies in the CALIFA survey has increased since this analysis was performed, and therefore, the addition of these new galaxies in the study can improve the statistical significance of the results.

The high spatial resolution provided by AMUSING data allowed us to improve the study on the radial oxygen abundance distribution. This dataset helped us to increase the number of H II regions detected in individual galaxies with respect to previous studies. In addition, we can avoid the dilution effects and reduce the contamination of the diffuse emission in the detected regions, effects that affected the spaxel-by-spaxel analysis with CALIFA.



In this analysis we developed a new methodology to automatically fit the abundance radial profiles, finding that 55 galaxies of the sample exhibit a single negative gradient. The remaining 47 galaxies also display, as well as this negative trend, either an inner drop in the abundances (21), an outer flattening (10), or both (16), which suggests that these features are a common property of disc galaxies. We confirm the results found with CALIFA: the presence and depth of the inner drop depends on the stellar mass of the galaxies with the most massive systems presenting the deepest abundance drops, while there is no such dependence in the case of the outer flattening. As opposite to the previous study, where the radial position of these features was deduced based on visual inspections of the general shape of the gradient, in this analysis the developed methodology allowed us to determine automatically their actual location. We find that the inner drop appears always around  $0.5 r_e$ , while the position of the outer flattening varies over a wide range of galactocentric distances. Regarding the main negative gradient, we find a characteristic slope in the sample of  $\alpha_{O/H} = -0.10 \pm 0.03 \text{ dex}/r_e$  (compatible with the value recovered from the CALIFA data). This slope is independent of the presence of bars and the density of the environment. However, when inner drops or outer flattenings are detected, slightly steeper gradients are observed. This suggests that radial motions might play an important role in shaping the abundance profiles. Besides, we defined a new normalisation scale ('the abundance scale length',  $r_{O/H}$ ) for the radial profiles based on the characteristic abundance gradient, with which all the galaxies show a similar position for the inner drop ( $\sim 0.5 r_{O/H}$ ) and the outer flattening ( $\sim 1.5 r_{O/H}$ ). Finally, the analysis of the dispersion around the negative gradient arises no significant dependence with any property of the galaxies, with values compatible with the uncertainties associated with the derivation of the abundances.

The developed methodology to fit automatically the oxygen abundance radial profiles has meant a significant improvement in the characterisation of the inner drop and the outer flattening. As future work we want to apply this methodology to the CALIFA sample of galaxies in order to compare more directly the results based on both samples as in this case the location of the inner and outer features was fixed. In addition, the AMUSING survey is an ongoing project that is still observing new galaxies in the forthcoming semesters, increasing the size of the sample. The addition of these galaxies in the analysis will improve the statistical significance of the results. Besides, we want to properly assess if the dependence of the inner abundance drop with the galaxy mass is a direct consequence of this parameter or it is related with other properties that correlates with it such as the bulge-disc ratio. Another interesting aspect that deserves a more detailed analysis in a future work is the correlation between  $r_e$  and  $r_{O/H}$ . In this regard, the use of the CALIFA sample can help us to determine if the disc effective radius

for the mass (i.e. the radius at which half of the total mass of the galaxy is contained) is a better scale parameter than the classical  $r_e$ , which would mean that the growth rate of the disc abundance follows the mass growth rate.

### Study of the arm and interarm abundance gradients

Spiral arms are one of the most distinctive features in disc galaxies. These structures can exhibit different patterns, namely grand design and flocculent arms, with easily distinguishable characteristics. However, their origin and the mechanisms shaping them are unclear. The overall role of spirals in the chemical evolution of disc galaxies is another unsolved question. In particular, it has not been fully explored if the H II regions of spiral arms present different properties from those located in the interarm regions. Along this thesis we also studied the radial oxygen abundance gradient of the arm and interarm SF regions of a subsample of 63 galaxies using CALIFA data. We focused the analysis on three characteristic parameters of the profile: slope, zero-point, and scatter. The sample was morphologically separated into flocculent versus grand design spirals and barred versus unbarred galaxies. We find subtle but statistically significant differences between the arm and interarm distributions for flocculent galaxies, while no significant differences are found for grand design systems. In addition, we find an increase in the scatter when moving away from the spiral arms for flocculent galaxies, whereas grand designs present a similar scatter within the interarm region. All this suggests that the mechanisms generating the spiral structure in both type of galaxies may be different. Grand design arms would be linked to quasi-stationary density waves, which move across the disc affecting the gas content of the entire galaxy and diluting possible differences between the arm and interarm regions. On the other hand, flocculent arms would be associated with transient local density instabilities, that affect always the same material (SF regions in the arms), increasing the differences between the arm and the interarm regions. Another possibility is that these differences may be due to a higher star formation *outside* the spiral arms for the flocculent galaxies and a more concentrated star formation in the arms for the grand design ones. We also find small differences in barred galaxies, not observed in unbarred systems, hinting that bars may affect the chemical distribution of these galaxies but not strongly enough as to be reflected in the overall abundance distribution.

In sight of these results, it is interesting to investigate if the found abundance differences are accompanied with variations in other gas properties. Since the developed methodology for the abundance distribution analysis of the arm and interarm allows for its direct application to other parameters, as future work we plan to extend this analysis to other gas properties such as the electron density ( $n_e$ ), the dust attenuation ( $A_V$ ), and the ionising

parameter ( $U$ ). On the other hand, the extension of the analysed sample considering all finally observed CALIFA data can help us to increase the number of grand design galaxies in the sample in order to assess if the lack of differences found in this subgroup is the result of the low number of these objects analysed.

### Study of non-radial abundance variations

For this study we take advantage again of the high spatial resolution of AMUSING data to analyse the presence of possible non-radial abundance variations in order to better investigate the subtle differences found in the arm/interarm analysis performed with CALIFA data. With this purpose, we analysed in the first place the existence of local abundance variations based on a subsample of 24 galaxies. For these galaxies we derived the residual abundance distribution by subtracting the radial profile to the observed distribution. We find differences in the residual abundances spatially coincident with the location of the highest light residuals (that seem to correspond to the spiral arms in most cases). We quantified these variations with the slope ( $\gamma$ ) of the correlation between the abundance residuals and the normalised light residuals ( $g$ -band). We observed a clear correlation in 18 galaxies, being in some cases positive (11,  $\gamma > 0.1$ ) and negative in others (7,  $\gamma < -0.1$ ). We considered the cases were  $-0.1 < \gamma < 0.1$  as a lack of correlation between both parameters. Positive  $\gamma$  values correspond to more metal-rich SF regions in the brightest areas of the disc with respect to the rest of it, while negative values indicate the opposite, that is, more metal-poor SF regions in the brightest areas than in the surroundings. Analysing the dependence of  $\gamma$  with some properties of the galaxies, we find a correlation with the morphology of the spiral arms (flocculent vs. grand design arms), the characteristic abundance (which corresponds to the abundance at one disc effective radius and is representative of the average value across the disc), and the galaxy mass. This fact suggests that these properties might be the main drivers of local abundance variations in spiral galaxies. In particular, the correlation with the galaxy mass might be related to the ability of the galaxies to retain metals, as there is a larger local metal loss in low-massive galaxies with low escape velocities than in more massive systems (Barrera-Ballesteros et al. submitted).

However we note that all these results are still preliminary. As future work we plan to perform more tests to confirm them and study in more depth the physical mechanisms that might cause the observed trends in order to properly interpret them. Moreover, the increase of the analysed galaxies with forthcoming observations of AMUSING project will allow us to strengthen the statistical significance of the results.

Finally, in a second part of the study, we analyse the presence of azimuthal patterns in the abundance distribution associated with dynamic ef-

fects. We have developed a methodology that has been applied to NGC 6754, a galaxy of the sample for which some of the highest local abundance variations have been measured. For this galaxy, we also analysed the velocity distribution to find some possible links between kinematics and the observed pattern in the azimuthal abundance variations (as suggested by theoretical works). We find that the trailing (leading) edge of the NGC 6754 spiral arms show signatures of tangentially slower, radially outward (tangentially faster, radially inward) streaming motions of metal-rich (poor) gas over a large range of radii. These results show direct evidence of gas radial migration for the first time. We compared our results with the gas behaviour in an N-body disc simulation showing spiral morphological features rotating with a similar speed as the gas at every radius, in good agreement with the observed trend. This indicates that the spiral arm features in NGC 6754 may be transient, with a pattern speed decreasing with radius.

As future work, we plan to extend the analysis of the azimuthal abundance distribution and the gas kinematics to the rest of the 24 galaxies in the sample in order to determine the azimuthal patterns of the galaxies and assess the role of radial migration in these other cases.

*Las preguntas que no podemos contestar son las que más nos enseñan. Nos enseñan a pensar. Si le das a alguien una respuesta, lo único que obtiene es cierta información. Pero si le das una pregunta, él buscará sus propias respuestas.*

— Patrick Rothfuss

# Conclusiones y trabajo futuro

A PESAR DEL CONOCIMIENTO que hemos adquirido en la búsqueda de la comprensión total del Universo, cómo se forman las galaxias y evolucionan es aún materia de debate. En esta tesis hemos intentado arrojar algo de luz en este tema de estudio analizando la distribución de abundancias del gas ionizado asociado con formación estelar presente en estos sistemas.

Nuestro estudio se sustenta en dos conjuntos de datos diferentes basados en técnicas de espectroscopía de campo integral (IFS, de las siglas en inglés): una muestra de 122 galaxias extraída de la muestra *madre* de CALIFA, y una muestra de 102 galaxias parte del proyecto AMUSING. El tamaño de ambas muestras nos permite establecer conclusiones estadísticamente significativas. Con el objetivo de caracterizar la distribución en 2D de las abundancias de oxígeno hemos llevado a cabo una serie de análisis enfocados en diferentes aspectos de dicha distribución. A continuación presentaremos las conclusiones principales de cada uno de estos análisis y las líneas de estudio abiertas a raíz de este trabajo. Aunque todos estos resultados están basados en el uso del calibrador propuesto en Marino et al. (2013) para el índice O3N2 a la hora de derivar los valores de abundancia, hemos revisado otros calibradores a lo largo de la tesis para evaluar el efecto del calibrador adoptado sobre los resultados. Hemos mostrado que todos los resultados cualitativos no depen-

den de la elección del calibrador, aunque los valores en sí medidos para los diferentes parámetros analizados pueden cambiar.

### Estudio de la distribución radial de abundancias de oxígeno

Este análisis fue llevado a cabo en primer lugar *spaxel por spaxel* usando la muestra de CALIFA (122 galaxias), aprovechando así toda la información 2D para mapear adecuadamente la distribución de abundancias. Este tipo de análisis es posible porque el tamaño del spaxel de los cubos de datos de CALIFA es del orden del tamaño de una región H II, impidiéndonos resolver su estructura de ionización. Con esta premisa, analizamos también las abundancias de oxígeno derivadas para las regiones H II individuales con el propósito de realizar un estudio comparativo, obteniendo resultados equivalentes con ambos procedimientos. Además del gradiente negativo exhibido por las galaxias, se observaron una caída interna y/o un aplanamiento externo en el perfil radial de abundancias. Respecto a la tendencia negativa, encontramos que hay un gradiente característico de abundancias entre 0.5 y 2.0  $r_e$  de  $\alpha_{O/H} = -0.075 \pm 0.016$  dex/ $r_e$  cuando normalizamos las distancias galactocéntricas al radio efectivo del disco. Realizando una serie de pruebas de KS, determinamos que esta pendiente es independiente de propiedades de las galaxias como la morfología, la magnitud absoluta y la presencia o ausencia de barras. En particular, las galaxias barradas no parecen presentar gradientes más planos, como parecían simulaciones numéricas y fue descrito en antiguos estudios (p.ej. Zaritsky et al. 1994). De forma interesante, encontramos que un gran número de galaxias con valores de abundancia fiables a partir de dos radios efectivos (57) presentan un aplanamiento del gradiente en estas partes externas. Este aplanamiento no está asociado con ninguna característica morfológica, lo que sugiere que es una propiedad común de las galaxias de disco. Finalmente, detectamos una caída o truncamiento de la abundancia en las regiones internas del disco en 27 galaxias de la muestra; esta caída sólo es visible en los sistemas más masivos.

Para este estudio, los parámetros morfológicos (inclinación y ángulo de posición) de las galaxias necesarios para derivar las distribuciones de abundancias de proyectadas fueron calculados llevando a cabo un análisis de los momentos de luz (Walcher et al. 2014). Sin embargo, más tarde durante el curso de esta tesis volvimos a obtener estos parámetros como resultado de una descomposición fotométrica en 2D de las galaxias de CALIFA (Méndez-Abreu et al. 2017). La comparación de los valores de estos parámetros entre ambas metodologías muestra notables diferencias para un porcentaje pequeño de galaxias (sobre el 15%). Como trabajo futuro queremos evaluar el efecto de estas diferencias en la derivación de la distribución radial de abundancias para así verificar la robustez de nuestros resultados. Además, el número de galaxias observadas en el proyecto CALIFA ha aumentado desde que este análisis fue llevado a cabo, y por lo tanto, la inclusión de es-

tas nuevas galaxias en el estudio nos puede ayudar a mejorar la significancia estadística de los resultados.

La alta resolución espacial de los datos de AMUSING nos permitió mejorar el estudio de la distribución radial de abundancias de oxígeno. Este conjunto de datos nos ayudó a aumentar el número de regiones H II detectadas en galaxias individuales con respecto a previos estudios. Además, pudimos evitar los efectos de dilución y reducir la contaminación de la emisión difusa en las regiones detectadas, efectos que estaban presentes en el análisis spaxel por spaxel con CALIFA. En este análisis con AMUSING desarrollamos una nueva metodología para ajustar automáticamente los perfiles radiales, encontrando que 55 galaxias de la muestra exhiben un único gradiente negativo. Las restantes galaxias también presentan, además de esta tendencia negativa, una caída interna en la abundancia (21), un aplanamiento externo (10), o ambos (16), lo que sugiere que estas características son un distintivo común de las galaxias de disco. Confirmamos los resultados encontrados con CALIFA: la presencia y profundidad de la caída interna depende de la masa estelar de las galaxias, con los sistemas más masivos presentando las caídas de abundancia más pronunciadas, mientras que no existe tal dependencia en el caso del aplanamiento externo. Al contrario que en el estudio anterior, donde la posición radial de estas características fue deducida visualmente a partir de la forma general del perfil radial, en este análisis la metodología desarrollada nos permitió determinar automáticamente su posición real. Encontramos que la caída interna aparece siempre en torno a  $0.5 r_e$ , mientras que la posición del aplanamiento externo varía dentro de un rango amplio de distancias galactocéntricas. Respecto al gradiente negativo, encontramos una pendiente característica en la muestra de  $\alpha_{O/H} = -0.10 \pm 0.03 \text{ dex}/r_e$  (compatible con el valor calculado con los datos de CALIFA). Esta pendiente es independiente de la presencia de barras y la densidad del ambiente. Sin embargo, cuando se detectan caídas internas o aplanamientos externos en la abundancia, se observan gradientes ligeramente más pronunciados. Este hecho sugiere que movimientos radiales del gas pueden jugar un papel importante moldeando los perfiles de abundancia. Por otro lado, definimos una nueva escala de normalización (la ‘escala de abundancia’,  $r_{O/H}$ ) de los perfiles radiales basada en el gradiente de abundancias característico, con la cuál todas las galaxias presentan una posición galactocéntrica similar de la caída interna ( $\sim 0.5 r_{O/H}$ ) y del aplanamiento externo ( $\sim 1.5 r_{O/H}$ ). Finalmente, el análisis de la dispersión en torno al gradiente negativo no muestra una dependencia significativa con ninguna propiedad de las galaxias, con valores compatibles con las incertidumbres asociadas a la derivación de las abundancias.

La metodología desarrollada para ajustar automáticamente los perfiles radiales de abundancia de oxígeno han resultado una mejora significativa en la caracterización de la caída interna de abundancias y del aplanamiento

externo. Como trabajo futuro planeamos aplicar esta metodología a la muestra de galaxias de CALIFA con el fin de llevar a cabo una comparación más directa de los resultados basados en las dos muestras utilizadas, ya que en este caso la localización de estas desviaciones (interna y externa) fue fijada. Además, el cartografiado de AMUSING es un proyecto en curso que sigue observando nuevas galaxias en los próximos semestres, aumentando el tamaño de la muestra. La inclusión de estas galaxias en el análisis mejorará la significancia estadística de los resultados. Por otro lado, queremos evaluar en mayor profundidad si la dependencia de la caída interna de la abundancia con la masa de la galaxia es consecuencia directa de este parámetro o surge a raíz de otras propiedades que correlan con ésta, como el cociente bulbo-disco. Otro aspecto interesante que merece un análisis más detallado como trabajo futuro es la correlación entre  $r_e$  y  $r_{OH}$ . En este sentido, el uso de la muestra de CALIFA puede ayudarnos a determinar si el radio efectivo de la masa (es decir, el radio que contiene la mitad de la masa total de la galaxia) es un mejor parámetro de escala que el clásico  $r_e$  (obtenido a partir de la luz), lo que significaría que la tasa de crecimiento de la abundancia del disco sigue a la de la masa.

### Estudio de los gradientes de abundancia del brazo y del interbrazo

Los brazos espirales son una de los rasgos más distintivos de las galaxias de disco. Estas estructuras pueden presentar diferentes patrones, concretamente brazos *gran diseño* o *floculentos*, con características fácilmente distinguibles. Sin embargo, su origen y los mecanismos que las generan no están claros. El papel de los brazos espirales en la evolución química de las galaxias de disco es otra pregunta aún sin resolver. En particular, no se ha explorado en profundidad si las regiones H II de los brazos espirales presentan diferentes propiedades de las que se encuentran en la zona interbrazo. A lo largo de esta tesis también estudiamos los gradientes radiales de abundancia de oxígeno de las regiones de formación estelar (regiones SF, por sus siglas en inglés) de una submuestra de 63 galaxias usando los datos de CALIFA. Enfocamos el análisis en tres parámetros característicos del gradiente: la pendiente, la ordenada en el origen, y la dispersión. La muestra fue separada morfológicamente en galaxias floculentas y gran diseño y también en barradas y no barradas. Encontramos diferencias sutiles pero estadísticamente significativas entre las distribuciones del brazo y del interbrazo para galaxias floculentas, mientras que no se encuentran diferencias significativas para los sistemas gran diseño. Además, encontramos un aumento en la dispersión a medida que nos alejamos de los brazos espirales en las primeras, mientras que las últimas presentan una dispersión similar en toda la región interbrazo. Todo esto sugiere que los mecanismos que generan la estructura espiral en ambos tipos de galaxias pueden ser diferentes. Los brazos gran diseño estarían asociados con ondas de densidad cuasi-estacionarias, que se mueven a



través del disco afectando al contenido en gas de toda la galaxia y diluyendo posibles diferencias entre las regiones SF del brazo y del interbrazo. Por otro lado, los brazos floculentos estarían vinculados con inestabilidades locales y transitorias de la densidad, que afectan siempre al mismo material (regiones SF en los brazos), aumentando las diferencias entre las zonas brazo e interbrazo. Otra posibilidad es que estas diferencias se deban a una mayor formación estelar *fuera* de los brazos espirales para las galaxias floculentas y una formación estelar más concentrada en los brazos para las gran diseño. Encontramos también pequeñas diferencias en galaxias barradas, que no se observan en sistemas no barrados, siendo indicio de que las barras pueden afectar a la distribución química de estas galaxias pero no lo suficiente como para reflejarse en la distribución global de abundancias.

A la vista de estos resultados, sería interesante investigar si las diferencias encontradas en la abundancia vienen acompañadas de variaciones en otras propiedades del gas. Puesto que la metodología desarrollada para el análisis de la distribución de abundancias del brazo y del interbrazo nos facilita su aplicación directa a otros parámetros, como trabajo futuro planeamos extender este análisis a otras propiedades del gas como la densidad electrónica ( $n_e$ ), la extinción por polvo ( $A_V$ ) y el parámetro de ionización ( $U$ ). Por otra parte, la extensión de la muestra analizada considerando todas las galaxias finalmente observadas por el proyecto CALIFA puede ayudarnos a incrementar el número de sistemas gran diseño en la muestra con el fin de evaluar si la ausencia de diferencias encontrada en este subgrupo de galaxias es resultado del bajo número analizado de estos objetos.

### Estudio de las variaciones no radiales de la abundancia

Para este estudio sacamos provecho de nuevo de la alta resolución espacial de los datos de AMUSING para analizar la presencia de posibles variaciones no radiales en la abundancia con el objetivo de investigar en más detalle las sutiles diferencias encontradas en el análisis brazo/interbrazo llevado a cabo con los datos de CALIFA. Con este fin, analizamos en primer lugar la existencia de variaciones locales en la abundancia basándonos en una submuestra de 24 galaxias. Para estas galaxias derivamos la distribución residual de abundancias sustrayendo el perfil radial a la distribución observada. Encontramos diferencias en las abundancias residuales espacialmente coincidentes con la posición de los mayores residuos de luz (que parecen corresponder con los brazos espirales en la mayoría de los casos). Cuantificamos estas variaciones con la pendiente (parámetro  $\gamma$ ) de la correlación entre los residuos de abundancia y los residuos normalizados de luz (banda  $g$ ). Observamos una correlación clara en 18 galaxias, siendo en algunos casos positiva (11,  $\gamma > 0.1$ ) y negativa en otros (7,  $\gamma < -0.1$ ). Los casos con  $-0.1 < \gamma < 0.1$  se consideran como una ausencia de correlación entre ambos parámetros. Valores positivos de  $\gamma$  se asocian con la presencia de regiones

SF más metálicas en las áreas más brillantes del disco respecto al resto de éste, mientras que valores negativos indican lo opuesto, es decir, regiones SF menos metálicas en las áreas más brillantes que en los alrededores. Analizando la dependencia de  $\gamma$  con algunas propiedades de las galaxias encontramos una correlación con la morfología de los brazos espirales (floculentos o gran diseño), la abundancia característica (que se corresponde con la abundancia a un radio efectivo del disco, representativa del valor medio en todo el disco), y la masa de la galaxia. Este hecho sugiere que estas propiedades pueden ser los principales responsables de la existencia de variaciones locales de la abundancia en galaxias espirales. En particular, la correlación con la masa puede estar relacionada con la capacidad de estas galaxias para retener metales, ya que hay una mayor pérdida de metales en galaxias de baja masa con velocidades de escape menores que en sistemas más masivos (Barrera-Ballesteros et al. enviado).

Sin embargo, queremos resaltar que todos estos resultados son aún preliminares. Como trabajo futuro planeamos llevar a cabo más pruebas que confirmen estas conclusiones y estudiar en mayor profundidad los mecanismos físicos que puedan causar las tendencias observadas, con el fin de interpretarlas correctamente. Además, el aumento de galaxias a analizar con próximas observaciones concedidas al proyecto AMUSING nos permitirá reforzar la significancia estadística de los resultados.

Finalmente, como segunda parte de este estudio, analizamos la presencia de patrones acimutales en la distribución de abundancias asociados con efectos dinámicos. Hemos desarrollado una metodología que ha sido aplicada a NGC 6754, una galaxia de la muestra para la cuál se han medido algunas de las variaciones locales de abundancia más grandes. Para esta galaxia hemos analizado también la distribución de velocidades con el fin de encontrar posibles conexiones entre la cinemática del gas y el patrón observado en las variaciones acimutales de la abundancia (como han sugerido trabajos teóricos). Encontramos que el lado frontal, o *trailing*, (posterior, o *leading*) de los brazos espirales de NGC 6754 muestra indicios de movimientos tangencialmente más lentos y radialmente hacia afuera (tangencialmente más rápidos y radialmente hacia adentro) de gas rico (pobre) en metales a lo largo de un rango amplio de distancias galactocéntricas. Estos resultados muestran por primera vez evidencia directa de migración radial del gas. Comparamos nuestros resultados con el comportamiento del gas en una simulación de N-cuerpos de una galaxia de disco que presenta brazos espirales rotando a una velocidad similar a la del gas a cada radio, en concordancia con la tendencia observada. Ésto indica que la estructura espiral en NGC 6754 puede ser transitoria, con un patrón de velocidad que decrece con el radio.

Como trabajo futuro planeamos extender este análisis de la distribución acimutal de abundancias y la cinemática del gas a las 23 galaxias restantes

.....

de la muestra, con el objetivo de determinar los patrones acimutales de la abundancia en estas galaxias y evaluar el papel de la migración radial en estos otros casos.







# Appendices







# CALIFA sample characterisation tables

In this appendix we summarise the main properties of the CALIFA galaxies analysed in this thesis. We present several tables with general information (see Table A.1) and oxygen abundance information derived in this work (see Table A.2) for these galaxies. From left to right the columns correspond to

**Table A.1:** CALIFA sample characterisation I: general properties.

(a) Name of the galaxy; (b)–(c) right ascension and declination (referred to J2000); (d) morphological type; (e) arm classification into flocculent (F) or grand design (G) galaxy (AC) for the subsample analysed in Chapter 6; (f) redshift; (g) distance to the galaxy using the WMAP9 cosmology (Hinshaw et al. 2013); (h) the logarithm of the integrated stellar mass in units of solar masses; (i)  $g$ -band absolute magnitude; (j) disc effective radius ( $r_e$ , in kpc); and (k)–(l) position and inclination angles (see Sect. 3.4 for details in the derivation of these parameters).

**Table A.2:** CALIFA sample characterisation II: abundance information.

(a) Name of the galaxy; (b) oxygen abundance value at one effective radius ( $[\text{O}/\text{H}]_{r_e}$ ); (c) slope of the oxygen abundance gradient measured between 0.5 and 2.0  $r_e$  ( $\alpha_{\text{O}/\text{H}}$ ); (d) slope of the oxygen abundance gradient of the arm/interarm regions; (e) zero-point of the oxygen abundance gradient of the arm/interarm regions; and (f) dispersion of the oxygen abundance gradient of the arm/interarm regions. The errors on the measured parameters are given in parentheses.

<sup>†</sup> galaxies with low number of spaxels associated with SF regions needed to perform the linear fit of the oxygen abundance radial profile.

**Table A.1:** CALIFA sample characterisation I: general properties. Details are given in Appendix A above.

Name	RA [h m s]	DEC [° ′ ″]	Morph type	AC	z	Dist [Mpc]	log(M) [M <sub>⊙</sub> ]	M <sub>g</sub> [mag]	r <sub>e</sub> [kpc]	PA [°]	i [°]
(a)	(b)	(c)	(d)	(e)	(f)	(g)	(h)	(i)	(j)	(k)	(l)
IC0159	01 46 25.05	-08 38 11.83	SBdm	—	0.01265	55.25	9.82	-19.99	5.4	16	39
IC0674	11 11 06.36	+43 37 58.80	SBab	—	0.02643	116.65	10.91	-21.43	11.5	125	50
IC0776	12 19 03.12	+08 51 22.14	Sdm	—	0.00978	42.61	9.27	-19.11	8.4	86	56
IC1256	17 23 47.28	+26 29 11.47	SABb	—	0.01753	76.87	10.37	-20.73	6.8	91	54
IC1683	01 22 38.93	+34 26 13.67	SABb	—	0.01591	69.65	10.51	-20.45	4.8	166	54
IC4566	15 36 42.16	+43 32 21.55	SBb	—	0.02100	92.31	10.94	-21.27	10.3	148	46
MCG-01-10-019	03 40 42.98	-06 24 54.58	SABbc	—	0.01700	74.51	10.21	-20.62	12.0	12	55
NGC0001	00 07 15.86	+27 42 29.09	Sbc	F	0.01499	65.60	10.80	-21.07	6.0	108/97	37/51
NGC0036	00 11 22.30	+06 23 21.66	SBb	G	0.01972	86.58	10.90	-21.77	14.6	77/19	50/60
NGC0160	00 36 04.11	+23 57 28.48	Sa	—	0.01716	75.21	11.06	-21.55	11.4	49	51
NGC0165	00 36 28.92	-10 06 22.18	SBb	—	0.01921	84.32	10.59	-21.09	13.0	88	35
NGC0171	00 37 21.55	-19 56 03.23	SBb	—	0.01285	56.15	10.72	-21.26	7.0	112	51
NGC0180	00 37 57.70	+08 38 06.58	SBb	—	0.01719	75.34	10.89	-21.78	12.8	159	50
NGC0214	00 41 28.04	+25 29 57.77	SABbc	F	0.01483	64.89	10.85	-21.60	6.7	62/58	49/46
NGC0234	00 43 32.39	+14 20 33.25	SABc	F	0.01449	63.39	10.65	-21.40	6.4	75/71	32/29
NGC0237	00 43 27.84	-00 07 29.75	SBc	F	0.01359	59.40	10.28	-20.72	4.3	144/177	55/53
NGC0257	00 48 01.51	+08 17 49.45	Sc	G	0.01714	75.10	10.80	-21.60	8.7	92/94	55/52
NGC0309	00 56 42.66	-09 54 49.93	SBcd	G	0.01844	80.88	10.83	-22.38	13.4	108/109	33/28
NGC0447	01 15 37.64	+33 04 03.97	SBa	—	0.01827	80.12	11.39	-21.69	13.6	20	53
NGC0477	01 21 20.48	+40 29 17.34	SABbc	—	0.01925	84.52	10.50	-21.24	14.3	142	49
NGC0496	01 23 11.59	+33 31 45.37	Scd	F	0.01959	86.02	10.35	-20.93	10.9	38/34	55/56
NGC0570	01 28 58.64	-00 56 56.40	SBb	—	0.01780	78.06	10.96	-21.24	8.6	102	46
NGC0716	01 52 59.68	+12 42 30.49	SABb	F	0.01470	64.30	10.58	-20.72	5.5	57/63	50/62
NGC0768	01 58 40.94	+00 31 45.16	SBc	G	0.02271	99.97	10.55	-21.33	10.4	115/25	57/66

Table A.1: *Continued.*

Name	RA [h m s]	DEC [° ' '']	Morph type	AC	z	Dist [Mpc]	log(M) [M <sub>⊙</sub> ]	M <sub>g</sub> [mag]	r <sub>e</sub> [kpc]	PA [°]	i [°]
(a)	(b)	(c)	(d)	(e)	(f)	(g)	(h)	(i)	(j)	(k)	(l)
NGC0776	01 59 54.53	+23 38 39.41	SBb	G	0.01593	69.74	10.70	-21.26	6.9	142/144	46/29
NGC0787	02 00 48.62	-09 00 09.29	Sa	—	0.01525	66.74	10.96	-21.30	6.7	81	36
NGC0873	02 16 32.37	-11 20 54.53	Scd	F	0.01296	56.60	10.41	-21.17	4.3	122/141	31/32
NGC0941	02 28 27.88	-01 09 05.26	Scd	—	0.00519	22.54	9.35	-19.13	2.9	156	30
NGC0976	02 34 00.03	+20 58 36.30	Sbc	—	0.01387	60.63	10.80	-21.50	5.7	170	36
NGC0991	02 35 32.68	-07 09 15.95	SABcd	F	0.00492	21.37	9.61	-19.38	3.6	85/105	23/20
NGC1070	02 43 22.27	+04 58 06.02	Sb	—	0.01315	57.44	11.00	-21.73	7.1	2	35
NGC1093	02 48 16.14	+34 25 11.35	SBbc	—	0.01722	75.47	10.75	-20.82	7.3	109	52
NGC1094	02 47 27.83	-00 17 06.47	SABb	G	0.02088	91.79	10.72	-21.55	7.4	90/93	45/47
NGC1659	04 46 29.94	-04 47 19.86	SABbc	F	0.01500	65.65	10.59	-21.15	6.3	45/50	54/50
NGC1667	04 48 37.18	-06 19 11.93	SBbc	F	0.01490	65.17	10.80	-22.02	4.9	173/172	50/46
NGC2253	06 43 41.84	+65 12 22.97	SBbc	F	0.01249	54.54	10.47	-21.06	2.5	137/129	30/38
NGC2347	07 16 04.09	+64 42 40.79	SABbc	F	0.01534	67.14	10.72	-21.66	6.3	8/0	50/59
NGC2449	07 47 20.30	+26 55 48.72	SABab	—	0.01688	73.96	10.83	-20.98	5.9	23	60
NGC2486	07 57 56.49	+25 09 39.13	SBab	—	0.01614	70.70	10.58	-20.64	9.6	79	49
NGC2487	07 58 20.46	+25 08 57.16	SBb	—	0.01677	73.49	10.77	-21.68	12.0	42	48
NGC2530	08 07 55.61	+17 49 06.60	SABd	F	0.01745	76.49	10.19	-20.96	9.8	107/151	37/27
NGC2540	08 12 46.45	+26 21 42.41	SBbc	F	0.02165	95.20	10.50	-21.15	8.3	131/126	45/52
NGC2604	08 33 23.14	+29 32 19.72	SBd	F	0.00787	34.25	9.64	-19.97	4.1	171/36	28/23
NGC2639	08 43 38.07	+50 12 19.94	Sa	—	0.01206	52.66	11.18	-21.59	4.9	134	59
NGC2730	09 02 15.82	+16 50 17.84	SBcd	—	0.01380	60.33	10.11	-20.56	7.8	65	50
NGC2805	09 20 20.38	+64 06 10.69	Sc	—	0.00695	30.22	10.03	-20.30	7.9	18	41
NGC2906	09 32 06.22	+08 26 30.37	Sbc	F	0.00815	35.46	10.39	-20.14	3.4	87/82	59/56
NGC2916	09 34 57.60	+21 42 18.94	Sbc	G	0.01363	59.57	10.75	-21.57	8.1	13/16	54/49

Table A.1: *Continued.*

Name	RA [h m s]	DEC [° ′ ″]	Morph type	AC	z	Dist [Mpc]	log(M) [M <sub>⊙</sub> ]	M <sub>g</sub> [mag]	r <sub>e</sub> [kpc]	PA [°]	i [°]
(a)	(b)	(c)	(d)	(e)	(f)	(g)	(h)	(i)	(j)	(k)	(l)
NGC3057	10 05 39.51	+80 17 12.01	SBdm	F	0.00630	27.38	9.18	-19.01	6.0	2/3	55/55
NGC3106	10 04 05.25	+31 11 07.66	Sab	—	0.02193	96.45	11.31	-22.16	13.3	141	22
NGC3381	10 48 24.82	+34 42 41.08	SBd	F	0.00702	30.51	9.68	-19.74	3.1	48/49	45/35
NGC3614	11 18 21.33	+45 44 53.41	SABbc	F	0.00935	40.73	10.21	-20.72	9.6	98/99	44/51
NGC3687	11 28 00.60	+29 30 39.78	SBb	—	0.01001	43.63	10.28	-20.47	4.7	156	23
NGC3811	11 41 16.63	+47 41 26.92	SBbc	F	0.01192	52.05	10.45	-20.92	5.4	13/11	52/47
NGC4047	12 02 50.68	+48 38 10.32	Sbc	F	0.01297	56.66	10.68	-21.41	5.1	99/101	38/39
NGC4185	12 13 22.19	+28 30 39.46	SABbc	—	0.01483	64.89	10.72	-21.35	10.3	169	50
NGC4210	12 15 15.84	+65 59 07.15	SBb	G	0.01052	45.86	10.28	-20.46	4.4	91/94	43/43
NGC4470	12 29 37.78	+07 49 27.12	Sc	—	0.00933	40.66	9.98	-20.37	3.5	3	49
NGC4961	13 05 47.56	+27 44 02.90	SBcd	—	0.01034	45.07	9.68	-19.97	3.9	107	49
NGC5000	13 09 47.49	+28 54 24.98	SBbc	G	0.02066	90.77	10.66	-21.32	8.2	82/71	53/37
NGC5016	13 12 06.68	+24 05 42.04	Sbc	F	0.01059	46.18	10.23	-20.61	4.6	59/57	43/43
NGC5056	13 16 12.32	+30 57 01.12	SABc	F	0.02059	90.46	10.45	-21.43	8.6	0/1	54/59
NGC5157	13 27 16.85	+32 01 50.56	SBab	—	0.02631	116.11	11.27	-21.81	10.1	129	43
NGC5205	13 30 03.57	+62 30 41.62	SBbc	—	0.00752	32.73	9.88	-19.66	3.8	147	48
NGC5320	13 50 20.38	+41 21 58.39	SABbc	F	0.01061	46.28	10.29	-20.72	8.2	123/13	57/58
NGC5376	13 55 16.05	+59 30 23.80	SABb	F	0.00859	37.40	10.47	-20.31	3.8	65/65	52/55
NGC5378	13 56 51.01	+37 47 50.06	SBb	—	0.01206	52.63	10.62	-20.64	7.4	60	51
NGC5406	14 00 20.12	+38 54 55.51	SBb	—	0.01923	84.40	11.19	-21.94	9.7	68	28
NGC5480	14 06 21.58	+50 43 30.22	Scd	—	0.00801	34.86	10.14	-20.30	3.1	159	48
NGC5519	14 14 20.87	+07 30 57.24	SBb	—	0.02708	119.57	10.76	-21.40	19.3	89	45
NGC5520	14 12 22.81	+50 20 54.31	Sbc	F	0.00808	35.18	9.85	-19.77	3.4	66/65	55/60
NGC5533	14 16 07.74	+35 20 37.79	Sab	—	0.01485	64.97	11.23	-21.91	14.2	30	52

Table A.1: *Continued.*

Name	RA [h m s]	DEC [° ' '' ]	Morph type	AC	z	Dist [Mpc]	log(M) [M <sub>⊙</sub> ]	M <sub>g</sub> [mag]	r <sub>e</sub> [kpc]	PA [°]	i [°]
(a)	(b)	(c)	(d)	(e)	(f)	(g)	(h)	(i)	(j)	(k)	(l)
NGC5622	14 26 12.20	+48 33 50.33	Sbc	G	0.01465	64.10	10.22	-20.41	6.5	171/83	60/59
NGC5633	14 27 28.38	+46 08 47.69	Sbc	F	0.00964	41.99	10.27	-20.44	2.5	13/14	50/48
NGC5656	14 30 25.51	+35 19 15.71	Sb	—	0.01250	54.60	10.62	-21.11	4.3	56	51
NGC5657	14 30 43.59	+29 10 50.95	SBbc	—	0.01505	65.87	10.28	-20.48	6.9	2	58
NGC5665	14 32 25.74	+08 04 43.10	SABc	—	0.00907	39.52	10.22	-20.66	4.7	158	33
NGC5720	14 38 33.28	+50 48 54.86	SBbc	—	0.02753	121.61	10.85	-21.79	12.3	129	50
NGC5732	14 40 38.95	+38 38 16.15	Sbc	F	0.01442	63.07	9.93	-20.06	6.5	40/40	55/55
NGC5735	14 42 33.24	+28 43 35.22	SBbc	G	0.01450	63.43	10.38	-21.02	8.1	87/30	34/29
NGC5772	14 51 38.88	+40 35 56.98	Sab	F	0.01821	79.86	10.94	-21.56	9.4	39/36	55/58
NGC5829	15 02 42.00	+23 20 01.03	Sc	G	0.02089	91.82	10.53	-21.36	10.8	96/35	41/45
NGC5888	15 13 07.37	+41 15 52.67	SBb	—	0.03082	136.48	11.29	-22.06	11.4	158	57
NGC5947	15 30 36.59	+42 43 01.78	SBbc	F	0.02141	94.14	10.37	-21.02	7.7	62/62	34/35
NGC5957	15 35 23.22	+12 02 51.32	SBb	F	0.00779	33.91	10.28	-20.34	4.7	89/90	41/16
NGC6004	15 50 22.72	+18 56 21.37	SBbc	G	0.01480	64.76	10.71	-21.30	8.0	73/99	20/35
NGC6063	16 07 12.99	+07 58 44.36	Sbc	F	0.01136	49.55	10.06	-20.05	6.3	152/155	53/56
NGC6154	16 25 30.48	+49 50 24.94	SBab	—	0.02159	94.96	10.95	-21.63	9.4	134	50
NGC6155	16 26 08.33	+48 22 00.44	Sc	—	0.00980	42.69	10.12	-20.28	3.5	149	47
NGC6301	17 08 32.75	+42 20 20.83	Sbc	—	0.02928	129.53	11.02	-22.23	15.7	109	53
NGC6497	17 51 17.97	+59 28 15.13	SBab	—	0.02171	95.46	11.04	-21.39	21.9	127	49
NGC6941	20 36 23.47	-04 37 07.46	SBb	G	0.02156	94.82	10.93	-21.85	12.1	122/131	43/44
NGC7321	22 36 28.02	+21 37 18.37	SBbc	—	0.02381	104.88	10.81	-22.06	9.6	31	46
NGC7364	22 44 24.37	-00 09 43.56	Sab	—	0.01633	71.51	10.89	-21.41	5.9	65	50
NGC7466	23 02 03.46	+27 03 09.36	Sbc	F	0.02489	109.74	10.83	-21.29	12.3	21/25	58/67
NGC7489	23 07 32.70	+22 59 53.12	Sbc	F	0.02070	90.95	10.40	-21.79	10.6	165/164	57/56

Table A.1: *Continued.*

Name	RA [h m s]	DEC [° ′ ″]	Morph type	AC	z	Dist [Mpc]	log(M) [ $M_{\odot}$ ]	$M_g$ [mag]	$r_e$ [kpc]	PA [°]	$i$ [°]
(a)	(b)	(c)	(d)	(e)	(f)	(g)	(h)	(i)	(j)	(k)	(l)
NGC7591	23 18 16.26	+06 35 08.84	SBbc	G	0.01644	72.03	10.75	-21.35	8.4	160/148	54/61
NGC7625	23 20 30.14	+17 13 32.02	Sa	—	0.00578	25.10	10.07	-19.71	2.0	32	39
NGC7653	23 24 49.36	+15 16 32.16	Sb	F	0.01418	61.99	10.50	-21.11	6.2	163/163	28/34
NGC7691	23 32 24.42	+15 50 52.26	SBbc	—	0.01342	58.65	10.21	-20.97	8.9	157	39
NGC7716	23 36 31.45	+00 17 50.17	Sb	F	0.00867	37.76	10.32	-20.56	4.5	27/41	45/34
NGC7782	23 53 53.88	+07 58 14.16	Sb	—	0.01766	77.44	11.18	-21.94	10.8	178	57
NGC7787	23 56 07.82	+00 32 58.13	SABab	—	0.02186	96.15	10.51	-20.50	8.4	3	51
NGC7819	00 04 24.51	+31 28 19.24	Sc	F	0.01635	71.63	10.39	-20.68	8.4	87/102	58/58
NGC7824	00 05 06.24	+06 55 12.54	Sab	—	0.02006	88.11	11.30	-21.47	11.6	160	41
UGC00005	00 03 05.64	-01 54 49.79	Sbc	F	0.02383	104.96	10.83	-21.50	9.6	55/49	57/59
UGC00036	00 05 13.88	+06 46 19.31	SABab	—	0.02059	90.49	10.98	-20.94	8.6	9	53
UGC01918	02 27 32.48	+25 40 07.57	SBb	—	0.01646	72.10	10.56	-20.53	8.0	120	57
UGC02311	02 49 27.95	-00 52 22.76	SBbc	G	0.02300	101.27	10.74	-21.59	7.9	43/52	57/48
UGC03253	05 19 41.88	+84 03 09.43	SBb	—	0.01447	63.30	10.68	-20.43	6.5	67	52
UGC03973	07 42 32.82	+49 48 34.78	SBbc	—	0.02265	99.67	10.74	-21.86	7.7	60	57
UGC04195	08 05 06.90	+66 46 58.94	SBb	F	0.01699	74.45	10.50	-20.68	8.0	112/13	52/55
UGC04262	08 19 02.78	+83 15 59.26	SABbc	F	0.01967	86.37	10.60	-21.26	12.3	155/150	45/49
UGC04308	08 17 25.80	+21 41 07.76	SBc	—	0.01268	55.40	10.30	-20.95	6.7	111	41
UGC04375	08 23 11.24	+22 39 52.74	Sbc	—	0.00772	33.60	10.16	-19.90	6.1	178	46
UGC05108	09 35 26.28	+29 48 45.43	SBb	—	0.02800	123.71	10.89	-21.51	17.8	135	40
UGC07012	12 02 03.15	+29 50 52.73	SABcd	F	0.01203	52.52	9.45	-19.68	5.3	13/14	57/57
UGC08781	13 52 22.74	+21 32 21.66	SBb	G	0.02738	120.95	11.05	-21.69	17.6	171/165	59/54
UGC09291	14 28 36.89	+38 59 56.94	Scd	F	0.01157	50.50	10.34	-20.32	7.6	107/107	59/59
UGC09476	14 41 32.03	+44 30 45.97	Sbc	—	0.01273	55.59	10.21	-20.49	5.9	117	51

Table A.1: *Continued.*

Name	RA [h m s]	DEC [° ' '' ]	Morph type	AC	z	Dist [Mpc]	log(M) [M <sub>⊙</sub> ]	M <sub>g</sub> [mag]	r <sub>e</sub> [kpc]	PA [°]	i [°]
(a)	(b)	(c)	(d)	(e)	(f)	(g)	(h)	(i)	(j)	(k)	(l)
UGC09492	14 44 12.18	+07 56 58.70	SABab	—	0.02993	132.45	11.20	-21.62	11.1	66	59
UGC09777	15 14 15.15	+20 28 43.14	Sbc	F	0.01776	77.89	10.31	-20.47	7.7	145/146	53/55
UGC09842	15 25 05.80	+37 57 36.61	SBbc	G	0.03147	139.41	10.63	-21.18	14.3	169/64	60/65
UGC11649	20 55 27.62	-01 13 30.86	SBab	—	0.01346	58.84	10.66	-20.84	6.2	94/71	28/32
UGC12224	22 52 38.36	+06 05 37.03	Sc	F	0.01186	51.77	9.97	-20.48	7.8	31/36	34/32
UGC12633	23 30 13.64	+15 45 39.67	SABab	—	0.01399	61.15	10.37	-20.35	7.1	146	46
UGC12767	23 45 10.20	+07 02 31.60	SBb	—	0.01732	75.90	10.94	-21.79	12.2	34	30
UGC12816	23 51 50.69	+03 04 57.90	Sc	F	0.01751	76.75	9.82	-20.35	8.6	145/140	52/60
UGCA021	01 49 10.36	-10 03 40.46	SBdm	—	0.00642	27.89	9.45	-19.48	5.1	109	20

**Table A.2:** CALIFA sample characterisation II: oxygen abundance information. Details are given in Appendix A above.

Name	$[\text{O}/\text{H}]_{r_e}$ [dex]	$\alpha_{\text{O}/\text{H}}$ [dex/ $r_e$ ]	$\alpha_{\text{ar}} / \alpha_{\text{in}}$ [dex/ $r_e$ ]	$[\text{O}/\text{H}]_{0,\text{ar}} / [\text{O}/\text{H}]_{0,\text{in}}$ [dex]	$\Delta [\text{O}/\text{H}]_{\text{ar}} / \Delta [\text{O}/\text{H}]_{\text{in}}$ [dex]
(a)	(b)	(c)	(d)	(e)	(f)
IC0159	8.40 (0.06)	-0.03 (0.03)	—	—	—
IC0674	8.44 (0.07)	-0.10 (0.02)	—	—	—
IC0776	8.27 (0.05)	-0.08 (0.04)	—	—	—
IC1256	8.58 (0.06)	-0.15 (0.02)	—	—	—
IC1683	8.57 (0.05)	-0.08 (0.05)	—	—	—
IC4566	8.54 (0.03)	0.00 (0.04)	—	—	—
MCG-01-10-019	8.40 (0.06)	-0.12 (0.04)	—	—	—
NGC0001	8.56 (0.06)	-0.02 (0.02)	-0.051 (0.004) / -0.060 (0.004)	8.634 (0.006) / 8.629 (0.005)	0.052 (0.002) / 0.056 (0.002)
NGC0036	8.53 (0.07)	-0.04 (0.03)	-0.065 (0.009) / -0.089 (0.006)	8.620 (0.008) / 8.619 (0.008)	0.055 (0.002) / 0.058 (0.002)
NGC0160	8.53 (0.08)	-0.05 (0.07)	—	—	—
NGC0165	8.51 (0.04)	-0.07 (0.04)	—	—	—
NGC0171	8.58 (0.06)	-0.07 (0.02)	—	—	—
NGC0180†	—	—	—	—	—
NGC0214	8.58 (0.05)	-0.06 (0.02)	-0.052 (0.011) / -0.068 (0.003)	8.628 (0.010) / 8.644 (0.005)	0.055 (0.002) / 0.053 (0.002)
NGC0234	8.58 (0.05)	-0.07 (0.02)	-0.032 (0.006) / -0.087 (0.003)	8.625 (0.005) / 8.660 (0.004)	0.049 (0.002) / 0.057 (0.001)
NGC0237	8.56 (0.05)	-0.07 (0.02)	-0.109 (0.006) / -0.091 (0.003)	8.661 (0.008) / 8.653 (0.004)	0.044 (0.002) / 0.048 (0.001)
NGC0257	8.57 (0.05)	-0.07 (0.02)	-0.084 (0.006) / -0.098 (0.004)	8.645 (0.007) / 8.651 (0.004)	0.052 (0.002) / 0.057 (0.002)
NGC0309	8.50 (0.05)	-0.15 (0.03)	-0.158 (0.008) / -0.157 (0.006)	8.685 (0.008) / 8.662 (0.005)	0.053 (0.002) / 0.050 (0.001)
NGC0447†	—	—	—	—	—
NGC0477	8.43 (0.08)	-0.19 (0.06)	—	—	—
NGC0496	8.46 (0.06)	-0.14 (0.03)	-0.136 (0.011) / -0.153 (0.005)	8.610 (0.010) / 8.626 (0.005)	0.054 (0.003) / 0.061 (0.002)
NGC0570	8.47 (0.03)	-0.10 (0.03)	—	—	—
NGC0716	8.50 (0.06)	-0.09 (0.02)	-0.128 (0.011) / -0.075 (0.006)	8.658 (0.012) / 8.596 (0.007)	0.056 (0.004) / 0.054 (0.002)
NGC0768	8.41 (0.08)	-0.01 (0.02)	-0.116 (0.008) / -0.075 (0.005)	8.563 (0.007) / 8.510 (0.006)	0.055 (0.002) / 0.064 (0.001)



Table A.2: *Continued.*

Name	$[\text{O}/\text{H}]_{r_e}$ [dex]	$\alpha_{\text{O}/\text{H}}$ [dex/ $r_e$ ]	$\alpha_{\text{ar}} / \alpha_{\text{in}}$ [dex/ $r_e$ ]	$[\text{O}/\text{H}]_{0,\text{ar}} / [\text{O}/\text{H}]_{0,\text{in}}$ [dex]	$\Delta [\text{O}/\text{H}]_{\text{ar}} / \Delta [\text{O}/\text{H}]_{\text{in}}$ [dex]
(a)	(b)	(c)	(d)	(e)	(f)
NGC0776	8.56 (0.06)	-0.03 (0.02)	-0.081 (0.006) / -0.032 (0.003)	8.645 (0.007) / 8.569 (0.004)	0.060 (0.003) / 0.068 (0.002)
NGC0787	8.50 (0.06)	-0.04 (0.02)	—	—	—
NGC0873	8.53 (0.03)	-0.06 (0.02)	-0.078 (0.006) / -0.062 (0.004)	8.613 (0.006) / 8.604 (0.005)	0.032 (0.001) / 0.040 (0.001)
NGC0941	8.40 (0.06)	-0.03 (0.02)	—	—	—
NGC0976	8.48 (0.00)	-0.07 (0.02)	—	—	—
NGC0991	8.41 (0.06)	-0.09 (0.02)	-0.067 (0.009) / -0.044 (0.004)	8.471 (0.007) / 8.460 (0.004)	0.048 (0.001) / 0.057 (0.001)
NGC1070	8.53 (0.05)	-0.01 (0.02)	—	—	—
NGC1093	8.52 (0.06)	-0.09 (0.02)	—	—	—
NGC1094	8.50 (0.05)	-0.08 (0.02)	-0.111 (0.004) / -0.078 (0.005)	8.631 (0.005) / 8.581 (0.006)	0.042 (0.004) / 0.048 (0.002)
NGC1659	8.50 (0.06)	-0.09 (0.02)	-0.094 (0.007) / -0.110 (0.003)	8.596 (0.009) / 8.626 (0.004)	0.051 (0.002) / 0.059 (0.001)
NGC1667	8.56 (0.04)	-0.03 (0.02)	-0.031 (0.005) / -0.047 (0.002)	8.584 (0.007) / 8.603 (0.004)	0.040 (0.001) / 0.045 (0.001)
NGC2253	8.57 (0.06)	-0.01 (0.02)	-0.017 (0.007) / +0.002 (0.005)	8.597 (0.012) / 8.569 (0.009)	0.055 (0.002) / 0.059 (0.002)
NGC2347	8.53 (0.06)	-0.11 (0.02)	-0.122 (0.006) / -0.091 (0.003)	8.675 (0.007) / 8.629 (0.004)	0.063 (0.002) / 0.060 (0.001)
NGC2449	8.56 (0.05)	0.00 (0.02)	—	—	—
NGC2486	8.49 (0.05)	-0.07 (0.03)	—	—	—
NGC2487	8.54 (0.05)	-0.01 (0.02)	—	—	—
NGC2530	8.40 (0.06)	-0.09 (0.03)	-0.062 (0.015) / -0.127 (0.006)	8.468 (0.010) / 8.506 (0.005)	0.052 (0.002) / 0.060 (0.001)
NGC2540	8.49 (0.06)	-0.06 (0.02)	-0.122 (0.007) / -0.097 (0.004)	8.611 (0.009) / 8.596 (0.005)	0.042 (0.002) / 0.058 (0.001)
NGC2604	8.53 (0.06)	-0.04 (0.02)	-0.069 (0.013) / -0.053 (0.004)	8.441 (0.010) / 8.420 (0.004)	0.051 (0.001) / 0.059 (0.001)
NGC2639	8.57 (0.06)	-0.04 (0.02)	—	—	—
NGC2730	8.46 (0.05)	-0.05 (0.02)	—	—	—
NGC2805	8.44 (0.04)	-0.11 (0.03)	—	—	—
NGC2906	8.60 (0.04)	-0.03 (0.02)	-0.058 (0.007) / -0.040 (0.004)	8.652 (0.008) / 8.627 (0.005)	0.035 (0.001) / 0.042 (0.001)
NGC2916	8.56 (0.04)	-0.10 (0.02)	-0.126 (0.006) / -0.124 (0.004)	8.676 (0.006) / 8.671 (0.004)	0.038 (0.001) / 0.046 (0.001)

Table A.2: *Continued.*

Name	$[\text{O}/\text{H}]_{r_e}$ [dex]	$\alpha_{\text{O}/\text{H}}$ [dex/ $r_e$ ]	$\alpha_{\text{ar}} / \alpha_{\text{in}}$ [dex/ $r_e$ ]	$[\text{O}/\text{H}]_{0,\text{ar}} / [\text{O}/\text{H}]_{0,\text{in}}$ [dex]	$\Delta [\text{O}/\text{H}]_{\text{ar}} / \Delta [\text{O}/\text{H}]_{\text{in}}$ [dex]
(a)	(b)	(c)	(d)	(e)	(f)
NGC3057	8.27 (0.08)	-0.12 (0.07)	-0.147 (0.014) / -0.108 (0.008)	8.444 (0.011) / 8.414 (0.006)	0.066 (0.002) / 0.072 (0.001)
NGC3106	8.50 (0.05)	-0.06 (0.05)	—	—	—
NGC3381	8.50 (0.03)	-0.06 (0.02)	-0.083 (0.010) / -0.069 (0.002)	8.566 (0.014) / 8.564 (0.003)	0.056 (0.002) / 0.054 (0.001)
NGC3614	8.42 (0.06)	-0.22 (0.05)	-0.215 (0.013) / -0.207 (0.009)	8.649 (0.009) / 8.645 (0.006)	0.051 (0.002) / 0.052 (0.001)
NGC3687	8.50 (0.06)	-0.16 (0.02)	—	—	—
NGC3811	8.57 (0.04)	-0.08 (0.02)	-0.099 (0.005) / -0.102 (0.003)	8.646 (0.006) / 8.656 (0.004)	0.045 (0.001) / 0.041 (0.001)
NGC4047	8.57 (0.05)	-0.10 (0.02)	-0.129 (0.004) / -0.115 (0.003)	8.701 (0.006) / 8.683 (0.004)	0.045 (0.002) / 0.049 (0.001)
NGC4185	8.55 (0.05)	-0.08 (0.02)	—	—	—
NGC4210	8.58 (0.04)	-0.09 (0.02)	-0.059 (0.004) / -0.089 (0.003)	8.638 (0.006) / 8.661 (0.004)	0.047 (0.001) / 0.047 (0.001)
NGC4470	8.42 (0.02)	-0.02 (0.02)	—	—	—
NGC4961	8.42 (0.05)	-0.10 (0.02)	—	—	—
NGC5000	8.55 (0.06)	-0.07 (0.02)	-0.096 (0.007) / -0.049 (0.010)	8.632 (0.007) / 8.583 (0.012)	0.067 (0.002) / 0.066 (0.001)
NGC5016	8.54 (0.05)	-0.11 (0.02)	-0.109 (0.009) / -0.124 (0.004)	8.647 (0.009) / 8.666 (0.005)	0.046 (0.003) / 0.048 (0.002)
NGC5056	8.44 (0.05)	-0.13 (0.02)	-0.089 (0.006) / -0.079 (0.003)	8.523 (0.009) / 8.534 (0.003)	0.046 (0.001) / 0.059 (0.001)
NGC5157	8.55 (0.07)	-0.01 (0.02)	—	—	—
NGC5205	8.52 (0.06)	-0.04 (0.02)	—	—	—
NGC5320	8.50 (0.07)	-0.03 (0.02)	-0.240 (0.011) / -0.158 (0.003)	8.737 (0.010) / 8.657 (0.003)	0.052 (0.002) / 0.050 (0.001)
NGC5376	8.60 (0.05)	-0.04 (0.02)	+0.003 (0.009) / -0.019 (0.004)	8.607 (0.009) / 8.620 (0.006)	0.048 (0.002) / 0.051 (0.001)
NGC5378	8.53 (0.04)	-0.01 (0.03)	—	—	—
NGC5406	8.53 (0.06)	-0.03 (0.02)	—	—	—
NGC5480	8.57 (0.04)	-0.05 (0.02)	—	—	—
NGC5519 <sup>†</sup>	—	—	—	—	—
NGC5520	8.49 (0.04)	-0.09 (0.02)	-0.102 (0.008) / -0.091 (0.003)	8.612 (0.009) / 8.599 (0.004)	0.032 (0.001) / 0.046 (0.001)
NGC5533	8.49 (0.05)	-0.06 (0.03)	—	—	—

Table A.2: *Continued.*

Name	$[\text{O}/\text{H}]_{r_e}$ [dex]	$\alpha_{\text{O}/\text{H}}$ [dex/ $r_e$ ]	$\alpha_{\text{ar}} / \alpha_{\text{in}}$ [dex/ $r_e$ ]	$[\text{O}/\text{H}]_{0,\text{ar}} / [\text{O}/\text{H}]_{0,\text{in}}$ [dex]	$\Delta [\text{O}/\text{H}]_{\text{ar}} / \Delta [\text{O}/\text{H}]_{\text{in}}$ [dex]
(a)	(b)	(c)	(d)	(e)	(f)
NGC5622	8.53 (0.08)	-0.04 (0.02)	-0.104 (0.006) / -0.126 (0.004)	8.627 (0.008) / 8.648 (0.005)	0.050 (0.001) / 0.055 (0.001)
NGC5633	8.60 (0.03)	-0.06 (0.02)	-0.086 (0.007) / -0.073 (0.003)	8.677 (0.008) / 8.652 (0.005)	0.036 (0.001) / 0.041 (0.001)
NGC5656	8.55 (0.05)	-0.10 (0.02)	—	—	—
NGC5657	8.47 (0.07)	-0.04 (0.02)	—	—	—
NGC5665	8.50 (0.05)	-0.04 (0.03)	—	—	—
NGC5720	8.53 (0.05)	-0.13 (0.02)	—	—	—
NGC5732	8.47 (0.06)	-0.18 (0.03)	-0.184 (0.012) / -0.174 (0.006)	8.639 (0.009) / 8.634 (0.006)	0.047 (0.002) / 0.058 (0.001)
NGC5735	8.49 (0.06)	-0.16 (0.02)	-0.198 (0.005) / -0.140 (0.005)	8.693 (0.004) / 8.634 (0.004)	0.067 (0.002) / 0.068 (0.002)
NGC5772	8.52 (0.06)	-0.06 (0.02)	-0.042 (0.006) / -0.063 (0.004)	8.576 (0.007) / 8.591 (0.005)	0.065 (0.003) / 0.062 (0.002)
NGC5829	8.43 (0.05)	-0.07 (0.02)	-0.120 (0.010) / -0.109 (0.006)	8.545 (0.010) / 8.532 (0.006)	0.049 (0.002) / 0.051 (0.001)
NGC5888	8.54 (0.06)	-0.02 (0.02)	—	—	—
NGC5947	8.49 (0.05)	-0.10 (0.02)	-0.127 (0.005) / -0.111 (0.004)	8.615 (0.006) / 8.595 (0.005)	0.041 (0.001) / 0.052 (0.001)
NGC5957	8.56 (0.05)	-0.06 (0.02)	-0.113 (0.013) / -0.091 (0.006)	8.662 (0.012) / 8.643 (0.006)	0.050 (0.002) / 0.050 (0.001)
NGC6004	8.53 (0.06)	-0.03 (0.02)	-0.039 (0.006) / -0.054 (0.004)	8.604 (0.006) / 8.596 (0.005)	0.054 (0.002) / 0.057 (0.001)
NGC6063	8.48 (0.05)	-0.17 (0.02)	-0.104 (0.008) / -0.144 (0.004)	8.605 (0.009) / 8.628 (0.005)	0.053 (0.002) / 0.056 (0.001)
NGC6154	8.52 (0.07)	0.00 (0.02)	—	—	—
NGC6155	8.55 (0.03)	-0.07 (0.02)	—	—	—
NGC6301	8.51 (0.04)	-0.06 (0.02)	—	—	—
NGC6497 <sup>†</sup>	—	—	—	—	—
NGC6941	8.54 (0.06)	-0.05 (0.03)	-0.035 (0.007) / -0.059 (0.005)	8.578 (0.006) / 8.598 (0.006)	0.072 (0.002) / 0.069 (0.001)
NGC7321	8.52 (0.05)	-0.08 (0.02)	—	—	—
NGC7364	8.57 (0.07)	-0.03 (0.02)	—	—	—
NGC7466	8.47 (0.05)	-0.09 (0.02)	-0.090 (0.009) / -0.068 (0.006)	8.572 (0.009) / 8.554 (0.007)	0.043 (0.002) / 0.049 (0.002)
NGC7489	8.41 (0.06)	-0.15 (0.02)	-0.223 (0.005) / -0.171 (0.003)	8.622 (0.007) / 8.590 (0.004)	0.049 (0.001) / 0.062 (0.001)

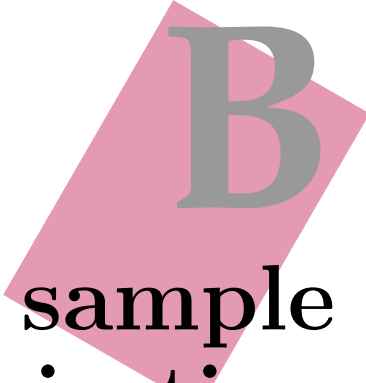
Table A.2: *Continued.*

Name	$[\text{O}/\text{H}]_{r_e}$ [dex]	$\alpha_{\text{O}/\text{H}}$ [dex/ $r_e$ ]	$\alpha_{\text{ar}} / \alpha_{\text{in}}$ [dex/ $r_e$ ]	$[\text{O}/\text{H}]_{0,\text{ar}} / [\text{O}/\text{H}]_{0,\text{in}}$ [dex]	$\Delta [\text{O}/\text{H}]_{\text{ar}} / \Delta [\text{O}/\text{H}]_{\text{in}}$ [dex]
(a)	(b)	(c)	(d)	(e)	(f)
NGC7591	8.52 (0.07)	-0.08 (0.02)	-0.071 (0.006) / -0.062 (0.004)	8.614 (0.009) / 8.594 (0.004)	0.062 (0.001) / 0.064 (0.001)
NGC7625	8.54 (0.04)	-0.03 (0.02)	—	—	—
NGC7653	8.52 (0.05)	-0.09 (0.02)	-0.115 (0.004) / -0.093 (0.004)	8.636 (0.005) / 8.608 (0.004)	0.050 (0.001) / 0.051 (0.001)
NGC7691	8.45 (0.07)	-0.10 (0.04)	—	—	—
NGC7716	8.49 (0.04)	-0.03 (0.02)	-0.043 (0.006) / -0.038 (0.003)	8.534 (0.006) / 8.528 (0.004)	0.041 (0.001) / 0.049 (0.001)
NGC7782	8.54 (0.06)	-0.04 (0.02)	—	—	—
NGC7787 <sup>†</sup>	—	—	—	—	—
NGC7819	8.49 (0.06)	-0.12 (0.02)	-0.139 (0.006) / -0.093 (0.005)	8.621 (0.008) / 8.581 (0.005)	0.060 (0.002) / 0.071 (0.002)
NGC7824	8.48 (0.05)	-0.03 (0.05)	—	—	—
UGC00005	8.52 (0.04)	-0.06 (0.02)	-0.054 (0.007) / -0.068 (0.004)	8.590 (0.008) / 8.599 (0.005)	0.041 (0.002) / 0.048 (0.002)
UGC00036	8.51 (0.06)	-0.13 (0.04)	—	—	—
UGC01918	8.53 (0.05)	-0.08 (0.04)	—	—	—
UGC02311	8.52 (0.04)	-0.05 (0.02)	-0.070 (0.006) / -0.051 (0.005)	8.580 (0.009) / 8.562 (0.008)	0.045 (0.001) / 0.051 (0.001)
UGC03253	8.52 (0.04)	-0.13 (0.02)	—	—	—
UGC03973	8.50 (0.05)	+0.08 (0.09)	—	—	—
UGC04195	8.52 (0.07)	-0.02 (0.02)	-0.090 (0.007) / -0.124 (0.005)	8.628 (0.007) / 8.652 (0.006)	0.056 (0.002) / 0.056 (0.002)
UGC04262	8.49 (0.10)	-0.25 (0.03)	-0.166 (0.008) / -0.182 (0.006)	8.656 (0.008) / 8.659 (0.006)	0.084 (0.002) / 0.079 (0.002)
UGC04308	8.52 (0.06)	-0.09 (0.02)	—	—	—
UGC04375	8.49 (0.04)	-0.12 (0.02)	—	—	—
UGC05108	8.49 (0.05)	-0.12 (0.05)	—	—	—
UGC07012	8.40 (0.08)	-0.11 (0.03)	-0.152 (0.072) / -0.112 (0.007)	8.510 (0.046) / 8.498 (0.006)	0.022 (0.002) / 0.068 (0.001)
UGC08781	8.48 (0.06)	-0.02 (0.03)	+0.007 (0.010) / -0.055 (0.009)	8.495 (0.010) / 8.539 (0.009)	0.056 (0.002) / 0.060 (0.001)
UGC09291	8.44 (0.06)	-0.18 (0.03)	-0.199 (0.007) / -0.152 (0.005)	8.629 (0.008) / 8.602 (0.005)	0.056 (0.002) / 0.060 (0.001)
UGC09476	8.49 (0.05)	-0.06 (0.02)	—	—	—

Table A.2: *Continued.*

Name	$[\text{O}/\text{H}]_{r_e}$ [dex]	$\alpha_{\text{O}/\text{H}}$ [dex/ $r_e$ ]	$\alpha_{\text{ar}} / \alpha_{\text{in}}$ [dex/ $r_e$ ]	$[\text{O}/\text{H}]_{0,\text{ar}} / [\text{O}/\text{H}]_{0,\text{in}}$ [dex]	$\Delta [\text{O}/\text{H}]_{\text{ar}} / \Delta [\text{O}/\text{H}]_{\text{in}}$ [dex]
(a)	(b)	(c)	(d)	(e)	(f)
UGC09492 <sup>†</sup>	—	—	—	—	—
UGC09777	8.48 (0.08)	0.00 (0.06)	-0.077 (0.015) / -0.020 (0.010)	8.552 (0.013) / 8.488 (0.011)	0.071 (0.005) / 0.074 (0.003)
UGC09842	8.50 (0.06)	-0.03 (0.02)	-0.103 (0.012) / -0.140 (0.008)	8.590 (0.013) / 8.610 (0.008)	0.060 (0.002) / 0.062 (0.001)
UGC11649	8.53 (0.07)	-0.10 (0.03)	—	—	—
UGC12224	8.47 (0.06)	-0.13 (0.05)	-0.173 (0.013) / -0.122 (0.006)	8.640 (0.011) / 8.588 (0.006)	0.054 (0.002) / 0.056 (0.001)
UGC12633	8.47 (0.02)	-0.03 (0.02)	—	—	—
UGC12767 <sup>†</sup>	—	—	—	—	—
UGC12816	8.42 (0.06)	-0.07 (0.02)	-0.094 (0.008) / -0.070 (0.004)	8.506 (0.008) / 8.485 (0.005)	0.055 (0.003) / 0.068 (0.002)
UGCA021	8.35 (0.06)	-0.11 (0.06)	—	—	—





# AMUSING sample characterisation tables

In this appendix we summarise the main properties of the AMUSING galaxies analysed in this thesis. We present several tables with general information (see Table B.1) and oxygen abundance information derived in this work (see Table B.2) for these galaxies. From left to right the columns correspond to

**Table B.1:** CALIFA sample characterisation I: general properties.

(a) Name of the galaxy; (b)–(c) right ascension and declination (referred to J2000); (d) morphological type from *HyperLeda*; (e) redshift; (f) disc effective radius ( $r_e$  in kpc), derived from the surface brightness profile of the galaxies by fitting ellipses to the  $g$ -band light distribution (see Sect. 5.1 for details); (g)–(h) position and inclination angles (details are given in Sect. 3.4); (i)  $r$ -band absolute magnitude in the AB magnitude system derived from the flux density in a  $r$ -band image recovered from the data; (j)  $g-r$  colours; (k)–(l) integrated stellar mass (in  $\log M_\odot$ ) and mass density (in  $\log M_\odot/\text{pc}^2$ ), calculated using the mass-luminosity ratio presented in Bell & de Jong (2001, see Sect. 5.5 for more information); (m) specific star formation rate (in  $\text{yr}^{-1}$ ), derived by adopting the classical relation presented in Kennicutt (1998) based on dust-corrected  $\text{H}\alpha$  luminosities (more details are given in Sect. 5.6); and (n) classification according to the density of the environment (isolated, S; part of a group of at least three galaxies, G; in pair, P; and with evidence of real interactions, I) based on information found in the literature (references are given in the notes below).

**Notes.** <sup>(1)</sup> Galaxy discarded from the analysis of the abundance distribution performed from Sect 5.2 on for: (a) having a very powerful AGN in the centre that can contaminate the emission coming from the H II regions, (b) having a ring-like structure, what affects the accuracy of the derivation of the abundance gradient, (c) being very distorted due to a recent interacting, and (d) being in a very advanced stage of merging. <sup>(2)</sup> Despite this classification by *HyperLeda*, it is clear the presence of a spiral structure observed with our data. <sup>(3)</sup> References: (a) Vorontsov-Velyaminov (1977), (b) Tully (2015), (c) Focardi et al. (2006), (d) Mendoza-Castrejón et al. (2015), (e) Mazzuca et al. (2006), (f) Haberman et al. (2012), (g) White et al. (1999), (h) Ramella et al. (2002), (i) Focardi & Kelm (2002), (j) Yang et al. (2007), (k) Dopita et al. (2002), (l) Casasola et al. (2004), (m) Martínez-Delgado et al. (2010), (n) Foster et al. (2014), (o) Keel et al. (2013), (p) Ganda et al. (2007), (q) van den Bergh (2007), (r) Berlind et al. (2006), (s) Knapen et al. (2014), (t) Hernández-Ibarra et al. (2016), (u) Madore et al. (2009), (v) Couto da Silva & de Souza (2006), and (w) Merchán & Zandivarez (2005).

**Table B.2:** CALIFA sample characterisation II: abundance information.

(a) Name of the galaxy; (b) characteristic abundance (oxygen abundance value at one disc effective radius,  $[O/H]_{re}$ ); (c) slope of the oxygen abundance gradient ( $\alpha_{O/H}$ ); (d) zero-point of the oxygen abundance gradient ( $[O/H]_0$ ); (e) galactocentric distance at which the inner drop in the abundances appear ( $h_D$ ), in units of  $r_e$  (if this feature is present); (f) galactocentric distance at which the radial gradients flatten ( $h_F$ ), in units of  $r_e$  (if this feature is present); (g) abundance scale length ( $r_{O/H}$ ), defined as the radial position at which the abundance distribution of a galaxy decays 0.09 dex (given by the decrease in the abundance in one disc effective radius attending to the common abundance gradient found, see Sect. 5.5 for details); (h)  $h_D$ , in units of  $r_{O/H}$ ; (i)  $h_F$ , in units of  $r_{O/H}$ ; and (j) scatter relative to the oxygen abundance gradient (see Sect. 5.6 for more information).

† galaxies for which the derivation of  $r_{O/H}$  is infeasible because the radial abundance distribution displays a very flat profile. \* Galaxy discarded from the analysis of the abundance distribution performed from Sect 5.2 on. See Notes (1) in Table B.1 for details.



**Table B.1:** *AMUSING* sample characterisation I: general properties. Details are given in Appendix B above.

Name	RA [h]	Dec [°]	Morph type	z	$r_e$ [kpc]	PA [°]	i [°]	$M_r$ [mag]	$g-r$ [mag]	$\log M$ [ $M_\odot$ ]	$\log \sigma$ [ $M_\odot/\text{pc}^2$ ]	sSFR [ $\text{yr}^{-1}$ ]	Density of env.
(a)	(b)	(c)	(d)	(e)	(f)	(g)	(h)	(i)	(j)	(k)	(l)	(m)	(n)
2MASXJ00351050+2315184	00.59	+23.26	Sc	0.037	17.2	+81	63	-21.5	-0.44	10.9	1.7	-10.9	S
2MASXJ01460987-6727579	01.77	-67.47	SABab	0.087	10.8	+5	41	-22.0	0.47	11.3	2.2	-10.8	S
2MASXJ01504127-1431032	01.84	-14.52	—	0.034	6.2	-72	57	-21.0	0.52	10.8	2.4	-10.3	S
2MASXJ06380745-7543288	06.64	-75.72	—	0.040	6.3	+65	35	-21.4	0.51	11.0	2.4	-10.4	S
2MASXJ07353554-6246099	07.59	-62.77	Scd	0.011	1.3	-60	39	-18.8	0.70	9.8	2.6	-10.3	S
2MASXJ09092454-0443026	09.16	-04.72	SBa	0.046	4.8	-89	24	-21.1	0.26	10.6	2.2	-10.3	S
2MASXJ09151727-2536001	09.25	-25.60	SBa	0.053	5.8	-85	51	-21.2	0.46	10.9	2.5	-10.1	S
2MASXJ10064866-0741124	10.11	-07.69	Sbc	0.055	14.0	-21	59	-22.1	0.42	11.1	2.0	-10.6	S
2MASXJ23451480-2947009	23.75	-29.78	—	0.034	5.0	-59	61	-20.2	0.43	10.6	2.4	-10.1	S
APMUKS(BJ)B033105.19-262232.9	03.55	-26.21	—	0.040	4.6	+9	39	-19.6	0.36	10.3	2.0	-10.3	S
CGCG023-005	15.96	+01.11	—	0.033	5.6	+15	52	-21.2	0.32	10.9	2.5	-10.2	S
CGCG044-035	13.23	+06.96	SBbc	0.024	6.0	-32	68	-20.1	0.37	10.5	2.3	-10.4	G <sup>(3h)</sup>
CGCG048-051	14.89	+02.97	Sm	0.028	5.7	0	50	-20.9	0.46	10.8	2.3	-10.7	S
CGCG063-098	09.90	+09.19	Sbc	0.030	3.5	+84	28	-21.2	0.60	10.8	2.7	-11.2	S
ESO075-G049	22.03	-70.04	—	0.038	5.0	+80	38	-21.8	0.44	11.1	2.7	-10.3	S
ESO184-G082	19.58	-52.84	SBd	0.009	2.0	-35	30	-18.6	0.21	9.8	2.2	-10.1	S
ESO235-G37	21.03	-48.27	Sbc	0.019	6.5	-29	62	-20.3	0.48	10.5	2.1	-10.7	S
ESO287-G040	21.62	-47.04	SBbc	0.031	13.6	-38	42	-21.1	0.54	10.9	1.7	-10.4	I <sup>(31,u)</sup>
ESO298-G28	02.33	-37.82	Sc	0.017	12.6	+21	59	-21.9	0.45	11.2	2.1	-10.8	S
ESO462-G009	20.36	-31.29	Sb	0.019	5.0	-70	40	-20.9	0.51	10.7	2.3	-10.4	S
ESO478-G006	02.16	-23.42	SBc	0.018	7.8	-75	52	-21.6	0.45	11.3	2.6	-10.1	S
ESO488-G30	05.81	-24.38	SBa	0.040	16.0	+52	37	-24.0	0.22	11.6	2.2	-11.0	G <sup>(3b)</sup>
ESO506-G004	12.36	-24.17	Sc	0.013	5.7	+85	60	-21.2	0.61	11.0	2.7	-10.4	S
ESO510-G034	14.00	-25.38	—	0.038	9.5	-75	66	-21.9	0.59	11.0	2.3	-10.9	S

Table B.1: *Continued.*

Name	RA [h]	Dec [°]	Morph type	z	$r_e$ [kpc]	PA [°]	i [°]	$M_r$ [mag]	$g-r$ [mag]	log M [ $M_\odot$ ]	log $\sigma$ M [ $M_\odot/\text{pc}^2$ ]	sSFR [ $\text{yr}^{-1}$ ]	Density of env.
(a)	(b)	(c)	(d)	(e)	(f)	(g)	(h)	(i)	(j)	(k)	(l)	(m)	(n)
ESO570-G020	11.39	-22.27	SBcd	0.028	6.8	+71	51	-21.2	0.51	11.0	2.4	-10.4	S
ESO602-G025	22.52	-19.03	Scd	0.025	15.1	-10	69	-22.1	0.38	11.3	2.3	-10.2	S
GALEXASCJ125413.02-073849.5	12.90	-07.65	Sc	0.014	4.4	+53	28	-18.4	0.28	10.0	1.6	-10.4	S
GALEXASCJ195932.30-565932.4	19.99	-56.99	—	0.057	9.9	+60	41	-22.0	0.32	11.2	2.2	-10.4	S
IC0344	03.69	-04.67	SABcd	0.018	6.4	+45	59	-20.9	0.32	10.8	2.4	-10.3	G <sup>(3b)</sup>
IC0577	09.93	+10.50	SABd	0.030	7.0	-5	27	-22.5	0.20	11.3	2.6	-10.4	P <sup>(3b,t)</sup>
IC1158	16.03	+01.71	SABd	0.006	2.3	-47	55	-19.4	0.42	10.0	2.5	-10.6	S
IC2160	05.92	-76.92	Sc	0.016	5.2	-75	39	-21.5	0.42	11.0	2.6	-10.3	S
IC5179	22.27	-36.84	SBbc	0.011	7.6	+55	61	-21.9	0.48	11.4	2.8	-9.9	S
LCRSB232926.0-413242	23.54	-41.27	—	0.049	10.4	-37	63	-21.1	0.34	10.8	2.0	-10.5	S
LCBS0801P	04.92	-20.00	—	0.080	13.8	+30	38	-22.2	0.44	11.3	2.0	-10.5	S
MCG+00-06-003	01.95	-00.21	—	0.046	8.0	+36	61	-21.6	0.44	11.0	2.4	-11.0	S
MCG+03-31-093	12.29	+16.37	—	0.023	4.7	+50	34	-20.6	0.20	10.6	2.2	-10.4	S
MCG+04-55-47	23.71	+27.09	Scd	0.025	4.7	+7	49	-20.5	0.42	10.6	2.3	-10.3	G <sup>(3b)</sup>
MCG-01-33-034	12.88	-09.78	SBa	0.009	2.4	-66	51	-19.6	0.47	10.0	2.3	-10.0	S
MCG-01-57-021	22.67	-02.42	Sa	0.010	8.2	-88	52	-20.3	0.33	10.7	2.0	-10.6	S
MCG-02-01-014	00.07	-11.17	SB0a	0.038	15.1	-50	43	-20.9	0.33	10.9	1.6	-10.2	P <sup>(3e)</sup>
MCG-02-07-33	02.57	-10.84	—	0.016	7.4	+73	72	-21.4	0.30	11.0	2.6	-10.3	G <sup>(3b)</sup>
MCG-03-07-040	02.60	-17.26	Scd	0.032	9.5	-5	52	-21.2	0.27	10.9	2.1	-10.2	P
MCG-03-10-052	03.91	-19.19	SBa	0.025	5.3	+28	55	-21.5	0.50	11.1	2.7	-10.4	S
NGC0232 <sup>(1a)</sup>	00.71	-23.56	S0 <sup>0(2)</sup>	0.022	5.1	+38	41	-21.3	0.67	—	—	—	I <sup>(3k,l)</sup>
NGC1080	02.75	-04.71	Sb	0.026	9.1	+5	36	-22.0	0.37	11.3	2.3	-10.3	S
NGC1309	03.37	-15.40	Sb	0.007	3.8	+72	27	-21.0	0.34	11.0	2.8	-10.2	S
NGC1516A <sup>(1d)</sup>	04.14	-08.83	—	0.033	6.3	-30	30	-22.6	0.44	—	—	—	I <sup>(3b)</sup>

Table B.1: *Continued.*

Name	RA [h]	Dec [°]	Morph type	z	$r_e$ [kpc]	PA [°]	i [°]	$M_r$ [mag]	$g-r$ [mag]	$\log M$ [ $M_\odot$ ]	$\log \sigma$ [ $M_\odot/\text{pc}^2$ ]	sSFR [ $\text{yr}^{-1}$ ]	Density of env.
(a)	(b)	(c)	(d)	(e)	(f)	(g)	(h)	(i)	(j)	(k)	(l)	(m)	(n)
NGC1566	04.33	-54.94	SBc	0.005	1.7	+21	56	-18.6	0.51	10.1	2.8	-10.6	G <sup>(3b)</sup>
NGC1578	04.40	-51.60	SBc	0.020	4.9	-28	27	-21.9	0.49	11.1	2.6	-10.5	S
NGC1590	04.52	+07.63	Sbc	0.014	3.3	-68	44	-21.3	0.10	11.1	3.1	-10.2	G <sup>(3b)</sup>
NGC1591	04.49	-26.71	SBbc	0.014	6.2	+33	50	-21.3	0.17	11.1	2.6	-10.3	G <sup>(3b)</sup>
NGC1762	05.06	+01.57	—	0.016	7.3	-3	51	-22.4	0.33	11.4	2.7	-10.5	S
NGC1954	05.55	-14.06	SABa	0.010	6.2	-33	59	-21.9	0.41	10.7	2.2	-10.2	G <sup>(3b)</sup>
NGC2370	07.42	+23.78	Sb	0.018	7.9	+43	61	-22.1	0.56	11.2	2.6	-10.3	G <sup>(3b)</sup>
NGC2466	07.75	-71.41	Sc	0.018	5.8	-7	23	-21.9	0.34	11.2	2.6	-10.0	S
NGC2906	09.54	+08.44	Sbc	0.007	5.0	+82	56	-21.1	0.50	10.9	2.7	-10.8	S
NGC2930	09.63	+23.20	SABbc	0.022	10.6	-47	51	-20.9	0.22	10.5	1.5	-9.9	G <sup>(3g,h)</sup>
NGC3120	10.09	-34.22	Sc	0.009	3.9	0	52	-20.5	0.45	10.7	2.6	-10.5	G <sup>(3b)</sup>
NGC3244	10.42	-39.83	Sbc	0.009	4.2	0	31	-20.0	0.58	10.7	2.4	-10.2	G <sup>(3b)</sup>
NGC3278	10.53	-39.95	Sb	0.010	3.4	+56	53	-21.1	0.42	10.9	3.0	-10.0	G <sup>(3b)</sup>
NGC3318	10.62	-41.63	SB0a	0.009	7.4	+81	63	-20.8	0.38	11.1	2.6	-10.1	S
NGC3363	10.75	+22.08	SABab	0.019	6.6	+3	58	-21.5	0.46	11.1	2.6	-10.5	S
NGC3389	10.81	+12.53	Sc	0.004	5.0	-71	62	-20.0	0.27	10.6	2.4	-10.2	G <sup>(3b,q)</sup>
NGC3447 <sup>(1e)</sup>	10.89	+16.77	S0a	0.004	2.0	+1	57	-17.4	0.33	—	—	—	I <sup>(3s,t)</sup>
NGC3451	10.91	+27.24	SB0a	0.004	4.2	+54	67	-19.9	0.35	10.5	2.5	-10.1	G <sup>(3b)</sup>
NGC3464	10.91	-21.07	Sbc	0.012	9.5	-72	49	-21.3	0.40	11.1	2.2	-10.4	S
NGC3512	11.07	+28.04	SBbc	0.005	2.6	-50	33	-19.9	0.49	10.4	2.5	-10.4	G <sup>(3b,f)</sup>
NGC3905	11.82	-09.73	SBab	0.019	11.8	-80	42	-22.7	0.43	11.6	2.4	-10.5	S
NGC4451	12.48	+09.26	SBcd	0.003	2.1	-13	54	-19.6	0.37	10.4	2.9	-10.4	G <sup>(3b)</sup>
NGC4487	12.52	-08.05	SABc	0.003	8.0	+70	54	-20.8	0.38	10.8	2.1	-10.5	P <sup>(3b,p)</sup>
NGC4651	12.73	+16.39	—	0.003	3.6	+70	50	-21.5	0.42	11.0	3.0	-10.6	I <sup>(3m,n)</sup>

Table B.1: *Continued.*

Name	RA [h]	Dec [°]	Morph type	z	$r_e$ [kpc]	PA [°]	i [°]	$M_r$ [mag]	$g-r$ [mag]	$\log M$ [ $M_\odot$ ]	$\log \sigma$ [ $M_\odot/\text{pc}^2$ ]	sSFR [ $\text{yr}^{-1}$ ]	Density of env.
(a)	(b)	(c)	(d)	(e)	(f)	(g)	(h)	(i)	(j)	(k)	(l)	(m)	(n)
NGC4806	12.94	-29.50	SB0a	0.008	2.9	+28	37	-20.0	0.29	10.6	2.6	-10.2	S
NGC4900	13.01	+02.50	SBbc	0.003	7.8	-80	20	-21.4	0.35	10.7	1.8	-10.3	G <sup>(3b)</sup>
NGC4965	13.12	-28.23	SBc	0.008	13.4	-27	37	-20.4	0.41	11.3	2.0	-10.4	P <sup>(3b,f)</sup>
NGC5339	13.90	-07.93	SBm	0.009	4.4	+25	34	-20.8	0.44	10.7	2.4	-10.7	S
NGC5584	14.37	-00.39	SABc	0.005	8.4	-23	45	-19.0	0.41	—	—	-10.3	S
NGC6708	18.93	-53.72	SABbc	0.009	2.1	-6	41	-21.2	0.38	10.9	3.3	-10.0	G <sup>(3b)</sup>
NGC6754	19.19	-50.64	SABbc	0.011	8.7	+86	63	-20.9	-0.14	11.0	2.4	-10.8	S
NGC7119A	21.77	-46.52	SABbc	0.032	9.9	-45	57	-22.6	0.39	11.6	2.7	-10.2	I <sup>(3i,v)</sup>
NGC7469 <sup>(1a)</sup>	23.05	+08.87	SBb	0.016	3.4	-59	38	-22.2	0.43	—	—	—	I <sup>(3b,d)</sup>
NGC7580 <sup>(1c)</sup>	23.29	+14.00	S0a	0.016	2.9	+52	33	-20.8	0.39	—	—	—	G <sup>(3b,j)</sup>
NGC7742	23.74	+10.77	Sb	0.006	0.9	0	0	-20.1	0.50	10.4	3.4	-10.3	P <sup>(3b,e)</sup>
PGC004701	01.31	-07.45	Sbc	0.018	8.5	-18	28	-20.2	0.41	10.7	1.8	-10.4	P <sup>(3a)</sup>
PGC055442	15.56	+21.14	E <sup>(2)</sup>	0.024	3.8	+15	46	-21.5	0.55	10.9	2.8	-11.0	P <sup>(3c)</sup>
PGC128348	23.55	-60.57	—	0.015	4.1	+35	34	-20.0	0.34	10.4	2.2	-10.4	S
PGC1285465	11.00	+05.56	Sc	0.056	10.6	+10	59	-21.0	0.49	10.6	1.8	-10.4	S
SDSSJ011557.69+004135.9	01.27	+00.69	Sbc	0.043	6.2	-80	20	-20.1	0.32	10.4	1.7	-10.4	G <sup>(3i,w)</sup>
SDSSJ090202.19+101759.7	09.03	+10.30	—	0.042	10.9	+23	46	-20.3	-0.18	10.3	1.2	-10.7	S
UGC00272	00.46	-01.20	Sdm	0.013	8.6	-53	70	-19.6	0.28	10.4	1.9	-10.4	G <sup>(3b)</sup>
UGC01333	01.86	+00.26	Sc	0.059	19.0	-80	46	-22.8	0.89	12.6	3.1	-9.7	S
UGC01395	01.92	+06.61	Sb	0.017	7.0	-34	44	-21.3	0.49	11.0	2.4	-10.5	S
UGC02019	02.54	+00.62	Sbc	0.021	4.5	+67	38	-21.3	0.17	11.0	2.7	-10.5	G <sup>(3b,f)</sup>
UGC03634 <sup>(1b)</sup>	07.03	+14.14	Sbc	0.026	7.4	-57	52	-22.3	0.68	—	—	—	S
UGC05378	10.01	+04.41	Sb	0.014	2.9	-79	59	-19.3	0.30	10.2	2.4	-10.3	S
UGC05691	10.49	+22.01	SABb	0.054	20.0	-49	44	-22.6	0.48	11.4	1.8	-10.6	S

Table B.1: *Continued.*

Name	RA [h]	Dec [°]	Morph type	$z$	$r_e$ [kpc]	PA [°]	$i$ [°]	$M_r$ [mag]	$g-r$ [mag]	$\log M$ [ $M_\odot$ ]	$\log \sigma$ [ $M_\odot/\text{pc}^2$ ]	sSFR [ $\text{yr}^{-1}$ ]	Density of env.
(a)	(b)	(c)	(d)	(e)	(f)	(g)	(h)	(i)	(j)	(k)	(l)	(m)	(n)
UGC06332 (1b)	11.32	+20.81	S0a	0.021	8.6	-35	33	-21.8	0.73	—	—	—	S
UGC09530	14.80	+09.66	Scd	0.029	16.8	+89	46	-22.9	-0.09	11.7	2.3	-11.0	G <sup>(3g,i,d)</sup>
UGC11001	17.84	+14.29	Sc	0.014	6.8	-48	67	-21.0	0.36	11.0	2.6	-10.3	G <sup>(3b)</sup>
UGC11214	18.38	+12.43	Sbc	0.009	4.8	0	20	-20.5	0.34	10.6	2.2	-10.4	S
UGC11816	21.82	+00.45	Sb	0.016	6.2	0	18	-20.8	0.25	10.9	2.2	-10.6	S
UGC12158	22.70	+20.00	SABc	0.031	11.0	0	0	-21.9	0.42	11.2	2.0	-10.9	S

**Table B.2:** *AMUSING* sample characterisation II: oxygen abundance information. Details are given in Appendix B above.

Name	[O/H] <sub>re</sub> [dex]	Slope [dex/ <i>r<sub>e</sub></i> ]	Zero-point [dex]	<i>h<sub>D</sub></i> [ <i>r<sub>e</sub></i> ]	<i>h<sub>F</sub></i> [ <i>r<sub>e</sub></i> ]	<i>R<sub>O/H</sub></i> [kpc]	<i>h<sub>D</sub></i> [ <i>r<sub>O/H</sub></i> ]	<i>h<sub>F</sub></i> [ <i>r<sub>O/H</sub></i> ]	Scatter [dex]
(a)	(b)	(c)	(d)	(e)	(f)	(g)	(h)	(i)	(j)
2MASXJ00351050+2315184	8.29	-0.27	8.56	—	—	5.0	—	—	0.053
2MASXJ01460987-6727579	8.52	-0.08	8.60	—	—	11.1	—	—	0.041
2MASXJ01504127-1431032	8.56	-0.17	8.73	0.8	2.3	9.4	0.5	1.5	0.036
2MASXJ06380745-7543288	8.59	-0.15	8.73	0.6	2.8	7.6	0.5	2.3	0.062
2MASXJ07353554-6246099	8.56	-0.07	8.64	0.9	—	1.5	0.7	—	0.052
2MASXJ09092454-0443026	8.44	-0.13	8.57	—	—	3.9	—	—	0.030
2MASXJ09151727-2536001	8.55	-0.03	8.58	—	—	10.3	—	—	0.024
2MASXJ10064866-0741124	8.45	-0.09	8.54	—	1.1	16.2	—	1.0	0.038
2MASXJ23451480-2947009	8.37	-0.14	8.51	—	1.3	4.2	—	1.6	0.092
APMUKS(BJ)B033105.19-262232.9	8.53	-0.09	8.62	0.5	—	6.1	0.4	—	0.022
CGCG023-005	8.47	-0.14	8.61	—	1.4	5.4	—	1.5	0.049
CGCG044-035	8.40	-0.12	8.51	—	—	6.1	—	—	0.033
CGCG048-051 †	8.60	-0.01	8.62	—	—	—	—	—	0.045
CGCG063-098	8.61	-0.07	8.68	—	—	6.0	—	—	0.022
ESO075-G049	8.55	-0.05	8.60	—	—	11.0	—	—	0.036
ESO184-G082 †	8.34	0.00	8.34	—	—	3.2	—	—	0.061
ESO235-G37	8.48	-0.09	8.57	—	—	7.8	—	—	0.038
ESO287-G040	8.54	-0.14	8.68	—	—	17.0	—	—	0.062
ESO298-G28	8.55	-0.19	8.74	0.8	—	15.1	0.7	—	0.042
ESO462-G009 †	8.55	0.00	8.56	—	—	—	—	—	0.058
ESO478-G006	8.56	-0.18	8.74	0.6	1.6	10.3	0.5	1.2	0.021
ESO488-G30	8.54	-0.15	8.69	—	—	17.5	—	—	0.062
ESO506-G004	8.62	-0.06	8.68	—	—	11.0	—	—	0.046
ESO510-G034	8.56	-0.06	8.62	—	—	14.6	—	—	0.022

Table B.2: *Continued.*

Name	$[O/H]_{re}$ [dex]	Slope [dex/ $r_e$ ]	Zero-point [dex]	$h_D$ [ $r_e$ ]	$h_F$ [ $r_e$ ]	$R_{O/H}$ [kpc]	$h_D$ [ $r_{O/H}$ ]	$h_F$ [ $r_{O/H}$ ]	Scatter [dex]
(a)	(b)	(c)	(d)	(e)	(f)	(g)	(h)	(i)	(j)
ESO570-G020	8.50	-0.16	8.66	0.4	—	7.4	0.4	—	0.043
ESO602-G025	8.51	-0.24	8.66	0.4	0.7	9.9	0.7	1.0	0.026
GALEXASCJ125413.02-073849.5	8.26	-0.14	8.40	—	1.0	4.0	—	1.1	0.060
GALEXASCJ195932.30-565932.4	8.61	-0.21	8.81	0.6	2.0	11.8	0.5	1.7	0.066
IC0344	8.36	-0.19	8.54	—	0.9	5.1	—	1.2	0.060
IC0577	8.51	-0.14	8.65	0.4	—	7.4	0.4	—	0.033
IC1158	8.56	-0.04	8.60	—	—	2.8	—	—	0.092
IC2160	8.53	-0.14	8.67	1.0	2.5	9.6	0.5	1.3	0.054
IC5179	8.53	-0.15	8.67	0.3	1.2	8.2	0.3	1.1	0.026
LCRSB232926.0-413242	8.43	-0.16	8.59	—	2.1	6.9	—	3.1	0.045
LCSBS0801P	8.53	-0.20	8.73	—	—	10.9	—	—	0.057
MCG+00-06-003	8.58	-0.13	8.71	—	—	16.0	—	—	0.049
MCG+03-31-093	8.51	-0.11	8.61	—	—	4.4	—	—	0.054
MCG+04-55-47	8.55	-0.06	8.61	0.4	—	8.3	0.2	—	0.027
MCG-01-33-034 †	8.39	-0.01	8.40	—	—	—	—	—	0.081
MCG-01-57-021	8.40	-0.23	8.63	—	—	4.5	—	—	0.051
MCG-02-01-014	8.41	-0.26	8.67	—	—	9.2	—	—	0.064
MCG-02-07-33	8.53	-0.08	8.61	—	—	10.1	—	—	0.075
MCG-03-07-040	8.41	-0.23	8.64	—	1.6	4.7	—	3.2	0.072
MCG-03-10-052	8.50	-0.06	8.56	—	—	11.3	—	—	0.049
NGC0232 †*	8.57	+0.01	8.56	—	—	—	—	—	—
NGC1080	8.55	-0.12	8.67	0.4	—	10.3	0.3	—	0.048
NGC1309	8.44	-0.17	8.61	0.4	1.0	3.4	0.4	1.1	0.024
NGC1516A *	8.52	-0.05	8.57	—	—	5.6	—	—	—

Table B.2: *Continued.*

Name	$[O/H]_{re}$ [dex]	Slope [dex/ $r_e$ ]	Zero-point [dex]	$h_D$ [ $r_e$ ]	$h_F$ [ $r_e$ ]	$R_{O/H}$ [kpc]	$h_D$ [ $r_{O/H}$ ]	$h_F$ [ $r_{O/H}$ ]	Scatter [dex]
(a)	(b)	(c)	(d)	(e)	(f)	(g)	(h)	(i)	(j)
NGC1566 †	8.58	0.00	8.59	—	—	2.1	—	—	0.033
NGC1578 †	8.59	-0.03	8.62	—	—	—	—	—	0.049
NGC1590 †	8.60	-0.02	8.62	—	—	—	—	—	0.017
NGC1591	8.51	-0.12	8.60	—	0.9	6.3	—	0.9	0.047
NGC1762	8.57	-0.12	8.69	0.6	—	11.1	0.4	—	0.040
NGC1954	8.61	-0.12	8.73	—	2.6	10.9	—	1.5	0.086
NGC2370	8.57	-0.09	8.66	0.5	—	11.6	0.4	—	0.043
NGC2466	8.54	-0.14	8.68	0.4	2.0	7.3	0.4	1.6	0.040
NGC2906	8.56	-0.04	8.60	—	—	6.2	—	—	0.056
NGC2930	8.24	-0.28	8.52	—	—	4.0	—	—	0.040
NGC3120	8.58	-0.10	8.68	0.8	—	6.3	0.5	—	0.062
NGC3244	8.50	-0.19	8.69	0.4	—	4.0	0.4	—	0.040
NGC3278	8.55	-0.09	8.64	0.4	1.2	4.6	0.3	0.9	0.015
NGC3318	8.50	-0.10	8.59	—	—	8.4	—	—	0.041
NGC3363	8.61	-0.07	8.68	0.9	—	13.6	0.4	—	0.049
NGC3389	8.38	-0.29	8.58	—	0.7	3.0	—	1.2	0.101
NGC3447 *	8.40	-0.03	8.42	—	—	1.5	—	—	—
NGC3451	8.48	-0.03	8.51	—	—	4.8	—	—	0.049
NGC3464	8.52	-0.23	8.75	0.6	—	9.1	0.6	—	0.050
NGC3512	8.57	-0.09	8.66	0.6	—	3.5	0.5	—	0.049
NGC3905	8.58	-0.22	8.80	0.8	—	14.7	0.6	—	0.057
NGC4451	8.53	-0.13	8.66	0.4	1.2	2.2	0.4	1.1	0.025
NGC4487	8.46	-0.09	8.55	—	—	6.9	—	—	0.062
NGC4651	8.55	-0.17	8.72	0.8	1.4	4.4	0.7	1.1	0.047



Table B.2: *Continued.*

Name	$[O/H]_{re}$ [dex]	Slope [dex/ $r_e$ ]	Zero-point [dex]	$h_D$ [ $r_e$ ]	$h_F$ [ $r_e$ ]	$R_{O/H}$ [kpc]	$h_D$ [ $r_{O/H}$ ]	$h_F$ [ $r_{O/H}$ ]	Scatter [dex]
(a)	(b)	(c)	(d)	(e)	(f)	(g)	(h)	(i)	(j)
NGC4806	8.46	-0.08	8.55	—	—	3.3	—	—	0.053
NGC4900	8.36	-0.30	8.65	0.3	—	3.8	0.6	—	0.046
NGC4965	8.40	-0.10	8.50	—	—	10.0	—	—	0.069
NGC5339	8.57	-0.06	8.63	—	—	6.5	—	—	0.031
NGC5584	8.41	-0.36	8.60	0.1	0.3	2.6	0.2	1.1	0.036
NGC6708	8.52	-0.14	8.67	0.5	1.6	2.5	0.4	1.3	0.036
NGC6754	8.54	-0.12	8.67	0.4	—	10.3	0.3	—	0.049
NGC7119A	8.51	-0.15	8.66	0.5	1.6	11.9	0.4	1.3	0.031
NGC7469 †*	8.53	0.00	8.53	—	—	—	—	—	—
NGC7580 *	8.53	-0.03	8.57	—	—	2.1	—	—	—
NGC7742	8.56	-0.04	8.60	—	—	2.5	—	—	0.040
PGC004701	8.46	-0.11	8.57	—	—	7.3	—	—	0.052
PGC054442	8.51	-0.05	8.56	—	—	7.0	—	—	0.058
PGC128348	8.45	-0.09	8.54	—	—	5.5	—	—	0.052
PGC1285465	8.46	-0.15	8.62	—	—	10.4	—	—	0.031
SDSSJ011557.69+004135.9	8.36	-0.07	8.43	—	—	8.0	—	—	0.039
SDSSJ090202.19+101759.7	8.20	-0.14	8.34	—	—	5.0	—	—	0.048
UGC00272	8.32	-0.08	8.40	—	—	7.4	—	—	0.049
UGC01333	8.58	-0.12	8.69	—	—	28.4	—	—	0.052
UGC01395	8.56	-0.07	8.63	—	—	10.1	—	—	0.059
UGC02019	8.53	-0.08	8.61	0.4	—	7.6	0.2	—	0.030
UGC03634 †*	8.61	-0.01	8.62	—	—	—	—	—	—
UGC05378	8.54	-0.13	8.67	0.7	—	4.1	0.5	—	0.047
UGC05691	8.55	-0.18	8.73	0.8	—	26.5	0.6	—	0.051

Table B.2: *Continued.*

Name	$[O/H]_{re}$ [dex]	Slope [dex/ $r_e$ ]	Zero-point [dex]	$h_D$ [ $r_e$ ]	$h_F$ [ $r_e$ ]	$R_{O/H}$ [kpc]	$h_D$ [ $r_{O/H}$ ]	$h_F$ [ $r_{O/H}$ ]	Scatter [dex]
(a)	(b)	(c)	(d)	(e)	(f)	(g)	(h)	(i)	(j)
UGC06332 <sup>†*</sup>	8.59	0.00	8.59	—	—	—	—	—	—
UGC09530	8.39	-0.31	8.70	0.3	—	10.8	0.4	—	0.083
UGC11001	8.43	-0.18	8.61	0.3	1.2	5.7	0.4	1.4	0.027
UGC11214	8.45	-0.11	8.56	—	—	2.6	—	—	0.070
UGC11816	8.51	-0.26	8.77	—	—	5.2	—	—	0.083
UGC12158	8.56	-0.09	8.65	—	—	10.6	—	—	0.065



# CALIFA sample characterisation plots

In this appendix we include a graphic summary of the main results derived in this thesis for the CALIFA subsample of galaxies. For each galaxy we show a figure divided into eight or five panels, depending on whether the galaxy is part of the arm-interarm abundance distribution analysis. A complete description of each panel is given below.

**Figure C.1-122:** Graphic characterisation of CALIFA galaxies.

**First row:** RGB colour images of the galaxy, using SDSS  $r$ -,  $i$ - and  $z$ -band images recovered from the data (in red, green and blue respectively, **left**) and narrow-band images centred in the emission lines  $[\text{N II}]\lambda 6584$ ,  $\text{H}\alpha$ , and  $[\text{O III}]\lambda 5007$  (in red, green and blue respectively, **right**).

**Second row (left):**  $\text{H}\alpha$  map in units of  $(\log_{10}) 10^{-16} \text{ erg s}^{-1} \text{ cm}^{-2} \text{ arcsec}^{-1}$ . The detected  $\text{H II}$  regions are shown as black segmented contours.

**Second row (right):** Location of the spaxels classified as SF regions (blue dots) and AGNs (red dots) according to the BPT diagram superimposed on the IFS-based  $\text{H}\alpha$  map of the galaxy.

**Third row (left):** Radial density distribution of the spaxels in the oxygen abundance-galactocentric distance space. The radial distances are deprojected and normalised to the disc effective radius. The diamonds represent the mean oxygen abundance values, with the error bars indicating the corresponding standard deviations, for bins of  $0.25 r_e$ . The red solid line corresponds to the error-weighted linear fit derived for mean values within the range between  $0.5$  and  $2.0 r_e$  (yellow diamonds). The violet dots repre-

sent the oxygen abundances derived for the individual H II regions, and the dashed black line is the linear regression for these points.

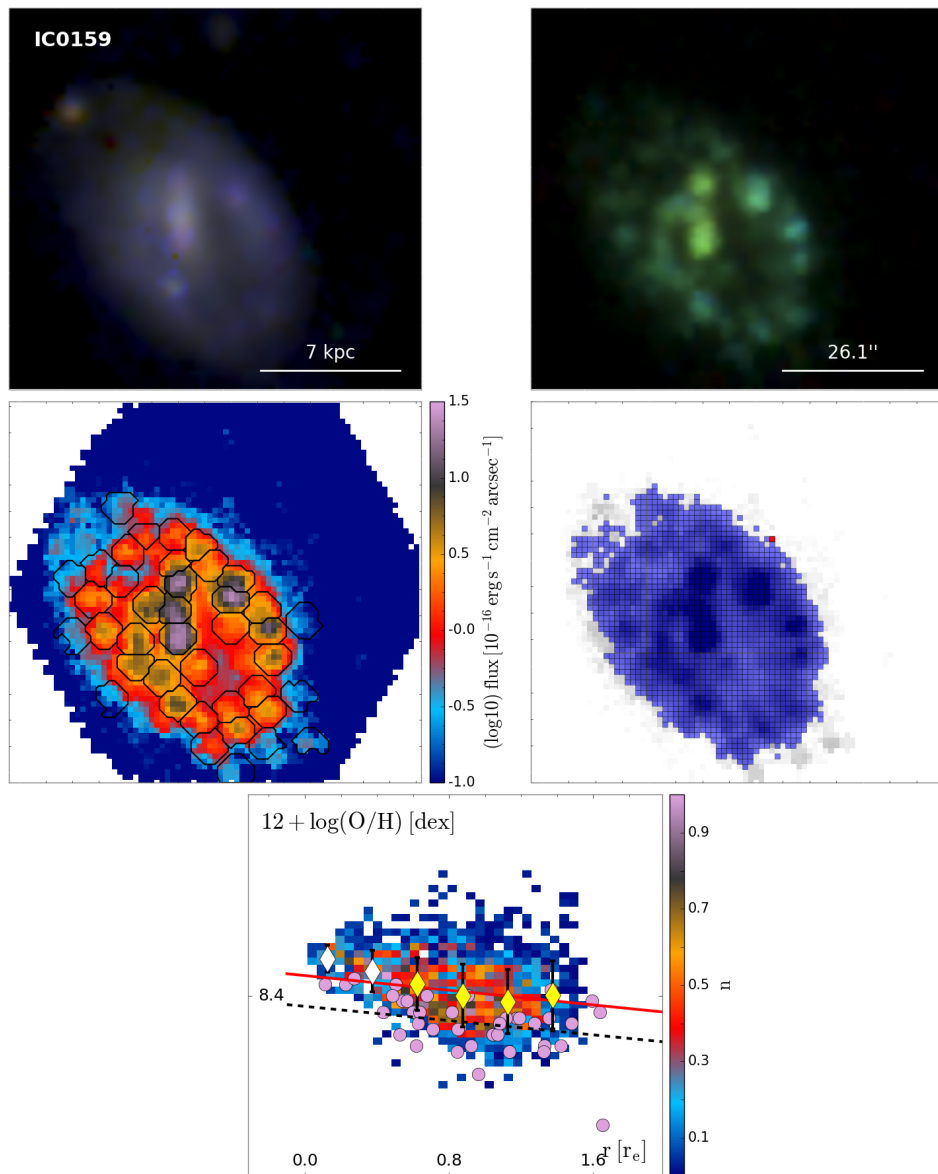
**Third row (right)<sup>†</sup>:** Outline of the spiral arms on the deprojected SDSS  $g$ -band image of the galaxy.

**Fourth row (left)<sup>†</sup>:** Colour map of the deprojected 2D oxygen abundance distribution of the galaxy. The abundance values of the spaxels belonging to the spiral arms are shown as opaque dots and the values of the spaxels located in the interarm region as transparent dots.

**Fourth row (right)<sup>†</sup>:** Radial density distribution in the oxygen abundance-galactocentric distance space of the spaxels located in the spiral arms (green contours) and those associated with the interarm region (orange colour map). The radial distances are deprojected and normalised to the disc effective radius. The outermost contour encircles 100% of the total number of spaxels, decreasing by 20% in each consecutive contour. The lines represent the error-weighted linear fit derived for the arm (green dashed line) and interarm (orange solid line) distributions. Finally, the inset indicates the number of spaxels of each distribution that contribute to the derivation of the gradient, i.e. located within the radial range  $0.5-2.0 r_e$ .

<sup>†</sup> these panels are shown only for the galaxies part of the arm-interarm abundance distribution analysis carried out in Chapter 6.

**Note.** In the printed edition of this thesis, we present an abridged version of the appendix including the graphic characterisation for five galaxies of the CALIFA sample. The full version for the 122 galaxies of the sample is available in the electronic edition.



Arm-interarm abundance distribution analysis

not feasible for this galaxy.

See Sect. 6. 1 for more details.

**Figure C.1:** IC 0159. See Appendix C above for a description of each panel.

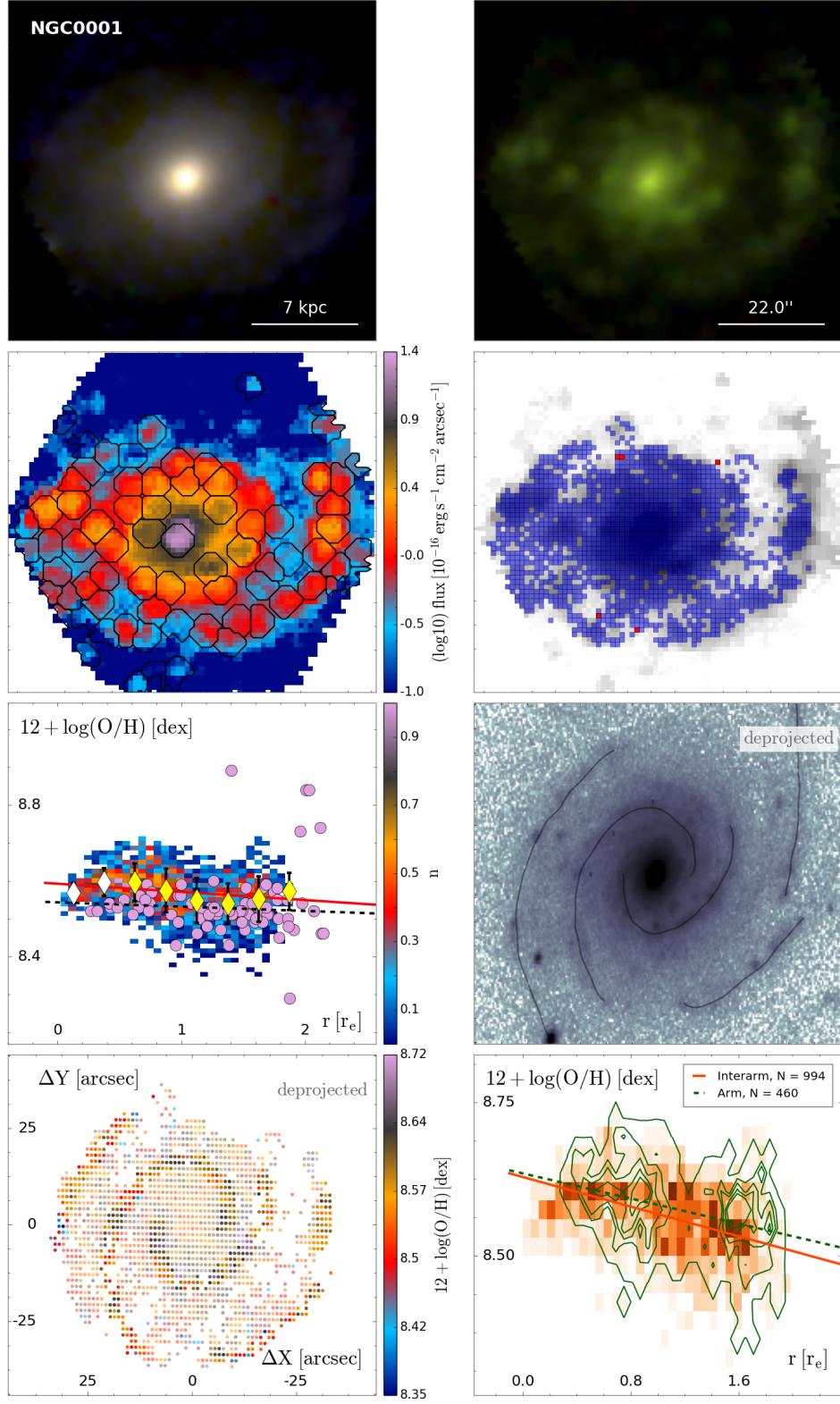


Figure C.2: NGC 0001. See Appendix C above for a description of each panel.

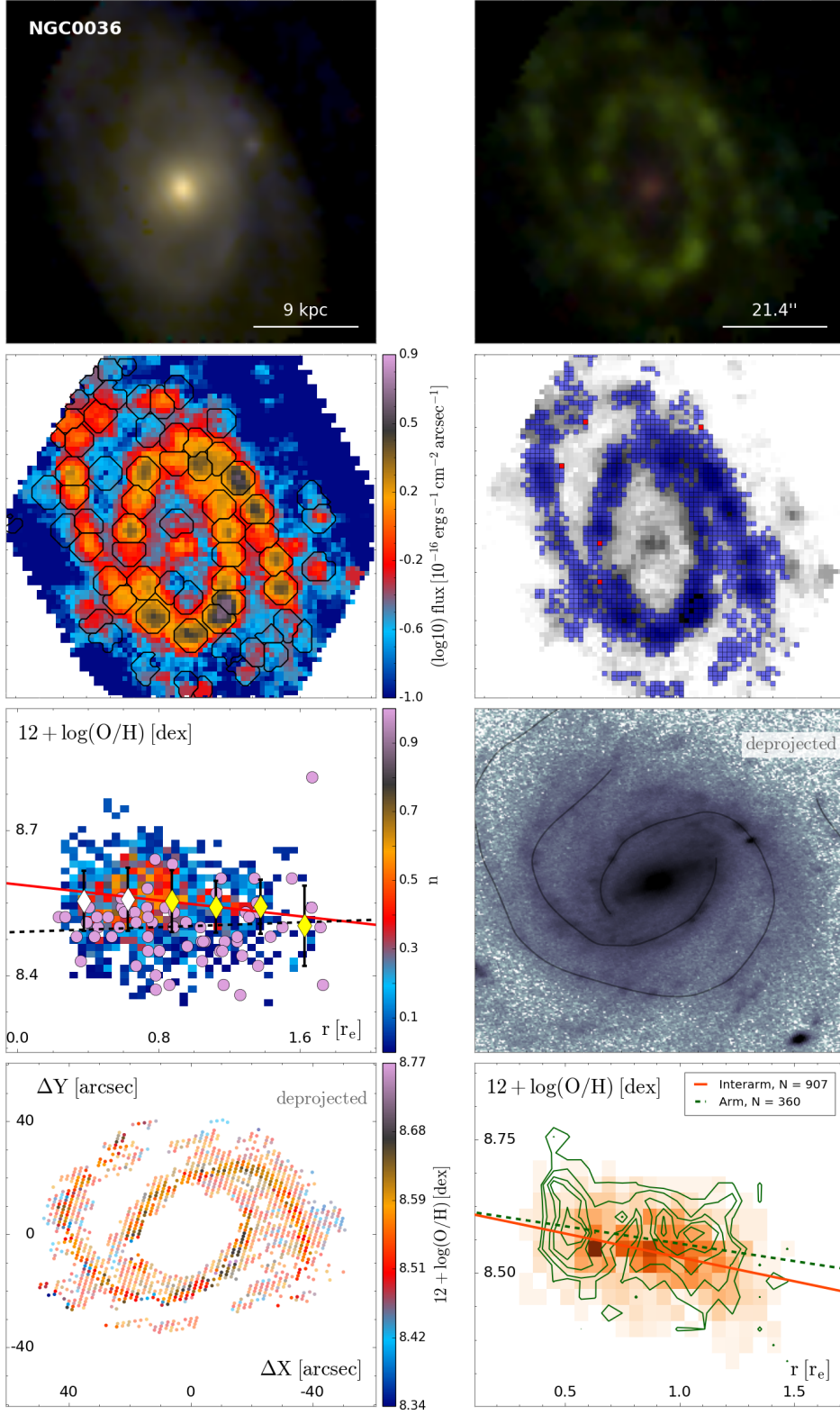
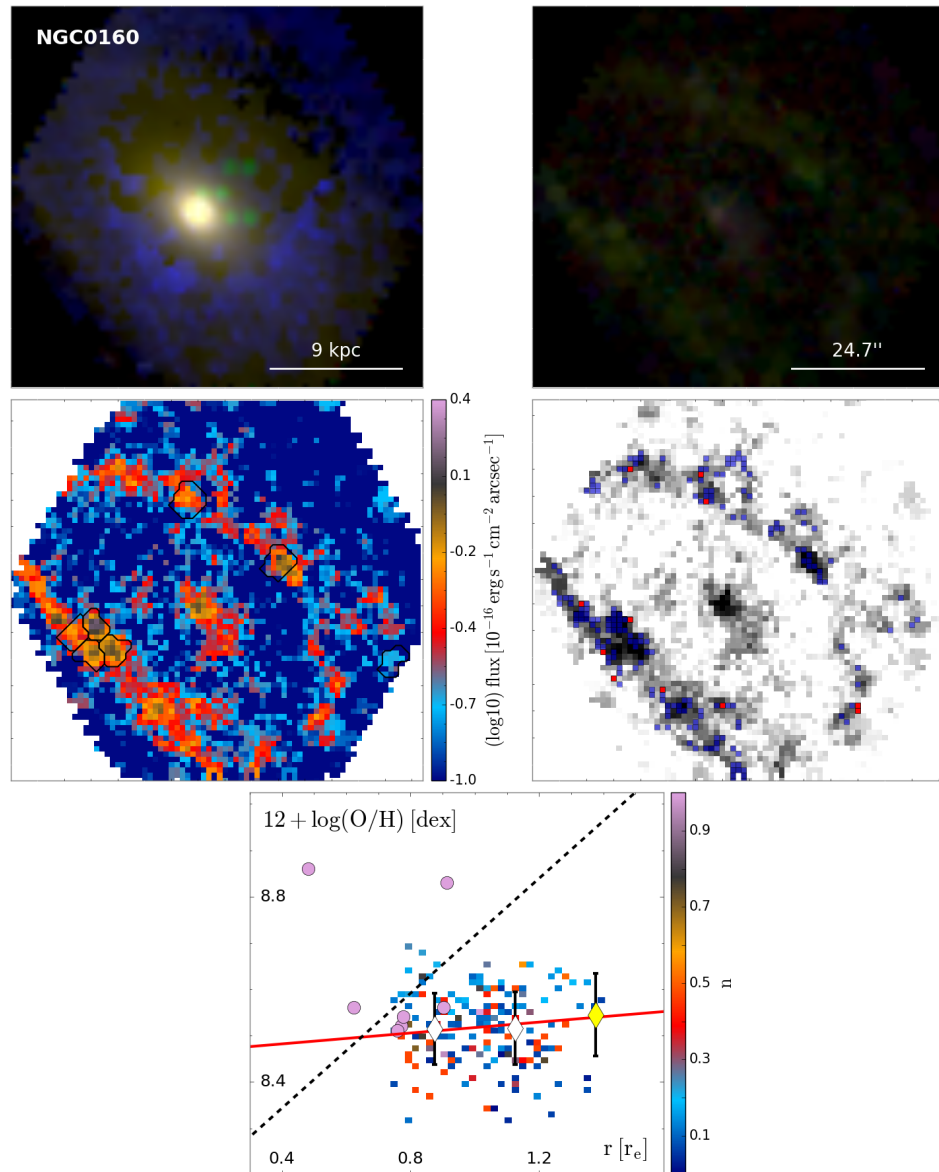


Figure C.3: NGC 0036. See Appendix C above for a description of each panel.



Arm-interarm abundance distribution analysis

not feasible for this galaxy.

See Sect. 6.1 for more details.

**Figure C.4:** NGC 0160. See Appendix C above for a description of each panel.



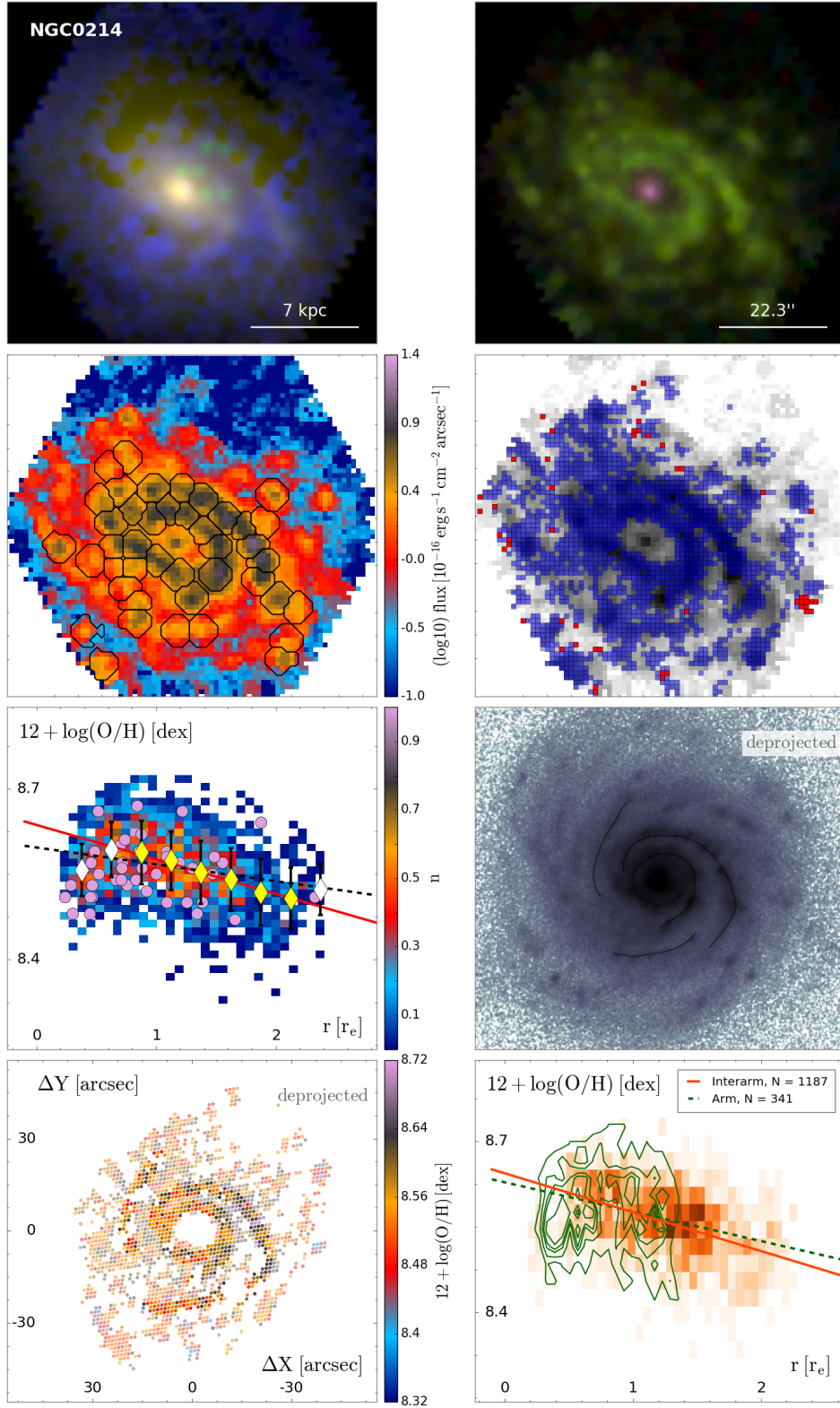


Figure C.5: NGC 0214. See Appendix C above for a description of each panel.



# D

## AMUSING sample characterisation plots

In this appendix we include a graphic summary of the AMUSING galaxies analysed in this thesis. We present a series of plots with RGB images and the main results derived from the analysis of the radial abundance distribution (see Figure D.1). Finally, for the subsample analysed in Chapter 7, the main results of the analysis of the local abundance variations are also represented (see Figures D.1-??). A complete description of the panels of each figure is given below.

**Figure D.1:** Graphic characterisation of AMUSING galaxies.

**Left** and **middle-left** panels show two RGB colour images of the galaxies, using SDSS  $r$ -,  $i$ - and  $z$ -band images recovered from the data (in red, green and blue respectively, left) and narrow-band images centred in the emission lines  $[\text{N II}]\lambda 6584$ ,  $\text{H}\alpha$ , and  $[\text{O III}]\lambda 5007$  (in red, green and blue respectively, middle-left). The **middle-right** panels present the  $\text{H}\alpha$  map of the galaxies together with the ionised regions detected by HIIEXPLORER (with  $\text{S/N} > 3$ ) shown as black segmented contours. Finally, the **right** panels show the deprojected oxygen abundance radial distribution of the H II regions (violet circles) normalised to the disc effective radius. The solid blue line represents the fit to this distribution, and the dashed vertical lines correspond to the radial position of the inner drop and/or outer flattening, if present.

**Note.** In the printed edition of this thesis, we present an abridged version of the Figure D.1 including the graphic characterisation for 18 galaxies of the AMUSING sample. The full version for the 102 galaxies of the sample is available in the electronic edition.

**Figure D.1-24:** Graphic characterisation of the local abundance variations.

**Top left** panels show a SDSS  $g$ -band image of the galaxies recovered from the data. The **top right** panels represent the normalised  $g$ -band light residuals. A mask has been applied to avoid some regions of the image in the derivation of the residuals (see Sect. 7.2.2 for details). **Middle left** panels show the 2D abundance distribution of the galaxies using only the spaxels associated with SF regions (see Sect. 3.2.2). **Middle right** panels represent the 2D residual abundance distribution after removing the characteristic radial profile. The **bottom left** panels show the distribution of the residual gas abundances (blue histogram) together with its Gaussian fit (black solid line). Deviations from the Gaussian distribution are highlighted with darker colours. Finally, the **bottom right** panels represent the correlation between the abundance residuals and the  $g$ -band light residuals in bins of 0.1 along the x-axis (blue dots). Only the bins containing at least 1% of the total number of spaxels have been represented. The error-weighted linear fit to these bins is shown as a blue solid line.

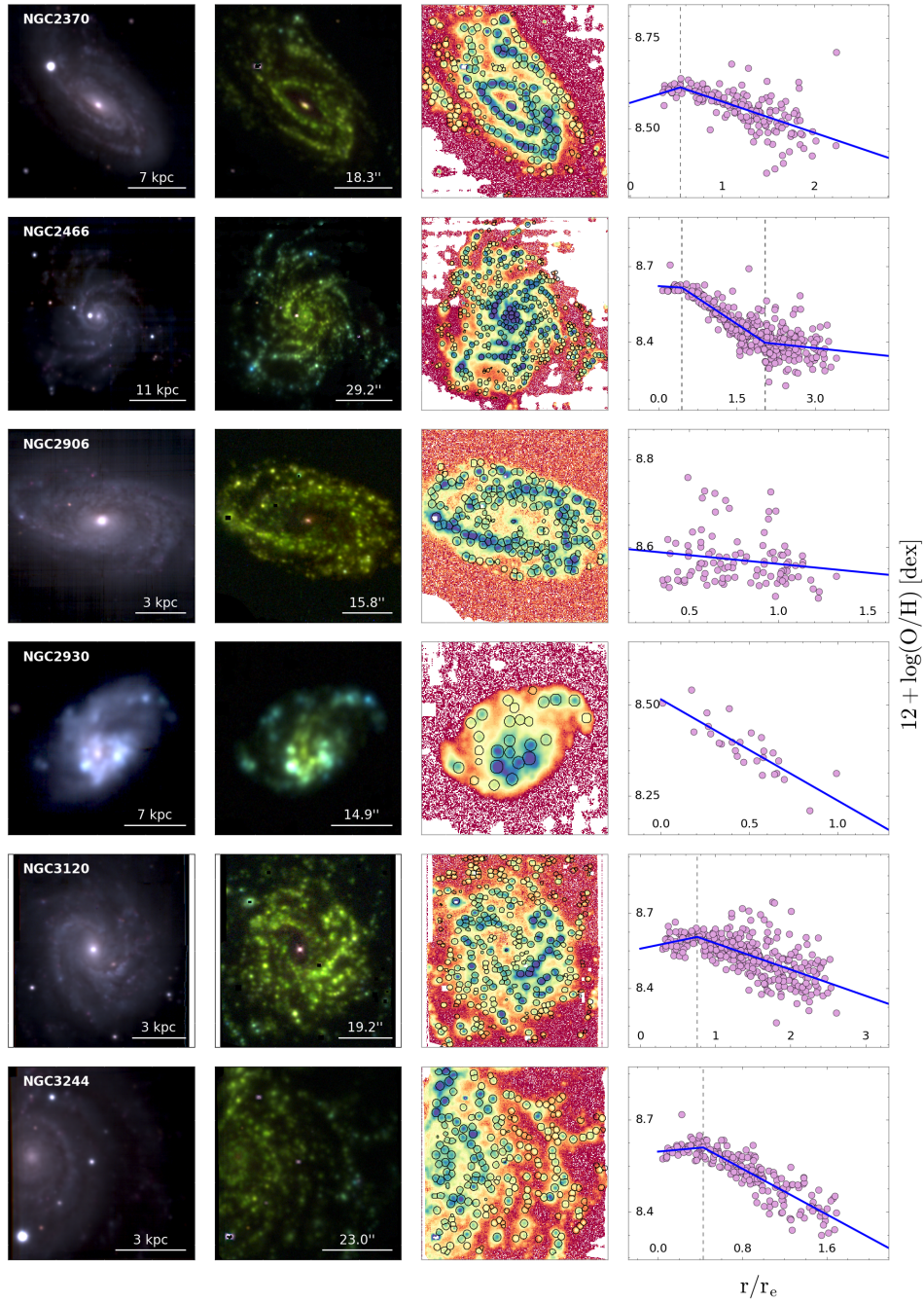


**Figure D.1:** *AMUSING* sample characterisation plots. See Appendix D above for a description of each panel.

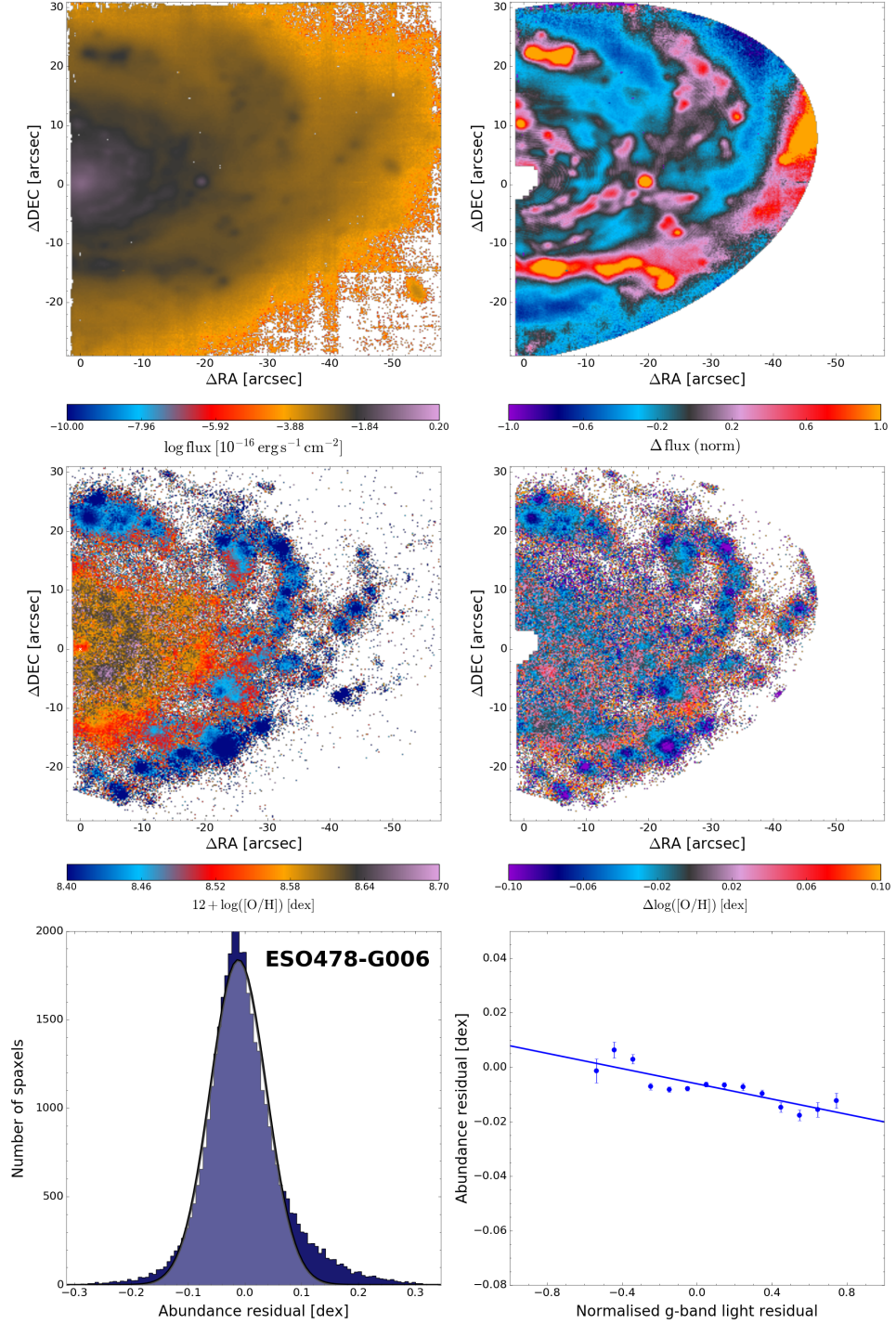


**Figure D.1:** Non-radial variations of the abundance distribution of ESO478-G006. See Appendix D above for a description of each panel.

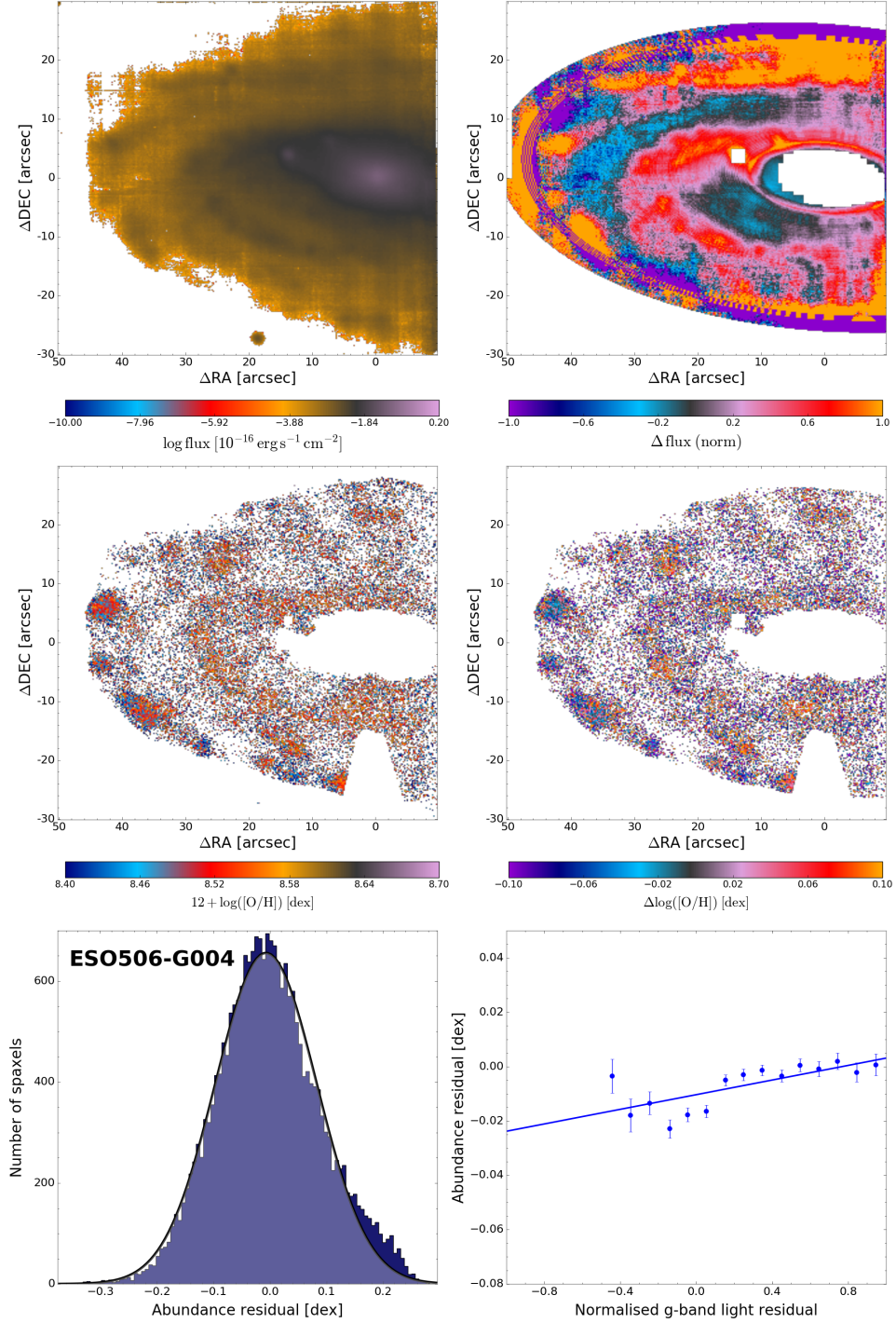


**Figure D.2:** Non-radial variations of the abundance distribution of ESO506-G004. See Appendix D above for a description of each panel.

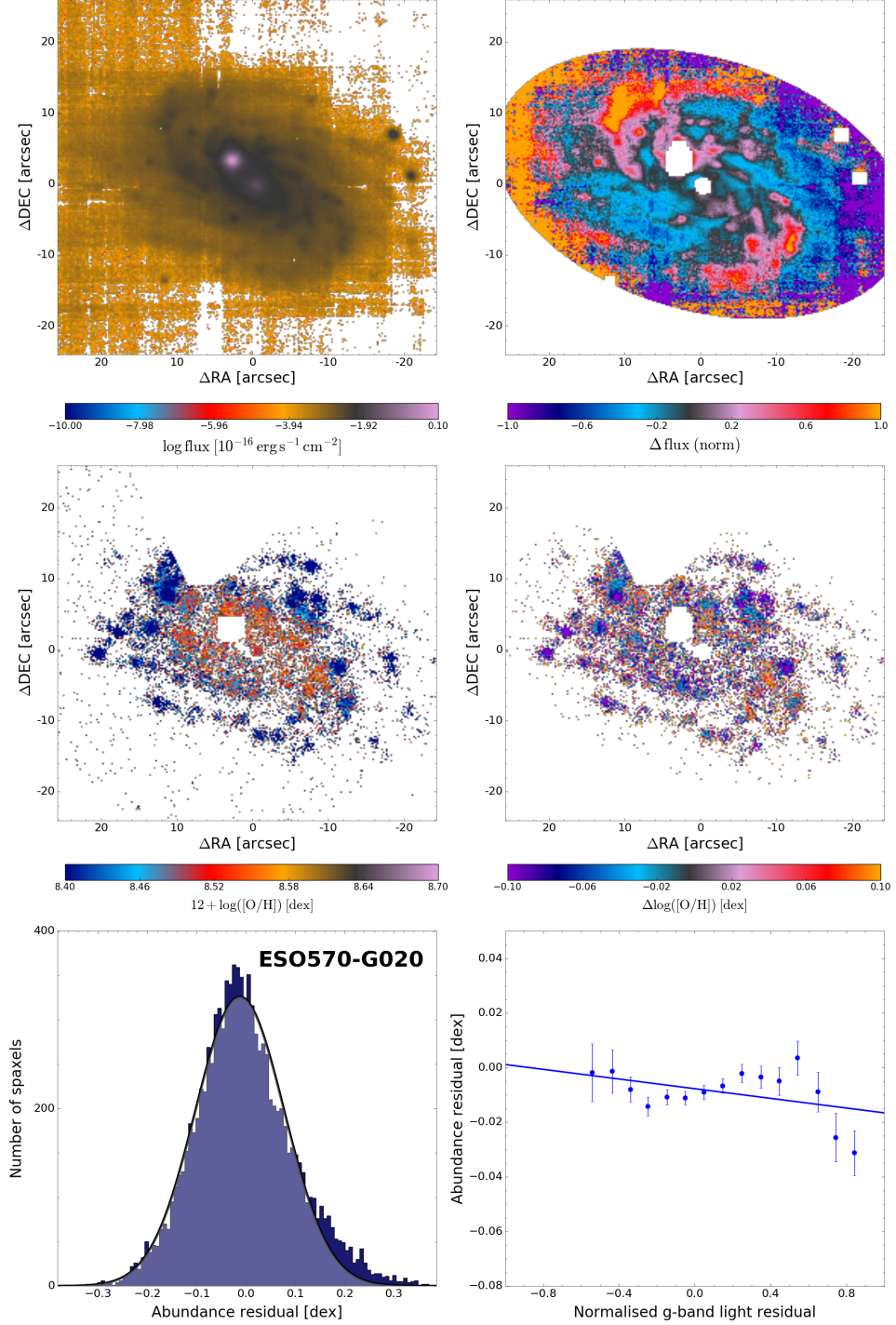


**Figure D.3:** Non-radial variations of the abundance distribution of ESO570-G020. See Appendix D above for a description of each panel.



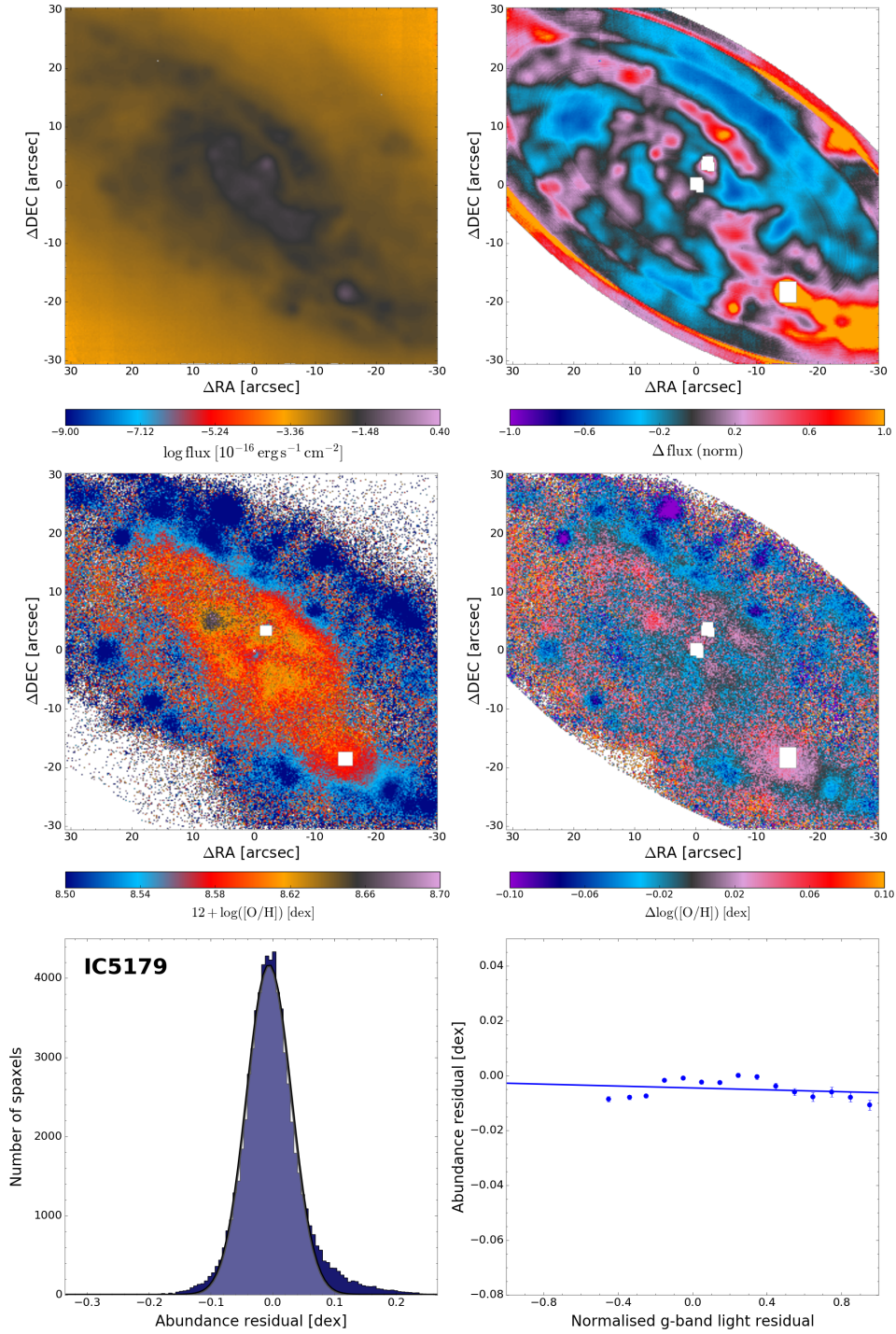


**Figure D.4:** Non-radial variations of the abundance distribution of IC5179. See Appendix D above for a description of each panel.

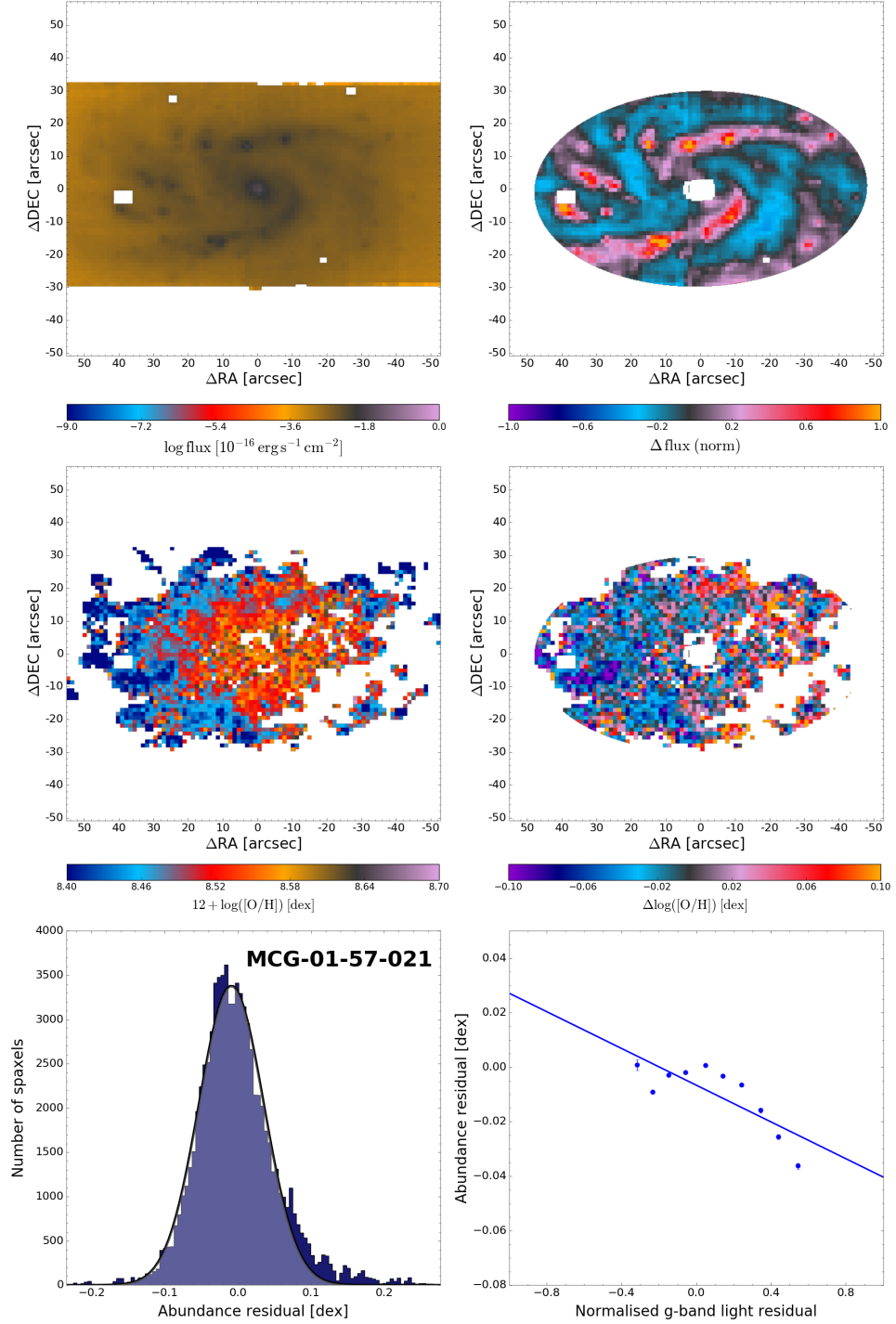


**Figure D.5:** Non-radial variations of the abundance distribution of MCG-01-57-021. See Appendix D above for a description of each panel.

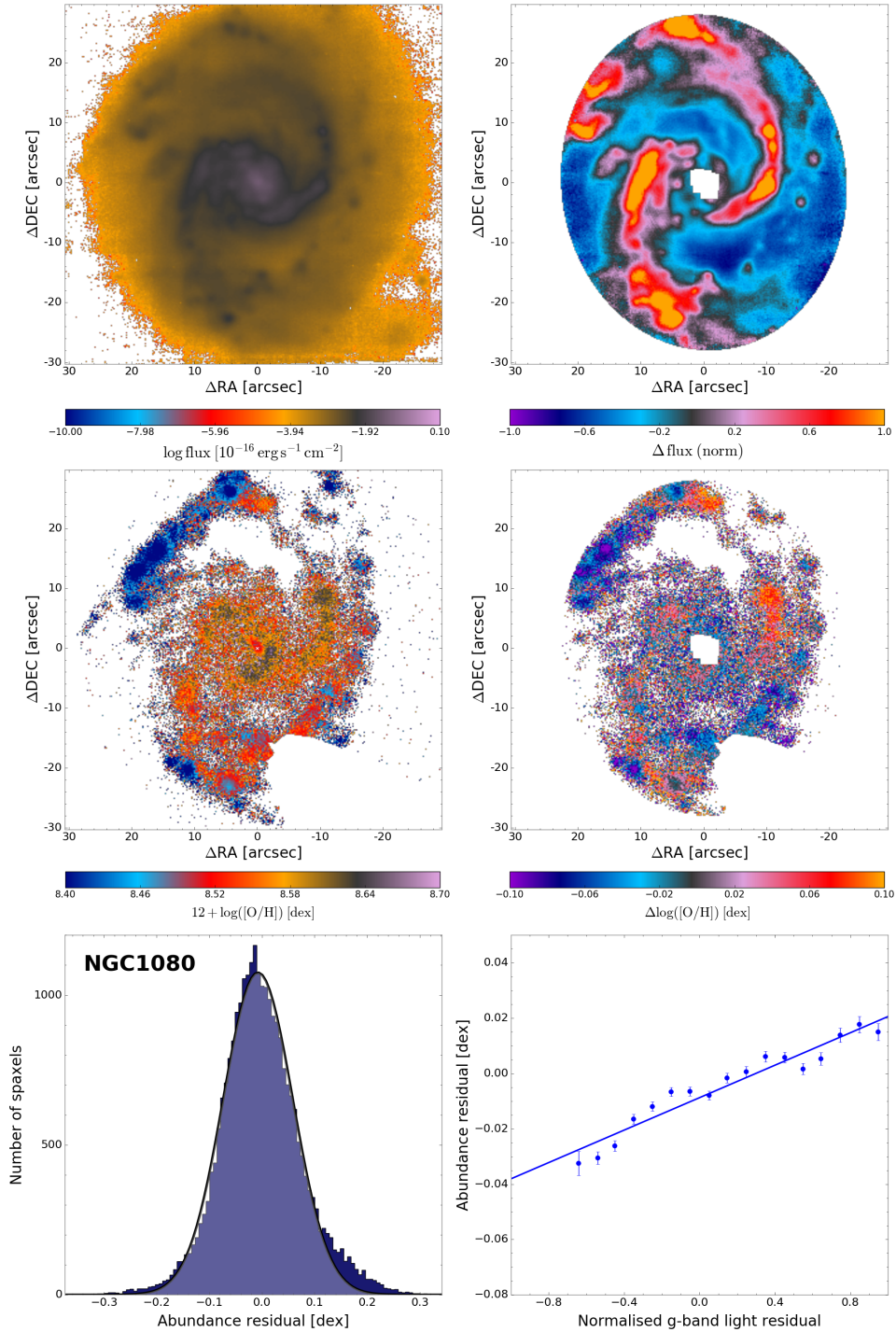


**Figure D.6:** Non-radial variations of the abundance distribution of NGC1080. See Appendix D above for a description of each panel.

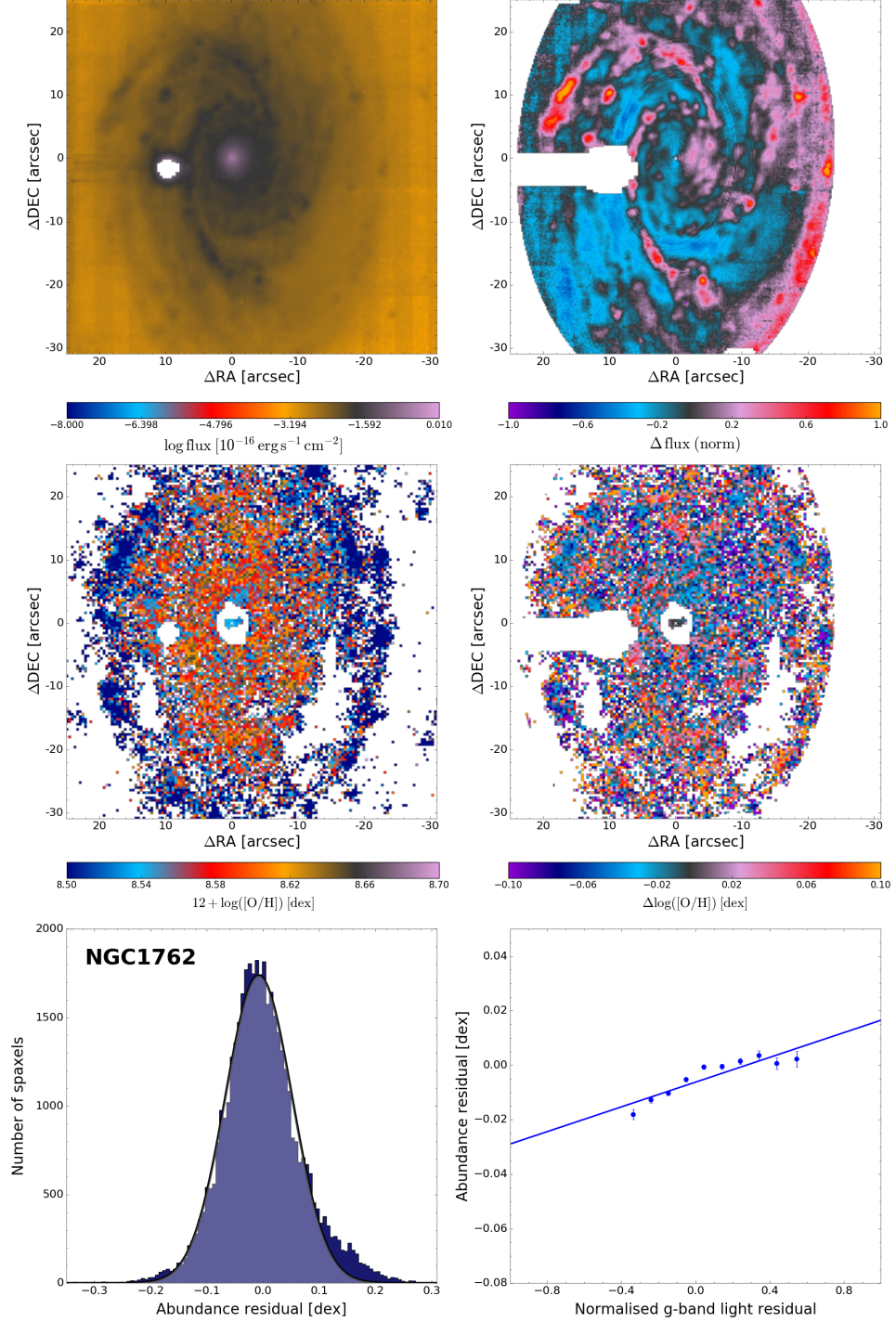


**Figure D.7:** Non-radial variations of the abundance distribution of NGC1762. See Appendix D above for a description of each panel.

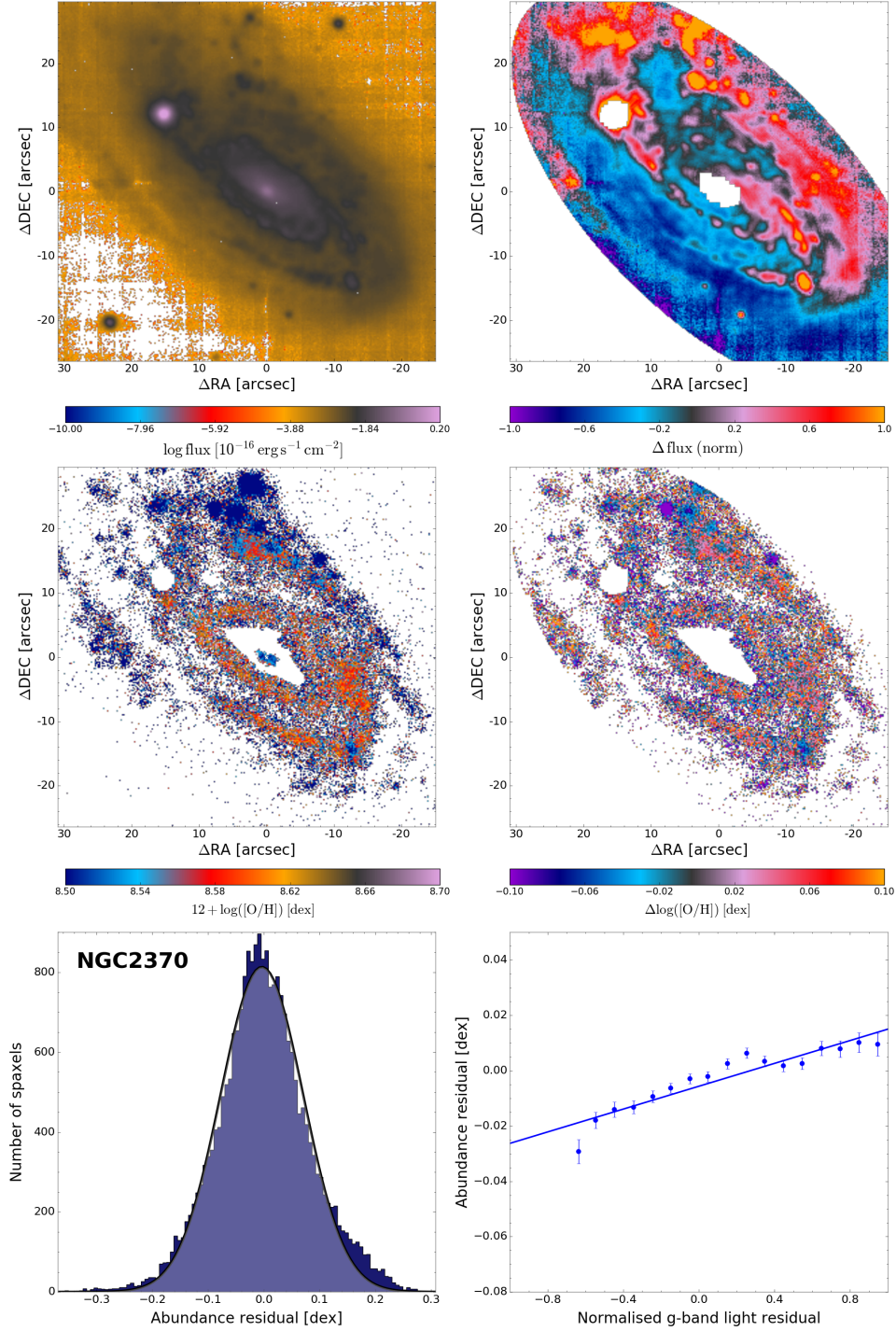


**Figure D.8:** Non-radial variations of the abundance distribution of NGC2370. See Appendix D above for a description of each panel.

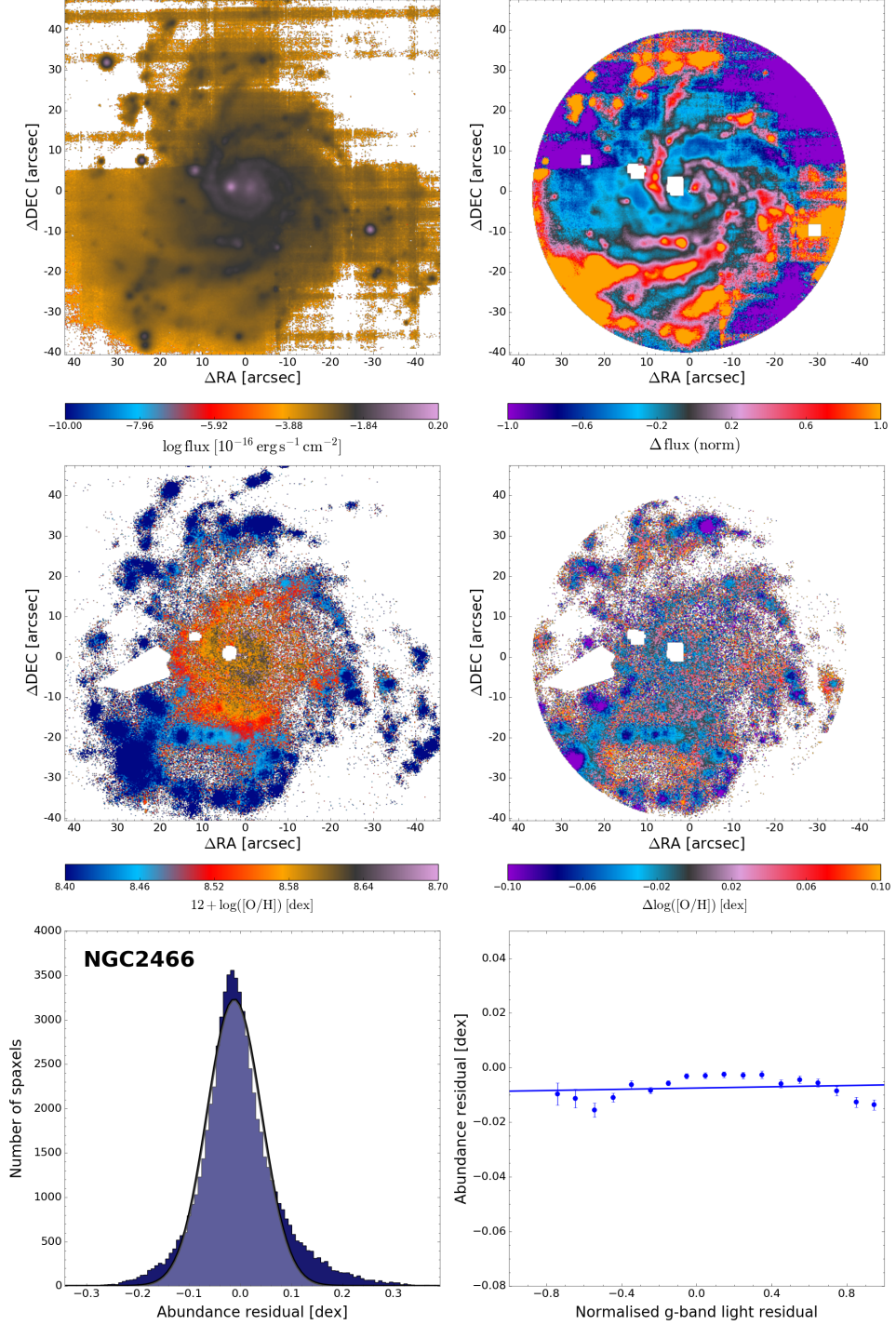


**Figure D.9:** Non-radial variations of the abundance distribution of NGC2466. See Appendix D above for a description of each panel.

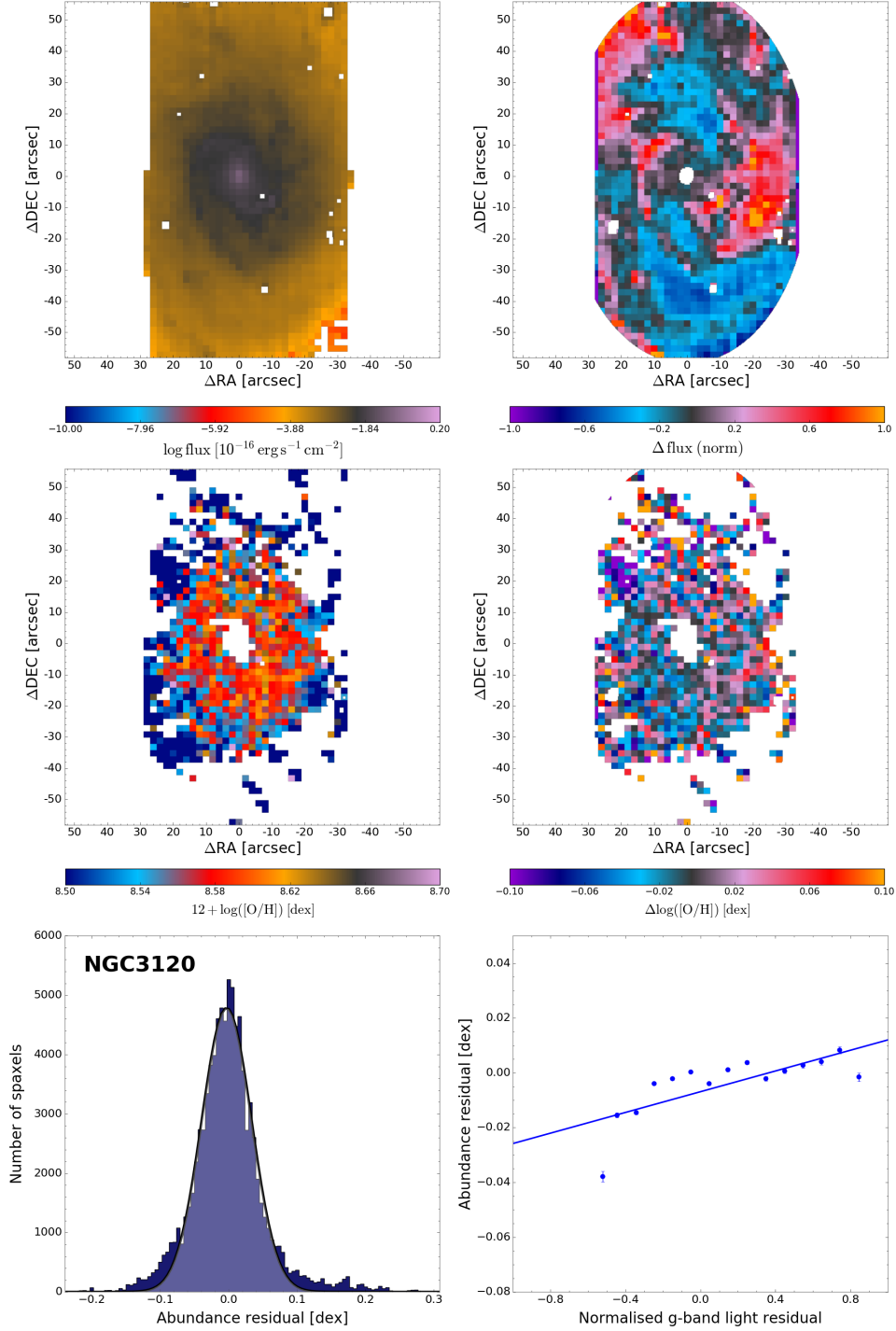


**Figure D.10:** Non-radial variations of the abundance distribution of NGC3120. See Appendix D above for a description of each panel.

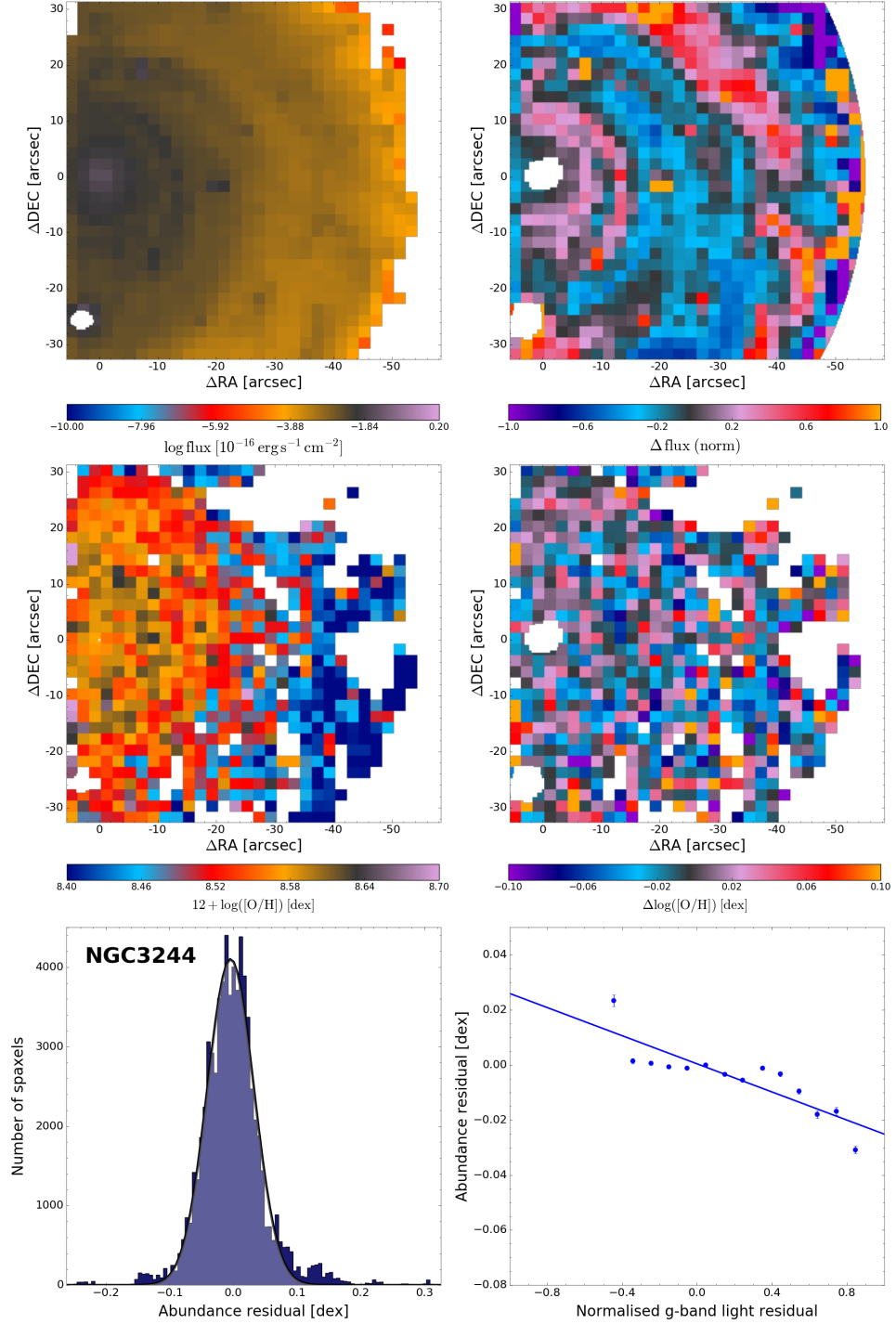


**Figure D.11:** Non-radial variations of the abundance distribution of NGC3244. See Appendix D above for a description of each panel.



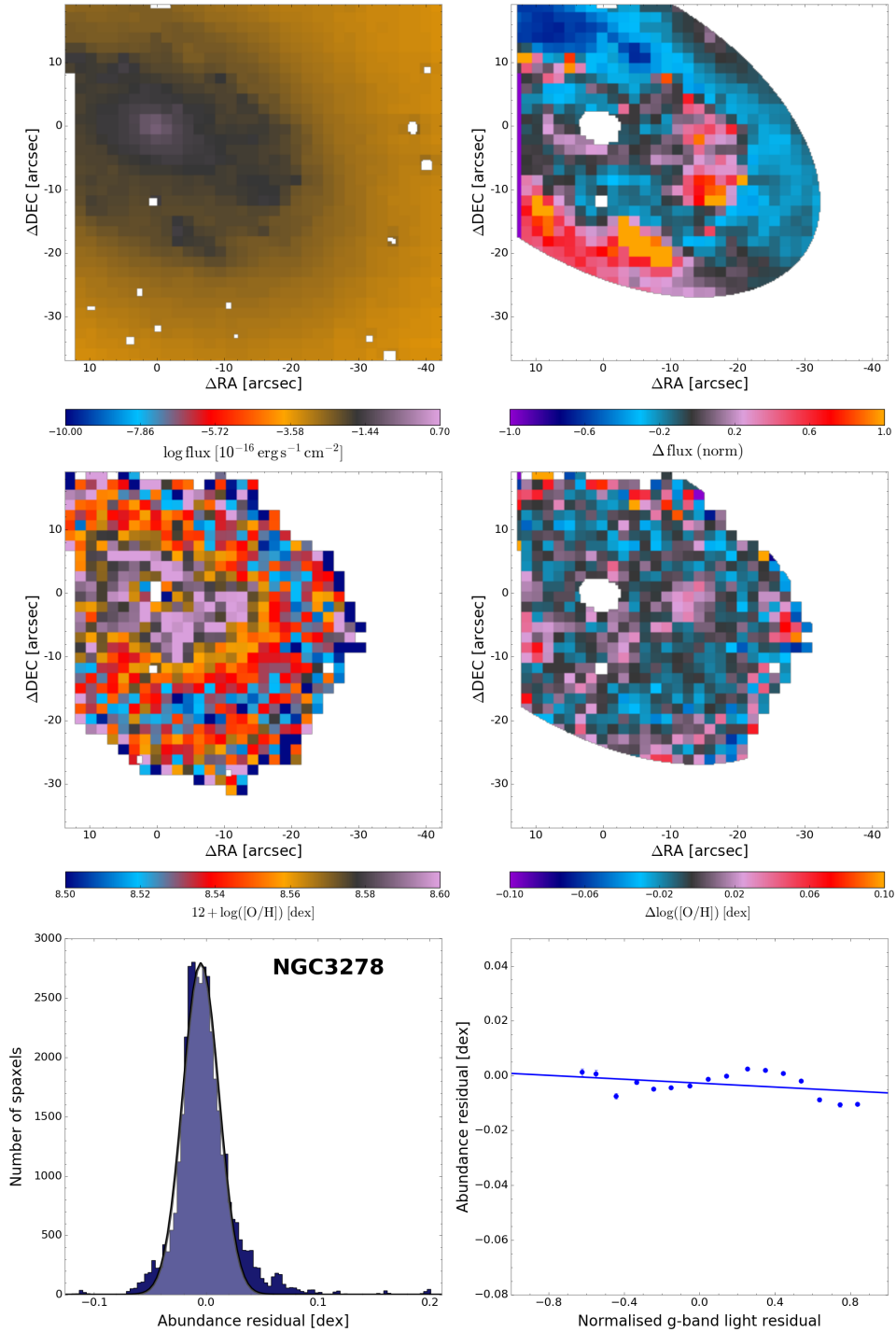


**Figure D.12:** Non-radial variations of the abundance distribution of NGC3278. See Appendix D above for a description of each panel.

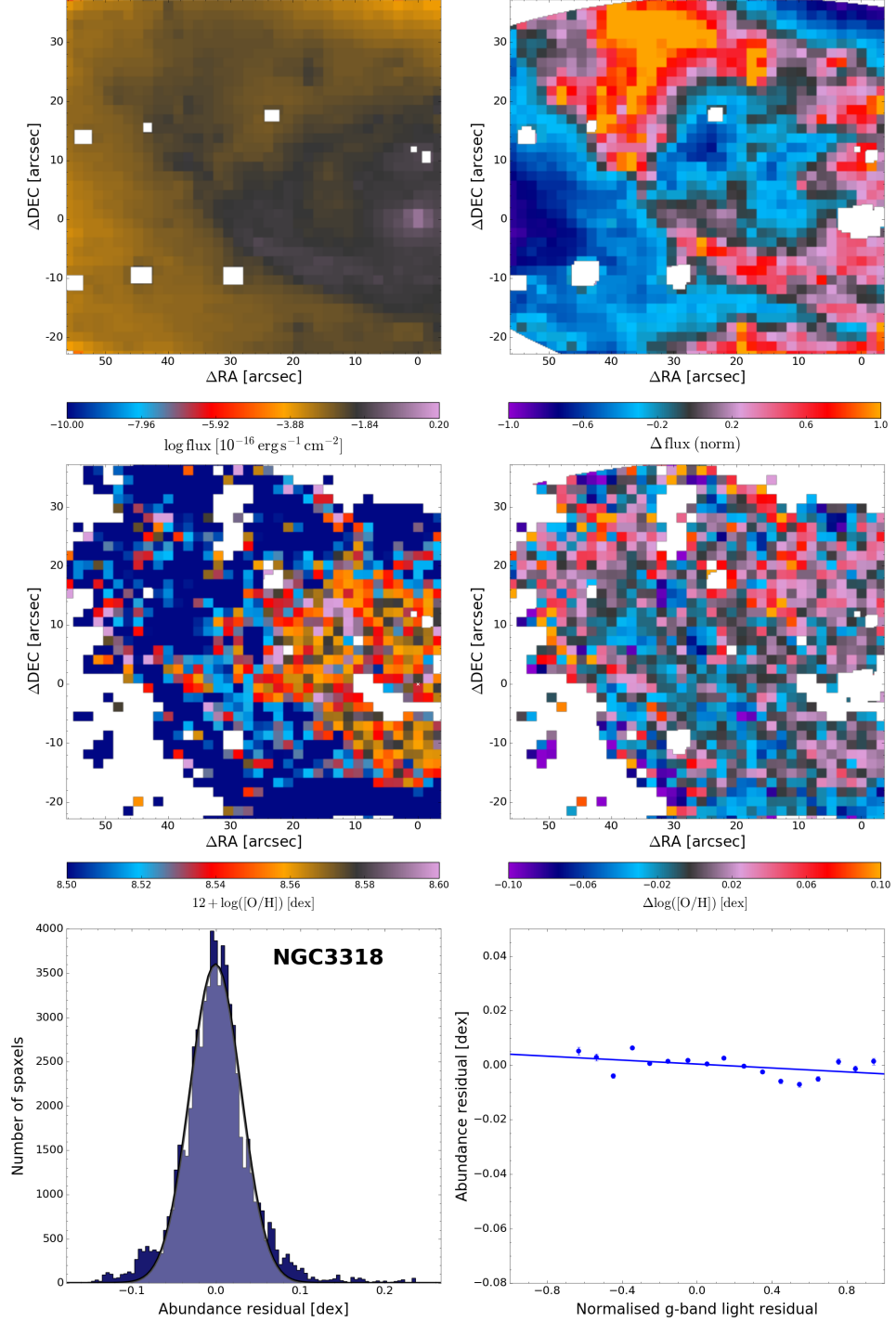


**Figure D.13:** Non-radial variations of the abundance distribution of NGC3318. See Appendix D above for a description of each panel.

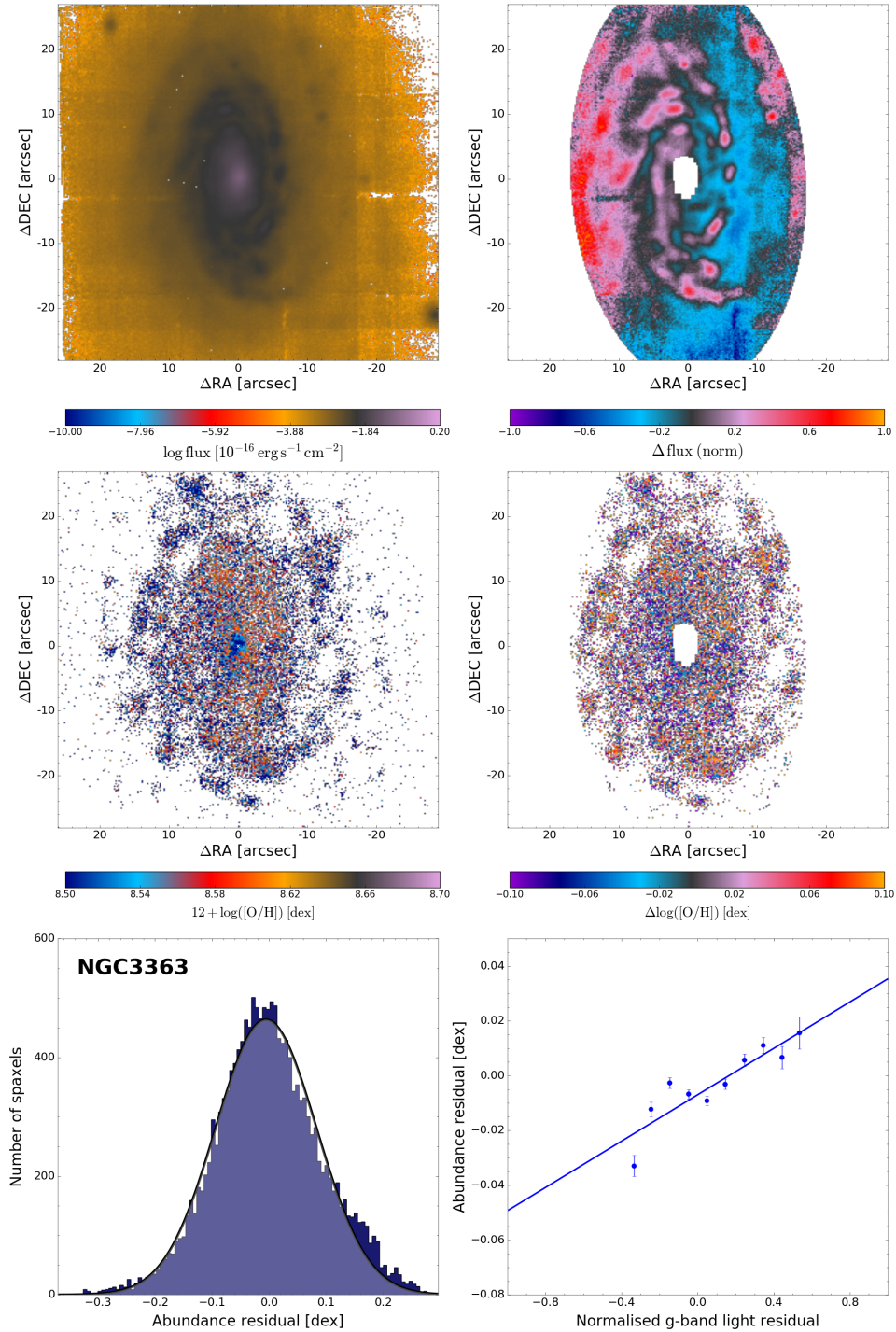


**Figure D.14:** Non-radial variations of the abundance distribution of NGC3363. See Appendix D above for a description of each panel.

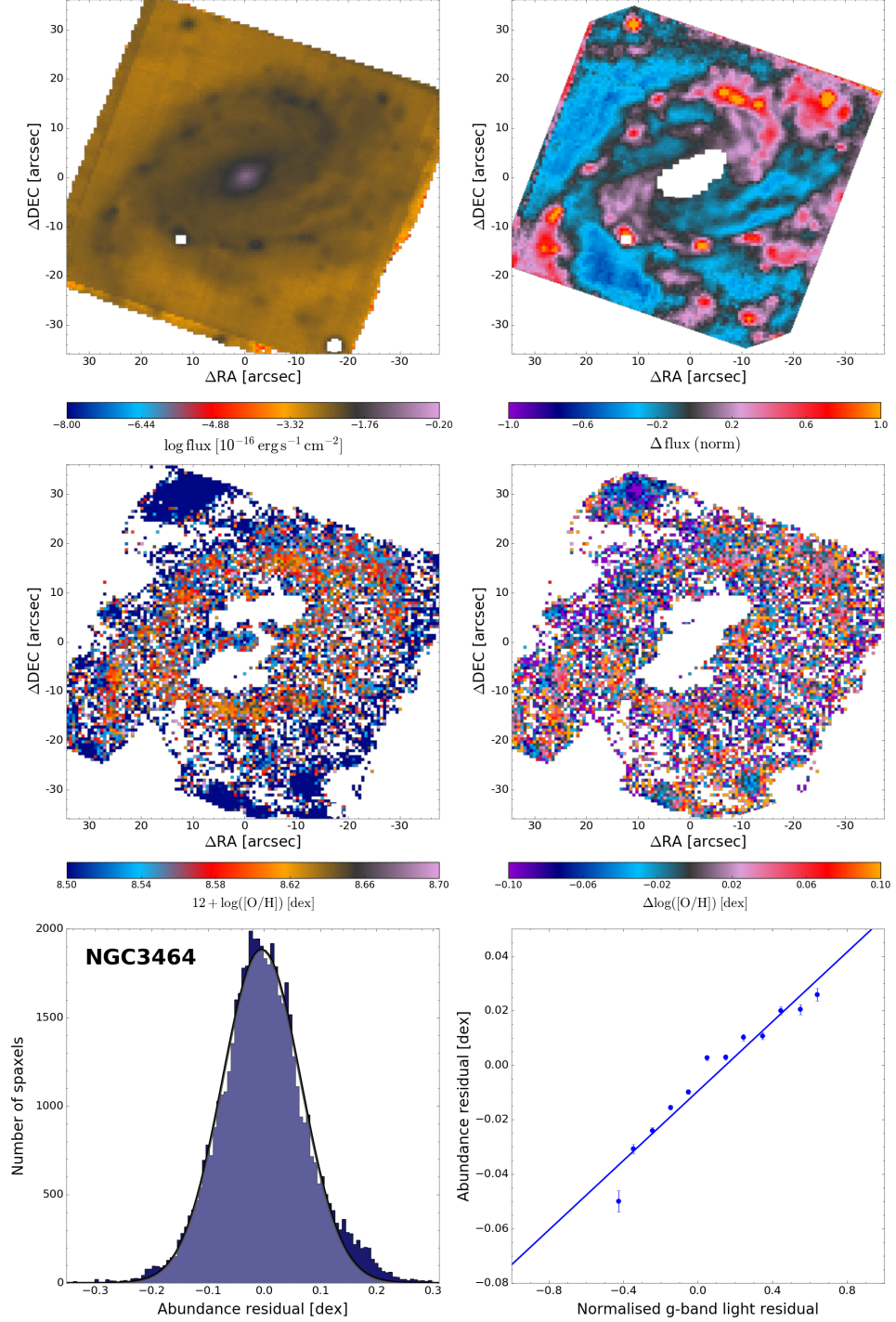


**Figure D.15:** Non-radial variations of the abundance distribution of NGC3464. See Appendix D above for a description of each panel.

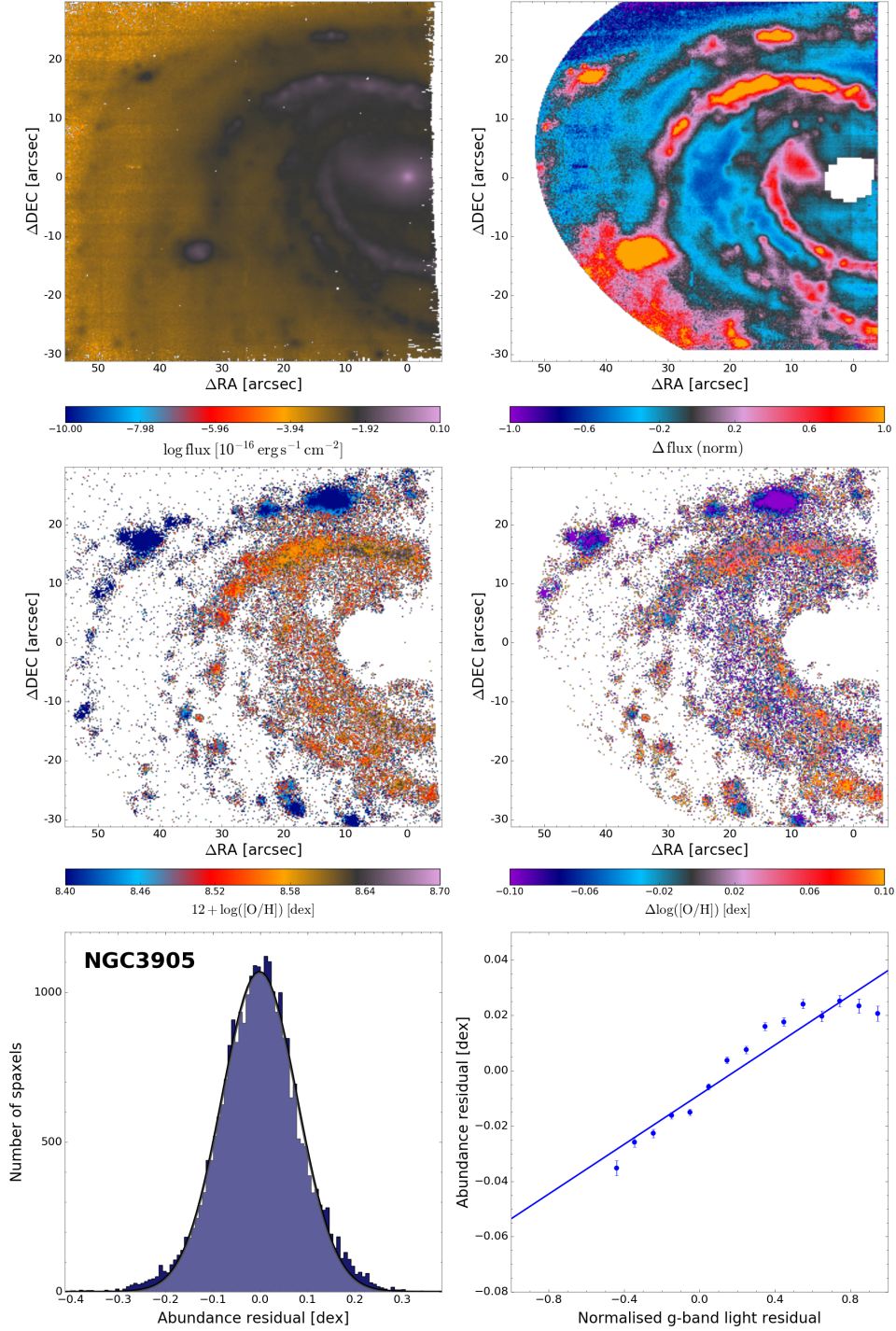


**Figure D.16:** Non-radial variations of the abundance distribution of NGC3905. See Appendix D above for a description of each panel.

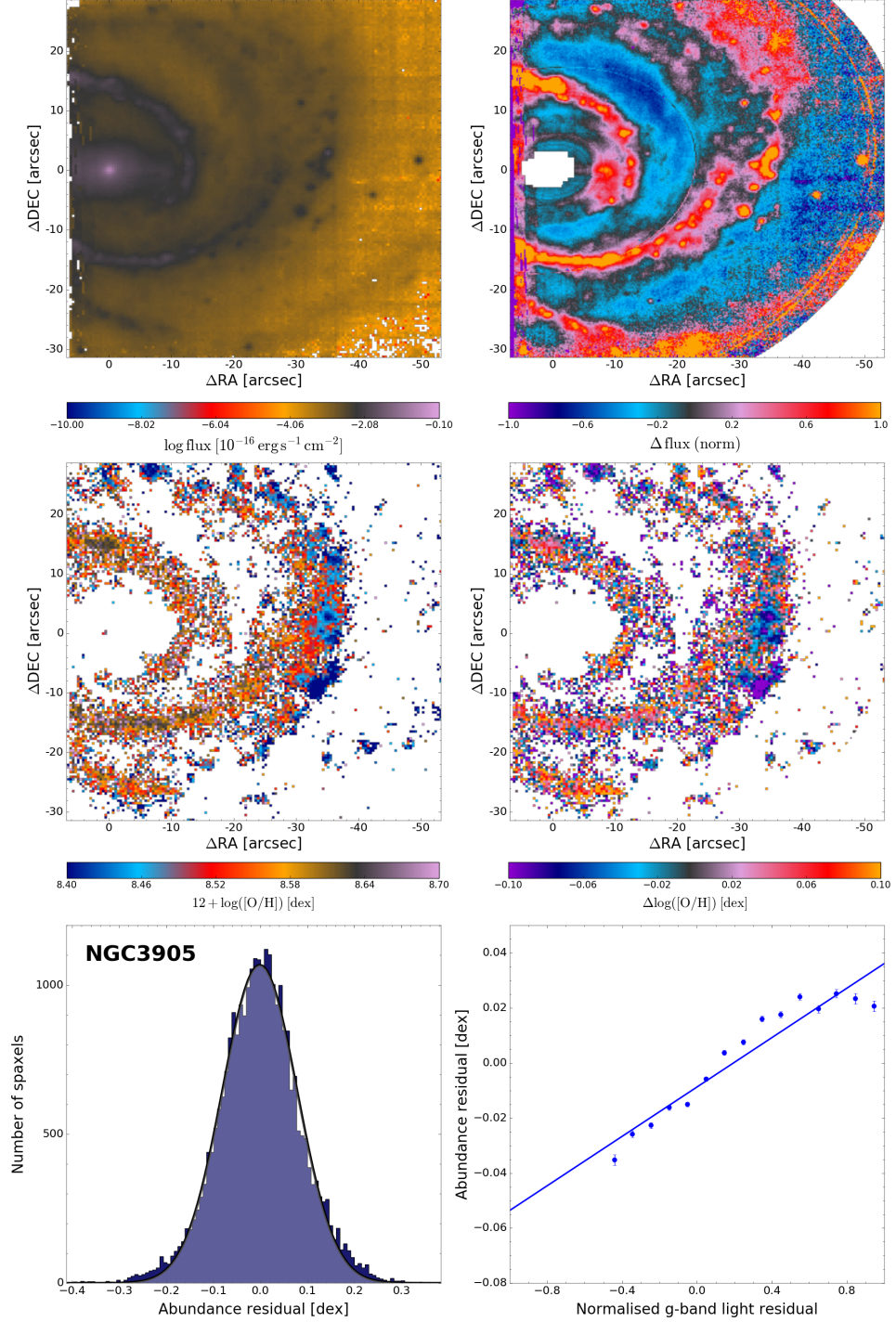


**Figure D.17:** Non-radial variations of the abundance distribution of NGC3905. See Appendix D above for a description of each panel.

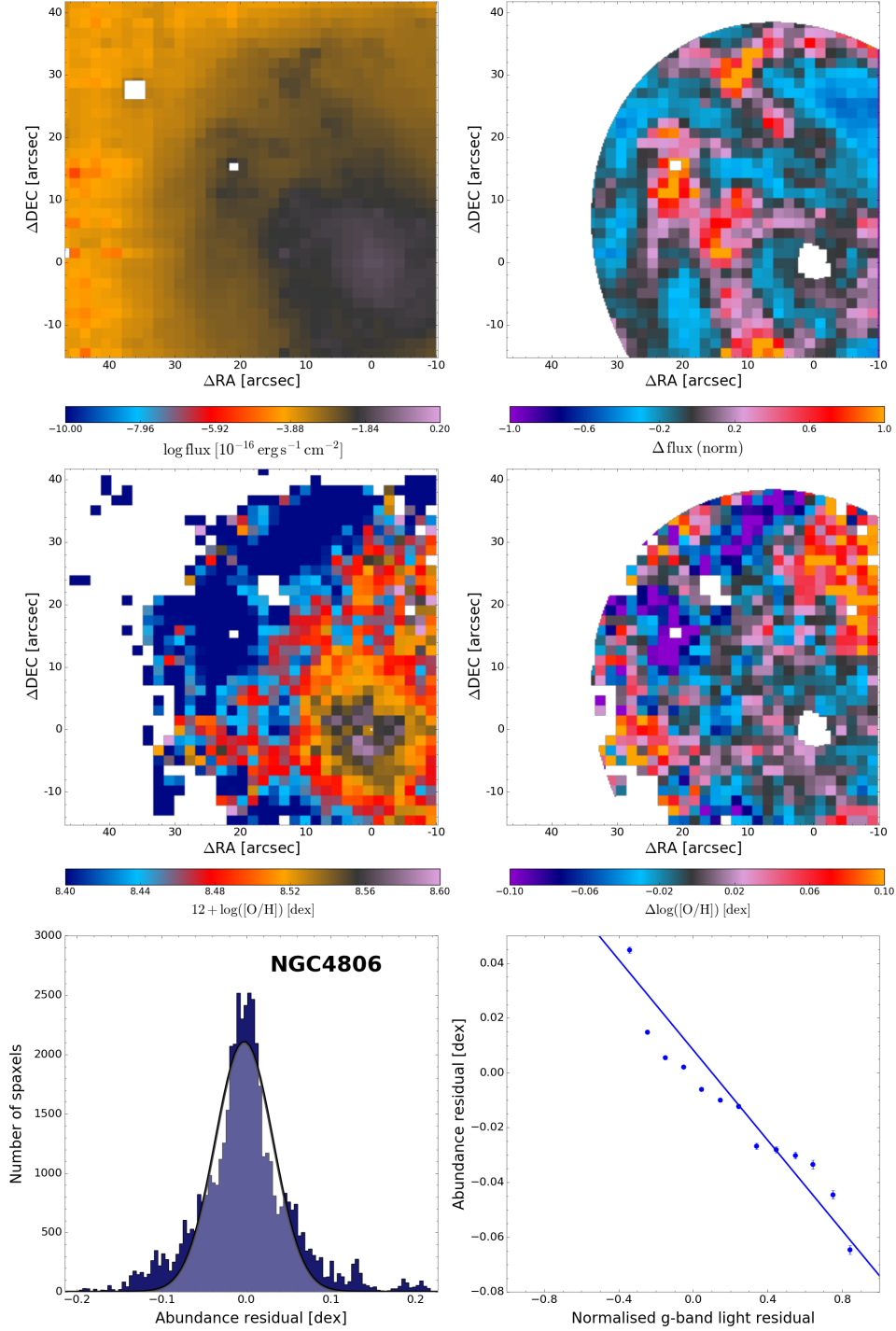


**Figure D.18:** Non-radial variations of the abundance distribution of NGC4806. See Appendix D above for a description of each panel.

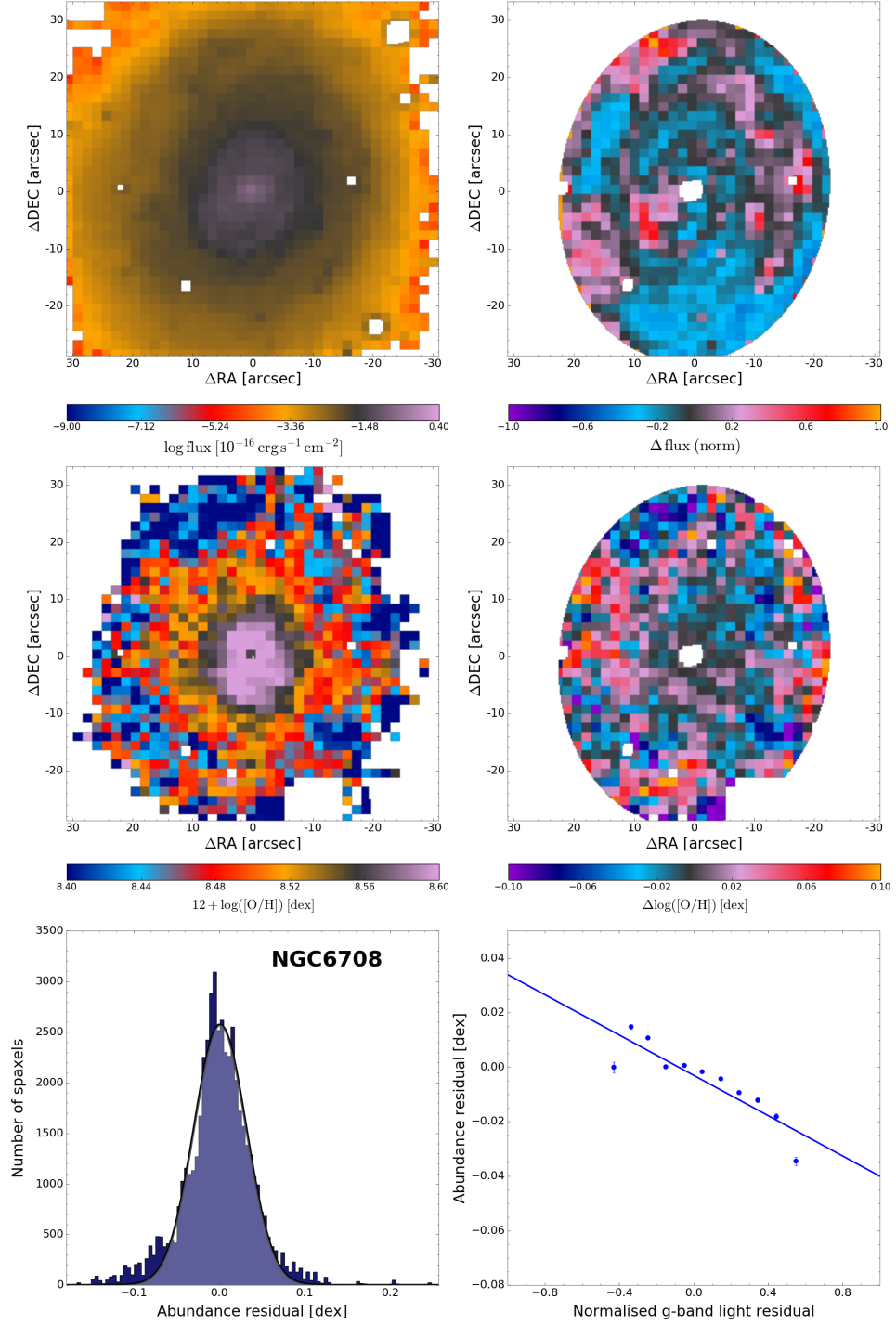


**Figure D.19:** Non-radial variations of the abundance distribution of NGC6708. See Appendix D above for a description of each panel.



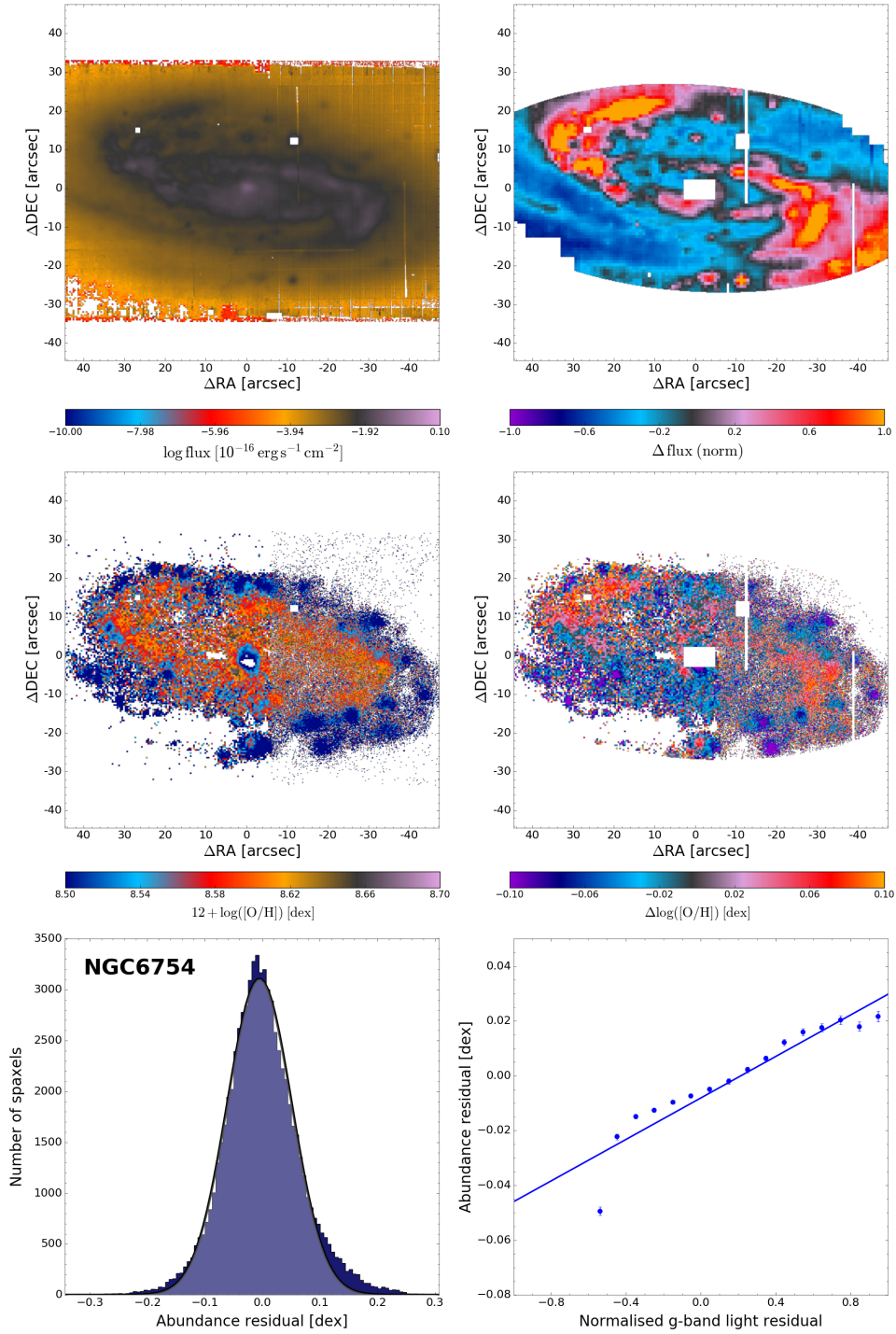


**Figure D.20:** Non-radial variations of the abundance distribution of NGC6754. See Appendix D above for a description of each panel.

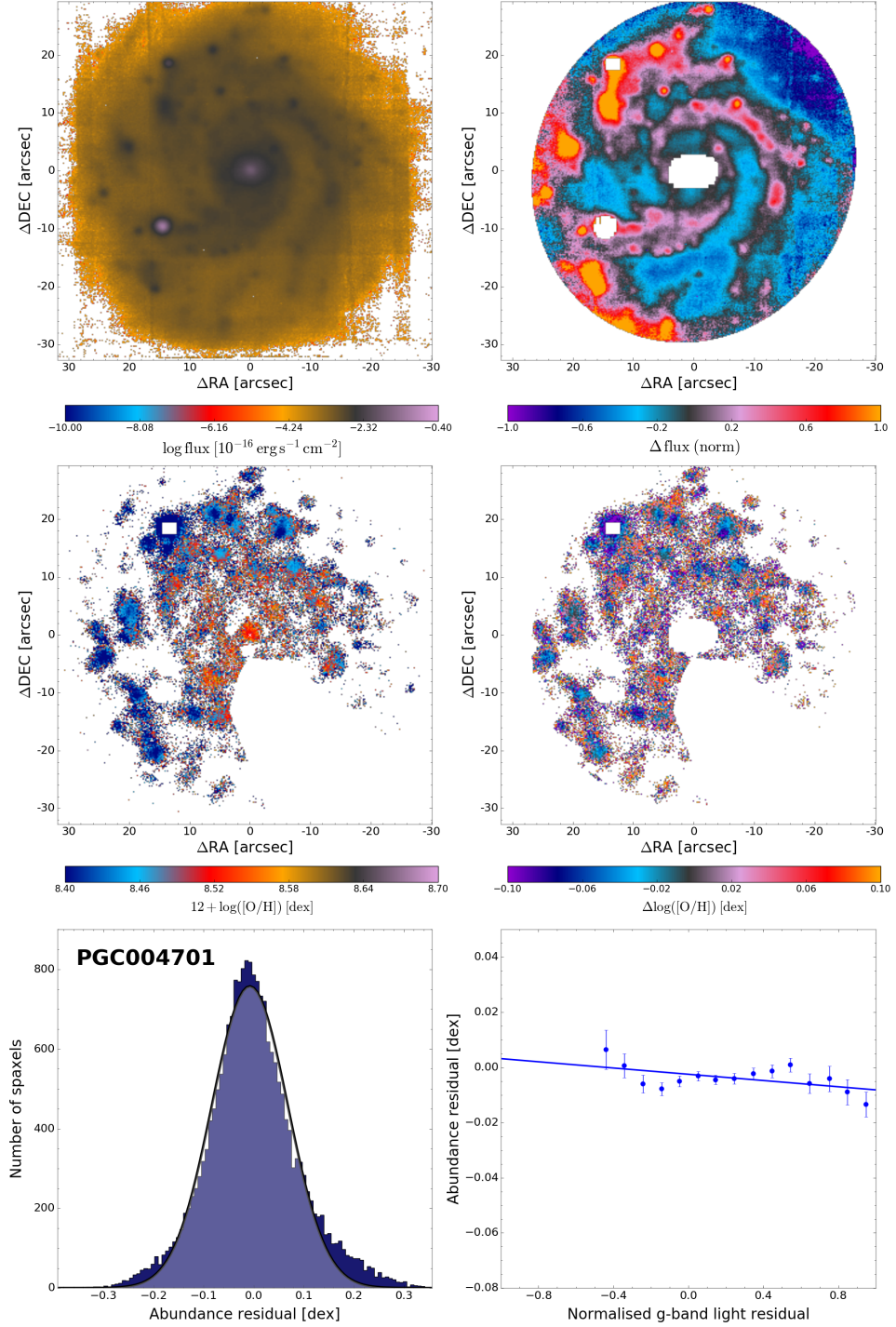


**Figure D.21:** Non-radial variations of the abundance distribution of PGC004701. See Appendix D above for a description of each panel.

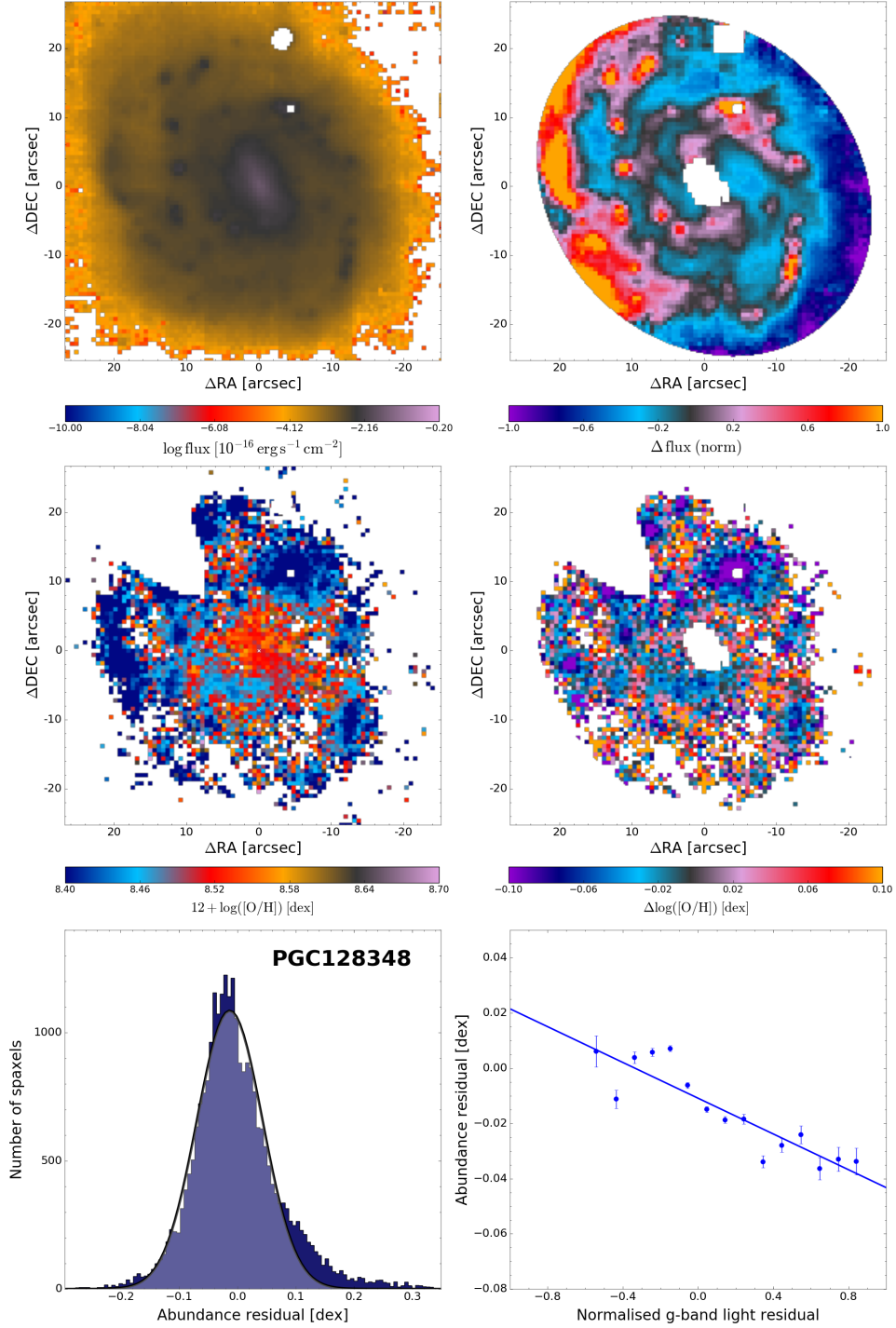


**Figure D.22:** Non-radial variations of the abundance distribution of PGC128348. See Appendix D above for a description of each panel.

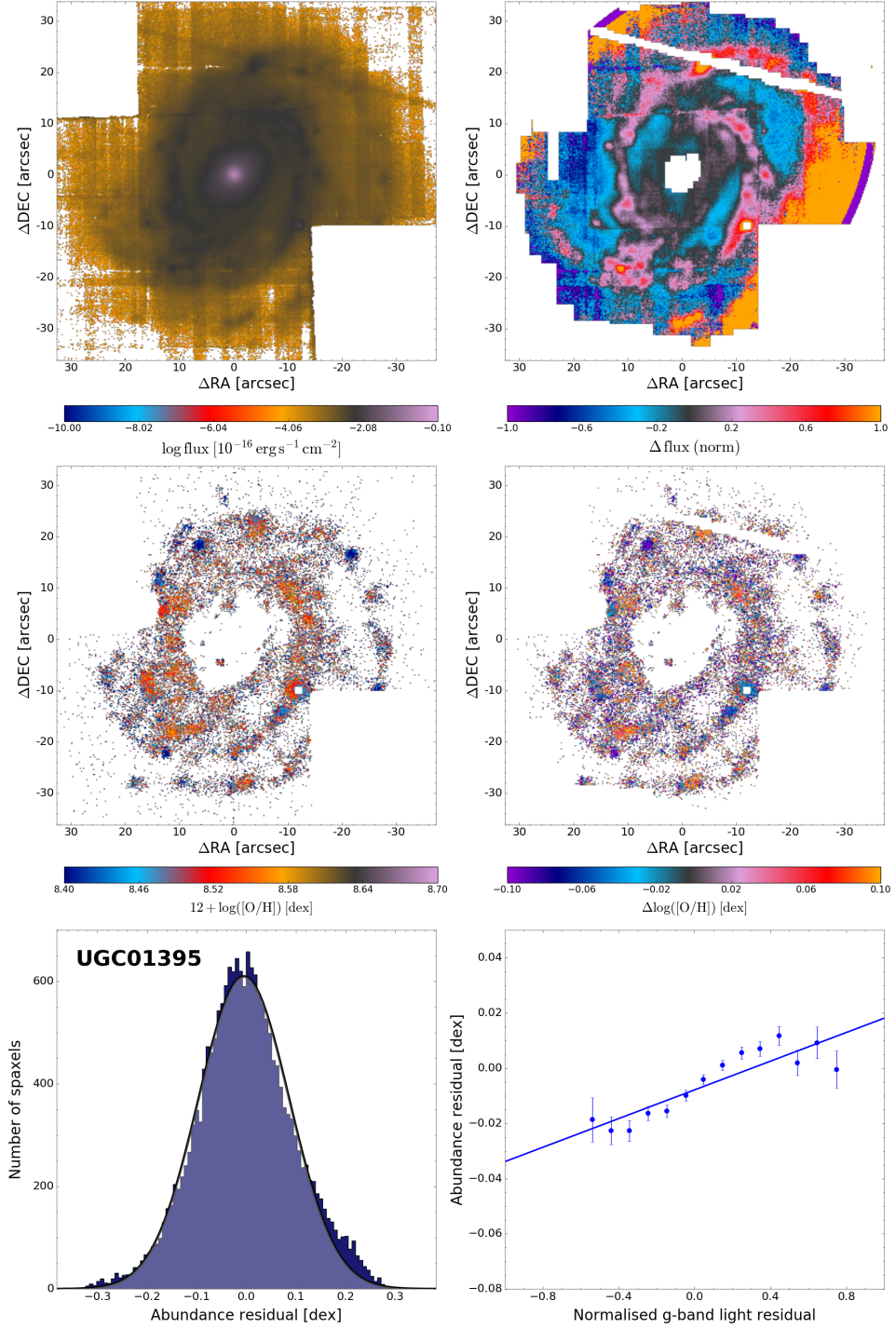


**Figure D.23:** Non-radial variations of the abundance distribution of UGC01395. See Appendix D above for a description of each panel.

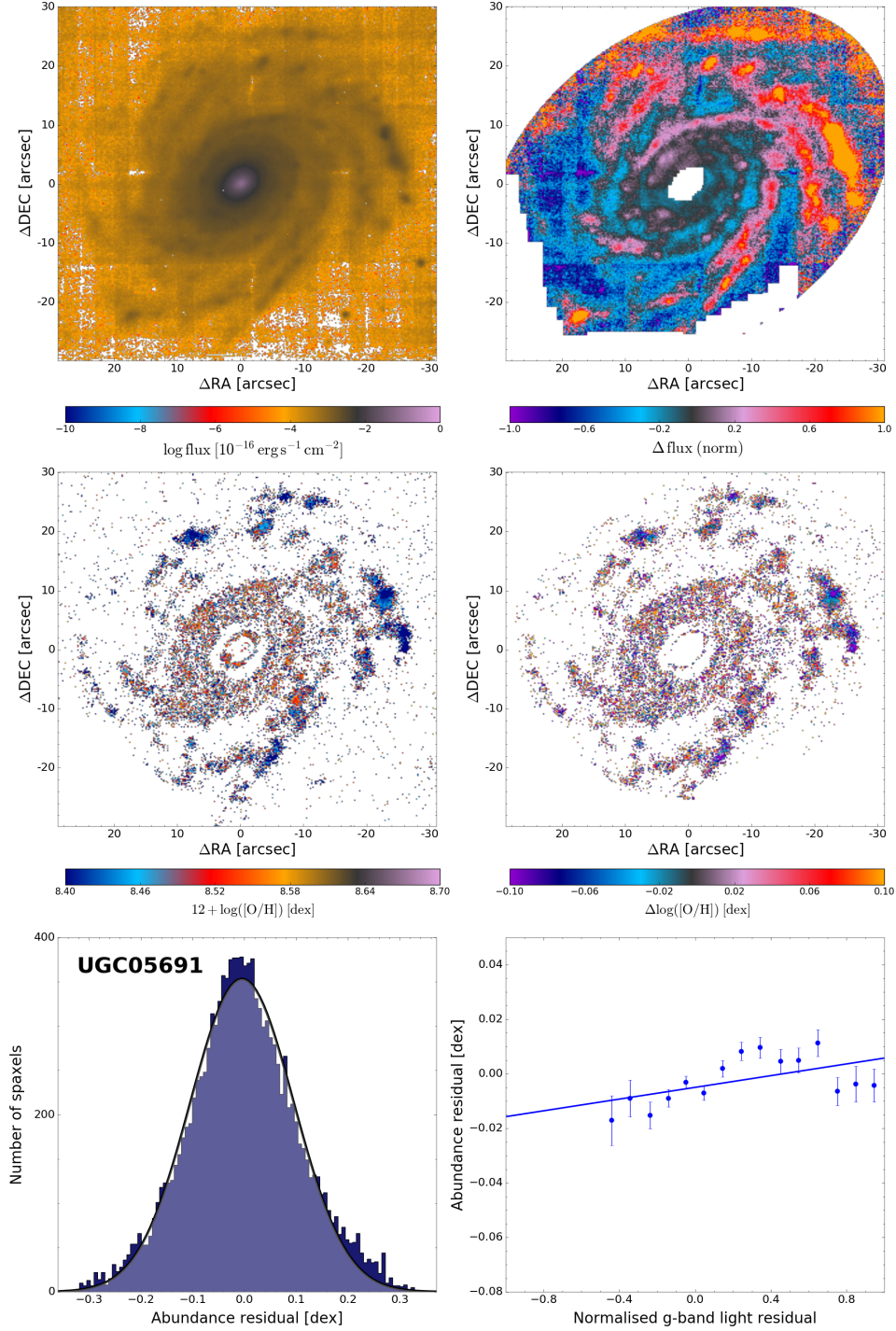


**Figure D.24:** Non-radial variations of the abundance distribution of UGC05691. See Appendix D above for a description of each panel.

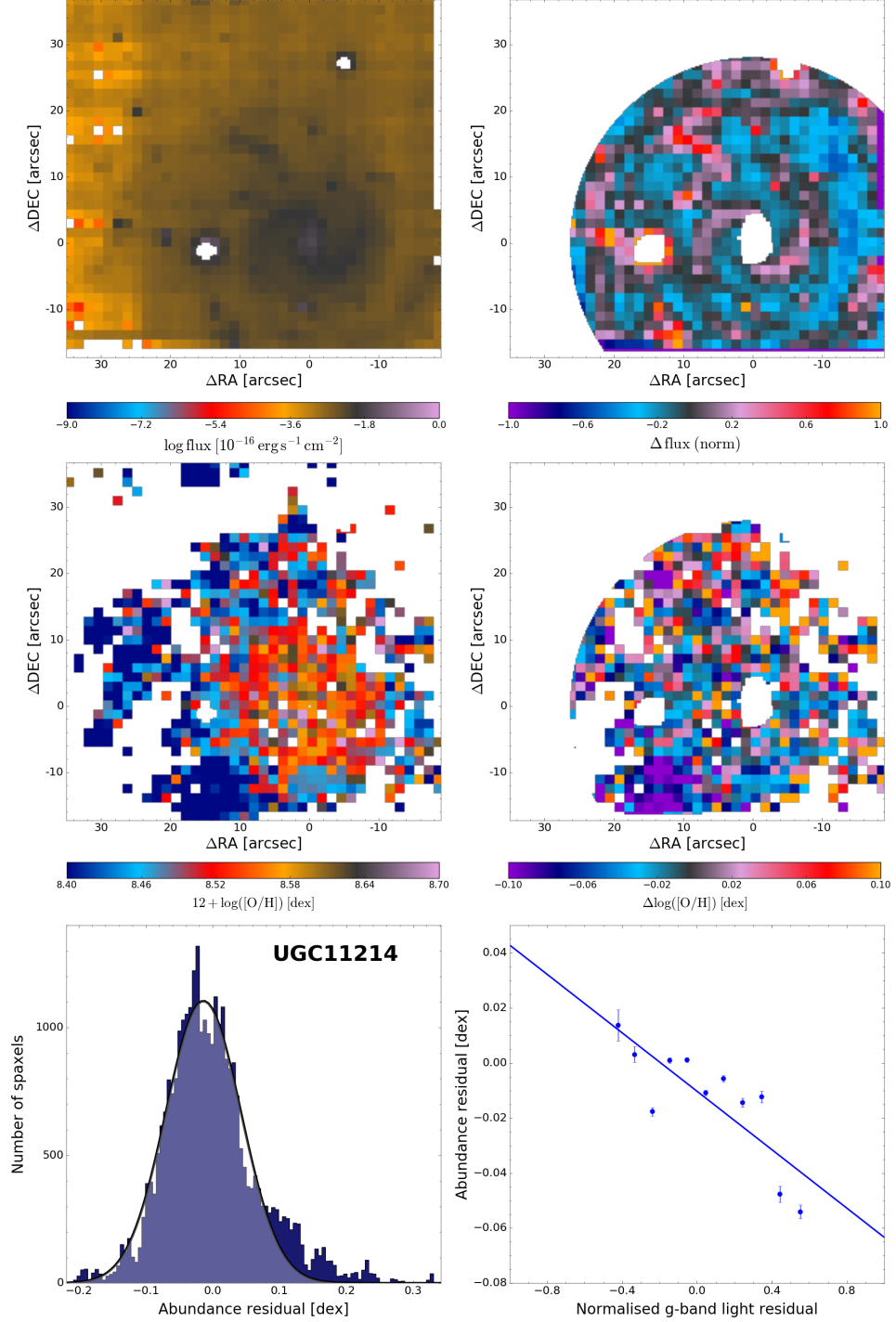


**Figure D.25:** Non-radial variations of the abundance distribution of UGC11214. See Appendix D above for a description of each panel.

# List of Acronyms

**AD test** Anderson-Darling test

**AGN** active galactic nuclei

**AMUSING** All-weather MUse Supernova Integral-field Nearby Galaxies

**CALIFA** Calar Alto Legacy Integral Field Area

**CMD** colour-magnitude diagram

**DSS2** Second Digitized Sky Survey

**FoV** field-of-view

**FWHM** Full Width at Half Maximum

**GANDALF** Gas AND Absorption Line Fitting

**GASP2D** GALaxy Surface Photometry 2 Dimensional Decomposition

**i** inclination angle

**IFS** Integral Field Spectroscopy

**IGM** intergalactic medium

**ISM** interstellar medium

**KS test** Kolmogorov-Smirnov test

**LOS** line-of-sight

**MC** Monte Carlo

**MW** Milky Way

**PA** position angle

**PMAS** Potsdam Multi-Aperture Spectrograph

**PPak** PMAS fiber Package

**pPXF** penalized pixel-fitting

.....  
**r<sub>e</sub>** disc effective radii

**r<sub>e</sub>** disc effective radius

**S/N** Signal to Noise ratio

**SBP** surface brightness profile

**SDSS** Sloan Digital Sky Survey

**SF** star formation

**SFH** star formation history

**SFR** star formation rate

**SSP** simple stellar populations

**STECKMAP** STEllar Content and Kinematics via Maximum A Posteriori  
likelihood

**ULySS** Université de Lyon Spectroscopic analysis Software



# List of Figures

1.1	Schematic representation of the Hubble sequence . . . . .	10
1.2	Types of galaxy morphologies . . . . .	11
1.3	Schematic representation of the galaxy colour-magnitude diagram. . . . .	12
1.4	Classification of disc galaxies according to the spiral structure	14
1.5	The Orion Nebula (M42) . . . . .	18
1.6	Typical spectrum of an H II region . . . . .	20
1.7	O/H gradients in M101 and M33 from Smith (1975) . . . . .	23
2.1	CALIFA's mandala . . . . .	32
2.2	Characterisation of the CALIFA subsample of galaxies . . . . .	34
2.3	$(B - V)$ vs $M_V$ diagram of the CALIFA subsample of galaxies	35
2.4	Characterisation of the AMUSING subsample of galaxies . . . . .	39
2.5	SFR-stellar mass plane of the CALIFA and AMUSING samples	40
3.1	Example of the performance of FIT3D on a typical CALIFA spectrum . . . . .	48
3.2	Example of the performance of FIT3D on two typical AMUSING spectra of H II regions . . . . .	49
3.3	BPT diagrams of CALIFA and AMUSING galaxies . . . . .	52
3.4	Distribution of the selected star forming regions in NGC 0165 and PGC 128348 . . . . .	53
3.5	Comparison among abundance empirical calibrators with CALIFA . . . . .	58
3.6	Comparison among abundance empirical calibrators with AMUSING . . . . .	60
3.7	Comparison of the PA and $i$ angles for CALIFA galaxies . . . . .	62
4.1	Radial abundance distribution of NGC 0165 . . . . .	67
4.2	Distribution of the linear fit parameters for the oxygen abundance gradients of the CALIFA sample . . . . .	69
4.3	Distribution of the abundance slopes as a function of different galaxy properties for CALIFA sample . . . . .	71
4.4	Radial distribution of the oxygen abundance for the entire CALIFA sample . . . . .	75

4.5	Average oxygen abundance radial profiles for different stellar-mass bins based on the CALIFA sample . . . . .	77
4.6	Distribution of slope values of the oxygen abundance gradients of the CALIFA sample using alternative calibrators . . .	83
4.7	Distribution of the abundance slopes as a function of different galaxy properties for CALIFA sample using alternative calibrators . . . . .	84
4.8	Radial distribution of the oxygen abundance for the entire CALIFA sample with alternative calibrators . . . . .	85
5.1	Oxygen abundance radial profiles of the H II regions in four AMUSING galaxies . . . . .	93
5.2	Distribution of slope values of the main abundance gradients in the AMUSING sample . . . . .	94
5.3	Distribution of slopes depending on different galaxy properties for AMUSING sample . . . . .	96
5.4	Location of the inner abundance drop and the outer flattening for the AMUSING sample . . . . .	100
5.5	Radial distribution of the oxygen abundance for the entire AMUSING sample . . . . .	102
5.6	Correlation between $r_{O/H}$ and $r_e$ for AMUSING galaxies . . .	103
5.7	Location of the inner abundance drop and the outer flattening for the AMUSING sample in units of $r_{O/H}$ . . . . .	104
5.8	Radial distribution of the oxygen abundance normalised to $r_{O/H}$ for the entire AMUSING sample . . . . .	105
5.9	Distribution of the stellar mass values for galaxies in the AMUSING sample with and without presence of the abundance inner drop and the outer flattening . . . . .	106
5.10	Dependence of the scatter relative to the radial abundance gradients on different galaxy properties for AMUSING sample	109
5.11	Distribution of slope values of the main abundance gradients in the AMUSING sample using the D16 and M13-N2 calibrators	112
5.12	Distribution of slopes depending on different galaxy properties for AMUSING sample using the D16 and M13-N2 calibrators . . . . .	112
5.13	Location of the inner abundance drop and the outer flattening for the AMUSING sample using the D16 and M13-N2 calibrators . . . . .	113
5.14	Location of the inner abundance drop and the outer flattening for the AMUSING sample in units of $r_{O/H}$ using the D16 and M13-N2 calibrators . . . . .	113
5.15	Radial distribution of the oxygen abundance normalised to $r_{O/H}$ for the entire AMUSING sample using the D16 and M13-N2 calibrators . . . . .	114

6.1	Examples of different spatial coverages of the SF spaxels in two galaxies . . . . .	121
6.2	Arm classification for eight example galaxies . . . . .	122
6.3	Arm and interarm abundance gradients for NGC0257 . . . . .	123
6.4	Comparison of the arm and interarm abundance gradients between flocculent and grand design galaxies . . . . .	126
6.5	Dependence of the scatter of the oxygen abundances in the interarm regions with the angular distance to the spiral arms . . . . .	128
6.6	Comparison of the arm and interarm abundance gradients between barred and unbarred galaxies. . . . .	130
6.7	Arm width along the arm extension . . . . .	132
7.1	Non-radial abundance variations of NGC 1762 . . . . .	142
7.2	Relation between abundance residuals and galaxy properties.I . . . . .	146
7.3	Relation between abundance residuals and galaxy properties.II . . . . .	147
7.4	2D maps of the gas oxygen abundance, H $\alpha$ LOS velocity, and their corresponding residual distributions for NGC 6754 . . . . .	152
7.5	Azimuthal profiles of the oxygen abundance residuals and H $\alpha$ LOS velocity residuals for NGC 6754 . . . . .	154
7.6	Schematic representation of the gas motions along the spiral arms of NGC 6754 . . . . .	155
7.7	Chemodynamical results of the residual gas metallicity and residual velocity fields from simulations . . . . .	157
C.1	CALIFA sample characterisation plots: IC 0159 . . . . .	205
C.2	CALIFA sample characterisation plots: NGC 0001 . . . . .	206
C.3	CALIFA sample characterisation plots: NGC 0036 . . . . .	207
C.4	CALIFA sample characterisation plots: NGC 0160 . . . . .	208
C.5	CALIFA sample characterisation plots: NGC 0214 . . . . .	209
D.1	AMUSING sample characterisation plots . . . . .	213
D.1	Non-radial abundance variations: ESO478-G006 . . . . .	214
D.2	Non-radial abundance variations of ESO506-G004 . . . . .	215
D.3	Non-radial abundance variations: ESO570-G020 . . . . .	216
D.4	Non-radial abundance variations: IC5179 . . . . .	217
D.5	Non-radial abundance variations: MCG-01-57-021 . . . . .	218
D.6	Non-radial abundance variations: NGC1080 . . . . .	219
D.7	Non-radial abundance variations: NGC1762 . . . . .	220
D.8	Non-radial abundance variations: NGC2370 . . . . .	221
D.9	Non-radial abundance variations: NGC2466 . . . . .	222
D.10	Non-radial abundance variations: NGC3120 . . . . .	223
D.11	Non-radial abundance variations: NGC3244 . . . . .	224
D.12	Non-radial abundance variations: NGC3278 . . . . .	225
D.13	Non-radial abundance variations: NGC3318 . . . . .	226

.....

D.14 Non-radial abundance variations: NGC3363 . . . . .	227
D.15 Non-radial abundance variations: NGC3464 . . . . .	228
D.16 Non-radial abundance variations: NGC3905 (E) . . . . .	229
D.17 Non-radial abundance variations: NGC3905 (W) . . . . .	230
D.18 Non-radial abundance variations: NGC4806 . . . . .	231
D.19 Non-radial abundance variations: NGC6708 . . . . .	232
D.20 Non-radial abundance variations: NGC6754 . . . . .	233
D.21 Non-radial abundance variations: PGC004701 . . . . .	234
D.22 Non-radial abundance variations: PGC128348 . . . . .	235
D.23 Non-radial abundance variations: UGC01395 . . . . .	236
D.24 Non-radial abundance variations: UGC05691 . . . . .	237
D.25 Non-radial abundance variations: UGC11214 . . . . .	238

# List of Tables

4.1	Oxygen abundance gradient slopes derived with different calibrators and distance normalisations for CALIFA sample . . .	69
7.1	Slopes of the linear fit in the abundance vs. light residuals correlation . . . . .	145
A.1	CALIFA sample characterisation I: general properties . . . .	178
A.2	CALIFA sample characterisation II: oxygen abundance information . . . . .	184
B.1	AMUSING sample characterisation I: general properties . . .	193
B.2	AMUSING sample characterisation II: oxygen abundance information . . . . .	198



# References

- [1] Abazajian, K. N., Adelman-McCarthy, J. K., Agüeros, M. A., et al. 2009, *ApJS*, 182, 543
- [2] Aguerri, J. A. L., Méndez-Abreu, J., & Corsini, E. M. 2009, *A&A*, 495, 491
- [3] Aller, L. H., ed. 1984, *Astrophysics and Space Science Library*, Vol. 112, Physics of thermal gaseous nebulae
- [4] Alloin, D., Collin-Souffrin, S., Joly, M., & Vigroux, L. 1979, *A&A*, 78, 200
- [5] Alonso-Herrero, A. & Knapen, J. H. 2001, *AJ*, 122, 1350
- [6] Athanassoula, E. 1992, *MNRAS*, 259, 345
- [7] Baba, J., Morokuma-Matsui, K., Miyamoto, Y., Egusa, F., & Kuno, N. 2016, *MNRAS*, 460, 2472
- [8] Baba, J., Saitoh, T. R., & Wada, K. 2013, *ApJ*, 763, 46
- [9] Bacon, R., Accardo, M., Adjali, L., et al. 2010, in *Proc. SPIE*, Vol. 7735, *Ground-based and Airborne Instrumentation for Astronomy III*, 773508
- [10] Bacon, R., Copin, Y., Monnet, G., et al. 2001, *MNRAS*, 326, 23
- [11] Bacon, R., Vernet, J., Borisova, E., et al. 2014, *The Messenger*, 157, 13
- [12] Baldry, I. K., Balogh, M. L., Bower, R., Glazebrook, K., & Nichol, R. C. 2004, in *American Institute of Physics Conference Series*, Vol. 743, *The New Cosmology: Conference on Strings and Cosmology*, ed. R. E. Allen, D. V. Nanopoulos, & C. N. Pope, 106–119
- [13] Baldwin, J. A., Ferland, G. J., Martin, P. G., et al. 1991, *ApJ*, 374, 580
- [14] Baldwin, J. A., Phillips, M. M., & Terlevich, R. 1981, *PASP*, 93, 5
- [15] Bally, J., Ginsburg, A., Silvia, D., & Youngblood, A. 2015, *A&A*, 579, A130
- [16] Balsaer, D. S., Rood, R. T., Bania, T. M., & Anderson, L. D. 2011, *ApJ*, 738, 27
- [17] Bamford, S. P., Nichol, R. C., Baldry, I. K., et al. 2009, *MNRAS*, 393, 1324

- [18] Barnes, J. E. & Hernquist, L. 1996, *ApJ*, 471, 115
- [19] Barrera-Ballesteros, J. K., Heckman, T. M., Zhu, G. B., et al. 2016, *MNRAS*, 463, 2513
- [20] Belfiore, F., Maiolino, R., Tremonti, C., et al. 2017, *MNRAS*, 469, 151
- [21] Bell, E. F. & de Jong, R. S. 2001, *ApJ*, 550, 212
- [22] Bell, E. F., Wolf, C., Meisenheimer, K., et al. 2004, *ApJ*, 608, 752
- [23] Bell, E. F., Zheng, X. Z., Papovich, C., et al. 2007, *ApJ*, 663, 834
- [24] Belley, J. & Roy, J.-R. 1992, *ApJS*, 78, 61
- [25] Berg, D. A., Skillman, E. D., Croxall, K. V., et al. 2015, *ApJ*, 806, 16
- [26] Berlind, A. A., Frieman, J., Weinberg, D. H., et al. 2006, *ApJS*, 167, 1
- [27] Bershadsky, M. A., Verheijen, M. A. W., Swaters, R. A., et al. 2010, *ApJ*, 716, 198
- [28] Bertin, G. & Lin, C. C. 1996, *Spiral structure in galaxies a density wave theory*, ISBN0262023962
- [29] Bilitewski, T. & Schönrich, R. 2012, *MNRAS*, 426, 2266
- [30] Bird, J. C., Kazantzidis, S., & Weinberg, D. H. 2012, *MNRAS*, 420, 913
- [31] Blanton, M. R., Hogg, D. W., Bahcall, N. A., et al. 2003, *ApJ*, 594, 186
- [32] Blanton, M. R. & Moustakas, J. 2009, *ARA&A*, 47, 159
- [33] Block, D. L. & Wainscoat, R. J. 1991, *Nature*, 353, 48
- [34] Bohlin, R. C. & Savage, B. D. 1981, *ApJ*, 249, 109
- [35] Boissier, S. & Prantzos, N. 1999, *MNRAS*, 307, 857
- [36] Boissier, S. & Prantzos, N. 2000, *MNRAS*, 312, 398
- [37] Boulanger, F., Cox, P., & Jones, A. P. 2000, in *Infrared Space Astronomy, Today and Tomorrow*, ed. F. Casoli, J. Lequeux, & F. David, 251
- [38] Bovy, J. & Rix, H.-W. 2013, *ApJ*, 779, 115
- [39] Bresolin, F. 2007, *ApJ*, 656, 186
- [40] Bresolin, F. 2011, *ApJ*, 730, 129



- [41] Bresolin, F., Garnett, D. R., & Kennicutt, Jr., R. C. 2004, *ApJ*, 615, 228
- [42] Bresolin, F., Gieren, W., Kudritzki, R.-P., et al. 2009a, *ApJ*, 700, 309
- [43] Bresolin, F., Kennicutt, R. C., & Ryan-Weber, E. 2012, *ApJ*, 750, 122
- [44] Bresolin, F., Ryan-Weber, E., Kennicutt, R. C., & Goddard, Q. 2009b, *ApJ*, 695, 580
- [45] Bundy, K., Bershadsky, M. A., Law, D. R., et al. 2015, *ApJ*, 798, 7
- [46] Caplan, J., Deharveng, L., Peña, M., Costero, R., & Blondel, C. 2000, *MNRAS*, 311, 317
- [47] Cappellari, M. & Emsellem, E. 2004, *PASP*, 116, 138
- [48] Cappellari, M., Emsellem, E., Krajnović, D., et al. 2011, *MNRAS*, 413, 813
- [49] Cardelli, J. A., Clayton, G. C., & Mathis, J. S. 1989, *ApJ*, 345, 245
- [50] Carigi, L. 2000, *Rev. Mexicana Astron. Astrofis.*, 36, 171
- [51] Carraro, G., Geisler, D., Villanova, S., Frinchaboy, P. M., & Majewski, S. R. 2007, *A&A*, 476, 217
- [52] Casasola, V., Bettoni, D., & Galletta, G. 2004, *A&A*, 422, 941
- [53] Castellanos, M., Díaz, A. I., & Terlevich, E. 2002, *MNRAS*, 329, 315
- [54] Cavichia, O., Mollá, M., Costa, R. D. D., & Maciel, W. J. 2014, *MNRAS*, 437, 3688
- [55] Cedrés, B. & Cepa, J. 2002, *A&A*, 391, 809
- [56] Cedrés, B., Cepa, J., Bongiovanni, Á., et al. 2012, *A&A*, 545, A43
- [57] Chemin, L., Huré, J.-M., Soubiran, C., et al. 2016, *A&A*, 588, A48
- [58] Cheung, E., Conroy, C., Athanassoula, E., et al. 2015, *ApJ*, 807, 36
- [59] Chiappini, C., Matteucci, F., & Romano, D. 2001, *ApJ*, 554, 1044
- [60] Christensen, T., Petersen, L., & Gammelgaard, P. 1997, *A&A*, 322, 41
- [61] Cid Fernandes, R., Mateus, A., Sodré, L., Stasińska, G., & Gomes, J. M. 2005, *MNRAS*, 358, 363
- [62] Cid Fernandes, R., Pérez, E., García Benito, R., et al. 2013, *A&A*, 557, A86

- [63] Cid Fernandes, R., Stasińska, G., Mateus, A., & Vale Asari, N. 2011, MNRAS, 413, 1687
- [64] Comparella, J. & Quillen, A. C. 2012, ArXiv e-prints [[arXiv]1207.5753]
- [65] Comte, G. 1975, A&A, 39, 197
- [66] Couto da Silva, T. C. & de Souza, R. E. 2006, A&A, 457, 405
- [67] Croom, S. M., Lawrence, J. S., Bland-Hawthorn, J., et al. 2012, MNRAS, 421, 872
- [68] Croxall, K. V., Pogge, R. W., Berg, D. A., Skillman, E. D., & Moustakas, J. 2016, ApJ, 830, 4
- [69] Dalcanton, J. J. 2007, ApJ, 658, 941
- [70] Daniel, K. J. & Wyse, R. F. G. 2015, MNRAS, 447, 3576
- [71] Davé, R., Finlator, K., & Oppenheimer, B. D. 2011, MNRAS, 416, 1354
- [72] Davé, R., Finlator, K., & Oppenheimer, B. D. 2012, MNRAS, 421, 98
- [73] de Mello, D. F., Sulentic, J. W., de Souza, R. E., Reduzzi, L., & Rampazzo, R. 1996, A&A, 308, 387
- [74] Debattista, V. P., Mayer, L., Carollo, C. M., et al. 2006, ApJ, 645, 209
- [75] Deharveng, L., Peña, M., Caplan, J., & Costero, R. 2000, MNRAS, 311, 329
- [76] Denicoló, G., Terlevich, R., & Terlevich, E. 2002, MNRAS, 330, 69
- [77] Di Matteo, P., Haywood, M., Combes, F., Semelin, B., & Snaith, O. N. 2013, A&A, 553, A102
- [78] Diaz, A. I. 1989, in *Evolutionary Phenomena in Galaxies*, ed. J. E. Beckman & B. E. J. Pagel, 377–397
- [79] Díaz, A. I. & Pérez-Montero, E. 2000, MNRAS, 312, 130
- [80] Dobbs, C. & Baba, J. 2014, PASA, 31, e035
- [81] Dobbs, C. L. & Bonnell, I. A. 2008, MNRAS, 385, 1893
- [82] Dopita, M. A. & Evans, I. N. 1986, ApJ, 307, 431
- [83] Dopita, M. A., Fischera, J., Sutherland, R. S., et al. 2006, ApJS, 167, 177

- [84] Dopita, M. A., Kewley, L. J., Sutherland, R. S., & Nicholls, D. C. 2016, *Ap&SS*, 361, 61
- [85] Dopita, M. A., Pereira, M., Kewley, L. J., & Capaccioli, M. 2002, *ApJS*, 143, 47
- [86] Dopita, M. A., Sutherland, R. S., Nicholls, D. C., Kewley, L. J., & Vogt, F. P. A. 2013, *ApJS*, 208, 10
- [87] Dressler, A. 1980, *ApJ*, 236, 351
- [88] Dutil, Y. & Roy, J.-R. 1999, *ApJ*, 516, 62
- [89] Edmunds, M. G. & Greenhow, R. M. 1995, *MNRAS*, 272, 241
- [90] Elmegreen, B. G. 1990, *Annals of the New York Academy of Sciences*, 596, 40
- [91] Elmegreen, D. M. 1981, *ApJS*, 47, 229
- [92] Elmegreen, D. M., Chromey, F. R., Bissell, B. A., & Corrado, K. 1999, *AJ*, 118, 2618
- [93] Elmegreen, D. M. & Elmegreen, B. G. 1982, *MNRAS*, 201, 1021
- [94] Elmegreen, D. M. & Elmegreen, B. G. 1987, *ApJ*, 314, 3
- [95] Esteban, C., Bresolin, F., Peimbert, M., et al. 2009, *ApJ*, 700, 654
- [96] Esteban, C., Carigi, L., Copetti, M. V. F., et al. 2013, *MNRAS*, 433, 382
- [97] Esteban, C., Fang, X., García-Rojas, J., & Toribio San Cipriano, L. 2017, *MNRAS*, 471, 987
- [98] Esteban, C., García-Rojas, J., Peimbert, M., et al. 2005, *ApJ*, 618, L95
- [99] Esteban, C., Peimbert, M., García-Rojas, J., et al. 2004, *MNRAS*, 355, 229
- [100] Esteban, C., Peimbert, M., Torres-Peimbert, S., & Escalante, V. 1998, *MNRAS*, 295, 401
- [101] Faber, S. M., Willmer, C. N. A., Wolf, C., et al. 2007, *ApJ*, 665, 265
- [102] Falcón-Barroso, J. & Knapen, J. H. 2013, *Secular Evolution of Galaxies*
- [103] Falcón-Barroso, J., Sánchez-Blázquez, P., Vazdekis, A., et al. 2011, *A&A*, 532, A95

- [104] Fathi, K., Beckman, J. E., Zurita, A., et al. 2007, *A&A*, 466, 905
- [105] Ferguson, A. M. N. & Clarke, C. J. 2001, *MNRAS*, 325, 781
- [106] Ferland, G. J. 2001, *PASP*, 113, 41
- [107] Ferrière, K. M. 2001, *Reviews of Modern Physics*, 73, 1031
- [108] Fich, M. & Silkey, M. 1991, *ApJ*, 366, 107
- [109] Focardi, P. & Kelm, B. 2002, *A&A*, 391, 35
- [110] Focardi, P., Zitelli, V., Marinoni, S., & Kelm, B. 2006, *A&A*, 456, 467
- [111] Foster, C., Lux, H., Romanowsky, A. J., et al. 2014, *MNRAS*, 442, 3544
- [112] Freeman, K. C. 1970, *ApJ*, 160, 811
- [113] Freudling, W., Romaniello, M., Bramich, D. M., et al. 2013, *A&A*, 559, A96
- [114] Friedli, D. 1998, in *Astronomical Society of the Pacific Conference Series*, Vol. 147, *Abundance Profiles: Diagnostic Tools for Galaxy History*, ed. D. Friedli, M. Edmunds, C. Robert, & L. Drissen, 287
- [115] Friedli, D. & Benz, W. 1995, *A&A*, 301, 649
- [116] Friedli, D., Benz, W., & Kennicutt, R. 1994, *ApJ*, 430, L105
- [117] Fu, J., Hou, J. L., Yin, J., & Chang, R. X. 2009, *ApJ*, 696, 668
- [118] Galbany, L., Anderson, J. P., Rosales-Ortega, F. F., et al. 2016, *MNRAS*, 455, 4087
- [119] Ganda, K., Peletier, R. F., McDermid, R. M., et al. 2007, *MNRAS*, 380, 506
- [120] García-Benito, R., Zibetti, S., Sánchez, S. F., et al. 2015, *A&A*, 576, A135
- [121] García-Rojas, J., Esteban, C., Peimbert, M., et al. 2006, *MNRAS*, 368, 253
- [122] García-Rojas, J., Esteban, C., Peimbert, M., et al. 2004, *ApJS*, 153, 501
- [123] Garnett, D. R. 1986, *PASP*, 98, 1041
- [124] Garnett, D. R., Shields, G. A., Skillman, E. D., Sagan, S. P., & Dufour, R. J. 1997, *ApJ*, 489, 63

- [125] Gibson, B. K., Pilkington, K., Brook, C. B., Stinson, G. S., & Bailin, J. 2013, *A&A*, 554, A47
- [126] Goetz, M. & Koeppen, J. 1992, *A&A*, 262, 455
- [127] Gomes, J. M., Papaderos, P., Kehrig, C., et al. 2015, ArXiv e-prints [[arXiv]1511.02191]
- [128] Gonçalves, T. S., Martin, D. C., Menéndez-Delmestre, K., Wyder, T. K., & Koekemoer, A. 2012, *ApJ*, 759, 67
- [129] González Delgado, R. M., Cerviño, M., Martins, L. P., Leitherer, C., & Hauschildt, P. H. 2005, *MNRAS*, 357, 945
- [130] González Delgado, R. M., García-Benito, R., Pérez, E., et al. 2015, *A&A*, 581, A103
- [131] González Delgado, R. M. & Pérez, E. 1997, *ApJS*, 108, 199
- [132] González Delgado, R. M., Pérez, E., Cid Fernandes, R., et al. 2014, *A&A*, 562, A47
- [133] Grand, R. J. J., Kawata, D., & Cropper, M. 2012, *MNRAS*, 421, 1529
- [134] Grand, R. J. J., Kawata, D., & Cropper, M. 2015, *MNRAS*, 447, 4018
- [135] Grand, R. J. J., Springel, V., Kawata, D., et al. 2016, *MNRAS*, 460, L94
- [136] Habergham, S. M., James, P. A., & Anderson, J. P. 2012, *MNRAS*, 424, 2841
- [137] Hammer, F., Puech, M., Chemin, L., Flores, H., & Lehnert, M. D. 2007, *ApJ*, 662, 322
- [138] Hayden, M. R., Holtzman, J. A., Bovy, J., et al. 2014, *AJ*, 147, 116
- [139] Helmboldt, J. F., Walterbos, R. A. M., Bothun, G. D., & O’Neil, K. 2005, *ApJ*, 630, 824
- [140] Henry, R. B. C., Kwitter, K. B., Jaskot, A. E., et al. 2010, *ApJ*, 724, 748
- [141] Hernández-Ibarra, F. J., Krongold, Y., Dultzin, D., et al. 2016, *MNRAS*, 459, 291
- [142] Hinshaw, G., Larson, D., Komatsu, E., et al. 2013, *ApJS*, 208, 19
- [143] Ho, I.-T., Kudritzki, R.-P., Kewley, L. J., et al. 2015, *MNRAS*, 448, 2030

- [144] Ho, I.-T., Seibert, M., Meidt, S. E., et al. 2017, *ApJ*, 846, 39
- [145] Ho, L. C., Filippenko, A. V., & Sargent, W. L. W. 1997, *ApJ*, 487, 579
- [146] Holmes, L., Spekkens, K., Sánchez, S. F., et al. 2015, *MNRAS*, 451, 4397
- [147] Hubble, E. 1943, *ApJ*, 97, 112
- [148] Hubble, E. P. 1926, *ApJ*, 64
- [149] Huntley, J. M. 1978, *ApJ*, 225, L101
- [150] Husemann, B., Jahnke, K., Sánchez, S. F., et al. 2013, *A&A*, 549, A87
- [151] Izotov, Y. I., Stasińska, G., Meynet, G., Guseva, N. G., & Thuan, T. X. 2006, *A&A*, 448, 955
- [152] Jester, S., Schneider, D. P., Richards, G. T., et al. 2005, *AJ*, 130, 873
- [153] Julian, W. H. & Toomre, A. 1966, *ApJ*, 146, 810
- [154] Karachentsev, I. D., Karachentseva, V. E., Huchtmeier, W. K., & Makarov, D. I. 2004, *AJ*, 127, 2031
- [155] Kauffmann, G., Heckman, T. M., Tremonti, C., et al. 2003a, *MNRAS*, 346, 1055
- [156] Kauffmann, G., Heckman, T. M., White, S. D. M., et al. 2003b, *MNRAS*, 341, 33
- [157] Kauffmann, G., Heckman, T. M., White, S. D. M., et al. 2003c, *MNRAS*, 341, 54
- [158] Kawata, D. & Gibson, B. K. 2003, *MNRAS*, 340, 908
- [159] Kawata, D., Hunt, J. A. S., Grand, R. J. J., Pasetto, S., & Cropper, M. 2014, *MNRAS*, 443, 2757
- [160] Kawata, D., Okamoto, T., Gibson, B. K., Barnes, D. J., & Cen, R. 2013, *MNRAS*, 428, 1968
- [161] Keel, W. C., Manning, A. M., Holwerda, B. W., et al. 2013, *PASP*, 125, 2
- [162] Kehrig, C., Monreal-Ibero, A., Papaderos, P., et al. 2012, *A&A*, 540, A11
- [163] Kelz, A., Verheijen, M. A. W., Roth, M. M., et al. 2006, *PASP*, 118, 129

- [164] Kendall, S., Kennicutt, R. C., & Clarke, C. 2011, MNRAS, 414, 538
- [165] Kennicutt, Jr., R. C. 1988, ApJ, 334, 144
- [166] Kennicutt, Jr., R. C. 1998, ApJ, 498, 541
- [167] Kennicutt, Jr., R. C., Bresolin, F., & Garnett, D. R. 2003, ApJ, 591, 801
- [168] Kennicutt, Jr., R. C., Edgar, B. K., & Hodge, P. W. 1989a, ApJ, 337, 761
- [169] Kennicutt, Jr., R. C. & Garnett, D. R. 1996, ApJ, 456, 504
- [170] Kennicutt, Jr., R. C., Keel, W. C., & Blaha, C. A. 1989b, AJ, 97, 1022
- [171] Kewley, L. J. & Dopita, M. A. 2002, ApJS, 142, 35
- [172] Kewley, L. J., Dopita, M. A., Sutherland, R. S., Heisler, C. A., & Trevena, J. 2001, ApJ, 556, 121
- [173] Kewley, L. J. & Ellison, S. L. 2008, ApJ, 681, 1183
- [174] Kewley, L. J., Rupke, D., Zahid, H. J., Geller, M. J., & Barton, E. J. 2010, ApJ, 721, L48
- [175] Knapen, J. H. 1998, MNRAS, 297, 255
- [176] Knapen, J. H., Erroz-Ferrer, S., Roa, J., et al. 2014, A&A, 569, A91
- [177] Knapp, G. 1995, S&T, 89, 20
- [178] Kobulnicky, H. A. & Kewley, L. J. 2004, ApJ, 617, 240
- [179] Koeppen, J. 1994, A&A, 281, 26
- [180] Koleva, M., Prugniel, P., Bouchard, A., & Wu, Y. 2009, A&A, 501, 1269
- [181] Kormendy, J. & Kennicutt, Jr., R. C. 2004, ARA&A, 42, 603
- [182] Krühler, T., Kuncarayakti, H., Schady, P., et al. 2017, ArXiv e-prints [[arXiv]1702.05430]
- [183] Kumamoto, J. & Noguchi, M. 2016, ApJ, 822, 110
- [184] Lacey, C. G. & Fall, S. M. 1985, ApJ, 290, 154
- [185] Li, Y., Bresolin, F., & Kennicutt, Jr., R. C. 2013, ApJ, 766, 17
- [186] Lilliefors, H. W. 1967, JASA, 62, 399402

- [187] Lin, C. C. & Shu, F. H. 1964, *ApJ*, 140, 646
- [188] Lintott, C., Schawinski, K., Bamford, S., et al. 2011, *MNRAS*, 410, 166
- [189] Lopez, L. A., Krumholz, M. R., Bolatto, A. D., Prochaska, J. X., & Ramirez-Ruiz, E. 2011, *ApJ*, 731, 91
- [190] López-Hernández, J., Terlevich, E., Terlevich, R., et al. 2013, *MNRAS*, 430, 472
- [191] López-Sánchez, Á. R., Dopita, M. A., Kewley, L. J., et al. 2012, *MNRAS*, 426, 2630
- [192] López-Sánchez, Á. R., Esteban, C., García-Rojas, J., Peimbert, M., & Rodríguez, M. 2007, *ApJ*, 656, 168
- [193] López-Sánchez, Á. R., Westmeier, T., Esteban, C., & Koribalski, B. S. 2015, *MNRAS*, 450, 3381
- [194] Maciel, W. J., Lago, L. G., & Costa, R. D. D. 2006, *A&A*, 453, 587
- [195] Madore, B. F., Nelson, E., & Petrillo, K. 2009, *ApJS*, 181, 572
- [196] Makarov, D., Prugniel, P., Terekhova, N., Courtois, H., & Vauglin, I. 2014, *A&A*, 570, A13
- [197] Marino, R. A., Gil de Paz, A., Castillo-Morales, A., et al. 2012, *ApJ*, 754, 61
- [198] Marino, R. A., Gil de Paz, A., Sánchez, S. F., et al. 2015, *ArXiv e-prints* [[arXiv]1509.07878]
- [199] Marino, R. A., Gil de Paz, A., Sánchez, S. F., et al. 2016, *A&A*, 585, A47
- [200] Marino, R. A., Rosales-Ortega, F. F., Sánchez, S. F., et al. 2013, *A&A*, 559, A114
- [201] Marinova, I. & Jogee, S. 2007, *ApJ*, 659, 1176
- [202] Markwardt, C. B. 2009, in *Astronomical Society of the Pacific Conference Series*, Vol. 411, *Astronomical Data Analysis Software and Systems XVIII*, ed. D. A. Bohlender, D. Durand, & P. Dowler, 251
- [203] Mármol-Queraltó, E., Sánchez, S. F., Marino, R. A., et al. 2011, *A&A*, 534, A8
- [204] Martin, P. & Belley, J. 1996, *ApJ*, 468, 598



- [205] Martin, P. & Roy, J.-R. 1992, *ApJ*, 397, 463
- [206] Martin, P. & Roy, J.-R. 1994, *ApJ*, 424, 599
- [207] Martin, P. & Roy, J.-R. 1995, *ApJ*, 445, 161
- [208] Martínez-Delgado, D., Gabany, R. J., Crawford, K., et al. 2010, *AJ*, 140, 962
- [209] Masset, F. & Tagger, M. 1997, *A&A*, 322, 442
- [210] Mast, D., Rosales-Ortega, F. F., Sánchez, S. F., et al. 2014, *A&A*, 561, A129
- [211] Masters, K. L., Nichol, R. C., Hoyle, B., et al. 2011, *MNRAS*, 411, 2026
- [212] Matteucci, F. & Francois, P. 1989, *MNRAS*, 239, 885
- [213] Mazzuca, L. M., Sarzi, M., Knapen, J. H., Veilleux, S., & Swaters, R. 2006, *ApJ*, 649, L79
- [214] McCall, M. L., Rybski, P. M., & Shields, G. A. 1985, *ApJS*, 57, 1
- [215] McGaugh, S. S. 1991, *ApJ*, 380, 140
- [216] Melnick, J. & Sargent, W. L. W. 1977, *ApJ*, 215, 401
- [217] Méndez-Abreu, J., Aguerri, J. A. L., Corsini, E. M., & Simonneau, E. 2008, *A&A*, 478, 353
- [218] Méndez-Abreu, J., Debattista, V. P., Corsini, E. M., & Aguerri, J. A. L. 2014, *A&A*, 572, A25
- [219] Méndez-Abreu, J., Ruiz-Lara, T., Sánchez-Menguiano, L., et al. 2017, *A&A*, 598, A32
- [220] Mendoza-Castrejón, S., Dultzin, D., Krongold, Y., González, J. J., & Elitzur, M. 2015, *MNRAS*, 447, 2437
- [221] Merchán, M. E. & Zandivarez, A. 2005, *ApJ*, 630, 759
- [222] Mihos, J. C. & Hernquist, L. 1996, *ApJ*, 464, 641
- [223] Mihos, J. C., Keating, K. M., Holley-Bockelmann, K., Pisano, D. J., & Kassim, N. E. 2012, *ApJ*, 761, 186
- [224] Minchev, I., Chiappini, C., & Martig, M. 2014, *A&A*, 572, A92
- [225] Minchev, I. & Famaey, B. 2010, *ApJ*, 722, 112

- [226] Minchev, I., Famaey, B., Combes, F., et al. 2011, *A&A*, 527, A147
- [227] Minchev, I., Famaey, B., Quillen, A. C., et al. 2012, *A&A*, 548, A126
- [228] Minchev, I. & Quillen, A. C. 2008, *MNRAS*, 386, 1579
- [229] Miralles-Caballero, D., Díaz, A. I., Rosales-Ortega, F. F., Pérez-Montero, E., & Sánchez, S. F. 2014, *MNRAS*, 440, 2265
- [230] Mo, H., van den Bosch, F. C., & White, S. 2010, *Galaxy Formation and Evolution*
- [231] Mollá, M. & Díaz, A. I. 2005, *MNRAS*, 358, 521
- [232] Moré, J. J., Garbow, B. S., & Hillstrom, K. E. 1980, Argonne National Laboratory Report ANL-80-74 [[arXiv]0806.2988]
- [233] Morisset, C., Delgado-Inglada, G., Sánchez, S. F., et al. 2016, *A&A*, 594, A37
- [234] Moustakas, J., Kennicutt, Jr., R. C., Tremonti, C. A., et al. 2010, *ApJS*, 190, 233
- [235] Ocvirk, P., Pichon, C., Lançon, A., & Thiébaud, E. 2006a, *MNRAS*, 365, 74
- [236] Ocvirk, P., Pichon, C., Lançon, A., & Thiébaud, E. 2006b, *MNRAS*, 365, 46
- [237] O'dell, C. R. 2001, *ARA&A*, 39, 99
- [238] Oey, M. S. & Kennicutt, Jr., R. C. 1993, *ApJ*, 411, 137
- [239] Oey, M. S., Parker, J. S., Mikles, V. J., & Zhang, X. 2003, *AJ*, 126, 2317
- [240] Oppenheimer, B. D. & Davé, R. 2008, *MNRAS*, 387, 577
- [241] Oppenheimer, B. D., Davé, R., Kereš, D., et al. 2010, *MNRAS*, 406, 2325
- [242] Osterbrock, D. & Flather, E. 1959, *ApJ*, 129, 26
- [243] Osterbrock, D. E. 1989, *Astrophysics of gaseous nebulae and active galactic nuclei*
- [244] Osterbrock, D. E., Tran, H. D., & Veilleux, S. 1992, *ApJ*, 389, 305
- [245] Pagel, B. E. J., Edmunds, M. G., Blackwell, D. E., Chun, M. S., & Smith, G. 1979, *MNRAS*, 189, 95

- [246] Pagel, B. E. J., Simonson, E. A., Terlevich, R. J., & Edmunds, M. G. 1992, *MNRAS*, 255, 325
- [247] Papaderos, P., Gomes, J. M., Vílchez, J. M., et al. 2013, *A&A*, 555, L1
- [248] Pasetto, S., Natale, G., Kawata, D., et al. 2016, *MNRAS*, 461, 2383
- [249] Patterson, M. T., Walterbos, R. A. M., Kennicutt, R. C., Chiappini, C., & Thilker, D. A. 2012, *MNRAS*, 422, 401
- [250] Pedicelli, S., Bono, G., Lemasle, B., et al. 2009, *A&A*, 504, 81
- [251] Peimbert, A. 2003, *ApJ*, 584, 735
- [252] Peimbert, A., Peimbert, M., & Ruiz, M. T. 2005, *ApJ*, 634, 1056
- [253] Peimbert, M. 1979, in *IAU Symposium*, Vol. 84, *The Large-Scale Characteristics of the Galaxy*, ed. W. B. Burton, 307–315
- [254] Peimbert, M. & Costero, R. 1969, *Boletín de los Observatorios Tonantzintla y Tacubaya*, 5, 3
- [255] Peimbert, M. & Spinrad, H. 1970, *ApJ*, 159, 809
- [256] Peimbert, M., Storey, P. J., & Torres-Peimbert, S. 1993, *ApJ*, 414, 626
- [257] Pérez, E., Cid Fernandes, R., González Delgado, R. M., et al. 2013, *ApJ*, 764, L1
- [258] Pérez-Montero, E. 2014, *MNRAS*, 441, 2663
- [259] Pérez-Montero, E. 2017, *PASP*, 129, 043001
- [260] Pérez-Montero, E. & Contini, T. 2009, *MNRAS*, 398, 949
- [261] Pérez-Montero, E. & Díaz, A. I. 2005, *MNRAS*, 361, 1063
- [262] Pettini, M. & Pagel, B. E. J. 2004, *MNRAS*, 348, L59
- [263] Pilkington, K., Few, C. G., Gibson, B. K., et al. 2012, *A&A*, 540, A56
- [264] Pilyugin, L. S. 2000, *A&A*, 362, 325
- [265] Pilyugin, L. S., Ferrini, F., & Shkvarun, R. V. 2003, *A&A*, 401, 557
- [266] Pilyugin, L. S. & Thuan, T. X. 2005, *ApJ*, 631, 231
- [267] Pilyugin, L. S., Vílchez, J. M., & Contini, T. 2004, *A&A*, 425, 849
- [268] Pilyugin, L. S., Vílchez, J. M., & Thuan, T. X. 2010, *ApJ*, 720, 1738

- [269] Pogge, R. W., Owen, J. M., & Atwood, B. 1992, *ApJ*, 399, 147
- [270] Portinari, L. & Chiosi, C. 2000, *A&A*, 355, 929
- [271] Postman, M. & Geller, M. J. 1984, *ApJ*, 281, 95
- [272] Prantzos, N. & Boissier, S. 2000, *MNRAS*, 313, 338
- [273] Qu, Y., Di Matteo, P., Lehnert, M. D., van Driel, W., & Jog, C. J. 2011, *A&A*, 535, A5
- [274] Quillen, A. C., Dougherty, J., Bagley, M. B., Minchev, I., & Comparetta, J. 2011, *MNRAS*, 417, 762
- [275] Quillen, A. C., Minchev, I., Bland-Hawthorn, J., & Haywood, M. 2009, *MNRAS*, 397, 1599
- [276] Quiroza, C., Rood, R. T., Bania, T. M., Balsler, D. S., & Maciel, W. J. 2006, *ApJ*, 653, 1226
- [277] Ramella, M., Geller, M. J., Pisani, A., & da Costa, L. N. 2002, *AJ*, 123, 2976
- [278] Reid, I. N., Brewer, C., Brucato, R. J., et al. 1991, *PASP*, 103, 661
- [279] Rich, J. A., Torrey, P., Kewley, L. J., Dopita, M. A., & Rupke, D. S. N. 2012, *ApJ*, 753, 5
- [280] Roberts, M. S. & Haynes, M. P. 1994, *ARA&A*, 32, 115
- [281] Rosa, D. A., Dors, O. L., Krabbe, A. C., et al. 2014, *MNRAS*, 444, 2005
- [282] Rosales-Ortega, F. F., Díaz, A. I., Kennicutt, R. C., & Sánchez, S. F. 2011, *MNRAS*, 415, 2439
- [283] Rosales-Ortega, F. F., Kennicutt, R. C., Sánchez, S. F., et al. 2010, *MNRAS*, 405, 735
- [284] Rosales-Ortega, F. F., Sánchez, S. F., Iglesias-Páramo, J., et al. 2012, *ApJ*, 756, L31
- [285] Roth, M. M., Kelz, A., Fechner, T., et al. 2005, *PASP*, 117, 620
- [286] Roškar, R., Debattista, V. P., Quinn, T. R., & Wadsley, J. 2012, *MNRAS*, 426, 2089
- [287] Roy, J.-R. 1996, in *Astronomical Society of the Pacific Conference Series*, Vol. 91, IAU Colloq. 157: Barred Galaxies, ed. R. Buta, D. A. Crocker, & B. G. Elmegreen, 63

- [288] Roy, J.-R. & Kunth, D. 1995, *A&A*, 294, 432
- [289] Roy, J.-R. & Walsh, J. R. 1997, *MNRAS*, 288, 715
- [290] Rozas, M., Knapen, J. H., & Beckman, J. E. 1996, *A&A*, 312, 275
- [291] Rozas, M., Zurita, A., Heller, C. H., & Beckman, J. E. 1999, *A&AS*, 135, 145
- [292] Rubin, R. H., Simpson, J. P., Haas, M. R., & Erickson, E. F. 1991, *PASP*, 103, 834
- [293] Rudolph, A. L., Fich, M., Bell, G. R., et al. 2006, *ApJS*, 162, 346
- [294] Ruiz-Lara, T., Pérez, I., Florido, E., et al. 2016, *MNRAS*, 456, L35
- [295] Rupke, D. S. N., Kewley, L. J., & Barnes, J. E. 2010a, *ApJ*, 710, L156
- [296] Rupke, D. S. N., Kewley, L. J., & Chien, L.-H. 2010b, *ApJ*, 723, 1255
- [297] Sackett, P. D. 1997, *ApJ*, 483, 103
- [298] Sánchez, S. F. 2006, *Astronomische Nachrichten*, 327, 850
- [299] Sánchez, S. F., Cardiel, N., Verheijen, M. A. W., et al. 2007, *A&A*, 465, 207
- [300] Sánchez, S. F., Galbany, L., Pérez, E., et al. 2015, *A&A*, 573, A105
- [301] Sánchez, S. F., García-Benito, R., Zibetti, S., et al. 2016a, *ArXiv e-prints* [[arXiv]1604.02289]
- [302] Sánchez, S. F., Kennicutt, R. C., Gil de Paz, A., et al. 2012a, *A&A*, 538, A8
- [303] Sánchez, S. F., Pérez, E., Sánchez-Blázquez, P., et al. 2016b, *Rev. Mexicana Astron. Astrofis.*, 52, 171
- [304] Sánchez, S. F., Pérez, E., Sánchez-Blázquez, P., et al. 2016c, *Rev. Mexicana Astron. Astrofis.*, 52, 21
- [305] Sánchez, S. F., Rosales-Ortega, F. F., Iglesias-Páramo, J., et al. 2014, *A&A*, 563, A49
- [306] Sánchez, S. F., Rosales-Ortega, F. F., Jungwiert, B., et al. 2013, *A&A*, 554, A58
- [307] Sánchez, S. F., Rosales-Ortega, F. F., Kennicutt, R. C., et al. 2011, *MNRAS*, 410, 313

- [308] Sánchez, S. F., Rosales-Ortega, F. F., Marino, R. A., et al. 2012b, *A&A*, 546, A2
- [309] Sánchez, S. F. & Sánchez-Menguiano, L. 2017, in *Revista Mexicana de Astronomía y Astrofísica Conference Series*, Vol. 49, *Revista Mexicana de Astronomía y Astrofísica Conference Series*, 28–32
- [310] Sánchez-Blázquez, P., Rosales-Ortega, F. F., Méndez-Abreu, J., et al. 2014, *A&A*, 570, A6
- [311] Sánchez-Menguiano, L., Pérez, I., Zurita, A., et al. 2015, *MNRAS*, 450, 2670
- [312] Sánchez-Menguiano, L., Sánchez, S. F., Kawata, D., et al. 2016a, *ApJ*, 830, L40
- [313] Sánchez-Menguiano, L., Sánchez, S. F., Pérez, I., et al. 2017, *A&A*, 603, A113
- [314] Sánchez-Menguiano, L., Sánchez, S. F., Pérez, I., et al. 2016b, *A&A*, 587, A70
- [315] Sanders, N. E., Caldwell, N., McDowell, J., & Harding, P. 2012, *ApJ*, 758, 133
- [316] Sarzi, M., Falcón-Barroso, J., Davies, R. L., et al. 2006, *MNRAS*, 366, 1151
- [317] Scalo, J. & Elmegreen, B. G. 2004, *ARA&A*, 42, 275
- [318] Scannapieco, C., Tissera, P. B., White, S. D. M., & Springel, V. 2008, *MNRAS*, 389, 1137
- [319] Scannapieco, C., White, S. D. M., Springel, V., & Tissera, P. B. 2009, *MNRAS*, 396, 696
- [320] Schawinski, K., Urry, C. M., Simmons, B. D., et al. 2014, *MNRAS*, 440, 889
- [321] Schiminovich, D., Wyder, T. K., Martin, D. C., et al. 2007, *ApJS*, 173, 315
- [322] Schlegel, D. J., Finkbeiner, D. P., & Davis, M. 1998, *ApJ*, 500, 525
- [323] Schönrich, R. & Binney, J. 2009, *MNRAS*, 396, 203
- [324] Searle, L. 1971, *ApJ*, 168, 327
- [325] Sellwood, J. A. & Binney, J. J. 2002, *MNRAS*, 336, 785

- [326] Sellwood, J. A. & Carlberg, R. G. 2014, *ApJ*, 785, 137
- [327] Sellwood, J. A. & Wilkinson, A. 1993, *Reports on Progress in Physics*, 56, 173
- [328] Shaver, P. A., McGee, R. X., Newton, L. M., Danks, A. C., & Pottasch, S. R. 1983, *MNRAS*, 204, 53
- [329] Sheth, K., Elmegreen, D. M., Elmegreen, B. G., et al. 2008, *ApJ*, 675, 1141
- [330] Shields, G. A. 1974, *ApJ*, 193, 335
- [331] Smith, H. E. 1975, *ApJ*, 199, 591
- [332] Soto, K. T., Lilly, S. J., Bacon, R., Richard, J., & Conseil, S. 2016, *MNRAS*, 458, 3210
- [333] Spitoni, E., Matteucci, F., & Marcon-Uchida, M. M. 2013, *A&A*, 551, A123
- [334] Stasińska, G. 1978, *A&A*, 66, 257
- [335] Stasińska, G., Vale Asari, N., Cid Fernandes, R., et al. 2008, *MNRAS*, 391, L29
- [336] Strateva, I., Ivezić, Ž., Knapp, G. R., et al. 2001, *AJ*, 122, 1861
- [337] Strömgren, B. 1939, *ApJ*, 89, 526
- [338] Takahashi, S., Ho, P. T. P., Teixeira, P. S., Zapata, L. A., & Su, Y.-N. 2013, *ApJ*, 763, 57
- [339] Terlevich, E., López-Hernández, J., Terlevich, R., & Rosa González, D. 2014, in *Massive Young Star Clusters Near and Far: From the Milky Way to Reionization*, 67–72
- [340] Thilker, D. A., Braun, R., & Walterbos, R. A. M. 2000, *AJ*, 120, 3070
- [341] Thornley, M. D. 1996, *ApJ*, 469, L45
- [342] Thornley, M. D. & Mundy, L. G. 1997, *ApJ*, 484, 202
- [343] Toomre, A. 1990, *Gas-hungry Sc spirals.*, ed. R. Wielen, 292–303
- [344] Toribio San Cipriano, L., García-Rojas, J., Esteban, C., Bresolin, F., & Peimbert, M. 2016, *MNRAS*, 458, 1866
- [345] Torrey, P., Cox, T. J., Kewley, L., & Hernquist, L. 2012, *ApJ*, 746, 108

- [346] Tremonti, C. A., Heckman, T. M., Kauffmann, G., et al. 2004, *ApJ*, 613, 898
- [347] Tsujimoto, T., Yoshii, Y., Nomoto, K., & Shigeyama, T. 1995, *A&A*, 302, 704
- [348] Tully, R. B. 2015, *AJ*, 149, 171
- [349] van den Bergh, S. 2007, *AJ*, 134, 1508
- [350] van der Kruit, P. C. & Freeman, K. C. 2011, *ARA&A*, 49, 301
- [351] van Zee, L., Salzer, J. J., Haynes, M. P., O'Donoghue, A. A., & Balonek, T. J. 1998, *AJ*, 116, 2805
- [352] Vazdekis, A., Sánchez-Blázquez, P., Falcón-Barroso, J., et al. 2010, *MNRAS*, 404, 1639
- [353] Veilleux, S., Cecil, G., & Bland-Hawthorn, J. 2005, *ARA&A*, 43, 769
- [354] Veilleux, S. & Osterbrock, D. E. 1987, *ApJS*, 63, 295
- [355] Vila-Costas, M. B. & Edmunds, M. G. 1992, *MNRAS*, 259, 121
- [356] Vilchez, J. M. & Esteban, C. 1996, *MNRAS*, 280, 720
- [357] Vlajić, M., Bland-Hawthorn, J., & Freeman, K. C. 2009, *ApJ*, 697, 361
- [358] Vlajić, M., Bland-Hawthorn, J., & Freeman, K. C. 2011, *ApJ*, 732, 7
- [359] Vogt, F. P. A., Pérez, E., Dopita, M. A., Verdes-Montenegro, L., & Borthakur, S. 2017, *ArXiv e-prints* [[arXiv]1701.01728]
- [360] Vorontsov-Velyaminov, B. A. 1977, *A&AS*, 28, 1
- [361] Wada, K., Baba, J., & Saitoh, T. R. 2011, *ApJ*, 735, 1
- [362] Walcher, C. J., Wisotzki, L., Bekeraité, S., et al. 2014, *A&A*, 569, A1
- [363] Weillbacher, P. M., Streicher, O., Urrutia, T., et al. 2014, in *Astronomical Society of the Pacific Conference Series*, Vol. 485, *Astronomical Data Analysis Software and Systems XXIII*, ed. N. Manset & P. Forshay, 451
- [364] Werk, J. K., Putman, M. E., Meurer, G. R., & Santiago-Figueroa, N. 2011, *ApJ*, 735, 71
- [365] Werk, J. K., Putman, M. E., Meurer, G. R., et al. 2010, *ApJ*, 715, 656
- [366] White, R. A., Bliton, M., Bhavsar, S. P., et al. 1999, *AJ*, 118, 2014



- [367] Willett, K. W., Lintott, C. J., Bamford, S. P., et al. 2013, *MNRAS*, 435, 2835
- [368] Wilman, D. J. & Erwin, P. 2012, *ApJ*, 746, 160
- [369] Wolf, C., Meisenheimer, K., Rix, H.-W., et al. 2003, *A&A*, 401, 73
- [370] Yang, X., Mo, H. J., van den Bosch, F. C., et al. 2007, *ApJ*, 671, 153
- [371] Yong, D., Carney, B. W., Teixeira de Almeida, M. L., & Pohl, B. L. 2006, *AJ*, 131, 2256
- [372] Zaritsky, D., Kennicutt, Jr., R. C., & Huchra, J. P. 1994, *ApJ*, 420, 87
- [373] Zinchenko, I. A., Pilyugin, L. S., Grebel, E. K., Sánchez, S. F., & Vílchez, J. M. 2016, *MNRAS*, 462, 2715
- [374] Zuckerman, B. 1973, *ApJ*, 183, 863
- [375] Zurita, A., Relaño, M., Beckman, J. E., & Knapen, J. H. 2004, *A&A*, 413, 73